UNIVERSIDAD AUTÓNOMA DE MADRID

PhD Thesis

Exciton-Polariton condensates in patterned microcavities

Author:

Elena Rozas Jiménez

Supervisors: Prof. Luis Viña

Prof. Mª Dolores Martín

DEPARTAMENTO DE FÍSICA DE MATERIALES

March 2020

A mi familia.

Abstract

This PhD thesis presents experimental studies of exciton-polariton condensates in GaAs-based microcavities that have been patterned with different structures considering the feasibility of their designs for polaritonic-based circuits. The strong light-matter coupling in the cavities gives rise to fascinating new effects that make polaritons appropriate candidates for nonlinear optical technologies: their bosonic nature, together with their light effective mass, facilitates their condensation in a macroscopic coherent phase that presents high similarities to Bose-Einstein condensates; their excitonic part leads to strong polariton-polariton Coulomb interactions; thanks to their photonic content, polaritons can be easily created and manipulated at will through optical excitation sources. Furthermore, the wavefunction of the photons emitted from the cavity is an exact copy of the intracavity polariton wavefunction and therefore, using simple optical techniques, it is possible to gain access to important information, such as the phase, wave vector or the spin of these quasiparticles, to name just a few.

In more detail, this thesis is organized as follows:

Chapter 1 presents the physics behind excitons-polaritons, with emphasis on the creation of polariton condensates in semiconductor microcavities. The semiconductor quasiparticles involved in the formation of polaritons, photons and excitons, are described individually. A general description of the propagation of light in microcavities and its interaction with excitons confined in the system is discussed. Special attention is also given to the concepts behind the Bose-Einstein condensation. Finally, the theoretical description for interference between condensates in momentum-space and the emergence of Josephson oscillations are presented.

Chapter 2 describes the experimental techniques used during the thesis. The imaging techniques for real- and momentum-space are presented, describing in detail the excitation and

detection conditions. Additionally, the chapter gathers the description of the different samples used in the experiments, all of them based on differently patterned GaAs microcavities.

In chapter 3 we present a study of the temperature effect on the coherence of traveling polariton condensates. We obtain interference fringes in momentum-space as a result of the interference between polariton condensates propagating with the same speed. In a similar fashion, we obtain interference fringes in real-space when condensates, traveling in opposite directions, meet. The fringes are analyzed through two different methods, obtaining the visibility of the fringes with the first one and the fraction of condensed to un-condensed polaritons with the second. Both methods evidence a gradual decay of the condensates' coherence with increasing temperature, and allow to obtain the critical temperature for the Bose-Einstein-like condensate phase transition. We compare our experimental findings with theoretical models, developed for atomic condensates, to describe the condensates' coherence fading with temperature.

In chapter 4 we report a detailed study of several coupler devices consisting of two parallel planar waveguides where a deviation of 45º at both ends of the structures has been introduced. We have characterized the photonic landscape experienced by polaritons along the couplers, which reveals that an additional discretization of the polaritons' wave vectors is introduced when the orientation of the waveguide is changed. As a consequence of the introduction of the 45º deviation in the waveguide, we find a deceleration when polariton condensates turn at the bends of the circuits where they propagate. We have found that, for certain coupler's parameters, the tunneling of polaritons between the two arms of the device is allowed, giving rise to the direct observation of Josephson oscillations. Finally, we study the coupler's sensitivity to linear polarization to investigate the possibility of benefiting from the spin degree of freedom. A peculiar oscillating behavior in the linear polarization at the output terminal is found.

In chapter 5, we study a compact counter-directional polariton router which operates as a polaritonic resonant tunnel diode. The device implements the means to control the propagation direction of polariton condensates making use of a photonic microdisk potential, which couples two lithographically defined waveguides and reverses the condensate's propagation direction. The device can feasibly be scaled to larger logic architectures without the requirement for any active external control parameters. Additionally, we investigate the ultrafast dynamics of the device via time-resolved photoluminescence measurements.

In chapter 6 we report the realization of a synthetic magnetic field for polaritons in a honeycomb lattice made of coupled semiconductor micropillars. First, we describe theoretically

how to implement a gauge field, engineering the lattice parameters. A strong synthetic field is induced by introducing an uniaxial strain in the lattice, giving rise to the formation of Landau levels at the Dirac points. We report direct evidences of polaritonic Landau levels in samples with different strain gradients, observing also the localization of the $n = 0$ Landau level wavefunction in one sublattice.

Resumen

Esta tesis doctoral presenta estudios experimentales de condensados de polaritones excitónicos en microcavidades basadas en GaAs, en las cuales han sido esculpidas diferentes estructuras, considerando la viabilidad de sus diseños para circuitos basados en polaritones. El acoplamiento fuerte de la luz con la materia en las cavidades da lugar a nuevos efectos fascinantes, haciendo de los polaritones unos candidatos excelentes para las tecnologías ópticas no lineales: su naturaleza bosónica, junto con su ligera masa efectiva, facilita su condensación en una fase macrocópica coherente que presenta grandes similitudes con los condensados de Bose-Einstein; su parte excitónica conduce a fuertes interacciones polaritón-polaritón de Coulomb; gracias a su contenido fotónico, los polaritones se pueden crear y manipular fácilmente a través de fuentes de excitación óptica. Además, la función de onda de los fotones emitidos desde la cavidad es una copia exacta de la función de onda del polaritón dentro de la cavidad y, por lo tanto, utilizando técnicas ópticas simples, es posible obtener acceso a información importante como la fase, el vector de onda o el espín de estas cuasipartículas, por nombrar solo algunas.

Esta tesis se organiza de la siguiente manera:

El capítulo 1 presenta la física subyacente a los polaritones excitónicos, con énfasis en la creación de condensados de polaritones en microcavidades semiconductoras. Las cuasipartículas semiconductoras implicadas en la formación de polaritones, fotones y excitones, se describen individualmente. Se analiza una descripción general de la propagación de la luz en microcavidades y su interacción con los excitones confinados en dicho sistema. También se presta especial atención a los conceptos básicos de la condensación Bose-Einstein. Finalmente, se presenta una descripción teórica de la interferencia entre condensados en el espacio de momentos y la aparición de las oscilaciones de Josephson.

El capítulo 2 describe las técnicas experimentales utilizadas durante la tesis. Se muestran las técnicas de imagen para el espacio real y el espacio de momentos, describiendo en detalle

las condiciones de excitación y detección. Además, el capítulo reúne la descripción de las diferentes muestras utilizadas en los experimentos, todas ellas basadas en microcavidades de GaAs con diferentes estructuras.

El capítulo 3 presenta un estudio sobre el efecto de la temperatura en la coherencia de condensados de polaritones que se propagan. Se obtienen franjas de interferencia en el espacio de momentos debido a la interferencia entre condensados de polaritones propagándose con la misma velocidad, es decir, el mismo vector de onda. De forma similar, se obtienen franjas de interferencia en el espacio real cuando los condensados, viajando en direcciones opuestas, coinciden en un punto de la muestra. Las franjas se analizan utilizando dos métodos diferentes: con el primero se obteniene la visibilidad de las franjas en el primero y con el segundo la proporción de polaritones condensados a no condensados. Ambos métodos muestran una disminución gradual de la coherencia de los condensados con el aumento de la temperatura, y permiten obtener la temperatura crítica para la transición de fase de un condensado tipo Bose-Einstein. Finalmente, se comparan los resultados experimentales con modelos teóricos, desarrollados para condensados atómicos, con el fin de describir el desvanecimiento de la coherencia de los condensados con la temperatura.

El capítulo 4 describe un estudio detallado de varios dispositivos acopladores, los cuales consisten en dos guías de ondas planas paralelas en las que se ha introducido una desviación de 45º en ambos extremos de la estructura. Se ha caracterizado el *escenario fotónico* experimentado por los polaritones, que revela una discretización adicional de los vectores de onda de los polaritones al cambiar la orientación de la guía de ondas. Como consecuencia de este cambio en la trayectoria, se encuentra una desaceleración en los condensados cuando giran en las curvas de los circuitos donde se propagan. Además, se ha encontrado que, para ciertos parámetros de los acopladores, se activa el acoplo de polaritones entre los dos brazos del dispositivo, dando lugar a la observación directa de las oscilaciones de Josephson. Por último, se estudia la sensibilidad del acoplador a la polarización lineal para investigar la posibilidad de explotación del espín de los polaritones. Se observa un comportamiento oscilante peculiar en análisis de la polarización lineal del terminal de salida.

El capítulo 5, muestra un enrutador contradireccional de polaritones que funciona como un diodo de túnel resonante. El dispositivo implementa los medios para controlar la dirección de propagación de los condensados mediante un potencial fotónico en forma de disco, al cual se acoplan dos guías de ondas definidas litográficamente, invirtiendo así la dirección de propagación del condensado. El dispositivo puede escalarse a arquitecturas lógicas mayores

sin la necesidad de ningún parámetro de control externo. También se investiga la dinámica ultrarrápida del dispositivo a través de mediciones de fotoluminiscencia resueltas en tiempo.

El capítulo 6 estudia la creación de un campo magnético artificial para polaritones en una red de panal de abeja hecha de micropilares de semiconductores acoplados. En primer lugar, se describe teóricamente cómo implementar un campo de *gauge* diseñando cuidadosamente la red. Es posible inducir un fuerte campo magnético (artificial) al introducir una deformación o tensión uniaxial en la red, dando lugar a la formación de los niveles de Landau en los puntos de Dirac. Se muestra además, evidencias directas de la aparición de niveles de Landau fotónicos en muestras con diferentes grados de deformación, observando también la función de ondas del nivel de Landau $n = 0$ localizada en una sola subred.

Acknowledgments

The success of the work presented in this thesis would have never been possible without the help and supervision of Prof. Luis Viña and Prof. María Dolores Martín, to whom I would like to express my deepest gratitude. Thank you for believing in me and letting me be part of the SEMICUAM group at the departamento de Física de Materiales of Universidad Autónoma de Madrid. From the very beginning you have supported me, trained me and shared your time and expertise, which are the most valuable gifts anyone could have received during these four years of work. But above all, thank you for your patience, especially in these last stressful times while writing the thesis. I hope to enjoy my next destination as much as I have done during my PhD.

This thesis would not have been possible without the high-quality samples grown by our outstanding international collaborators. I greatly acknowledge Prof. Pavlos Savvidis' group from the IESL-FORTH institution at Heraklion (Greece) and Prof. Sven Höfling's group from the Universität Würzburg (Germany) for providing the last-generation samples that have allowed to obtain the results presented in this work. I would also like to thank Prof. Marek Potemski from the Laboratoire National des Champs Magnétiques Intenses in Grenoble (France) for my first contact in a foreign laboratory, carrying out experiments and discussing the results.

I also greatly acknowledge the friendly and stimulating work environment found during my research stay in the "Topological Photonics" group leaded by Prof. Alberto Amo at the "Laboratoire de Physique des Lasers, Atomes et Molécules" (PhLAM), institution belonging to the CNRS and the Université de Lille (France). The enlightenment from Prof. Alberto Amo and Dr. Omar Jamadi have culminated in the redaction of chapter 6 of this thesis and the next publication of the results obtained during the stay.

I am grateful to the FPI scholarship with reference BES-2015-074708 from the Spanish MINECO grant No. MAT2014-53119-C2-1-R and No. MAT2017-83722-R for the financial

support during these four years of thesis, which not only has supported the work presented here but has allowed the spreading of the results in many international conferences and benefit from the research stay in the group of Prof. Alberto Amo.

Quisiera agradecer también a todas las personas que me han acompañado durante este viaje de cuatro años en Madrid, haciendo que cada día fuera una aventura nueva: Alex, David, Laura R., Laura S., Maria, Juanfran, Sergio, Iris, Mariano y Gus. Gracias por haberme aceptado desde el minuto 0 y por todos los buenos momentos compartidos, incluidos los pequeños viajes que hemos hecho. Aunque a partir de ahora estemos desperdigados por el mundo... sé que de aquí me llevo muy buenas amistades que durarán eras. Me gustaría hacer una mención espacial al grupo de "Vacanadas" por haberme apoyado en los duros días de escritura de esta tesis. Lo conseguimos muchachos!

Aitor, a ti tengo mucho que agradecerte, no solo me has aguantado durante los momentos de escribir la tesis, sino que no te has quejado ni una sola vez. Tu santa paciencia y tu apoyo han sido esenciales para acabar este viaje. Y sobretodo gracias por tu sentido del humor. Ahora ya solo queda esperar al siguiente viaje...

Finalmente, esta tesis va dedicada muy especialmente a mi familia: mamá, papá y Eva. Muchas gracias por vuestro amor y apoyo incondicional, por la paciencia y sobretodo por manternerme alimentada en los momentos difícles (ya sea con tartas o dulces de navidad). Sin vuestra ayuda, este camino que realmente empezó muchos años atrás, habría sido mucho más duro y no habría podido llegar hasta donde estoy hoy. Eva, gracias por mantener la frecuencia del amor estos últimos tiempos de estrés, tu me entiendes. Os lo debo todo. Al resto de familia, tanto si compartimos apellido como si no, teneis todo mi agradecimiento por el consuelo y los ánimos, solo he recibido cariño y paciencia de vuestra parte durante este viaje.

List of publications

- *Temperature dependence of the coherence in polariton condensates*
  E. Rozas, M. D. Martín, C. Tejedor, L. Viña, G. Deligeorgis, Z. Hatzopoulos and P.G. Savvidis
  Physical Review B **97**, 075442 (2018)

- *Counter-directional polariton coupler*
  M. Klaas, J. Beierlein, E. Rozas, S. Klembt, H. Suchomel, T. H. Harder, K. Winkler, M. Emmerling, H. Flayac., M. D. Martín, L. Viña, S. Höfling and C. Schneider
  Applied Physics Letters **114**, 061102 (2019)

- *Determination of polariton condensates' critical temperature*
  E. Rozas, M. D. Martín, C. Tejedor, L. Viña, G. Deligeorgis, Z. Hatzopoulos and P.G. Savvidis
  Physica Status Solidi B **256**, 1800519 (2019)

- *Direct observation of photonic Landau levels and helical edge states in strained honeycomb lattices*
  O. Jamadi, E. Rozas, G. Salerno, M. Milićević, T. Ozawa, I. Sagnes, A. Lemaître, L. Le Gratiet, A. Harouri, I. Carusotto, J. Bloch and A. Amo
  arXiv: 2001.10395 (2020)

- *Impact of the energetic landscape on polariton condensates' propagation along a coupler*
  E. Rozas, A. Yulin, I. Shelyk, M. D. Martín, L. Viña, M. Klaas, J. Beierlein, S. Klembt, S. Höfling and C. Schneider
  In processing (2020)

Contents

List of Figures

Nomenclature

Acronyms

1D One-dimensonal

2D Two-dimensonal

Al Aluminium

$Al_xGa_{1-x}As$ Aluminium Gallium Arsenide with a variable concentration x

As Arsenic

BEC Bose-Einstein Condensates

BS Beam Splitter

CCD Charge-Coupled Device

cw continuous wave

DBR Distributed Bragg Reflector

Fcc Face-centered cubic, refers to Bravais' lattices

FWHM Full Width at Half Maximum

Ga Gallium

GaAs Gallium Arsenide

GL Ginzburg-Landau equation

LBO Lithium triborate (LiB_3O_5)

LPB Lower Polariton Branch

MBE Molecular Beam Epitaxy

MC Microcavity

NA Numerical Aperture

O Oxigen

PL Photoluminescenece

QHE Quantum Hall Effect

QW Quantum Well

rpm revolutions per minute

SEM Scanning Electron Microscopy

Ti Titanium

UPB Upper Polariton Branch

WP Wave Packet

Physical constants

$\hbar$ Reduced Planck constant $\hbar = h/2\pi = 6.582119624\text{x}10^{-16}$ eV s

h Planck constant

e Electron charge $e = 1.602176565\text{x}10^{19}$ C

Symbols

α Attenuation constant

α_s Polariton scattering strength

δ Detuning of the cavity, indicating the energy difference between the cavity mode and the exciton level

Γ Gain saturation

γ Polariton loss rate

λ_0 Wavelength of an electromagnetic wave in vacuum

ω Angular frequency of an electromagnetic wave

υ Visibility of interference fringes

B Magnetic field

k Modulus of the wave vector of an electromagnetic wave in a media, $k = 2\pi n/\lambda_0$

k_0 Modulus of the wave vector of an electromagnetic wave in vacuum, $k = 2\pi/\lambda_0$

n Refractive index

P Degree of polarization.

P_{th} Power threshold density for polariton condensation. Expressed in units of kW/cm^2

Q Quality factor

T Temperature

T_C	Critical temperature
f_C	Fraction of condensed to uncondensed polariton population

Chapter 1

Introduction to exciton-polaritons

In this introductory chapter to the exciton-polariton field, a few concepts about their phenomenology are explained. In the first place, the structures where polaritons emerge are described, paying special attention to microcavities (MC). The results presented in this thesis are obtained in samples with this type of structures. Polaritons emerging from the strong coupling regime between photons and excitons are bosonic quasiparticles that can be described from a classical point of view. When the particle density increases or the temperature of the ensemble decreases, a new type of coherent macroscopic state, called Bose-Einstein condensate (BEC), can be achieved. The main properties of these condensates are explained in detail here. In the final part of the chapter, two particular phenomena for BEC systems are detailed: interference between two condensates and the appearance of the Josephson tunneling between two interacting condensates.

1.1 Semiconductor crystals

In nature, the crystalline structure is one way in which atoms are arranged to create a macroscopic solid. Atoms are repeated infinitely with a periodic pattern, called unit cell, so that the solid can be fully described by studying only a small section with few atoms. In 1830, Hessel classified for the first time the natural crystals based on their structure and crystalline symmetry enumerating 32 different groups (point groups). In 1850 Bravais defined discrete arrays of points that can form an infinite lattice by translation operations [1]. These sets of arrays, known as Bravais lattices, are clasified in 14 groups. Although crystal surfaces are

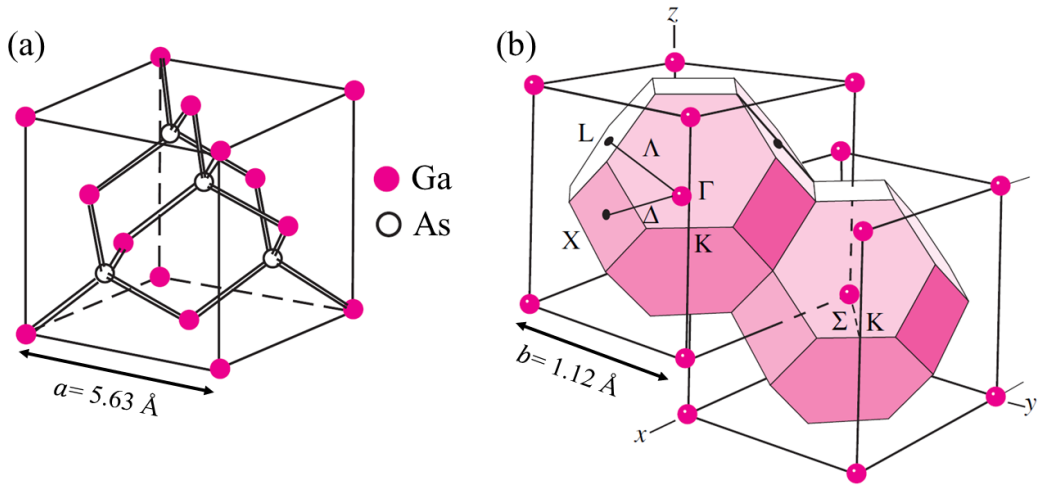

Figure 1.1. (a) The crystalline structure of GaAs with a zincblende unit cell. The lattice parameter is defined by $a = 5.63$ Å [2]. (b) The reciprocal lattice of the face-centered cubic (fcc) lattice shown with the 1st Brillouin zone. The lattice parameter is given by $b = 2\pi/a = 1.12$ Å^{-1} [2]. Special high-symmetry points are indicated by Γ, X and L, while high-symmetry lines joining some of these points are labeled as Λ and Δ. Adapted from [3].

visible and Bravais lattices are arrays of points not visible to the naked eye, they are used nowadays to classify crystals.

In the following the crystalline structure of GaAs will be discussed, as all the structures studied during this thesis are based on this material. The crystalline structure of GaAs, shown in Fig. 1.1(a), is a zincblende structure formed by two atoms arranged in a cubic structure. Its corresponding lattice is the *face-centered cubic* lattice (fcc) in the Bravais' classification since one of the atoms, in the case shown in the Fig. 1.1(a), Ga, is placed in every vertex and centered on each face of the cube. In this type of lattice As atoms, located inside the cube, are surrounded by four Ga atoms. The whole structure is contained in a cube with an arista of 5.63 Å, which is defined as the lattice parameter a [2]. This cube is the unit cell for this material and can reproduce the crystal structure by being periodically translated.

For any given lattice in real-space (also known as direct lattice) a reciprocal lattice can be defined. The latter represents the Fourier transform of the direct lattice. Therefore, both lattices can be described using the lattice parameter a. While the direct lattice only exists in real-space, the reciprocal lattice only exists in momentum-space (k-space). The unit cell in the reciprocal lattice is known as the 1st Brillouin zone. A scheme of the 1st Brillouin zone corresponding to the fcc lattice is shown in Fig. 1.1(b). The structure is now contained in a cube with a lattice parameter given by $b = 2\pi/a$. Note that the symmetry of the Brillouin

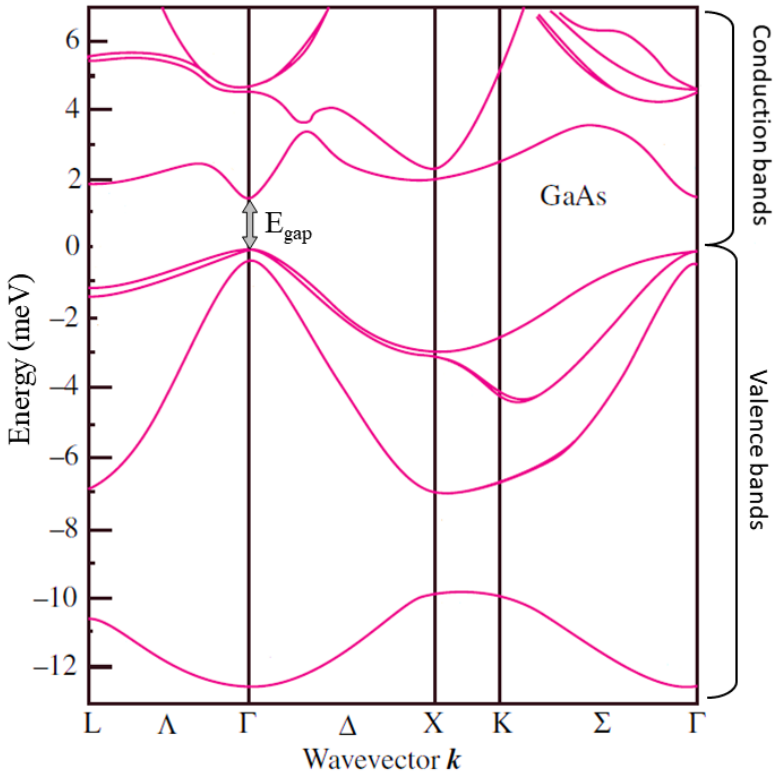

Figure 1.2. Electronic band structure of GaAs calculated by the pseudopotential method. The energy at the top of the valence bands have been taken to be zero. E_{gap} indicates the minimum energy difference between the valence and conduction bands. Adapted from [3].

zone is determined by the symmetry of the direct lattice. In this case, the symmetry of the lattice makes possible to define points (Γ, X and L) and directions (Λ and Δ) of high symmetry in Fig. 1.1(b).

In solid-state physics, the electronic band structure (band structure to simplify) of a crystal describes the energy states of carriers as a function of the momentum k. The band structure of GaAs is depicted in Fig. 1.2 and shows two kinds of energy bands: the valence ($E < 0$) and the conduction ($E > 0$) bands. In semiconductors there is an energy difference between the maximum of the valence band and the minimum of the conduction band, know as bandgap or E_{gap}. Depending on the value of the bandgap, a material can be defined as conductor, semiconductor or insulator. In $Al_xGa_{1-x}As$ alloys, the E_{gap} at room-temperature varies between 1.43 eV ($x = 0$), which is a direct bandgap, and 2.14 eV ($x = 1$), corresponding to an indirect bandgap [2]. At zero temperature and in the case of intrinsic (without impurities) GaAs, electrons fill the valence band leaving the conduction band empty, however, as the temperature is increased (or an optical excitation is performed), electrons can gain enough

energy to overcome the bandgap and populate the conduction band. As shown in Fig. 1.2, the band gap for GaAs is direct [it occurs between bands at the same wave vector ($k = 0$)]. Thanks to this feature, this compound is an ideal candidate for optical applications such as light-emitting devices, since transitions between the conduction and the valence bands (absorption or emission) are allowed and do not require a change in momentum.

1.2 Excitons

In the short introduction to the band structure of section 1.1, it has been discussed that at zero temperature, the ground state of a semiconductor is characterized by a filled valence band and an empty conduction band, which are separated by a gap. When an electron with charge $-e$ is excited from the valence band into the conduction band, the vacancy that remains in the valence band can be described as a quasiparticle, called hole, with a positive charge e. This description allows us to consider the valence band masses as positive despite the fact that from the single electron picture they have negative curvature, i.e., negative mass [see Fig. 1.2]. Negatively charged electrons in the conduction band and positively charged holes in the valence band are subject to Coulomb attraction. This interaction is responsible for the fact that the fundamental excitation in semiconductors is a bound electron-hole pair, named exciton. This quasiparticle is quantum mechanically analogous to a hydrogen atom, where an electron is bound to a proton via Coulomb interaction. Both systems show similarities such as their structure of the energy levels, which results in exciton levels 1s, 2s, 2p and so on. In this thesis, we only discuss Wannier-Mott excitons in which the Coulomb interaction is strongly screened by the valence electrons: the large dielectric constant results in weakly bound electrons and holes. This results in an extension of the exciton over tens of atomic sites in the crystal, a binding energy of the order of 10-100 meV and a Bohr radius of about a_B 100-10 Å[4]. The binding energy of the ground exciton state is given by [5],

$$E_B = \frac{\hbar^2}{2\mu_X a_B^2} \tag{1.1}$$

where μ_X is the electron-hole pair reduced effective mass. It is also worth mentioning that the exciton, made of two fermionic quasiparticles, behaves as a boson for low particle density.

If an exciton is confined, its energy and spatial extension are changed. The confinement of matter (electron, holes and excitons) can be easily attained in semiconductor heterostructures made of layers of different materials. In general, excitons can be confined along 1D (Quantum Well, QW), 2D (Quantum Wire) or 3D (Quantum Dot). In this thesis we will consider only

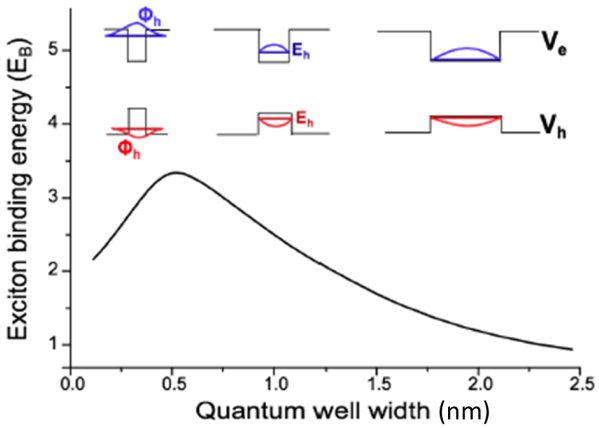

Figure 1.3. Exciton binding energy as a function of the QW width (scheme). The insets show the QW potential V_e and V_h and ground state energies, E_e and E_h, and wave functions, ϕ_e and ϕ_h, of electron (blue) and hole (red), respectively, for different QW widths (nm scale). Adapted from [5].

the case of 1D confinement, where the movement of excitons is restricted along the growth direction (z), while they can freely move in the $x-y$ plane. In these structures the quantum confinement effects become important when the when the size of the excitonic wavefunction is larger than (or comparable to) the confinement length. In our case, GaAs-based QWs, the quantum well width required to observe quantum confinement is of the order of tens of nm or less.

Fig. 1.3 shows the binding energy of excitons when they are confined in a QW. The potential profiles of electrons (V_e) and holes (V_h), are plotted along the growth direction of the QWs. Note that the size and depth of the QWs can be tuned just by changing the layer composition or its thickness. The evolution of E_b shows the strong sensitivity of excitons to nanometer-scale variations in the QW size.

1.3 Semiconductor microcavities

Devices based on optical microcavities are desirable for a wide range of applications since they confine light to small volumes in the micrometer-scale. As an example, microcavities made of III–V semiconductor materials are very useful to control the laser emission to enable data transmission over long-distances in optical fibers [6, 7]. An ideal cavity would indefinitely confine light without any loss and have resonant frequencies at specific wavelengths. However, in the real case, they are leaky and therefore, non-conservative. To understand the

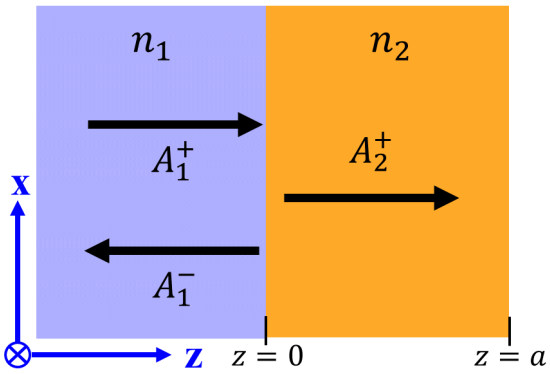

Figure 1.4. Scheme of an electromagnetic wave impinging on the interface between two media with refractive indexes n_1 and n_2. The arrows indicate the direction of the incident A_1^+, reflected A_1^- and transmitted A_2^+ waves in the z-direction. The interface is located at the plane $z = 0$. a is the length of the medium n_2.

behavior of light in these microcavities, a brief introduction to light propagation is explained below.

1.3.1 Classical description of light propagating in semiconductors

In this section we briefly describe the propagation of electromagnetic-waves in semiconductor (or dielectric) materials. We will consider two media with homogeneous refractive indexes n_1 and n_2 in the $x-y$ plane, across which a light wave travels. The light wave passes through the first medium impinging on the interface between both materials (at $z = 0$), where part of the wave is transmitted and a small fraction gets reflected. A schema of this scenario is shown in Fig. 1.4 where $A_i^{\pm}$ are amplitudes of the waves. The superscript denotes the direction of propagation $+z$ or $-z$ and the subscript $i = 1,2$ refers to the medium in which the electromagnetic wave is traveling. The reflection (r) and transmission (t) coefficients of the system, also known as the Fresnel coefficients, can be obtained by dividing these amplitudes [3],

$$r = \frac{A_1^-}{A_1^+} = \frac{n_1 - n_2}{n_1 + n_2} \tag{1.2a}$$

$$t = \frac{A_2^+}{A_1^+} = \frac{2n_1}{n_1 + n_2} \tag{1.2b}$$

The reflectivity R, which is defined as the ratio of the reflected to incident energy flux, and the transmittance T, which is the ratio of the transmitted to incident energy flux, results

$$R = |r|^2 \tag{1.3a}$$

$$T = \frac{n_2}{n_1}|t|^2 \tag{1.3b}$$

If the absorption in the system is negligible, then, the relation $R+T=1$ is satisfied. This theoretical framework can be extended for the case of multilayered structures applying appropriate boundary conditions at each interface. However, this would require solving a remarkably large number of equations, depending on the number of interfaces. For example, a structure of 25 layers, which approximately corresponds to one set of mirrors used in the samples of this thesis, would provide a system of 50 equations. An alternative, method known as the "transfer matrix method" allows to minimize the number of equations and to simplify the problem. To briefly explain this method a vector Θ is defined as,

$$\Theta(z) = \begin{pmatrix} E(z) \\ cB(z) \end{pmatrix} = \begin{pmatrix} E(z) \\ -\frac{i}{k}\partial_z E(z)) \end{pmatrix} \tag{1.4}$$

which depends on the amplitudes of the electric ($E(z)$) and magnetic ($B(z)$) fields of any light wave propagating in the z-direction. At the interface ($z=0$) where the change of n occurs, Θ is continuous. Assuming a wave traversing a layer extended from the interface to a distance a (see Fig. 1.4), the problem can be defined with the transfer matrix T_a [5].

$$\Theta(z=a) = T_a\Theta(z=0) \tag{1.5a}$$

$$T_a = \begin{pmatrix} cos(ka) & \frac{i}{n}sin(ka) \\ in\,sin(ka) & cos(ka) \end{pmatrix} \tag{1.5b}$$

In the case of a system composed by a large number of layers (m), the matrix is simply redefined as $T = \prod_{i=1}^{m} T_i$. The reflection and transmission coefficients of a system composed by m layers can be improved if the structure is sandwiched between two semi-infinite media [5].

1.3.2 Fabry-Perot interferometer

The confinement and manipulation of light can be achieved with a large number of different cavity designs [8]. However, the enhancement of light-matter interaction requires the use of small volumes and structures with dimensions typically of the same order of magnitude than the incident wavelength. Different confinement methods are used in the microcavities (MCs),

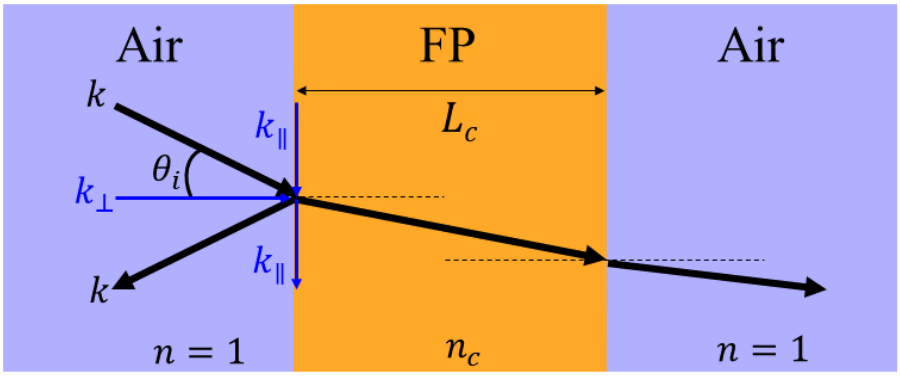

Figure 1.5. Sketch of a FP interferometer composed by a medium acting as a cavity with thickness L_c and refractive index n_c surrounded by air ($n = 1$). A beam with wave vector k (black arrow) impinges on the cavity at an angle θ_i with respect to the horizontal axis (marked with the dashed line). $k_\parallel$ is the in-plane component of the wave vector, which is parallel to the interface between air and cavity, and $k_\perp$ is the perpendicular component.

but, since in this thesis all the samples are Fabry-Perot style resonators (FP), we consider the FP interferometer of Fig. 1.5: an active medium surrounded by air, in which light incides from a slant angle θ_i, with $k_\perp$ the perpendicular and $k_\parallel$ the in-plane components of the wave vector. Let us write the wave vector as $\vec{k} = \vec{k_\perp} + \vec{k_\parallel}$. The cavity exhibits a photon energy dispersion given by [5]

$$E_c = \frac{\hbar c}{n_c}\sqrt{k_\perp^2 + k_\parallel^2} \tag{1.6}$$

where $k_\perp = 2\pi/\lambda_c = 2\pi n_c/\lambda_0$. λ_c is the wavelength of the light in the cavity. This wave vector can also be expressed as a function of the cavity parameters: the refractive index n_c and its thickness L_c as $k_\perp = N\pi/L_c$, where N is an integer number. This conversion is possible since λ_c meets the condition $L_c = N\lambda_c/2$. If one considers the approximation $k_\parallel \ll k_\perp$, a direct correspondence is found between the incident angle and the in-plane wave vector,

$$k_\parallel = \frac{2\pi}{\lambda_0} sin\left(\theta_i\right) \approx \frac{2\pi}{\lambda_0}\theta_i \tag{1.7}$$

Under this condition, the energy of the cavity photon in Eq. 1.6 can be approximated to

$$E_c \approx \frac{\hbar c}{n_c}k_\perp\left(1 + \frac{k_\parallel^2}{2k_\perp^2}\right) = E_c\left(k_\parallel = 0\right) + \frac{\hbar^2 k_\parallel^2}{2m_c} \tag{1.8}$$

where the first term $E_c\left(k_{\parallel}=0\right)=\hbar c k_{\perp}/n_c$ is the energy mode corresponding to a normal incidence. Here, the cavity photon mass is

$$m_c=\frac{E_c(k_{\parallel}=0)}{c^2/n_c^2} \tag{1.9}$$

The quality of the light confinement in a FP is determined through the Q-factor of the cavity, which measures the efficiency at concentrating the electromagnetic energy, and it is defined [5],

$$Q=\frac{\omega_c}{\Delta\omega_c} \tag{1.10}$$

where ω_c is the cavity frequency and $\Delta\omega_c$, the linewidth (FWHM) of the cavity mode. The Q-factor is used to express the fraction of energy that is lost in a single round-trip around the cavity, which can be obtained by simply calculating Q^{-1}. This parameter is also directly related to the leakage of the cavity produced by the imperfection of real mirrors. It can be employed to quantify the photon lifetime inside the cavity before it escapes from the structure,

$$\tau=\frac{Q}{\omega_c} \tag{1.11}$$

The photon lifetime not only increases with Q but also with the reflectivity between the interfaces of a FP construction. This can be deduced evaluating the Fabry-Perot finesse F, which is the ratio of the frequency separation between cavity modes and the linewidth of those modes. One can rewrite this parameter in terms of the reflectivity coefficient of the FP interfaces as [5],

$$F=\frac{\pi r}{1-r^2} \tag{1.12}$$

Therefore, higher reflective mirrors provide higher values of F, resulting in an improvement of the light confinement in the cavity and thus, the photon lifetime.

1.3.3 Distributed Bragg Mirrors

To construct a cavity with a large quality factor, the use of highly reflecting mirrors is essential. This can be achieved with distributed Bragg mirrors (DBRs), which are composed of alternating layers with high and low refraction indexes (n) in which each layer is made with an optical thickness (L) of $\lambda/4$, where λ is the incident wavelength in the medium. The

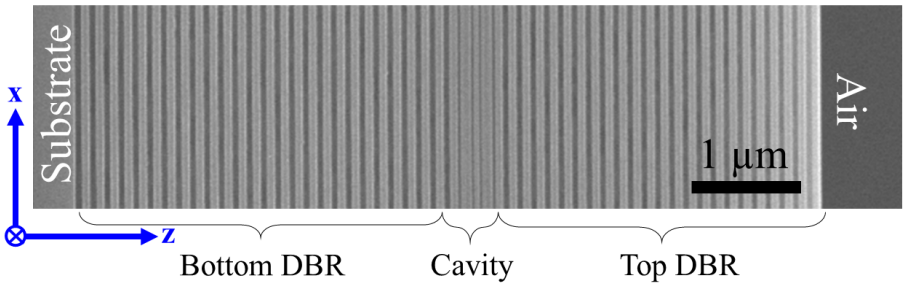

Figure 1.6. SEM image of the lateral view of a typical GaAs-based MC formed by a cavity layer sandwiched between two sets of DBRs. The cavity is grown in the z-direction on a substrate (left) and surrounded by a medium such as air (right). Courtesy of S. Höfling from the University of Würzburg.

finesse of this mirror is determined by the reflectivity of each mirror, which depends on the number of pair repetitions and the refractive index difference between the two semiconductors employed. The final composition of this structure can provide a reflectivity coefficient close to 1 in a restricted spectral region.

Analogously to the FP scheme, the incident radiation on the DBR will suffer multiple reflections as it passes through each interface of the structure. The constructive interference between the reflected light waves results in a high reflectivity for a certain spectral range. This region is called a stop-band, as it hinders the transmission of light across the structure in that spectral range. This is achieved by matching the optical length of each layer to $\lambda_0/4$, i.e., $n_1L_1 = n_2L_2 = \lambda_0/4$ and repeating this pair multiple times. Note that λ_0 is the desired wavelength of the incident light at which the reflectivity is maximum.

If a spacer layer (cavity) is placed between two DBRs, a semiconductor MC is formed, which can be considered as a 1D photonic crystal cavity with a central defect. Fig. 1.6 shows a typical MC where the substrate upon which it has been grown is found on the left side, while on the right end the MC is in contact with the medium in which it is placed, in our case, air. Similarly to a FP interferometer, the thickness of the spacer layer, L_c, determines the cavity mode wavelength λ_c through $L_c = N\lambda_c/2$, where N is an integer number. A direct consequence of the build-up of the cavity mode is a sharp increase in the transmission T at λ_c, which is given by [5],

$$T = \frac{(1-R_1)(1-R_2)}{\left[1-\sqrt{R_1R_2}\right]^2 + 4\sqrt{R_1R_2}sin^2(\phi/2)} \tag{1.13}$$

$R_{1,2}$ are the reflectances of the two bottom and top DBRs, respectively, and ϕ is the cavity phase shift of a photon at λ_c. This is evident in the reflectivity ($R = 1-T$) of the MC on

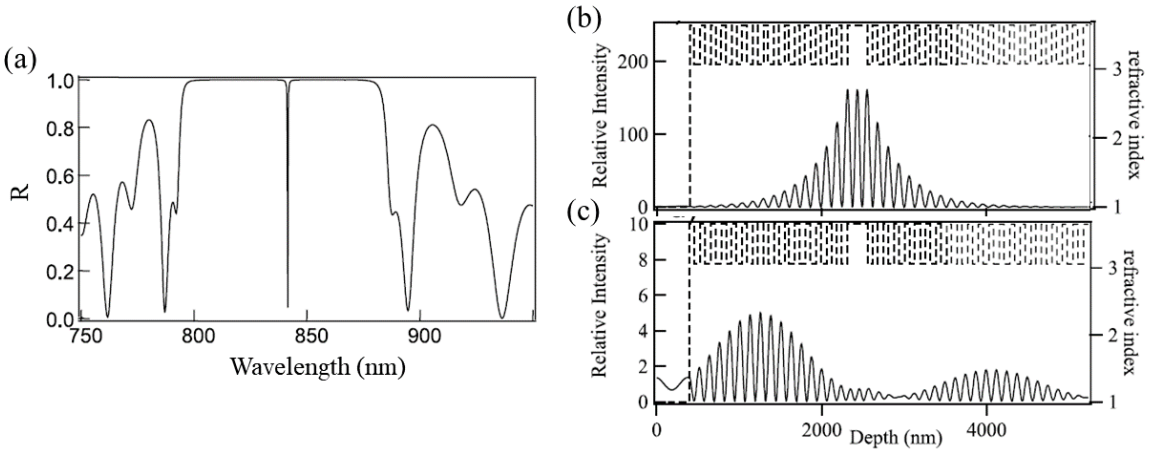

Figure 1.7. (a) Reflection of a planar DBR microcavity consisting of a top and bottom mirror with 15 and 21 repeats of GaAs/AlAs. A 240 nm-thick bulk GaAs cavity is incorporated. (b, c) field distributions corresponding to (a) at wavelengths of (b) 841 nm and (c) 787 nm. The dashed line depicts the refractive index of the MC. Adapted from [5].

the wavelength shown in Fig. 1.7(a). R is calculated considering a GaAs cavity introduced between 15 and 21 (top and bottom) DBRs of GaAs/AlAs pairs. A central flat band with $R \sim 1$ appears for a wide range of wavelengths above 800 nm. This plateau is known as the stop-band and becomes broader the higher the refractive index difference between layers and the larger the number of pair layers. As expected, R drops at the designed cavity wavelength at $\lambda_c = 841$ nm. Furthermore, several modes called Bragg modes arise in the limits of the stop-band.

To clarify the implications of the cavity and Bragg modes in the MC field distribution, the electric field of the modes corresponding to 841 and 787 nm are depicted in Fig. 1.7(b) and (c), respectively. The dashed line indicates the refraction index of the structure, indicating the presence of the cavity layer with a constant maximum refractive index at a depth of ∼2300 nm. Fig. 1.7(b) shows that for the cavity mode (841 nm) the light is mainly confined in the cavity, penetrating into the surrounding DBRs. The penetration depth of the electric field in the DBRs can be evaluated through the refractive indexes of the different materials that compose the MC as $L_{DBR} \approx \frac{\lambda_c n_1 n_2}{2n_c(n_1 - n_2)}$ [9]. The different layers reflect the light with the same phase, creating a constructive interference in the cavity. Therefore, the photons injected in the MC remain in the structure for a significant long time, which is consistent with a high

Q-factor. This factor can be also described with the reflectances of the two DBRs as [10]

$$Q = \frac{\omega_c}{\Delta\omega_c} \simeq \frac{\pi (R_1 R_2)^{1/4}}{1 - (R_1 R_2)^{1/2}} \tag{1.14}$$

where $\Delta\omega_c$ is the width of the cavity mode. If the cavity length is $L_c = \lambda_c/2$, Q is the average number of round trips a photon travels inside the cavity before it escapes [10]. It is worth mentioning that the maxima of the field amplitude inside the cavity in Fig. 1.7(b), can be employed to enhance the coupling of excitons and photons, opening the way to the achievement of strong light-matter coupling and the creation of polaritons in the MC. A different behavior to that of the cavity mode is observed in the field distribution of the first Bragg mode at 787 nm [see Fig. 1.7(c)]. Here, the electric field amplitude considerably decays, resulting in an almost zero intensity inside the cavity.

1.4 Polaritons: Light-matter coupling

Having discussed excitons and photons confined in a microcavity, we turn our attention to the photon-exciton coupling. The light-matter interaction in a MC can occur in two different regimes known as weak and strong coupling. In the weak coupling regime, the photon emitted has a negligible probability of being reabsorbed by the same active medium. The excitation of the medium is dissipated, therefore the weak coupling involves irreversible processes. This regime is also called perturbative, since the electromagnetic field acts as a perturbative term given by the Hamiltonian:

$$H \approx -\frac{e}{m}\mathbf{A}\cdot\mathbf{p} \tag{1.15}$$

where $\mathbf{A}$ is the vector potential of the electromagnetic field, $\mathbf{p}$ the momentum operator, and m the electron mass. The first order development in time-dependent perturbation theory gives the spontaneous emission rate, described by the Fermi golden rule. In this regime, polaritons have a finite radiative lifetime, resulting in an exponential decay of the population after a pulsed excitation. Nonetheless, the weak coupling also shows advantages: by acting on the electromagnetic density of states, it is possible to modify the transition probability, given by the Fermi Golden rule, and obtain the Purcell effect, in which the emission probability is enhanced or suppressed [11].

The strong coupling regime, also known as non-perturbative regime, occurs when a medium is excited and the photon emitted in a given mode can be reabsorbed again. Photons are

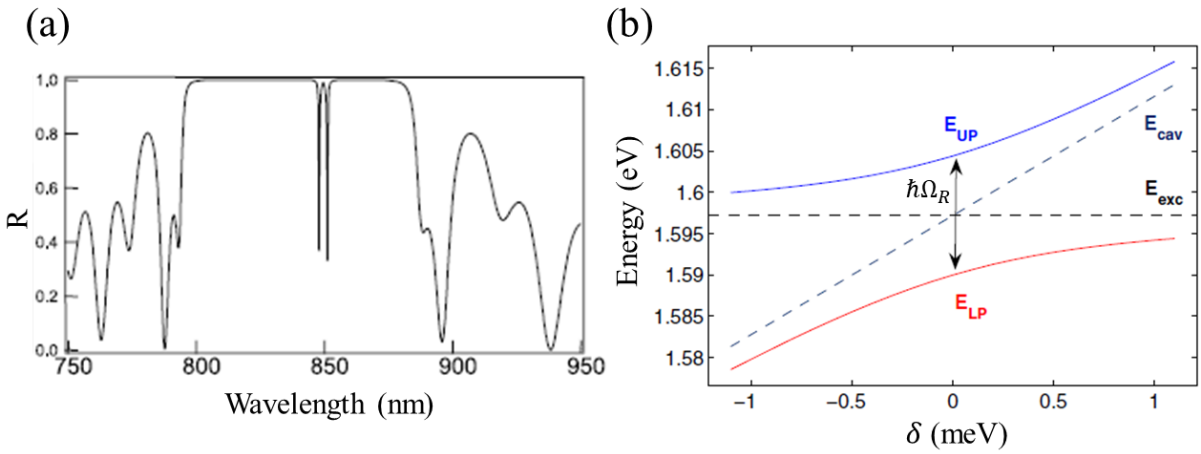

Figure 1.8. (a) Reflection of a planar DBR microcavity consisting of a top and bottom mirror with 15 and 21 repeats of GaAs/AlAs with 3 InGaAs QWs incorporated to the cavity [5]. (b) Anticrossing of the LP and UP energy levels when the cavity energy E_{cav} cross the exciton energy E_{exc}. δ is the energy difference between E_{cav} and E_{exc}. When E_{cav}=E_{exc}, the energy difference between the LP and the UP is $\hbar\Omega_R$. [10].

converted into excitons in a process in which the energy and the wave vector are conserved. If photons and excitons are confined in a cavity, as those explained in section 1.3, they can live longer than those created in a medium without confinement. If the energy exchange between photons (cavity field) and excitons becomes much faster than their decay rates, they have enough time to interact strongly giving rise to a new combined excitation. These elementary excitations of the system are no longer excitons or photons but a new type of quasi-particles known as exciton-polaritons, or polaritons to abbreviate. When the interaction between both particles is strong enough and polaritons are formed, the energy spectrum of the medium changes drastically. This is evidenced in Fig. 1.8(a), which shows the reflectivity of a MC with InGaAs QWs as an active medium. In contrast to the case shown in Fig. 1.7(a) where one dip with minimum reflectivity is observed in the stop-band, two dips with minimum reflectivity are seen in the stop-band. These two dips are called "lower" (LP) and "upper" (UP) polariton branches due to the analogy to two linearly-coupled harmonic oscillators. Due to the difference between the exciton and photon energies, polaritons display an anticrossing behavior [12] [see Fig. 1.8(b)]. At the resonance between the photon and exciton energy, a minimum energy separation known as the Rabi splitting energy ($\hbar\Omega_R$) is observed.

The first theoretical discussion of the strong coupling regime in solid state systems was made by Hopfield in 1958 [13]. This kind of coupling was also explored in other systems such as atoms (theoretically predicted by Jaymes and Cummings in 1963 [14]). However, it was not until 1977 when Ulbrich and Weisbuch observed polaritons for the first time in a

semiconductor (GaAs) [15]. Years later, polaritons were first reported in a semiconductor microcavity by Weisbuch *et al.* [16]. Polaritons aroused great interest due to their numerous characteristics and properties. They have a much lighter mass, of the order of $10^{-4}m_e$, compared to other systems such as atoms $10^3 m_e$, which makes easier to create polariton Bose-Einstein condensates than other kind of BECs in different systems (further information in section 1.5.2) [10]. They also exhibit a distinctive short lifetime, typically of 10-100 ps, which is of the order of that of photons [17]. Polariton-polariton interactions are inherited from their excitonic component, which arise mainly from the Coulomb exchange effects of the underlying fermionic species. This provides a typical mean field interaction of the order of ∼meV[18]. Another advantage of these quasi-particles is that their momentum and energy can be directly measured from the PL emerging from the MC. Polaritons decay by leakage through the DBRs, emitting photons that carry the same energy and momentum as the polaritons. This energy can be measured using spectroscopic techniques and the momentum can be obtained from the angular-resolved emission.

1.4.1 Hopfield coefficients

To describe the elementary excitations of an optically excited microcavity containing QWs in the strong coupling regime, we consider the coupling between two modes, the exciton and the photon, with infinite lifetimes, in which interactions between excitons are negligible. In a simple approximation, the system can be treated as two coupled harmonic oscillators allowing to easily understand how polaritons are composed and what are their energies. The Hamiltonian of the system is written in the second quantization formalism as,

$$\hat{H}_p = \sum E_C(k_\parallel)\hat{a}^\dagger_{k_\parallel}\hat{a}_{k_\parallel} + \sum E_X(k_\parallel)\hat{b}^\dagger_{k_\parallel}\hat{b}_{k_\parallel} + \sum \frac{\hbar\Omega_R}{2}\left(\hat{a}^\dagger_{k_\parallel}\hat{b}_{k_\parallel} + \hat{a}_{k_\parallel}\hat{b}^\dagger_{k_\parallel}\right) \tag{1.16}$$

The first, second and third terms describe the photons created in the cavity, the excitons and their mutual coupling, respectively. E_C and E_X describe the energies corresponding to photons and excitons, respectively. The coefficient Ω_R is the Rabi splitting, which determines the coupling energy between both particles. $\hat{a}^\dagger_{k_\parallel}$ ($\hat{b}^\dagger_{k_\parallel}$) and $\hat{a}_{k_\parallel}$ ($\hat{b}_{k_\parallel}$) are the corresponding creation and annihilation operators for a photon (exciton) with a wave vector $k_\parallel$. In the third term, two processes are considered: the simultaneous creation of a photon and the annihilation of an exciton (emission) and the creation of an exciton and the annihilation of a photon (absorption).

In the coupling process we only consider particles with the same in-plane wave vector $k_\parallel$. Therefore, to simplify the notation in the development of the equations, from now on we

redefine $k \equiv k_{\parallel}$. The above Hamiltonian can be diagonalized using the transformation matrix [5]:

$$\begin{pmatrix} \hat{P}_k \\ \hat{Q}_k \end{pmatrix} = \begin{pmatrix} C_k & X_k \\ X_k & -C_k \end{pmatrix} \begin{pmatrix} \hat{a}_k \\ \hat{b}_k \end{pmatrix} \tag{1.17}$$

where ($\hat{P}_k^{\dagger}$, $\hat{Q}_k^{\dagger}$) and ($\hat{P}_k$, $\hat{Q}_k$) correspond to the polariton creation and annihilation operators, or, in other words, to the to the creation and annihilation operator of the new eigenstates of the system. This matrix system leads the diagonalization from the basis of $(\hat{a}_k, \hat{b}_k)$ to $(\hat{P}_k, \hat{Q}_k)$. In the new basis the Hamiltonian is redefined as,

$$\hat{H}_p = \sum E_{LP}(k)\hat{P}_k^{\dagger}\hat{P}_k + \sum E_{UP}(k)\hat{Q}_k^{\dagger}\hat{Q}_k \tag{1.18}$$

As a result of the coupling between photons and excitons, the two new states called lower polariton and upper polariton are obtained. E_{LP} and E_{UP} are the corresponding energies or eigenvalues of each state. Therefore, the Hamiltonian defines polaritons with a given momentum as the result of a linear combination of photons and excitons with the same in-plane momentum k. Since polaritons are composed of excitons and photons it is reasonable to quantify their excitonic and photonic content. This can be done using the Hopfield coefficients, C_k and X_k, which define the photonic and excitonic content, respectively. Thus polaritons can be mathematically defined as [13],

$$\psi_P(k) = C_k\psi_C(k) + X_k\psi_X(k) \tag{1.19}$$

where ψ_C and ψ_X are the corresponding wave functions of photon and exciton. The combination of both wave functions, weighted with the Hopfield coefficients, provides the wave function of the polariton ψ_P. The Hopfield coefficients satisfy the relation,

$$|C_k|^2 + |X_k|^2 = 1 \tag{1.20}$$

By changing the ratio of C_k and X_k, one can interpolate between light and matter. This is usually done changing the photon energy at $k = 0$ (δ) by using a thickness wedge intentionally introduced in the cavity or modifying the temperature and therefore, the exciton energy. The

Hopfield coefficients can be expressed as [10],

$$|C_k|^2 = \frac{1}{2}\left(1 - \frac{\delta(k)}{\sqrt{\delta(k)^2 + (\hbar\Omega_R)^2}}\right) \tag{1.21a}$$

$$|X_k|^2 = \frac{1}{2}\left(1 + \frac{\delta(k)}{\sqrt{\delta(k)^2 + (\hbar\Omega_R)^2}}\right) \tag{1.21b}$$

Note that at zero detuning ($\delta = 0$), the lower and upper polaritons are composed by the same photonic and excitonic fractions, $|C_k|^2 = |X_k|^2 = 1/2$.

Additional information such as the eigenvalues of the Hamiltonian (Eq. 1.18) can be obtained from the diagonalization procedure [10].

$$E_{UP,LP}(k) = \frac{1}{2}\left[E_X(k) + E_c(k) \pm \sqrt{(\hbar\Omega_R)^2 + \delta(k)^2}\right] \tag{1.22}$$

The dispersions of each polariton mode and the Hopfield coefficients for LPs are depicted as solid lines in Fig. 1.9 *left* and *right*, respectively, for three detuning values: (a) $\delta = \hbar\Omega_R$, (b) $\delta = 0$, (c) $\delta = -\hbar\Omega_R$. The dispersions for the bare cavity photon and the exciton are indicated by dashed lines. The exciton mass is considerably heavier than that of the photon, therefore, E_X seems to be a flat band while E_c exhibits a parabolic dispersion described by Eq. 1.8. In the case of a positive detuning, Fig. 1.9(a), E_{UP} and E_{LP} resemble the photon and exciton dispersions, respectively. This behavior is originated by the large photonic fraction of the UPB while in the LPB there is a larger excitonic fraction. This is evidenced in the representation of the Hopfield coefficients for the LPB in which its excitonic fraction results in $|X(k)|^2 \geq 0.8$. At zero detuning, Fig. 1.9(b), a different behavior is found. In this case, at $k = 0$ the photon and exciton are at resonance, $E_c = E_X$. Therefore, following Eq. 1.22, the separation between the energies of UP and LP obtains its minimum value, $E_{UP} - E_{LP} = \hbar\Omega_R$. As explained above, under these circumstances both bands display the same photonic and excitonic fractions at $k = 0$. In the case of a negative detuning, Fig. 1.9(c), the photon dispersion crosses E_X. Therefore, the photon and exciton resonance is produced symmetrically at high $\pm k$ values. Again, at these points the interaction between the photons and the excitons results in a separation between the polariton branches equal to $\hbar\Omega_R$: E_{LP} and E_{UP} anticross when the cavity mode coincides with the exciton mode. The anticrossing of LP and UP is a well-known signature of the strong coupling regime [12]. The Hopfield coefficients show that the situation is inverted with respect to (a): now, the LPB shows a high photonic fraction at small k. Note that as $|\delta|$ is increased, the effect of the coupling becomes

less relevant, reaching a point where the eigenstates of the system are the pure photon and exciton modes.

In the proximity of $k = 0$ for $\delta \leq 0$, the polariton dispersions shows a clear parabolic dispersion, thus polaritons can be approximated by free particles, moving with an effective reduced mass dependent on their photonic and excitonic fractions.

$$\frac{1}{m_{LP}} = \frac{|X_0|^2}{m_X} + \frac{|C_0|^2}{m_c} \tag{1.23a}$$

$$\frac{1}{m_{UP}} = \frac{|C_0|^2}{m_X} + \frac{|X_0|^2}{m_c} \tag{1.23b}$$

where C_0 and X_0 are the coefficients given by Eq. 1.21 for $k = 0$. m_X is the effective exciton in-plane mass and m_c is the effective cavity-photon mass given by Eq. 1.9. Since $m_c \ll m_X$, the polariton mass can be estimated as

$$m_{LP}\left(k_{\|} \sim 0\right) \approx \frac{m_c}{|C_0|^2} \sim 10^{-4} m_X \tag{1.24a}$$

$$m_{UP}\left(k_{\|} \sim 0\right) \approx \frac{m_c}{|X_0|^2} \tag{1.24b}$$

1.5 Bose-Einstein Condensation

Matter can be observable commonly in nature in different states such as solid, liquid, gas and plasma. However, under particular conditions, a new state arises as it is the case of Bose-Einstein condensates (BECs), also known as the fifth state of matter. In 1924 Albert Einstein and Satyendra Nath Bose predicted the existence of BEC systems in which bosons in a gas occupy the same fundamental quantum state when the temperature is decreased close to zero [19, 20]. Under these conditions a macroscopic state exhibiting spontaneous coherence is formed. Although this discovery had great acceptance in the scientific community, it was not until 1995 when Eric Cornell and Carl Wieman obtained the first experimental evidence of the creation of a BEC that contained 2000 rubidium atoms [21]. Shortly after, Wolfgang Ketterle created a BEC of sodium atoms [22]. "For the achievement of Bose-Einstein condensation in dilute gases of alkali atoms, and for early fundamental studies of the properties of the condensates" Cornell, Wieman and Ketterle shared the Nobel Prize in Physics in 2001 [23]. Since their discovery these systems have arisen much interest, which has led to the realization of many different type of condensates using molecules, photons and quasi-particles. As a curiosity one can mention that in 2018, for the first time a BEC was created in space, in the

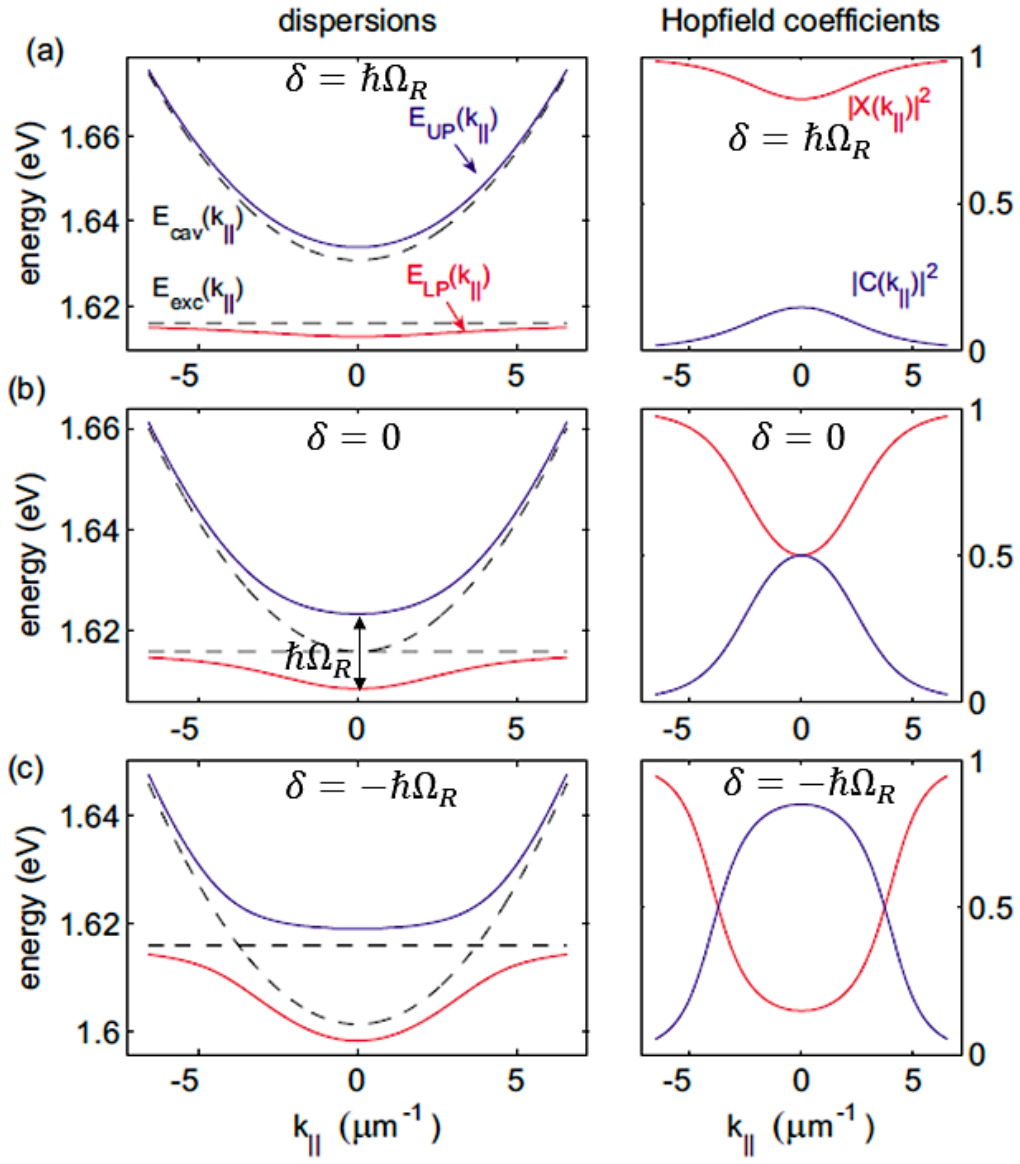

Figure 1.9. *Left*: Polariton dispersions (solid lines) at (a) $\delta = \hbar\Omega_R$, (b) $\delta = 0$, (c) $\delta = -\hbar\Omega_R$. When $E_c = E_X$, the energy separation between E_{UP} and E_{LP} is $\hbar\Omega_R$, as shown in (b). *Right*: corresponding Hopfield coefficients of the LP branch shown in *left*. Adapted from [10].

International Space Station [24]. In the experiment, a cloud of rubidium atoms was cooled to a temperature of 100 nK, holding the record for the coldest object created in space.

1.5.1 Ideal Bose gas

Due to the Pauli exclusion principle, only bosonic particles (integer spin) can form a Bose-Einstein condensate. When such a state is intended to be created using fermions, a Fermi liquid instead of a condensate is found. One interesting property of bosons is their natural tendency to accumulate in unlimited quantity in a degenerate state. If a gas of N non-interacting bosons in a volume V at a defined temperature T is considered, i.e., in thermal equilibrium, then, the distribution of particles follow a Bose-Einstein distribution given by,

$$n_j = \frac{1}{e^{\frac{E_j-\mu}{k_B T}} - 1} \tag{1.25}$$

where μ and k_B are the chemical potential and the Boltzmann constant, respectively. The energy of the particles in a state j is given by E_j. If one increases the number of particles in the Bose gas, as in the condensation process, the energy exchange between the particles will increase. Note that the chemical potential has to be smaller then the energy of particles so that the occupation number in a state is always positive, i.e., $E_j - \mu > 0$. This case can be described defining the particle number as,

$$n = n_0 + n_T = \frac{1}{e^{\frac{E_0-\mu}{k_B T}} - 1} + \sum_{j\neq 0} n_j \tag{1.26}$$

The number of particles in the fundamental state in the condensate is indicated as n_0, while those in any excited state outside of the condensate are n_T. For $\mu < E_0$, n_0 becomes massively occupied. This process together with the reduction of n_T, gives rise to the basis that leads to the BECs, experimentally shown by Cornell, Wieman and Ketterle [21, 22]. In a 3D gas, the particles are able to move in the volume, exhibiting a parabolic dispersion given by $E = E_0 + \frac{\hbar^2 k^2}{2m}$. Taking into account that n_T is proportional to the density of states, is it possible to define the density of states in the case $\mu = E_0$ as [25],

$$\frac{n_T}{V} = \int_{E_0}^{\infty} \frac{m k_B T}{2\pi\hbar^2}^{3/2} \frac{\sqrt{E-E_0}}{e^{\frac{E-E_0}{k_B T}} - 1} dE = \frac{2.612}{\lambda_B^3} \tag{1.27}$$

where the de Broglie wavelength is

$$\lambda_B = \sqrt{\frac{2\pi\hbar^2}{mk_BT}} \tag{1.28}$$

When the inter-particle separation is of the order or smaller than λ_B, particles collapse to the same fundamental state behaving as one macroscopic state. Moreover, it is possible to define a critical temperature for the phase transition for condensation in the limit defined by Eq. 1.27, i.e., $(n_T/V)\lambda_B^3 = 2.612$, obtaining

$$T_c \approx 3.3\frac{\hbar^2(n_T/V)^{2/3}}{mk_B} \tag{1.29}$$

Therefore, in the ideal case of a non-interacting bosonic gas in thermal equilibrium, the condensation will occur below T_c. In addition, due to the dependence on the mass of T_c, it is clear that the process will become easier for light particles since T_c will be larger than for massive ones.

1.5.2 Exciton-polariton Bose-Einstein condensates

Bose-Einstein condensation can be expected to occur for any bosonic quasi-particle, such as exciton-polaritons, which are investigated in this thesis. They have been largely considered as promising candidates to study condensation at liquid-helium temperatures, easily reached by standard cryogenic techniques. The properties displayed by polariton condensates differ from those known for other BEC systems, such as atomic condensates. Polaritons have a short lifetime, of the order of picoseconds, because of photons continuously leaking out of the cavity, which makes them non-conservative systems. Rather than being an obstacle, this fact allows to study the coherence properties of the condensates directly by measuring the luminiscence of the emitted photons. Such a simple procedure is not available for other BEC systems. As mentioned in section 1.4.1, the extremely pronounced dispersion of the polariton modes, as a result of the photonic character of polaritons, leads to a polariton effective mass of $10^{-4}m_e$. Hence, the temperature for condensation should be more easily achievable, allowing the condensation process even at room temperature. Note that since the lifetime of polaritons is comparable to or even smaller than the thermalization times, a precise temperature cannot be defined, thus, they are inherently out-of-equilibrium BEC systems.

Some studies, including the ones in this thesis, overcome this conundrum by ascribing to the condensate the temperature of the lattice where they reside.

The first theoretical proposal to consider polaritons for BEC systems was made by A. Imamoglu *et al.* in 1996, in which they discussed the use of non-equilibrium condensates to realize a polariton laser [26]. Later, P. G. Savvidis *et al.* and R. M. Stevenson *et al.* demonstrated the bosonic character of polaritons through a stimulated scattering process in pump-probe experiments [27, 28]. In 2006, Kasprzak *et al.* reported many properties that would be observed in equilibrium condensates, confirming the formation of a polariton BEC [29]; some of these properties are summarized in Fig. 1.10. The narrowing of the emission in momentum-space is one of the first indicators of condensation as shown in Fig. 1.10(a). Below threshold (left panels), the emission is widely distributed in momentum and energy, whereas above threshold (right panels), an intense peak is formed in the center of the emission at the fundamental state. Fig. 1.10(b) shows the polariton occupancy of this state, which for low excitation densities increases linearly. However, when condensation takes place (aprox. at 1 kW/cm^2), the occupancy increases exponentially and, additionally, the emission shows a sharp linewidth narrowing. Another evidence is the build up of linear polarization from a depolarized state [see Fig. 1.10(c)]. When polaritons are created non-resonantly, the emission is completely depolarized (blue diamonds) no matter what polarization state is selected for the excitation light. By contrast, when the condensate is formed, a linearly polarized emission spontaneously arises (green circles). The last feature of polariton condensates that we will highlight in this section is shown in Fig. 1.10(d), which displays the density of polaritons as a function of the energy for different power densities. Below excitation threshold (gray circles) the polariton gas is not thermalized, however polaritons show fully thermalization at threshold (red circles). This is revealed by the Boltzmann-like decay of the distribution. The transition to a Bose-Einstein distribution arises when the threshold has been exceeded, and the fundamental state is massively occupied. Finally, let us mention one of the key properties that finally convinced the atomic physics community about the formation of a Bose-Einstein-like condensate was the observation of spatial coherence. To unambiguously demonstrate the creation of a true condensate it is required that the original coherence of the excitation source used for the excitation is lost in the excitation process. This ensures the existence of a phase transition and, therefore, that the creation of the condensate is due to a spontaneous symmetry breaking and not to a phase inherited from the excitation. The process to guarantee this condition is discussed in the next section 1.5.3.

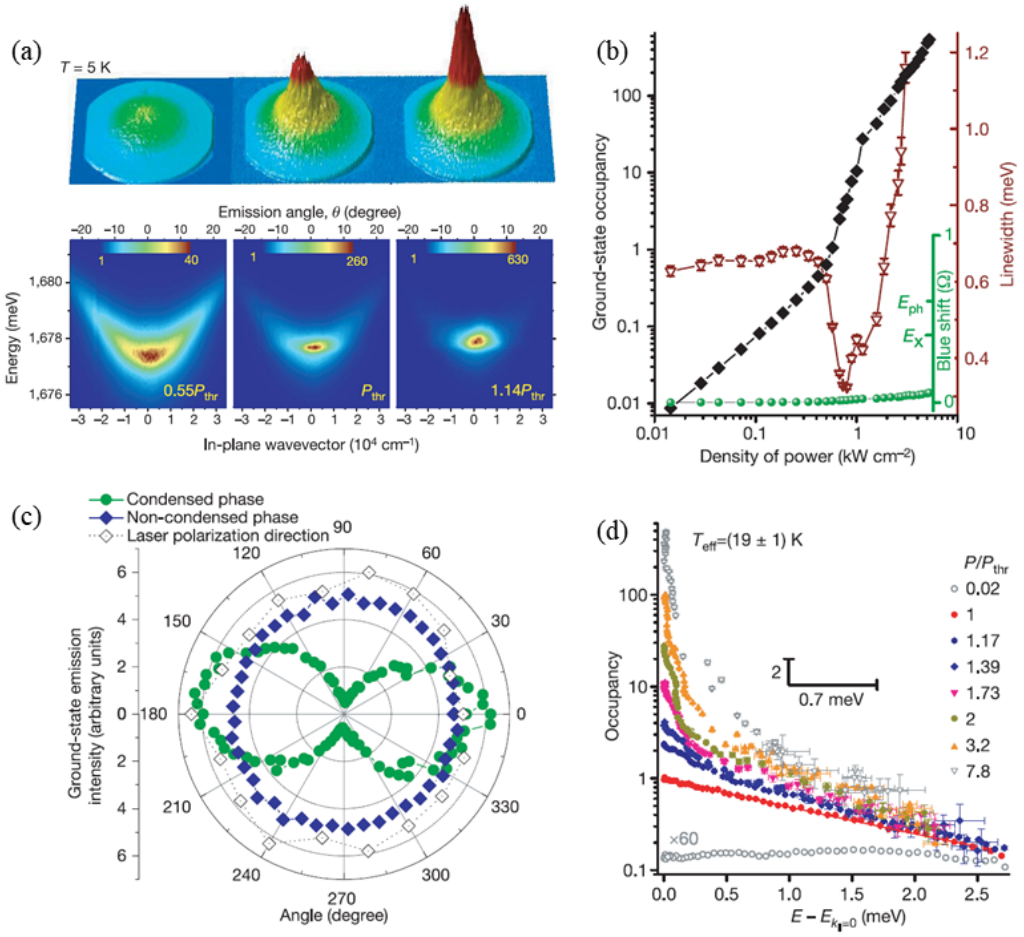

Figure 1.10. (a) *Top:* Pseudo-3D images of a polariton condensate far-field emission with the intensity displayed on the vertical axis (in arbitrary units). P_{thr} is the power density threshold for condensation. *Bottom:* Same data as in *top:* but resolved in energy. The horizontal axes display the emission angle and the in-plane momentum; the vertical axis displays the emission energy. (b) Occupancy of the $k_{\|} = 0$ ground state (black diamonds), its energy blue shift (green circles) and linewidth (red triangles) versus the excitation power density. (c) The polar plot displays the intensity of the ground state emission measured as a function of the angle of a linear analyzer below threshold (blue diamonds) and above threshold (green circles). Open diamonds represent the intensity of the linearly polarized emission above threshold, measured as a function of the linear polarization angle of the excitation laser. (d) Occupancy in ground- and excited-state levels, plotted in a semi-logarithmic scale for various excitation powers. For each excitation power, the zero of the energy scale corresponds to the energy of the $k_{\|} = 0$ ground state. Taken from [29].

1.5.3 Excitation and relaxation process

The creation process of a polariton condensate strongly depends on the way in which the microcavity is excited and, therefore, on how the driving field is injected. In the traditional non-resonant pumping scheme, the coherence of polaritons is not inherited from the excitation

laser [30]. Fig. 1.11 displays the relaxation process in which particles release the excess of energy by scattering events before creating the polariton condensate. This configuration involves pumping with light well above the LPB, creating initially hot photogenerated electron-hole pairs (gray spheres). Then, they relax into the exciton reservoir (blue spheres) at E_X very rapidly by emitting LO-phonons. After that, excitons in the reservoir undergo a second relaxation process, to the bottom of the LPB (red spheres), by phonon-polariton scattering. The relaxation process involves polaritons populating the lowest energy state, which is usually a few tens of meV below the reservoir, which makes the acoustic phonon scattering the most probable mechanism for the relaxation. Since the energy dispersion of polaritons is very steep compared to that of acoustic phonons, the relaxation takes place by small exchanges of energy and momentum. The process is schematically indicated with the blue arrow in Fig. 1.11. It is very inefficient and gives rise to the relaxation bottleneck,which has been theoretically and experimentally studied in detail using a Boltzmann description of polaritons [31, 32]. When high excitation conditions are employed, the bottleneck can be overcome in some cases by polariton-polariton scattering. In this way, the occupation of the polariton lower energy state is high enough to unleash the bosonic stimulation of the relaxation [33]. It is important to emphasize that due to the short lifetime of polaritons and the slow exciton-phonon scattering rate, only a small fraction of the generated excitons become cavity polaritons [34]. The polariton-polariton scattering can be also favored increasing the polariton lifetime by selecting DBR mirrors with higher reflectivity. Furthermore, increasing the number of QWs in the microcavity will reduce the carrier density in each QW allowing to overcome the difficulties related with the existence of the Mott transition of the excitons forming the polaritons [35].

Another excitation scheme can be considered for polariton condensates, in which they are created by resonantly exciting the LPB at a small k value. Therefore, the relaxation mechanisms explained above is no longer necessary. Under these conditions, polaritons emerge with the same energy and momentum as the excitation laser. Note that a direct consequence of this configuration is that the laser phase is directly imprinted in the polariton, hindering the posibility to study the spontaneous coherence properties of polariton condensates.

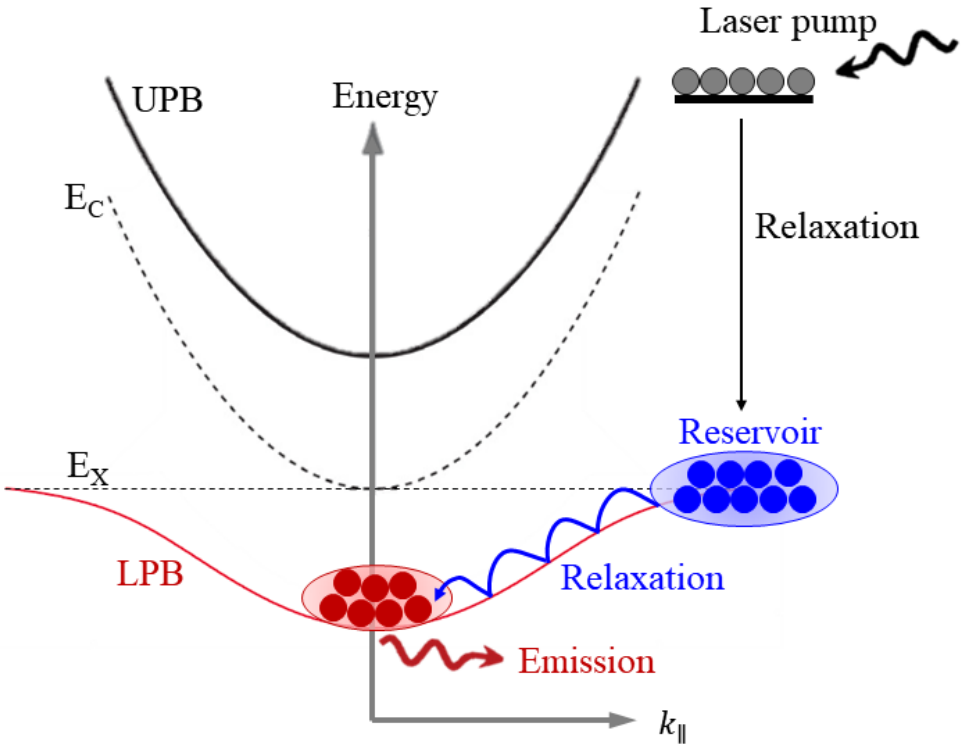

Figure 1.11. Non-resonant excitation scheme for microcavity polaritons. A laser excites the system at high energy creating an electron-hole plasma (grey spheres). They suffer a relaxation process in which they loose energy and accumulate at the excitonic level (E_X). This population accumulated at high k values is known as the excitonic reservoir (blue spheres) that continues losing energy until they arrive at the bottom of the LPB. At this point polaritons eventually form a macroscopic occupied state (red spheres) and the emitted photons allow to study their properties.

1.6 Interference between two condensates

Bose-Einstein condensation is one example of collective coherence of a many particles, state. Below a critical temperature particles spontaneously occupy the ground state, forming a coherent condensate. This coherence has been intensely studied both in atomic BECs [36] and polariton condensates [17, 37–53]. The coherence has been frequently investigated in real-space, by studying interference patterns, either for static condensates [50, 54, 55] or for moving ones when they meet in real-space [48, 56]. It is important to note that the interference can also occur in momentum-space, when condensates move with the same velocity, i. e., same momentum [57–59]. The existence of interference fringes in momentum-space is a very peculiar situation, which is characterized by the absence of contact between the condensates, demonstrating the existence of remote coherence in these systems, as predicted by Pitaevskii and Stringari [60].

To theoretically describe the appearance of these interference fringes, we consider the situation that we will use in our experiments: a system of two polariton condensates in a planar waveguide in which the movement is restricted to one dimension. A sketch of this scenario is depicted in Fig. 1.12. Two laser beams ($B_{1,2}$) separated by a distance d along the x axis impinge on the structure creating two propagating condensates at each excitation spot. The condensates are labeled as $\psi_{R,L}^{1,2}$ where the superscript indicates the laser source by which they are created and the subscript the direction of the propagation, right or left. Assuming that condensates are created under the same conditions, they acquire the same value of the momentum with a different sign depending on the direction of propagation: $k_x > 0$ for those going to the right and $k_x < 0$ for those going to the left. This translates into the fact that condensates moving in the same direction and created by different laser sources travel with a fixed distance d between them along the waveguide. Thus, ψ_R^1 and ψ_R^2 (or ψ_L^1 and ψ_L^2) are never in contact.

BECs, which are macroscopic states can be described as classical waves, therefore the wave function of condensates traveling towards the right is written as

$$\Psi_R(x) = \psi_R^1(x) + e^{i\varphi_R}\,\psi_R^2(x) \tag{1.30}$$

while for those traveling towards the left is

$$\Psi_L(x) = \psi_L^1(x) + e^{i\varphi_L}\,\psi_L^2(x) \tag{1.31}$$

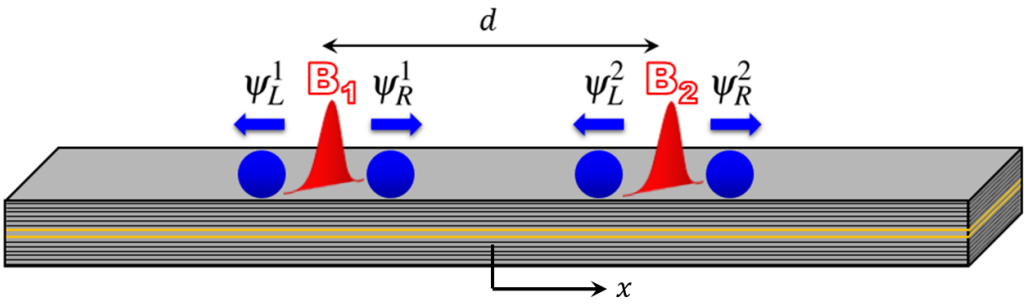

Figure 1.12. Sketch of polariton condensates propagating in a planar waveguide along the x direction. Two identical laser beams, labeled as B_1 and B_2, impinge on the waveguide separated by a fixed distance d. Two propagating condensates, illustrated as blue circles, are created by each laser beam. Their direction of movement is indicated by the arrows and the name: those moving to the right (left) are labeled with an R (L). The superscript 1 and 2 refers to the laser source.

The following steps are shown only for right propagation, however, a similar procedure can be performed to show the existence of interferences for left propagation. As already mentioned, the conditions to observe interference fringes in momentum-space require equal momentum for ψ_R^1 and ψ_R^2. The equal distance $d/2$ between the excitation beams and $x = 0$, allows to write the wave functions as $\psi_R^1(x-d/2) = \psi_R^2(x+d/2) = \psi_R(x)$. Using this result on Eq. 1.30 and writing the wave function in momentum-space, one obtains,

$$\Psi_R(k_x) = \psi_R^1(k_x) + e^{i\varphi}\,\psi_R^2(k_x) = e^{-ik_x(d/2)}\psi_R(k_x) + e^{i[k_x(d/2)+\varphi]}\psi_R(k_x) \tag{1.32}$$

where $\psi_R(k_x)$ represents the Fourier transform of $\psi_R(x)$. The modulus squared of this result provides the probability density of the momentum distribution:

$$|\Psi_R(k_x)|^2 = 2\,[1 + cos(k_x d + \varphi)]\,|\psi_R(k_x)|^2 \tag{1.33}$$

Therefore, the fact that the two propagating condensates have a constant phase difference between them, i.e. the existence of coherence between two condensates, yields to an interference pattern with a period of

$$\Delta k_x = \frac{2\pi}{d} \tag{1.34}$$

The longer the distance between the beams (d), the shorter the period. The observation of the fringes in momentum-space would not only confirm the existence of coherence between

condensates that have never been in contact but would also provide information of the spatial distribution of these condensates in real-space.

Following a similar procedure for the momentum-space, an analogous expression is found for an interference pattern in real-space. In this case, the fringes are produced by the overlap of condensates in real-space. In the proposed system of Fig. 1.12, only condensates traveling to the center of the guide can meet (ψ_R^1 and ψ_L^2), therefore, the final expression for the period of the fringes in real-space is given by

$$\xi = \frac{2\pi}{|k_R^1 - k_L^2|} \tag{1.35}$$

which depends on the difference in momenta of the propagating condensates.

1.7 Boson Josephson effect for polaritons

The successful creation of exciton-polariton condensates in microcavities has opened the path to use its macroscopic phase coherence for the study of quantum phenomena. One of the most remarkable manifestations of this quantum collective nature is the Josephson tunneling effect, in which a classically forbidden current can flow without dissipation. The Josephson effect was initially predicted in 1962 [61] with its first experimental demonstration in 1963 [62]. Years later, it was discovered in superconductors [63] and its study was extended to weakly coupled atomic BEC systems [64–67]. Due to the low temperature of atomic BECs, one can consider the dynamical effects arising between two atomic condensates confined in a potential using the mean field approach and more importantly, zero temperature approximation. The Josephson effect with special attention to the occurrence of Josephson oscillations and a population imbalance between traps has been reported in these systems [68, 69]. Exciton-polariton condensates have attracted a lot of attention to theoretically and experimentally study Josephson Junctions [44, 70, 71]. Due to the bosonic nature of polaritons, we consider the bosonic Josephson junction (BJJ) in which two macroscopic populations are trapped in a double QW. The Josephson effect results in an alternating current for a constant potential difference, i.e., the presence of Josephson oscillations [25]. A scheme of this model is shown in Fig. 1.13, in which the condensates are located in QWs (1 and 2) separated by a finite distance D. In the figure, the potential depth (V) and size (L) of the two wells are the same. We analyze below the consequences of the coupling between both condensates.

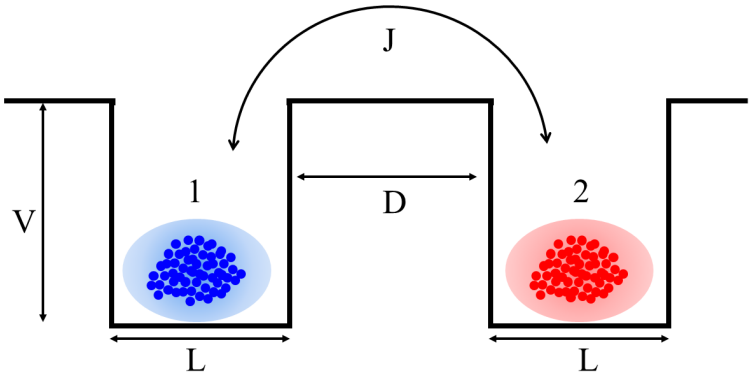

Figure 1.13. Two quantum well system in which a polariton condensate is located in each well, 1 and 2. V is the potential depth, L the length of the quantum wells and D the distance between them. The tunneling of particles is indicated by J.

Knowing the geometry of the trap, the coupling parameter J can be estimated as [25]

$$J \approx 4Ve^{-\sqrt{2mVD}/\hbar} \tag{1.36}$$

which depends on the separation and potential depth of the QWs. This approximation results from the assumption that the coupling is produced in the range of $D \gg L$. V and J are considered to be independent of the particle density, however, strictly speaking, this is not exact since the repulsive interaction between polaritons leads to the blue shift and the reduction of the trap's effective potential.

To describe the Josephson effect one defines the dynamical oscillation of two weakly linked BEC in the time dependent GP equations

$$\Psi(r,t) = \psi_1(t)\phi_1(r) + \psi_2(t)\phi_2(r) \tag{1.37}$$

where $\phi_1(r)$ and $\phi_2(r)$ are the ground states of the condensates in the QWs 1 and 2, respectively. The corresponding wavefunctions of each condensate are time dependent complex numbers given by,

$$\psi_{1,2} = \sqrt{N_{1,2}(t)}\, e^{i\theta_{1,2}(t)} \tag{1.38}$$

where $N(t)$ and $\theta(t)$ are the number of polaritons and their phase in each quantum well, respectively. These wavefunctions obey the two mode dynamical equations defined as [65]

$$i\hbar\frac{d\psi_1}{dt} = \left(E_1^0 + U_1|\psi_1|^2\right)\psi_1 - J\psi_2 \tag{1.39a}$$

$$i\hbar\frac{d\psi_2}{dt} = \left(E_2^0 + U_2|\psi_2|^2\right)\psi_2 - J\psi_1 \tag{1.39b}$$

where $E_{1,2}^0$ are the energies of the condensates' ground state. In the case of two symmetric potentials ($V_1 = V_2$), as it is the case shown in Fig. 1.13, the condition $E_1^0 = E_2^0$ is fulfilled. The inter-particle interaction is indicated by the non-linear terms using the variable $U_{1,2}$. The last term in both equations describes the amplitude of the Josephson coupling J between both populations. Note that to define this model the damping and finite temperature effects have been ignored. Introducing now in the equations new variables for the population imbalance (η) and the phase difference (θ)

$$\eta = \frac{N_1(t) - N_2(t)}{N_1(t) + N_2(t)}, \qquad \theta = \theta_2(t) - \theta_1(t) \tag{1.40}$$

Using the system of Eq. 1.39 and the definitions in Eq. 1.40 one can obtain the following set of two equations:

$$\frac{d\eta(t')}{dt'} = -\sqrt{1-\eta^2(t')}\,sin\left(\theta(t')\right) \tag{1.41a}$$

$$\frac{d\theta(t')}{dt'} = \Upsilon\eta(t') + \frac{\eta(t')}{\sqrt{1-\eta^2(t')}}cos\left(\theta(t')\right) + \Delta E \tag{1.41b}$$

where a new constant has been introduced, $\Upsilon = U(N_1+N_2)/2J$ with $U = U_1 + U_2/2$. In nondissipative systems, the total number of polaritons $N_1 + N_2 = |\psi_1|^2 + |\psi_2|^2$ is conserved. To simplify the development of the equations, a renormalization of time has also been introduced as $t' = 2tJ/\hbar$. The last term in the second equation (ΔE) characterizes the energy gap between the condensates population in the case of a non-symmetric double-well potential. In a Bosonic Josephson junction, created in an atomic system, this energy difference is determined by both the geometry of the QWs (or traps, depending on the system) and the nonlinearity of the atomic condensates [72]. By contrast, when polariton condensates are considered, the energy difference ΔE not only depends on $E_{1,2}^0$ but also on the interaction U and tunneling J between the condensates. However, since in the experiments performed in this thesis only symmetric confinements are considered, we focus on the case of $\Delta E = 0$. In our case, this confinement is created using multiple layers of materials with different refraction indexes, creating microcavities that in essence behave as QWs. Therefore, the

Hamiltonian of the system results [65],

$$H(\eta(t'),\theta(t')) = \Upsilon\frac{\eta^2(t')}{2} - \sqrt{1-\eta^2(t')}\,cos\left(\theta(t')\right) \tag{1.42}$$

Note that the total energy is fixed by the initial values of the parameters $\eta(t')$ and $\theta(t')$, since the rest of the parameters are constant with time. In the case of equal population in both QWs, i.e., $\eta = 0$, the Hamiltonian is described only by the phase difference between the condensates as $H(0,\theta(t')) = -cos\left(\theta(t')\right)$. It is possible to establish a connection between the system of equations of Eqs.1.41 to determine the polariton dynamics but also different dynamical aspects of the Josephson system. In particular, the Josephson tunneling can be evidenced through the presence of oscillations in the emission of polariton condensates. We extract the current I for polaritons, which can be determined from the Eqs. 1.41a using the relation $I \propto d\eta/dt'$,

$$I = -I_0 sin\left(\theta(t')\right) = -I_0 sin\left(\theta\left(\frac{2tJ}{\hbar}\right)\right) \tag{1.43}$$

where $I_0 = (N_1 + N_2)J/\hbar$ is the polariton current in the quantum wells. The Josephson tunneling results in the appearance of an alternating current, evidenced by the harmonic dependence of Eq. 1.43. On the right-hand side of the equation, the normalization of time has been undone, revealing a phase difference directly proportional to the tunneling parameter J. Therefore, one should expect the period of the harmonic function to be dependent with $J^{-1} \propto e^{\sqrt{2mVD}/\hbar}$, where the definition of Eq. 1.36 has been applied. If two QWs with equal V are considered, then, the period of the oscillations will increase with the distance D between both wells. If D becomes considerably large, the coupling will be suppressed and the current along the cavity will become negligible.

Chapter 2

Experimental techniques and samples

2.1 Experimental techniques

From an experimental point of view, polaritons created in a microcavity are the most accessible Bose Einstein Condensate systems, together with photon condensates [73]. There is a direct correspondence between polaritons and photons leaking out of the cavity since the latter, carry the same energy and momentum as polaritons in the QWs embedded in the cavities. Therefore, by measuring the external photon field through conventional optics, we obtain an insight of the basic properties of polaritons. Their photoluminescence can be measured under resonant or non-resonant conditions using a laser source, allowing to determine, for instance, the spatial distribution of the emission along the sample or to differentiate among a strong or weak coupling between the cavity and the exciton modes. Furthermore, by collecting the angle-resolved emission, the polariton dispersion is obtained, providing the momentum distribution of the carriers in the QWs. Thus, the determination of the experimental setup is a key factor when studying the spectral properties of polaritons in a semiconductor microcavity.

A general scheme of the experimental setup used in this thesis is shown in Fig. 2.1. The optical excitation is performed with a laser beam guided by optical elements before being focused on the sample surface. The path of the laser before arriving to the sample is modified accordingly to the purpose of the experiment. For example, to perform the experiments of chapter 3 and, as depicted in Fig. 2.1, the laser beam is divided into two different paths to achieve simultaneous excitation in two locations of the sample. Additionally, different elements can be placed in this part of the setup, such as an optical chopper to avoid the

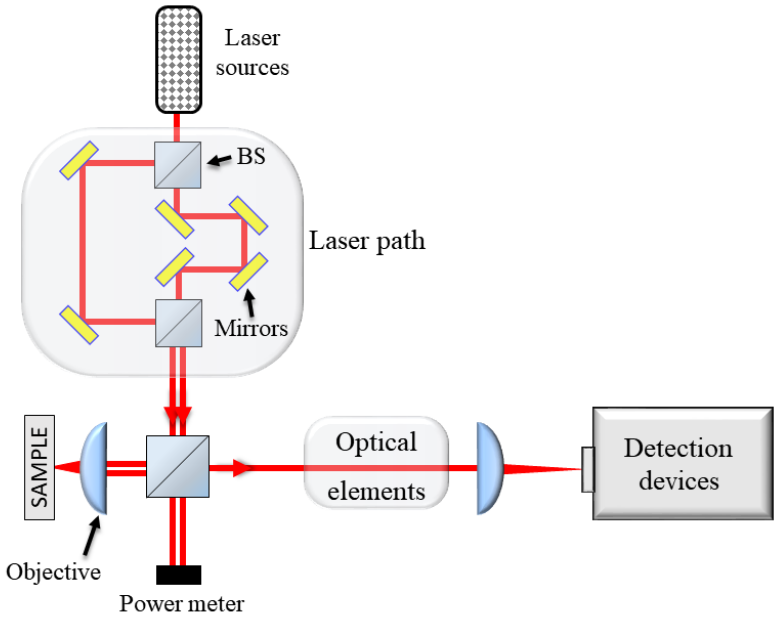

Figure 2.1. General scheme of the experimental setup showing the path of two laser beams generated from the same source. They are focused into the sample using an objective lens that also collects the emission. The latter is guided to the detection devices using different optical elements and finally, adding another lens, the emission is focalized in the entrance slit of the detectors. Different elements such as 50%-50% beam splitters (BS), mirrors, polarization optics and power meters are also employed.

sample heating or a polarizing filter to determine the direction of the electric field. Right before impinging the sample, the light beam from a Ti:Al_2O_3 laser propagates through a beam splitter with a 50:50 ratio, generating two identical signals that are directed into different trajectories: one is focused on the sample using a microscope objective, while the second is guided into a power meter, allowing the instantaneous monitoring of the pump power while exciting the samples. After the excitation, the polariton PL is measured in a reflection configuration using the same objective lens as that employed for the excitation. The emission beam acquires a plane wavefront after crossing the objective, which propagates parallel to the optical axis of the lens over a long distance. In order to analyze this emission, it is directed to the detection equipment. Let us consider, for the sake of simplicity, the case where only an objective is used in the setup and not additional optical elements are employed. In this case, by adding a lens after the objective, the emission is focused on the detection device and the setup acts as a simple optical microscope. However, in this part of the setup corresponding to the detection of the signal, further optical elements can be placed. If another lens is added, it is possible to obtain the angle-resolved emission and hence, to measure the

momentum distribution of polaritons. The selection of different sets of lenses will determine the magnification of the collected emission on the detection devices.

Complementarily to these optical elements, a spatial filter or pinholes can be placed in the setup to select specific parts of the emission either in real- or momentum-space. This filtering is done in some experiments to measure, for example, the emission from different spatial parts of the same microstructure while polariton condensates propagate along it. Moreover, additional bandpass filters are used to avoid any laser reflection that may hinder the collection of the polariton emission when measuring energy-integrated images. They block the laser wavelength and allow the rest of wavelengths of the emission spectrum to be collected. The details about the detection techniques of the polariton emission are explained in section 2.1.2.

2.1.1 Excitation conditions

The experiments presented in this thesis were performed with a system of lasers composed by a continuous wavelength (cw) laser and a tunable pulsed laser. The cw laser is a *Millennia Pro Spectra Physics* model, containing a Nd:YVO_4 and a LBO frequency-doubling crystal. It operates with a fixed wavelength of 532 nm and a maximum output power of 20 W. The cw laser pumps a pulsed laser cavity, which is a *Tsunami Spectra Physics* model based on a Ti:Al_2O_3 crystal. Using different optics sets, the output wavelength of this laser can be tuned between 700 nm and 1100 nm. For the experiments presented in this work, the excitation wavelength is chosen between 740 nm and 810 nm with an output power of 1.5 - 2.0 W obtained from the *Tsunami*.

The pulsed laser is mode-locked through an acousto-optical modulator operating in the picosecond range. The configuration yields a pulse duration of $\sim$ 2 ps with a repetition rate of 82 MHz (period of 12 ns). The pulse duration is measured using an autocorrelator (*Spectra Physics* model 409), in which the laser is split into two beams with different paths: the path is fixed in one of the beams while its copy is time-delayed. Both pulses overlap again in a non-linear crystal generating a new up-converted signal; the measurement of the time delay and the intensity provides the value of the temporal duration of the pulse.

In addition, the results presented in chapter 6 have been performed with a different system of lasers. As in the previous case, a cw laser with a wavelength of 532 nm pumps a second laser, which in this case is a cw, monomode, Ti:Al_2O_3 laser. The configuration of the laser allows to tune the output wavelength in a wide range. In particular, for these experiments it was set at 745 nm.

In the experiments, different lenses and microscope objectives have been employed to focus the laser on the samples. The details about the optical components of the setup are specified below, describing what has been needed for the different samples used in the experiments. We have used two different excitation schemes depending on the purpose of the experiment: quasi-resonant and non-resonant excitation. We start describing those employed for the latter case.

Non-resonant excitation

In this experimental scheme, the laser beam is tuned to high energies ($\sim$ 1.65 eV), typically 100 meV above the bottom of the LPB, corresponding to the wavelength of the first reflectivity minimum above the stop-band of the microcavity [see Fig. 1.7(a)]. Upon excitation, hot excitons are created, which eventually relax into polariton states, loosing the phase of the excitation laser. Therefore, the non-resonant excitation, allows studying the appearance of the spontaneous coherence when polaritons are condensed at the bottom of their LP dispersion [29]. This experimental scheme is used along this thesis to study the energy landscape and propagation of polariton condensates in GaAs-based microcavities; particularly, in the experiments described in chapters 4, 5 and 6.

Quasi-resonant excitation

In this case, the sample is pumped with the laser tuned to the energy of the excitonic reservoir. The energy difference between the excitonic reservoir and the polaritons created after the relaxation processes is usually 10 times smaller than in the case of non-resonant excitation. This excitation scheme is advantageous for studying the polariton-polariton interaction [74]. Under pure resonant conditions, polaritons would be injected with a phase, as well as a spatial and temporal coherence, directly imprinted by the laser source. However, under a quasi-resonant excitation, polaritons are created with a non-reversible dressing of excitons ensuring that they do not inherit any phase from the excitation laser. The experiments described in chapter 3 are performed under quasi-resonant excitation.

2.1.2 Detection conditions

During the experiments, the samples are kept in a cold finger cryostat connected to a He transfer line. A flow of He gas is pumped from an external dewar to the cryostat, decreasing the temperature of the sample to cryogenic values (down to 4 K). The flow can be controlled manually with different valves in the circuit making possible to determine a stable value of the temperature. For a fine adjustment, a programmable controller is used to guarantee an

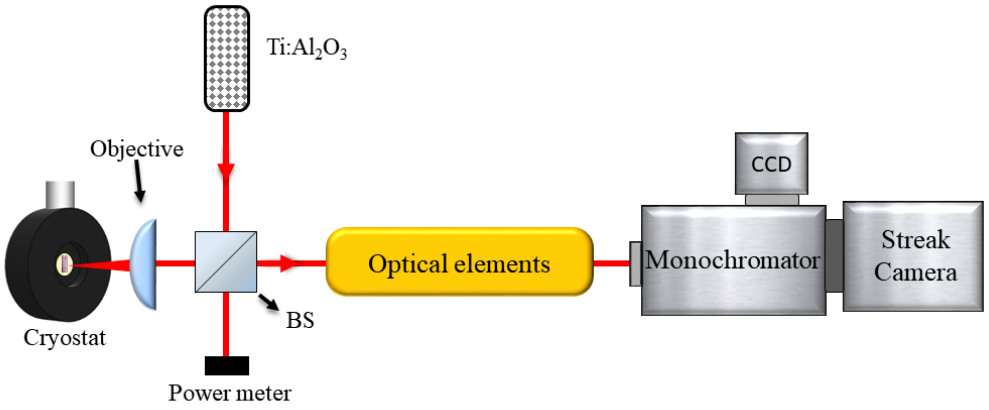

Figure 2.2. Scheme of the experimental setup. The excitation is performed by a Ti:Al_2O_3 laser, which is guided into a 50%-50% beam splitter (BS), and consequently to the sample. The latter is inside a cold finger cryostat. The emission is directed to the region marked with a yellow rectangle, in which different optical elements are located. Finally, the emission is driven into the detection devices composed by a monochromator coupled to a CCD and a streak camera.

accuracy of the order 0.5 K. The temperature is measured by means of a thermocouple placed on the sample holder, which is used to determine the actual temperature of the sample. For this reason, an optimal thermal conduction is ensured using silver paint to glue the sample on the sample holder in the cryostat. Additionally, the cryostat has a thermal shield consisting of a vacuum chamber. The pressure in this chamber is controlled externally with a high vacuum pump that maintains a pressure of the order of 10^{-7} mbar inside the cryostat. However, the pump is turned off to avoid vibration problems during the measurements.

The optical properties of a semiconductor microcavity can be widely study through its PL. As shown in Fig. 2.2, after exciting the sample with the laser source, the PL is collected with the same microscope objective as that of the excitation, which provides a spatial resolution given by $R = \lambda/2NA$ (NA is the numerical aperture of the objective and λ is the wavelength of the emission). The PL can be manipulated with different optical elements such as mirrors, lenses or slits. The region where these elements are placed, is indicated by the yellow rectangle in Fig. 2.2. The resulting emission is analyzed in a monochromator and detected using either a CCD camera or a streak camera. The description of the different optical elements placed in this part of the setup and the detection devices are explained below.

2.1.2.1 Energy-resolved photoluminescence

The experimental setup for energy-dependent measurements is shown in Fig. 2.3, where two different schemes of imaging techniques are depicted. The objective lens with a focal

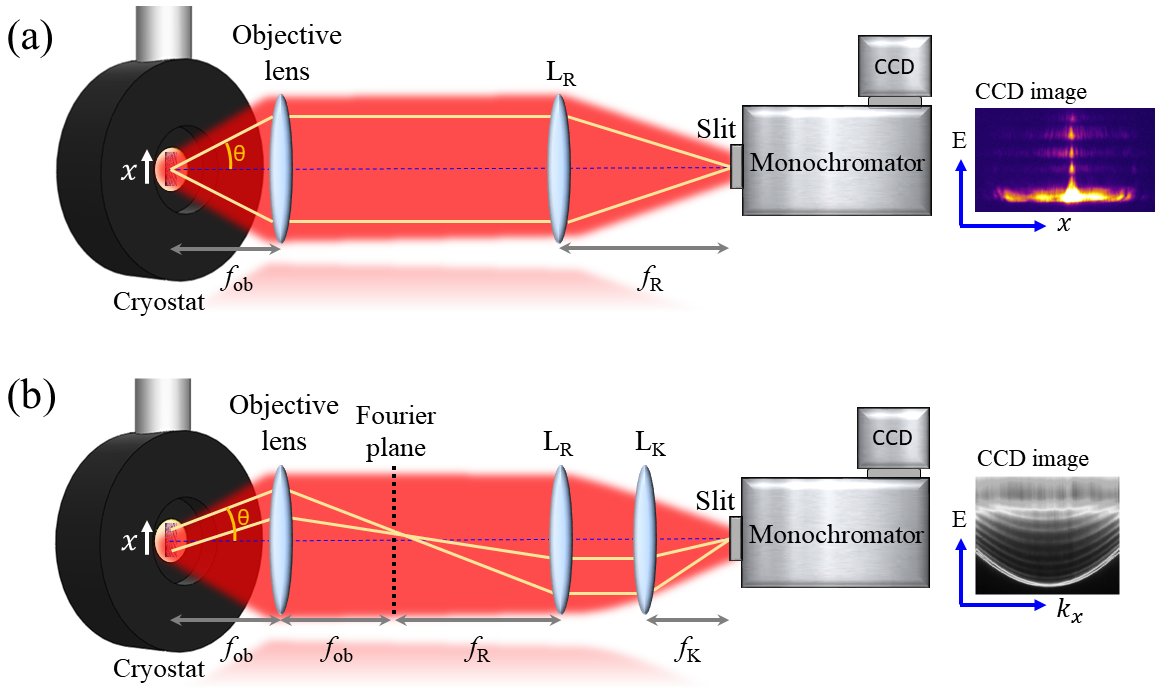

Figure 2.3. Scheme of the imaging technique for (a) real- and (b) momentum-space. The sample is placed in a cold finger cryostat. The PL of the sample is collected with an objective lens of focal length f_{ob}. The yellow lines represent the optical path of the sample emission departing with a given angle (θ) from a point of the sample. The PL is focused in a monochromator and a CCD camera. In (a), the PL is focused through the slit using the lens L_R, placed at its focal distance, f_R. The resulting image in the CCD camera is an energy (E) vs. x map, where x is the coordinate along the sample. In (b), an additional lens L_K, with a focal length f_K, is placed in the setup, focusing the Fourier plane generated between the objective and L_R. The resulting image is now an E vs. k_x map, where k_x is the wavector of polaritons.

distance f_{ob} collects the PL of the sample. Using a second lens (L_R) with longer focal distance (f_R), a spatially resolved spectrum is collected. In other words, the emission is resolved in real-space. A scheme of this technique is indicated in Fig. 2.3(a). The combination of these two lenses yields an optical magnification given by f_R/f_{ob}. When analyzing this emission with a monochromator equipped with a CCD, an energy vs x map is obtained, where x is the coordinate along the sample. Therefore, this experimental setup is equivalent to an optical emission microscope.

A slightly different setup is used to obtain the momentum distribution of the PL, also referred as k-space, in which another lens must be added to the setup. This configuration is described in Fig. 2.3(b) where L_K is placed between L_R and the spectrometer. In this case, points with different heights in the Fourier (momentum) plane, formed at the common focal plane of the

objective and L_R, are focused into the monochromator, thus, obtaining the angle-resolved emission of polaritons. Note that this setup performs experimentally a Fourier transform from a spatial coordinate to its conjugate momentum coordinate. As a result, an energy vs k_x map is obtained in the monochromator, where k_x is the momentum (or wavevector) of polaritons [as depicted at the right-hand side of Fig. 2.3(b)]. The specific position and focal distance of the L_K lens determines the momentum-space magnification, given by $f_K f_{ob}/f_R$. Note that this experimental set-up allows the simultaneous observation of real- and k-space, since only one lens must be added or removed from the setup. The switching between both configurations takes just a few seconds, keeping the excitation conditions constant.

The emission is directed and focused in the detection devices. The latter are formed by a monochromator (Acton SpectraPro 2500i model), with 500 mm of focal length, coupled to a CCD camera (Acton Pixis 1024 model) with a high resolution of 1024 x 1024 pixels. The entrance slit of the monochromator is generally $\sim$ 100 µm wide. However, it is easily adjusted with a micrometric screw to meet the required spectral resolution of each experiment. Since the PL beam is wider than the entrance slit, only a thin slice of the emission is analyzed. More advanced techniques, explained in section 2.1.2.3, allow to scan the full emission by analyzing consecutive slices. When the selected emission reaches the diffraction grating inside the monochromator, each energy component is diffracted at a different angle. Two different diffraction gratings with 600 and 1200 lines/mm have been employed in the experiments. The diffracted PL is directed towards the coupled CCD camera, resolving the emission intensity in energy and providing also the spatial or momentum distribution at each energy. Therefore, the image generated by the CCD contains the energy-dependent intensity map [Fig. 2.3(a)], or the momentum-dependent intensity map [Fig. 2.3(b)] for each slice of the PL that enters in the spectrometer. The energy resolution of these maps is determined by the width of the entrance slit and the characteristics of the diffraction gratings, resulting in a range of 0.4-0.5 meV for the parameters used in this thesis.

Alternatively, there is the possibility of using the CCD camera as a standard camera capable of recording real images of the sample. This allows to directly photograph the surface of the sample as well as the image of the k-space, depending on the collection lenses employed.

2.1.2.2 Time-resolved photoluminescence

Additionally to the energy-resolved measurements, the PL can also be time-resolved by means of a streak camera. This device is used to measure ultrafast light phenomena, such as the dynamics and transport of polaritons. We use a Hamamatsu C5680 streak camera

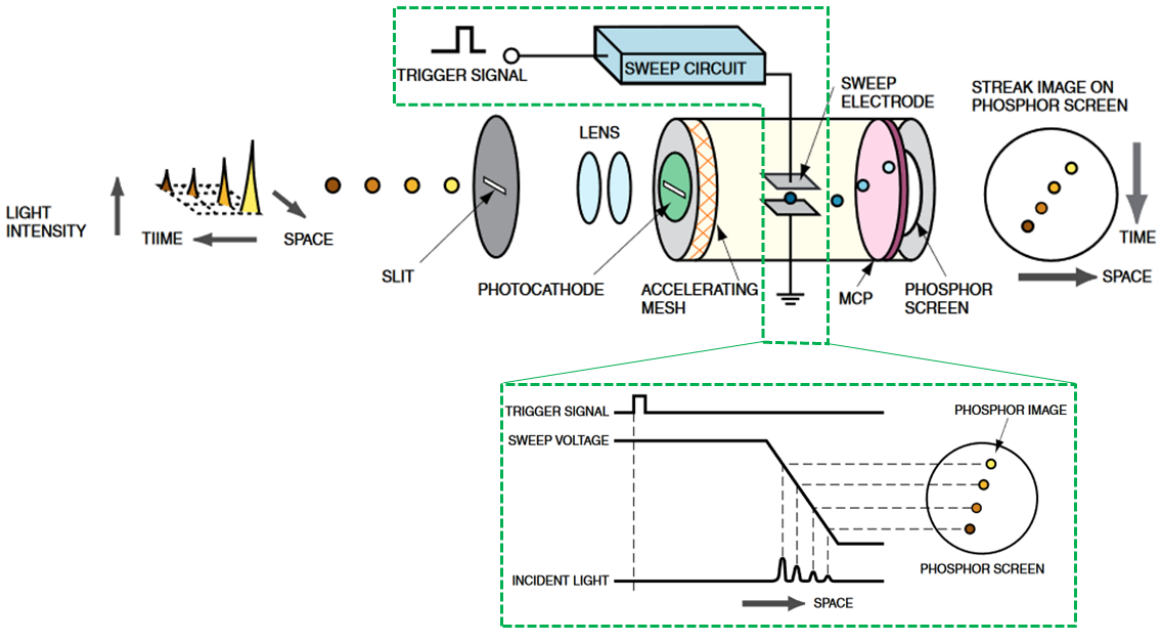

Figure 2.4. (a) Schematic representation of the operating principle of a streak camera. The incident signal impinges on the system from the left, resulting in the image of the phosphor screen (colored spots). The element MCP is a micro-channel plate. The inset, surrounded by a green dashed line, depicts the operating timing of the streak camera. The trigger signal, synchronized to the excitation pulse, indicates the beginning of the sweeping voltage, which deflects electrons on the phosphor screen obtaining a time-dependent PL. The generated time axis is the vertical axis of the image, while the horizontal axis is the position or energy of the PL. Adapted from Hamamatsu - guide to streak cameras - www.hamamatsu.com.

coupled to a Hamamatsu C13440 CMOS digital camera. The streak camera can be used in combination with the monochromator, obtaining the temporal dependence of the collected light as a function of the positions (x) or energies. Our streak camera allows to measure processes faster than 2 ns with a maximum resolution of 10 ps. Therefore, the use of a pulsed excitation source (2 ps of duration in this thesis), allows not only the observation of the relaxation process of the carriers (longer than the pulse duration) but also to monitor the rapid dynamics of polaritons, which have typical lifetimes of the order of 1-100 ps [10, 75–77].

The operating principle of the camera is depicted in Fig. 2.4. The PL arriving to the camera, drawn as colored spots, passes through a slit, where a set of lenses focus the emission onto a photocathode. In this part, electrons in a layer of metal absorb the energy of the incident photons, and accelerate due to the presence of an accelerating mesh. The electrons then pass between a pair of sweep electrodes, where a high-speed voltage is applied. A trigger signal synchronizes the voltage sweeping with the laser source, this process is shown in the inset of Fig. 2.4. The accelerated flow of electrons, arriving at different times, are deflected at

different angles in the vertical direction. After entering in the micro-channel plate (MCP) and being multiplied several thousands of times, they impact against a phosphor screen where they are converted again into photons. The first electron to arrive is placed in the higher-most position on the phosphor screen and from there, the rest of the electrons are placed sequentially from the top to the bottom of the screen. Therefore, the vertical component of the screen can be translated into a time axis. Furthermore, the brightness of the phosphor images is proportional to the intensity of the incident light. Depending on the optical elements installed in the setup, the horizontal axis of the image corresponds either to real-space, position or wavevector k. However, if the PL impinging on the streak camera does not come from different spatial positions but is dispersed first in different energies/wavelengths in the monochromator, the horizontal axis will provide the energy/wavelength of the emission.

The PL of a semiconductor microcavity cannot be time-resolved in a picosecond scale after a single-shot measurement due to its weak signal. However, a multiple shot measurement substantially improves the signal-to-noise ratio. If the setup is stable, each laser pulse excites the polariton condensate under the same conditions and one can record the dynamics repeatedly, once per pulse. Averaging over many acquisitions, a measurement with a high signal-to-noise ratio is obtained. Typically, the acquisition times during the experiments are of the order of 1 second. Taking into account the repetition rate of the pulsed excitation, 12 ps, a measurement of only 1 s is the result of averaging over $\sim$82 millions of pulses. This can be performed if the sweeping voltage that deviates the electrons is synchronized very precisely with the same repetition rate as that of the excitation, what is made in our setup thanks to a fast photodiode which samples a small signal obtained from the pulsed laser source.

2.1.2.3 Tomography

A more complete study of the polariton PL is obtained by reconstructing the 2D images, obtained with the techniques explained above, while introducing a third variable. This is achieved by sequentially translating the imaging lens (L_R or L_K) perpendicularly to the entrance slit (of the monochromator), which is oriented in the x-direction. The lenses are displaced with step-motors, which move the PL beam across the slit, allowing to record a new spectrum for each line scan (y) of the image.

An example of an energy-resolved tomography is described in Fig. 2.5(a). The polariton PL is measured with the monochromator, as explained in section 2.1.2.1, obtaining an E vs x map. As the imaging lens is displaced, a new acquisition is made for a different y position,

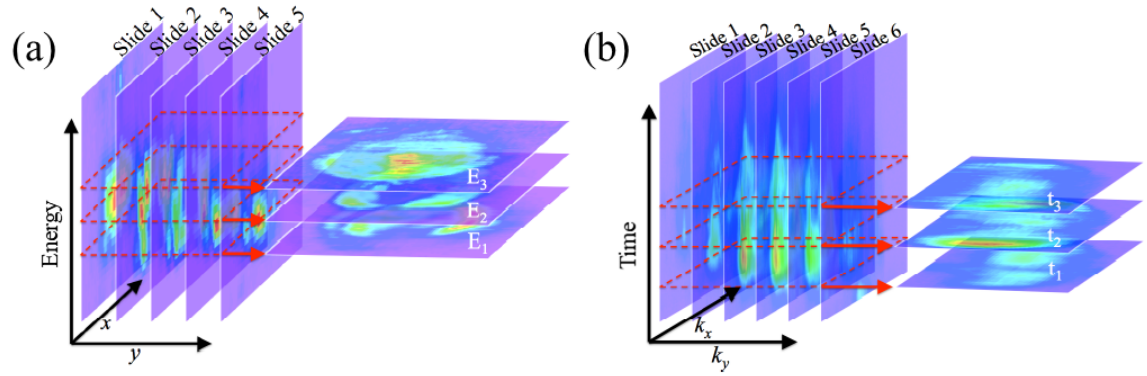

Figure 2.5. (a) Illustration of the **spectral** tomographic technique done in real-space. Each of the slices on the left side corresponds to a specific y and have energy versus x information. After the reconstruction, access to the real-space image for any energy is possible, as shown with the three reconstructed layers at $E_1 - E_3$. (b) **Temporal** tomographic technique. On the left side an illustration of the slicing of a momentum-space image is shown where each of the slices is an image taken at the output of the streak camera (k_x vs. time). Different slices correspond to subsequent k_y momentum-space positions. After the reconstruction, access to the full momentum-space image at any time t, is accessible by looking at the layer that corresponds to the desired time. Here (on the right side) three layers at three different times $t_1 - t_3$ are shown. Adapted from [78].

providing a second E-x map. This process is repeated until the full PL is recorded in slides. Note that the number of slides will determine the resolution of the tomography. As indicated by the red dashed squares in the figures, the measurements are reconstructed by taking the same row of data to form an x-y image for a specific energy value. The same procedure is used to energy resolve the momentum-space in which k_x-k_y maps are obtained.

As shown in Fig. 2.5(b), when the PL is time-resolved, the tomography technique allows to follow the polariton dynamics, in this case, in k-space. The same method developed for the energy-resolved tomography is followed for the time-resolved tomography technique. The signal is sent to a streak camera that measures the polariton distribution along k_x as a function of time. The step-motors scan the PL obtaining time dependent emissions for different k_y values. A special care must be taken during these measurements: since it can take several minutes to acquire the whole tomography, the pulsed laser needs to be extremely stable to preserve the same excitation conditions for each acquisition. The experiment is stored in a 3D matrix whose time-slices correspond to the condensate image at a specific time. The same procedure can be followed to time resolve the real-space in which x-y maps are obtained.

The step-motors and the image acquisition are controlled by software programs that allow to determine the size and number of steps (therefore, number of images), the time acquisition as well as other fundamental parameters, completely characterizing the tomography.

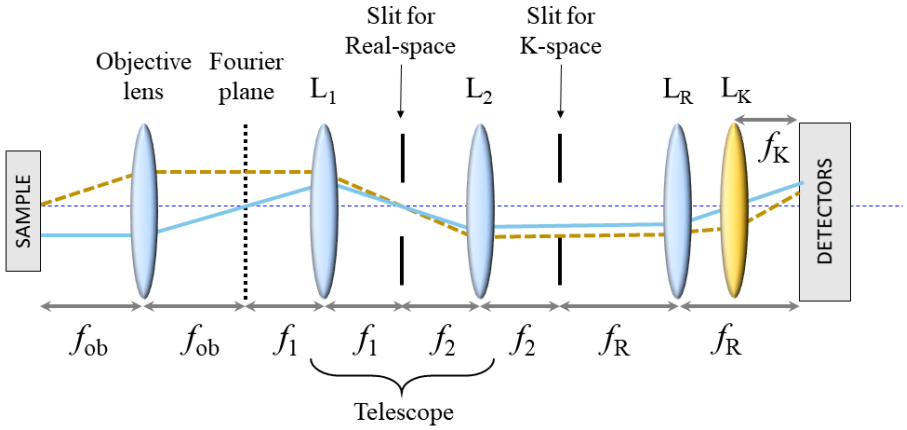

Figure 2.6. Real and momentum-space filtering technique. The objective lens, L_R and L_K form the regular setup used to image the momentum distribution. Their corresponding focal lengths are f_{ob}, f_R and f_K. The filtering in real-space is performed removing L_K and placing a slit in the common focal plane of L_1 and L_2, whose focal lengths are f_1 and f_2, respectively. The filtering in k-space is performed placing a slit between L_2 and L_R. As an example, the path of a emitted ray from the sample is depicted with a blue solid (yellow dashed) line when collecting the real- (k-) space.

2.1.2.4 Spatial Filter

Real and momentum-space filtering is used to locally analyze the polariton emission. This technique provides rich information about the dynamics and properties of the particles in certain regions of the sample selected at will. Fig. 2.6 describes the lens distribution of the filtering technique in real- and momentum-space. In this case, two lenses (L_1 and L_2) are added to the regular setup described in Fig. 2.2. In the real-space configuration, removing L_K (marked in yellow), a focused image of the emission is obtained at the common focal plane of L_1 and L_2, where the distances f_1 and f_2 coincide. We introduce a slit in this plane to filter out the contributions from non-desired regions of the sample. In a similar way, now adding L_K to the setup, the momentum-space can be also filtered by focusing the Fourier plane between L_2 and L_R, at the focal planes of both lenses. By placing another slit in this plane, we can directly manipulate the emission, for example, removing only $k < 0$ values while collecting the signal for $k > 0$. The filtering can be done individually, or simultaneously to obtain a doubly filtered image (in real- and k-space).

The combination of both lenses introduces a new magnification factor, creating a telescope system: in real-space is given by $\frac{f_R f_1}{f_{ob} f_2}$, while for momentum-space the expression results $\frac{f_{ob} f_K f_2}{f_R f_1}$. This technique has been employed during the experiments of chapters 4, 5 and 6.

2.2 Samples

Similarly to photonic architectures, the potential landscape of microcavities can be designed at will by creating structures that introduce a change in the index of refraction and/or energy-potential barriers. The samples are composed of semiconductor cavities that have been patterned to create confinement along different dimensions, thus, it is possible to guide polariton condensates through different paths. The samples presented in this chapter are planar microcavities that allow the creation of 2D condensates. The cavities, as explained in chapter 1, are formed by top and bottom DBRs consisting of parallel layers of $Al_xGa_{1-x}As$ alloys of nanometric width, which surround several sets of QWs. Different concentrations (x) of each component result in a nonidentical refractive index and therefore different reflectivity. Thus, the design of a microcavity offers a large number of possibilities when one considers the composition of the layers, their index of refraction and the number of layers.

The samples have been grown using a MBE reactor, allowing the creation of homogeneous layers by adjusting the deposition rate of the chemical elements that compose the cavity. The source elements (Al, Ga and As) are heated separately and directed at high velocity towards the substrate. The materials, in gas state, condense while reacting with each other to finally create the $Al_xGa_{1-x}As$ alloys. The composition of the generated layers can be controlled during the growth process by shutters in the effusion cells and by modifying the temperature of the sources. This technique allows to even obtain a single layer of atoms. Once the microcavities are created, they are patterned through etching methods, removing partially or totally the DBRs and QWs down to the substrate. This method allows to engineer the desired geometry in the sample with a strong lateral confinement. The large difference of refractive indexes, in this case the air and the semiconductor, produces a total internal reflection of the light at the interface between these regions, forcing the particles to redirect their trajectories along the structures.

In general, to achieve a homogeneous thickness of the different layers that compose the MC, the substrate is rotated while the source elements are deposited. The stop of this rotation, together with the spatial inhomogeneity of the molecular beams that reach the substrate, make it possible to introduce a wedge into the cavity so that its thickness increases along the radial direction. As a direct consequence, the cavity mode energy gradually shifts with the position on the sample. The presence of the wedge allows to select the detuning (δ), defined as the energy difference between the cavity mode and the exciton level, throughout the sample, from positive to negative values. Is it important to note that the effect of the

wedge does not require significant changes in the excitation conditions; simple corrections such as adjusting the laser focus is enough.

2.2.1 1D waveguides

In this section, we describe the sample discussed in the experiments of chapter 3. The sample has been provided by the group of Prof. Pavlos Savvidis from the IESL-FORTH institution at Heraklion (Greece). A scanning electron microscopy (SEM) image of the MC is shown in Fig. 2.7. It consists of a $5\lambda/2$ $Al_{0.3}Ga_{0.7}As$ cavity with four sets of three 10 nm GaAs QWs. These have been inserted at the antinodes of the electromagnetic field, resulting in 9.4 meV of Rabi splitting. The cavity is surrounded by two sets of DBRs: 32 pairs of $\lambda/4$ layers of $Al_{0.15}Ga_{0.85}As$ and AlAs are alternately placed on the top of the structure while 35 pairs are located at the bottom. Low power measurements of the photonic structure reveal a high Q-factor of 16 000.

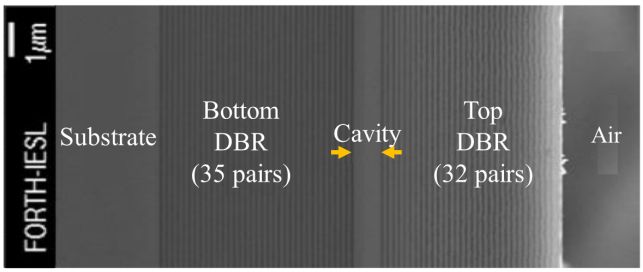

Figure 2.7. SEM image of the MC structure showing the lateral view of a cavity composed by a GaAs substrate, two sets of DBRs and the cavity. The orange arrows indicate the width of the cavity. Courtesy of Prof. P. G. Savvidis' group, IESL-FORTH, Greece.

The sample, grown by MBE, has been patterned through reactive ion etching to obtain planar waveguides with dimensions 20 x 300 μm. The pattern, consisting of ridges and pillars of several sizes, has been repeatedly printed over the sample, as shown in Fig. 2.8(a). However, we focus only on the ridge structures located in a region of the sample with a small detuning of $\delta = 0.6$ meV.

The calculated dispersion relations of the lower polariton modes reveal significant differences between the emission of polaritons in the direction along the ridge (k_x) and perpendicular to it (k_y). The dispersions for both cases, under non-resonant excitation, are depicted at the left and right panels of Fig. 2.8(b), respectively. The left panel, calculated for $k_y = 0$, shows a parabolic multiband dispersion between 1.5398 and 1.5420 eV, in which a large population is observed at the LPB in the full range of k_x. On the contrary, the dispersion

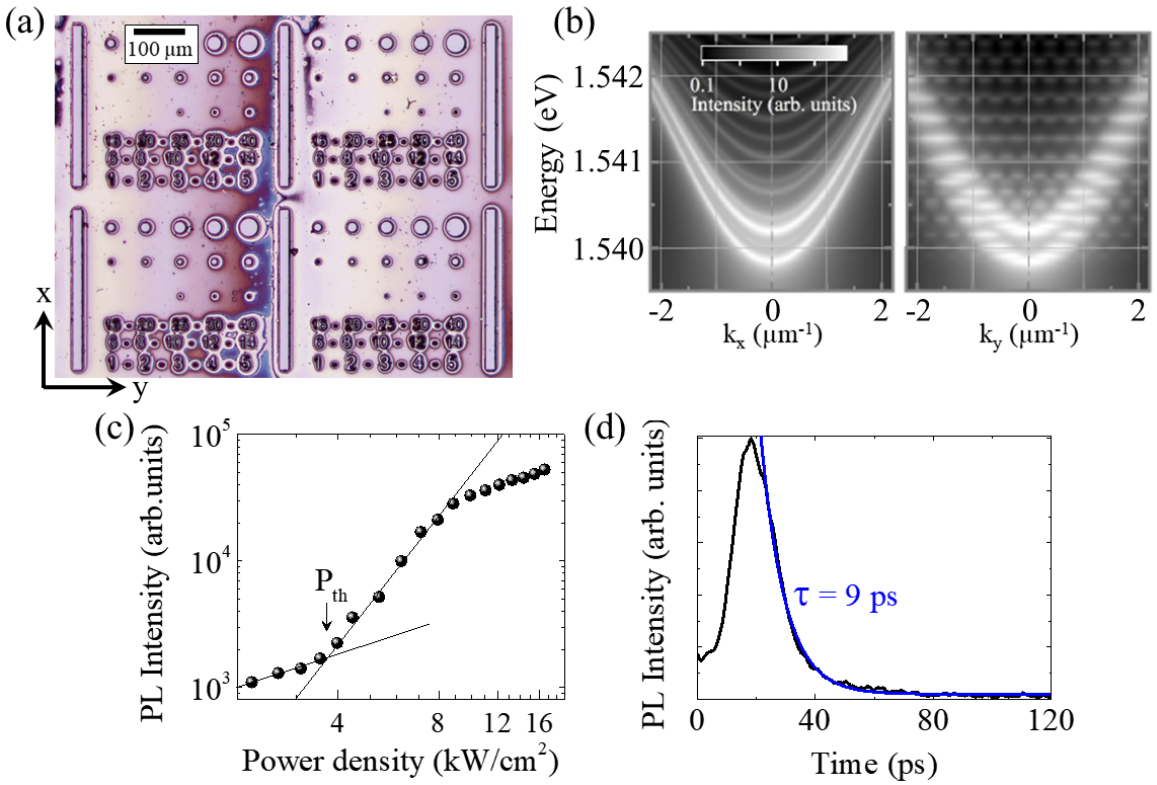

Figure 2.8. Characterization of a sample containing of planar waveguides. (a) Microscopy image of the sample displaying a series of vertical waveguides, 20 x 300 µm, and micropillars of different sizes. Only the former structures are studied. The x axis is defined parallel to the long dimension of the waveguides. (b) Calculated energy dispersion relations of lower polariton modes along k_x (at $k_y = 0$) and k_y (at $k_x = 0$), respectively. Taken from [78]. (c) Excitation power dependence of the PL intensity showing a non-linear increase above a condensation threshold P_{th}= 3.7 kW/cm^2. The solid lines are fits of the data indicating the threshold power at their intersection. The horizontal and vertical axis are in logarithmic scale. (d) Time-resolved emission exhibiting a fast decay of the population. An exponential decay fit of the data provides a polariton lifetime of 9 ps.

along k_y, calculated for $k_x = 0$, is completely discretized; the emission is split into several sub-bands whose antinodes are clearly visible. In these structures, polaritons are confined in the z-direction due to the presence of the DBRs, but an additional restriction appears along y due to the finite size of the ridge, 20 µm. Therefore, we can assume that these ridges confine polaritons in 1D. The lateral confinement in the etched microcavity yields to a discontinuity in the refractive index, created by the difference between the cavity and air. As a result, a quantization of the momentum is induced as $k_y = (j+1)\pi/L_y$, where L_y is the width of the cavity and j is the quantization number (integer and positive) that identifies each sub-band of the dispersion. Above these bands (not shown), a broad band originated from the excitonic recombination is observed between 1.5420 to 1.5480 eV.

The intensity emission in the excitation area of a ridge is depicted as a function of the excitation power density in Fig. 2.8(c), in which initially the polariton population increases linearly with the power density. However, a non-linearity is observed when polaritons condense. The fits of the two regions are depicted by the solids lines, giving a power density threshold for condensation of $P_{th} \sim 3.7$ kW/cm^2 at the intersection between both fits. The time resolved emission of a propagating polariton condensate is analyzed in Fig. 2.8. For this measurement the emission has been integrated in a region of 10 µm along the waveguide. A maximum in the signal is observed at 20 ps however, the intensity strongly decays after this time. Above 100 ps, the signal-to-noise ratio increases significantly. An exponential decay fit of the experimental data provides a polariton lifetime of 9 ps, revealing the rapid dynamics of polaritons in these samples.

2.2.2 1D directional couplers

In chapter 4, a sample consisting of numerous directional couplers with different size parameters is used in the experiments. The sample has been grown by MBE by the group of Prof. Sven Höfling at the University of Würzburg (Germany). A SEM image showing the different parts that compose the MC is displayed in Fig. 2.9. The cavity is embedded in two sets of DBRs consisting of 23 and 27 pairs of alternating layers of $Al_{0.2}Ga_{0.8}As$/AlAs in the upper and lower mirrors, respectively. The inset of the figure shows a cavity composed by three sets of 4 GaAs QWs (7 nm of nominal width) with AlAs barriers (4 nm width). A Q-factor of at least 5 000 has been determined experimentally by low power measurements.

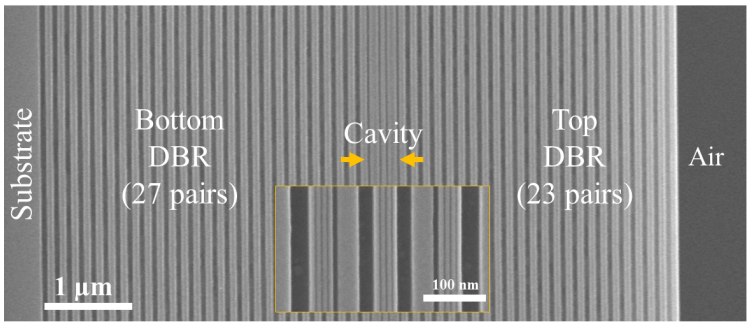

Figure 2.9. SEM image of the MC structure showing the lateral view of a cavity composed by a GaAs substrate, two sets of DBRs and the cavity. The orange arrows indicate the width of the cavity, this region is zoomed in the inset. Courtesy from Prof. S. Höfling's group, University of Würzburg, Germany.

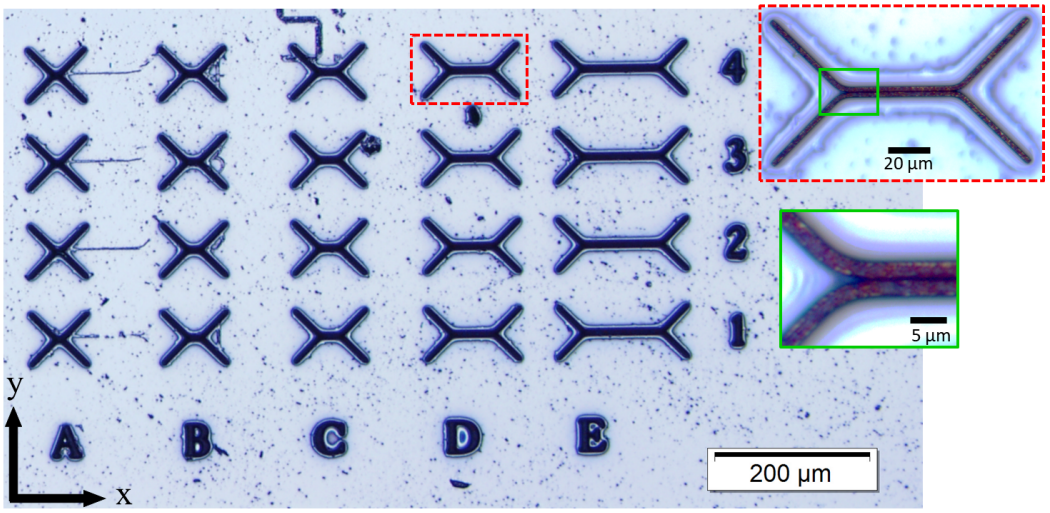

Figure 2.10. Microscopy image of the pattern formed by 20 couplers with different size parameters. The red inset shows an enlarged image of one structure with 50 µm of coupling length and 0.5 µm of separation distance between the waveguides. A small area indicated by the green square is zoomed to show in more detail the gap and the sharpness of the bent between the terminals and the coupling region.

The sample, with dimensions 11 x 4 mm, has been repeatedly patterned throughout the surface. Fig. 2.10 shows the pattern composed by 20 couplers with different dimensions. The couplers are formed by two parallel planar waveguides, similar to those of section 2.2.1, with 2 µm width and, in- and out-put terminals oriented at 45 °. To define the structures the cavity has been etched beyond the QWs. However, in the central region, it has been etched just down to the QWs, removing only the upper DBRs, to provide high confinement and, at the same time, allow photons to couple from one arm of the coupler to the other by evanescence. The strength of the coupling, is controlled by the distance between both waveguides, which ranges from 0.2 µm (row 1) up to 0.5 µm (row 4). The coupling length, i.e. the central region, is varied from < 2 µm (column A) up to 100 µm (column E). Additionally, the same pattern has been made for couplers with 6 µm width in which the gap size has been increased, ranging from 0.6 up to 1.5 µm. Such increase of the gap size results in the inefficiency of coupling polaritons between the two arms. During the design of the pattern, the length of the terminals has been fixed to 42 µm for all couplers as shown in Fig. 2.10.

It is important to mention that the experiments have been carried out in several regions of the sample. During the growth of the cavity a wedge was introduced, and, as a consequence, a spatial dependence on the energy of the cavity mode appears, providing different detunings at different locations. Fig. 2.11 shows the dispersion curves for three of these detunings, (a) -2.9 meV, (b) -7.5 meV and (c) -13.5 meV. Only negative detuning values are found in

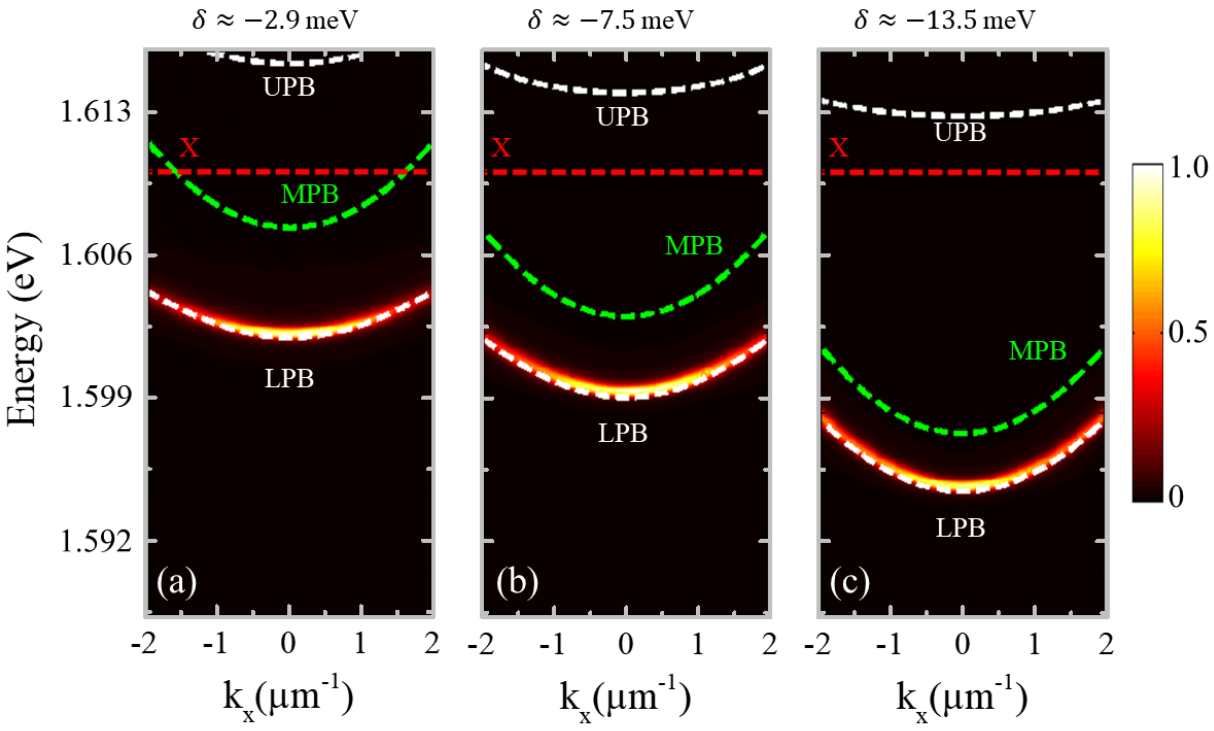

Figure 2.11. Dispersion relation of a GaAs microcavity at different detunings (a) -2.9 meV, (b) -7.5 meV and (c) -13.5 meV. The fits, indicated by the dashed lines, show the upper, middle and lower polariton modes (UPB, MPB and LPB) exhibiting a parabolic dispersion. The fit of the excitonic level (X) is indicated by the horizontal line. The emissions have been measured at 5 K. The experimental data has been provided by the group of Prof. S. Höfling from the Univ. of Würzburg.

this sample revealing the high photonic weight of the LPB. The fit of these dispersion bands (dashed lines) shows two additional polariton modes, MPB and UPB, however, they are not experimentally seen. The fit yields to a Rabi splitting between the UPB and LPB of 13.9 meV. In the most negative detuning case, (c), an emission linewidth of 0.3 meV is obtained, corresponding to an experimental Q factor of $\sim$5000. These results lead to a cavity-mode lifetime of the order of 2 ps, which is in accordance with the experimental value of the polariton lifetime, 4 ps.

In addition, the PL of one coupler at a detuning of $\delta = -19$ meV is studied for two excitation densities in Fig. 2.12. In this case, a structure with 6 μm width and 100 μm of coupling length, is pumped in the central region (x=0). The emission in real-space for a low power density (0.6 kW/cm^2), panel (a), shows the presence of excitons ($\sim$ 1.604 eV) and a small population of polaritons ($\sim$ 1.580 eV) created only at the excitation area. Outside this area, the emission contribution is negligible. The corresponding momentum-space is shown in panel (b) in which

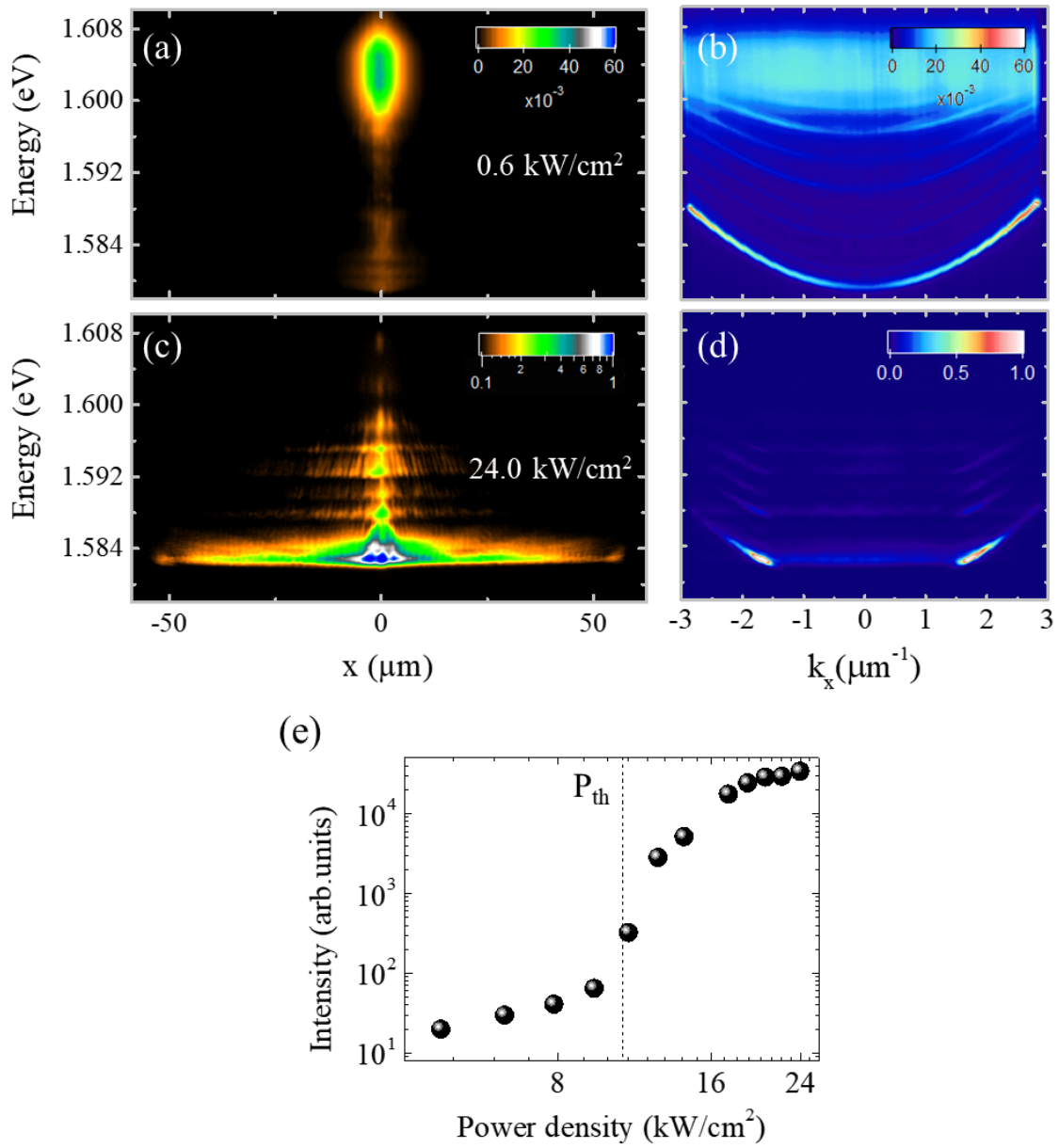

Figure 2.12. Time-integrated PL filtered at the coupling region of a coupler structure. The sample is excited non-resonantly at 1.664 eV. Panels (a) and (c) exhibit the emission along the waveguide (x) for excitation power densities of 0.6 kW/cm^2 (below threshold for propagation) and 24 kW/cm^2 (above threshold), respectively. Panels (b) and (d) compile the corresponding dispersion relations for the same excitation powers. To highlight the propagation in (c) the emission is shown in a logarithmic scale; the rest of the emissions are depicted in linear scales. (e) Power density dependence of the emission intensity showing a non-linear increase above the condensation threshold indicated by the dashed line at $P_{th} = 12$ kW/cm^2. Both axis are in logarithmic scale.

a broad excitonic band is observed between 1.608 and 1.600 eV. Below this energy, several polariton bands arising from the 1D confinement of the waveguide are clearly distinguished. By contrast, when the excitation density is increased up to 24 kW/cm^2, polaritons propagate along the structure, as evidenced from the blue-shifted emission ($\sim$ 1.583 eV) arising in the interval $-50 < x < 50$ µm in panel (c). This change in the polariton dynamics is also shown in the dispersion depicted in panel (d). The emission becomes narrower and contrary to the previous case, it is not formed by a complete band along k_x, but is composed of one mode propagating at two equal k-values with opposite signs. Since the movement is restricted in 1D, polaritons are only allowed to move away from $x = 0$ towards right (left) displaying a positive (negative) wavevector. The power dependent intensity of the emission is shown in panel (e), in which a linear regime is distinguished at values below 12 kW/cm^2 (dashed line). Above this power density threshold, the polariton condensate is formed and propagates along the structure, as evidenced in panel (c).

2.2.3 Polariton router

The sample used in the experiment described in chapter 5 has been grown by MBE by the group of Prof. Sven Höfling at the University of Würzburg (Germany). The microcavity consists of 36 AlAs/AlGaAs mirror pairs at the bottom and 32 pairs at the top. Between the DBRs, three stacks of four 13 nm GaAs compose the QWs in an AlGaAs 3/2 λ-width cavity. According to the low power measurements of the photonic structure, the sample exhibits a Q-factor of 12 000. A Rabi splitting of 9.4 meV has been determined between the upper and lower polariton branches by white light reflection measurements. The polariton router is located in a region of the sample with a detuning of -16 meV.

The device, which is composed by two parallel waveguides coupled to a microdisk, has been sculpted on the top of the sample. This geometry is depicted in Fig. 2.13(a), where a top view of the device, obtained by SEM, is shown. The microdisk device is deeply etched through the QWs layer to provide high photonic confinement. Several of these devices were produced with different waveguide widths ranging from 2 up to 4 µm. In the case of the microdisk, two diameters were also selected, 10 and 40 µm.

As a first step, we have characterized optically one of the waveguides coupled to the microdisk, in which polaritons are either injected or ejected from the router device. The emission intensity of the waveguide at different excitation power densities is depicted in Fig. 2.13(b) (left axis, black dots). A characteristic strong non-linearity is observed when a power density threshold of 12.7 kW/cm^2 is exceeded. Simultaneously, a drop in the emission

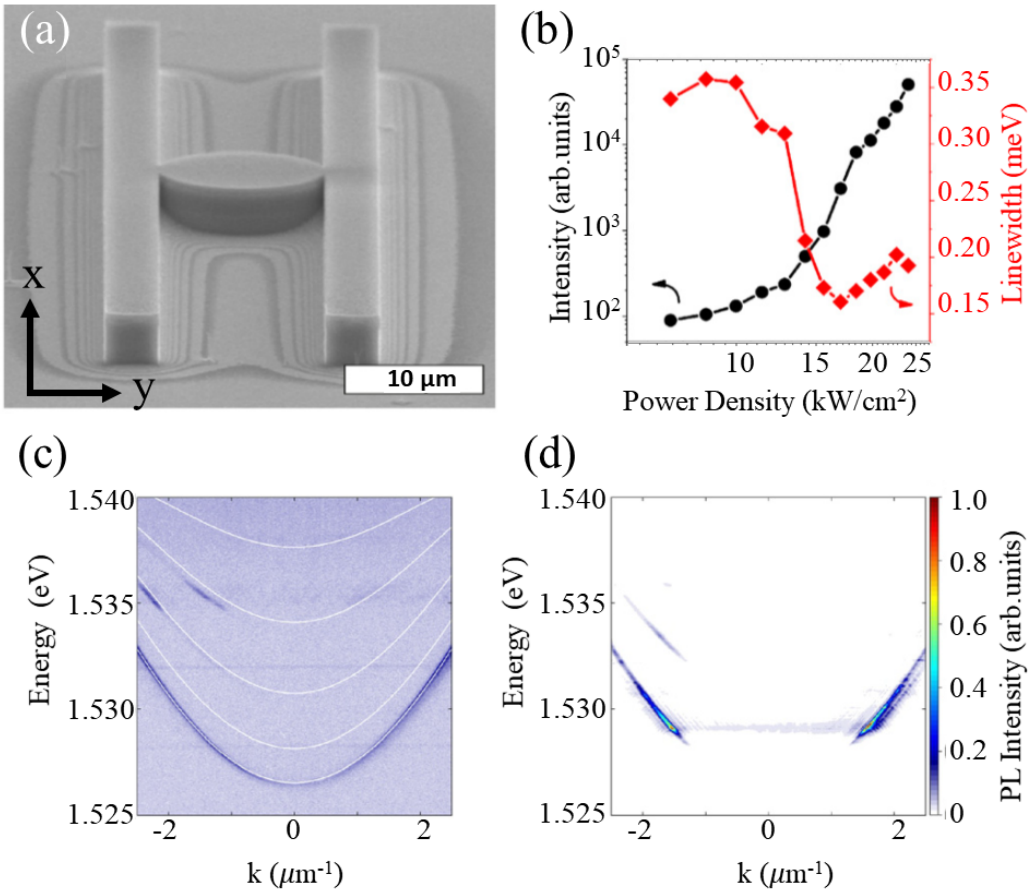

Figure 2.13. (a) SEM image of the microdisk device coupling two waveguides. (b) Input-output analysis of such a device extracted from the parameters of a Lorentzian fit of the emission at $k \approx 1.7\ \mu m^{-1}$. An intensity nonlinearity (left axis, circles) and a coherence buildup, evidenced by a linewidth drop (right axis, diamonds), are observed at the excitation threshold (12.7 kW/cm^2). (c) Dispersion relation in the linear regime with the subbands originating in the one-dimensional photonic confinement of the waveguides at an excitation power density of 7 kW/cm^2. (d) Momentum resolved condensate emission showing propagation along both directions of the waveguide, indicated by the selective population of distinct non-zero wavevectors at an input power density of 21 kW/cm^2.

linewidth (right axis, red diamonds) is also observed, revealing the coherence buildup and therefore, the creation of polariton condensates. At lower power densities, below threshold for condensation, the dispersion relation is composed by several bands arising from the quasi-1D confinement. This is evidenced in Fig. 2.13(c), in which the angle-resolved PL in the direction along the guide is measured for a power density of 7 kW/cm^2. Similar results are found to those of section 2.2.1 when comparing the dispersion of the waveguides: the movement of polaritons is not restricted along the waveguide (x), however, particles are confined in the transverse direction. The white lines show a fit of the bands for a square well photonic potential, yielding a waveguide width of 4.5 µm, that is in good agreement with the width directly measured in Fig. 2.13(a). Additionally, the dispersion has been measured above the threshold, 21 kW/cm^2 [see Fig. 2.13(d)]: the emission reveals the presence of moving polariton condensates exhibiting wave vectors at $k \approx \pm 1.7$ µm^{-1}.

2.2.4 Photonic honeycomb lattices

The sample, used in the experiments of chapter 6, has been provided by the group of Dr. Alberto Amo from the Laboratory of Physics of Lasers, Atoms and Molecules (PhLAM, France). It consists of a $Ga_{0.80}Al_{0.20}As$ semiconductor microcavity embedded in two sets of DBRs. The top (bottom) Bragg mirrors are composed by 28 (40) pairs of $\lambda/4$ alternating layers of $Ga_{0.05}Al_{0.95}As/Ga_{0.80}Al_{0.20}As$. Between both DBRs, 12 QWs 7 nm wide, have been grown at the three central maxima of the electromagnetic field confined in the cavity, yielding a Rabi splitting of 15 meV. All the experiments shown in chapter 6 have been performed at a temperature of 10 K and a detuning of $\delta \approx -7$ meV.

The planar microcavity grown by MBE, has been subjected to e-beam litography and inductively-coupled plasma etching down to the GaAs substrate; with this technique, honeycomb lattices made of overlapping micropillars have been created. The contrast between the refractive index of the semiconductor and the air is responsible of the additional lateral confinement in the microcavity. Thus, these micropillars generate quasi-3D confinement of polaritons, acting as artificial photonic atoms. In this experimental study, the micropillars forming the lattice have a diameter of 2.75 µm as evidenced in the SEM image of a single structure in Fig. 2.14(a). Its PL, depicted in Fig. 2.14(b), is composed by a series of discrete energy modes labeled as s, p and d bands. The fundamental s state shows a cylindrical distribution with a maximum intensity at $x = 0$. By contrast, the first excited state p, shows two spatial distributions originated from p_x and p_y orbitals. In both cases, the emission is located close to the edges, therefore, no emission is observed at $x \sim 0$ [see Fig. 2.14(b)]. A similar distribution is found for the d band.

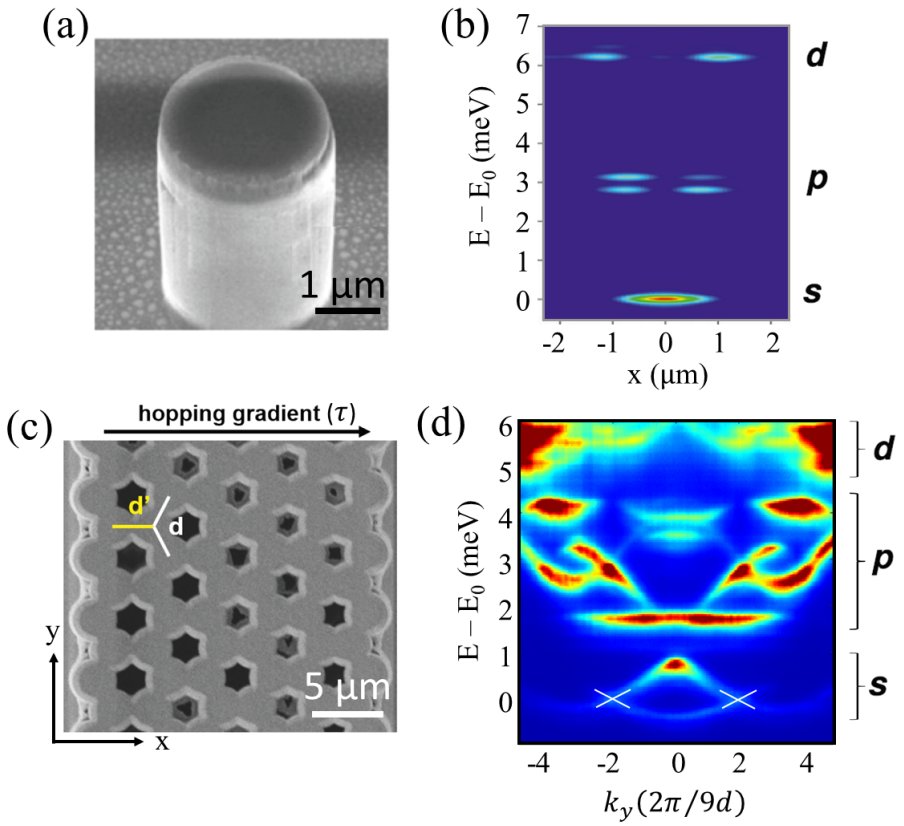

Figure 2.14. (a) Scanning electron microscopy image of a single micropillar. (b) PL of a micropillar evidencing s, p and d discrete modes. (c) Strained honeycomb lattice with a positive gradient (τ) along the x direction. The center-to-center pillar distance is marked as d' along x direction and d for the rest of them. (d) Dispersion relation of a honeycomb lattice with $\tau = 0$ at $k_x = 4\pi/3\sqrt{3}d$. The white lines mark the crossing of the two s bands, where a linear dispersion is expected and observed.

By coupling several micropillars, different systems such as honeycomb lattices can be obtained. In these type of configurations, the energy modes of the cavities overlap allowing photons to tunnel from one pillar to the next one. The strength of this coupling can be tuned by changing the interpillar distance. A honeycomb lattice made of these photonic resonators is shown in Fig. 2.14(c). The lithographic mask is designed to ensure an overlap of adjacent micropillars varying continuously the center-to-center distance (d') between 2.7 (left side) and 1.9 µm (right side). This effect is created only along the x direction, keeping constant d = 2.40 µm for the perpendicular direction, simulating a uniaxially strained lattice. The dispersion relation of a honeycomb lattice is depicted in Fig. 2.14(d) along the k_y direction for $k_x = 4\pi/3\sqrt{3}d$ (at $k_x = 0$ interference does not allow to observe the complete s band). Several groups of bands labelled as in Fig. 2.14(b), s, p and d, are separated by energy gaps. The coupling between the fundamental modes of the micropillars give rise to two s

bands similar to the π and π^* bands of graphene [79]. At the crossing between these bands, $k_y(2\pi/9d) = \pm 2$, linear dispersions similar to Dirac cones are observed.

Chapter 3

Temperature dependence of the coherence in polariton condensates

3.1 Introduction

A well known signature of Bose-Einstein condensation is the macroscopic occupation of the fundamental energy state in bosonic systems. When this macroscopic state is formed, below a critical temperature, it exhibits distinctive properties such as spatial and temporal coherence. This property has been extensively investigated in different systems, such as atomic BECs [80–82] or polariton condensates [17, 37–53, 83]. One of the most useful tools to analyze the coherence is through the study of the interference patterns, since it allows to observe fringes for either static [50, 54, 55] or propagating condensates [48, 56]. This phenomenon has been generally studied when two condensates meet in real-space. Nonetheless, recent experimental studies have focused on the interference in momentum-space arising from two condensates that propagate with the same velocity, circumventing the need of an encounter in real-space [57–59]. Particularly, Antón *et al.* reported for the first time the observation of interference fringes produced between two condensates that were spatially separated, revealing the existence of coherence in spite of never being in contact with one another [57].

The transition to a BEC state is strongly temperature dependent, as explained in section 1.5.1. The temperature dependence of the spatial coherence in trapped atomic condensates has been studied thoroughly, see for example the works of Bloch *et al.* [84] and Gati *et al.* [85, 86]. However, these studies are much more scarce in the field of polariton condensates, to the best of our knowledge only the work of Oullet-Plamondon *et al.* has investigated

the critical temperature (T_C) for condensation [87]. They reported on the dependence of polariton bistability with temperature, proposing that an increase in the latter leads to a significant incoherent excitonic population growth in the reservoir that interacts with the polariton population.

Therefore, to fill this gap, in this chapter, a time-resolved experimental study of the impact of the lattice temperature on the coherence of traveling polariton condensates is presented. As a result of the interference between spatially separated condensates, fringes are obtained in momentum-space for condensates traveling with the same velocity. Our experiments also reveal an additional set of fringes in real-space emerging from the crossing of two condensates moving in opposite directions in the structure. A gradual decay of the visibility with increasing temperature is observed in both spaces. A T_C for the BEC-like phase transition is inferred when the visibility of these fringes vanishes. Furthermore, since unfortunately, theoretical models to characterize the coherence fading with temperature do not exist for polariton condensates, our results are compared with available theoretical models for atomic condensates.

In section 3.2, the details of the experiment and the consecutive detection of the emission in real- and momentum-space are described. A detailed Fourier analysis of the interference fringes is performed in section 3.3. The critical temperature for the phase transition is obtained using two different methods presented in section 3.4: in the first one we study the visibility of the fringes as a function of the temperature and in the second one, we evaluate the fraction of condensed to uncondensed polariton populations. The latter method allows us to compare our findings with theories developed for atomic condensates. Finally, the conclusions are summarized in section 3.5.

3.2 Observing interference fringes in real- and momentum-space

To study the coherence of polariton condensates, we employ one of the simplest optical architectures: planar waveguides. The dimensions of a waveguide are 20 x 300 µm, which allows to obtain a quasi 1D-confinement of the condensates that propagate along its long dimension (x). Further details of this sample can be found in section 2.2.1. We pump the waveguide under quasi-resonant conditions with two pulsed laser beams at 1.5459 eV. They are focused on the sample surface with the same power density above the threshold for condensation using a microscope objective with NA$=0.4$ and $f = 10$ mm. The time delay

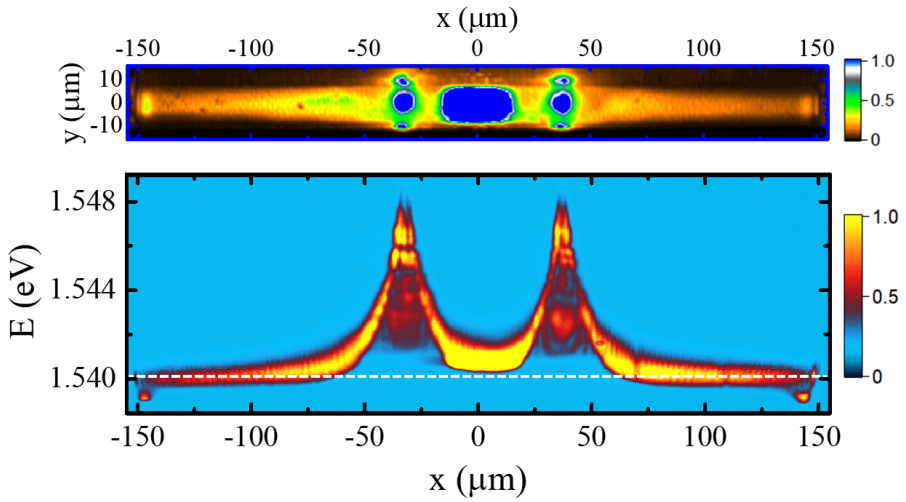

Figure 3.1. *Top*: Real-space map of a waveguide pumped by two laser beams separated by 70 μm. The excitation spots can be identified as the two blue circles. The emission is energy-integrated. *Bottom*: Energy relaxation process of polaritons along the structure. The emission is time-integrated. The laser is set at 1.5459 eV, well above the range of energies considered in the plot. Polaritons travel throughout the ridge when they achieve the minimum energy state, 1.5404 eV, marked with a white dashed line. Below this energy, two localized states are observed at both edges of the ridge. The emissions have been measured at 14 K with a power density of 10 kW/cm^2.

and the distance between the beams are controlled in order to excite simultaneously the structure with a fixed separation of d = 70 $\pm$ 1 μm. To achieve this separation, the beams are deviated from the optical axis of the objective, impinging the latter at different points but reaching the sample surface with the same angle of incidence. We adjust the angle of incidence so that polaritons are initially created, at $t = 0$, with zero momentum $k_{||} \sim 0$. These conditions are considered in the upper panel of Fig. 3.1 where a top view of the system shows the real-space map of the waveguide emission at a power density of 10 kW/cm^2. The position of both laser beams can be deduced from the two blue circles separated by 70 μm. The waveguide is entirely illuminated due to the emission of traveling polaritons. An additional maximum of intensity observed at $x \sim 0$ arises from different condensates confined between the excitation beams, producing the enhancement in the signal, as explained in detail below. It should also be noted that two localized states are observed at each edge of the waveguide ($\sim \pm 150$ μm). Due to the sample geometry, a potential trap is induced close to the edges, trapping a small polariton population in a reduced area of the waveguide. As a result, two localized states are found with a slightly higher emission intensity than the condensates traveling in the same region. The appearance of these localized states in a planar waveguide have been also observed in previous works of our group [88, 89].

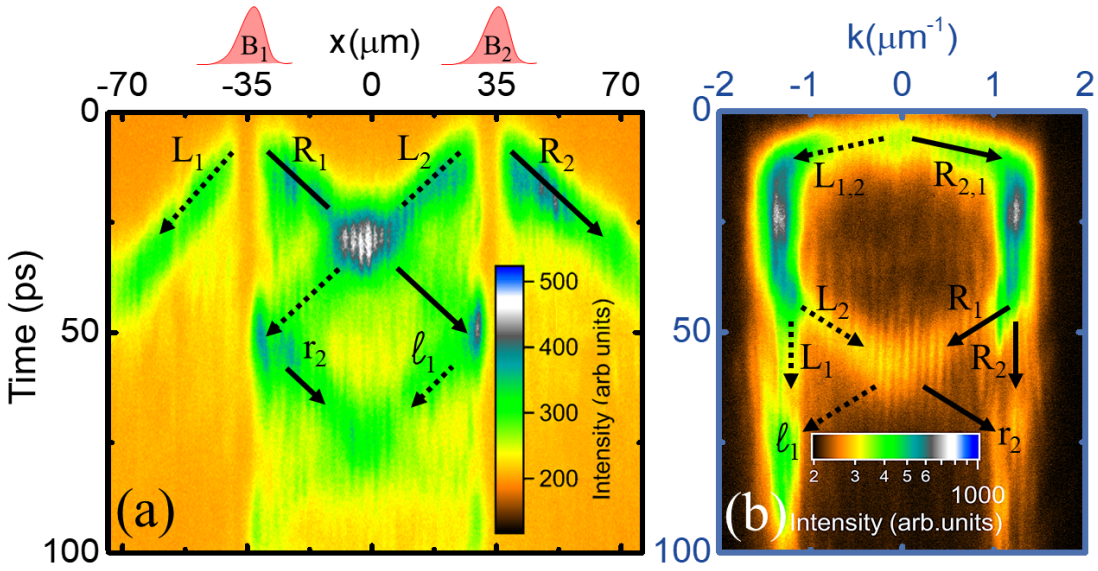

Figure 3.2. (a) Time-resolved PL emission along the ridge in real-space (x) as a function of time for T = 14 K. $B_{1,2}$, separated by 70 μm, mark the positions where the two laser beams impinge on the sample. $L_i(R_i)$ denote the WPs moving to the left (right), with the subscript, i, referring to the excitation beam. The intensity is in a linear false-color scale. (b) The corresponding emission in momentum-space (k) as a function of time. The intensity is in a logarithmic false-color scale. Both PL emissions have been measured with a power density of 6 kW/cm^2.

The energy relaxation process of polaritons along the structure is shown in the lower panel of Fig. 3.1 where it can be observed how the polariton populations, created by each laser beam, gradually decrease their energy as they move out of the excitation spots. When the power density of the laser beams is above the threshold for condensation, as in this case, condensates start traveling along the waveguide. The condensates propagate along the entire structure at 1.5404 eV, marked with the white dashed line. Beneath this energy, two localized states are found at each edge of the structure with an energy $\sim$ 1 meV lower than that of propagating condensates. They correspond to the trapped states observed at the same positions in Fig. 3.1 *Top*. Further details about the relaxation process of polaritons can be found in Appendix A.

Understanding the dynamics of the system is crucial to analyze in detail their emission. For this reason, we show the real (x) and momentum (k) distributions of the polariton condensates versus time in Fig. 3.2 for a fixed temperature of 14 K. We collect the time-resolved photoluminescence filtered at the energy of the propagating condensates, 1.5404 eV. In the real-space image, each excitation beam $B_{1,2}$, located at -35 μm and 35 μm respectively in Fig. 3.2(a), gives rise to two polariton wave packets (WPs) propagating in opposite directions. They are labeled as $L_i(R_i)$ referring to the direction in which they move, left(right),

and the excitation spot where they originate ($i = 1,2$). Their trajectory is indicated with dashed(solid) lines as a guide to the eye. A constant speed of 1.5 μm/ps is achieved by the four WPs and their emission can be followed up to $\sim$ 100 ps. Due to the optical configuration of the experiment and the size of the detection area, the PL of the WPs L_1 and R_2 can be monitored only during the first 45 ps. The numerical aperture of the microscope objective considerably limits the spatial region that can be monitored, resulting in a limitation of 150 μm out of the 300 μm long waveguide. The inner WPs, R_1 and L_2, move toward each other and interfere when meeting in the center of the structure, $x \sim 0$ at 35 ps. Far from being deviated, they continue traveling until they reach the vicinity of the excitation spots, B_2 and B_1 at 55 ps, where the WPs cannot overcome the potential barriers created by the excitonic reservoirs [90, 91]. Since they cannot go over the maxima of these barriers, the separation between R_1 and L_2 is slightly smaller than the distance between the laser beams by which they are initially created, 70 μm. Thus, they suffer a *soft* reflection: they decrease their speed until halting in the vicinity of the reservoirs and, eventually, they reverse their trajectory. As a consequence, R_1 (L_2) becomes ℓ_1 (r_2).

As seen in Fig. 3.2(a), apart from the actual interference between the inner WPs at 35 ps, the entire PL emission of the WPs shows weak fringes. The disorder present in the ridge originates back-scattered polaritons that interfere with those still traveling throughout the sample [92]. Nevertheless, we can distinguish between these two kinds of fringes, since those arising from disorder have a slightly larger periodicity as compared with those that occur when two condensates meet in real-space, i. e., back-scattered polaritons show a reduction of the wavevector k_x. The origin of these fringes is discussed in detail in Appendix D of Ref [78].

The corresponding time evolution of the WPs in momentum-space is displayed in Fig. 3.2(b). Condensates are initially created at $t = 0$ with $k \sim 0$ and, in few picoseconds, they evolve towards two states corresponding to WPs traveling towards the left or right directions of the ridge. Note that although two states are found in k-space, the emission corresponds to four WPs: $L_{1,2}$ propagate away from the excitation spots with momenta $k = -1.3$ μm^{-1} whereas $R_{1,2}$ propagate with $k = +1.3$ μm^{-1}. From the first moments, the emission shows weak interference fringes even when they have not yet reached this maximum momenta. The fringes emerge because, since their creation, condensates moving in the same direction evolve with the same acceleration. Once the WPs have acquired $k = \pm 1.3$ μm^{-1}, each trace shows a set of fringes caused by condensates propagating with exactly the same velocity and direction, i. e., occupying the same state in momentum-space. It is worthy to emphasize that in this particular case, coherence arises between polaritons that are spatially separated

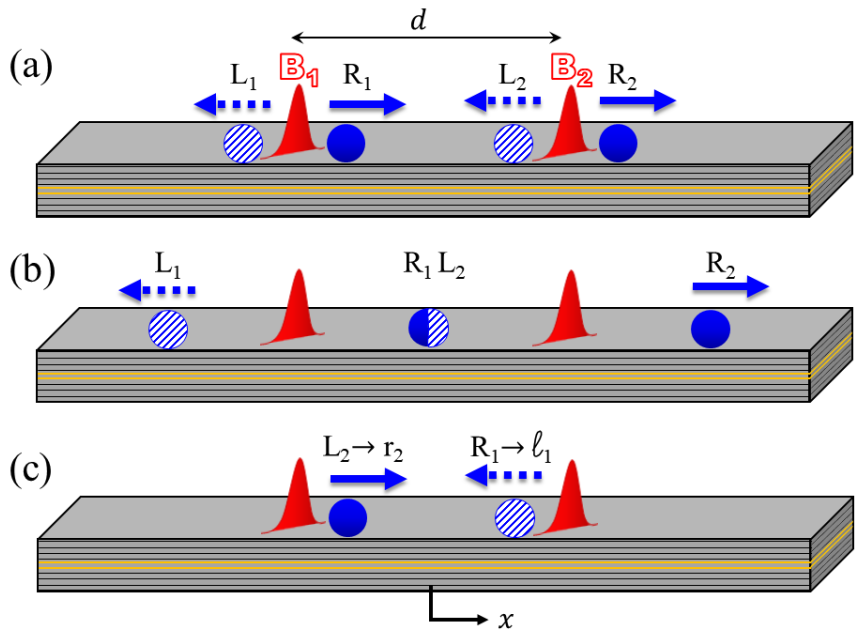

Figure 3.3. Schema of four polariton WPs propagating in a planar waveguide at three different times: (a) $t = 5$, (b) $t = 35$ and (c) $t = 55$ ps. The positions of the two laser beams impinging on the sample are indicated by $B_{1,2}$, separated by a distance d. The WPs moving to the left (white-blue circles) are labeled as L_i & ℓ_i, while those moving to the right (blue circles) are labeled as R_i & r_i. The subscript i refers to the excitation beam.

in the sample and have never been in contact before $t = 35$ ps [57]. During the first 40 ps, the WPs maintain a constant wave vector value showing that the crossing at the center of the structure in real-space does not affect them by any means, neither a deviation from the trajectory nor a decrease of their speed is observed. As already seen in Fig. 3.2(a), at ∼55 ps the inner WPs, L_2 and R_1 are located nearby the reservoirs. This is reflected in k-space as a reduction in the wave vector of both WPs. Due to the presence of the potential barriers they decelerate, losing gradually their momenta, until they coincide at $k \sim 0$, where another set of interference fringes, with different period, is obtained. Afterwards, both WPs reverse their trajectories and accelerate until they recover the same maximum wave vector as R_2 and L_1. Therefore, we re-label now L_2 and R_1 as r_2 and ℓ_1, respectively. In the meantime, the outer WPs, L_1 and R_2, propagate straight towards the edge of the waveguide with a constant speed.

At longer times, the intensity of the emission decays considerably with time due to the finite lifetime of polaritons and hence, after 75 ps, the PL can not be accurately analyzed. Despite this, an evidence of interference fringes is still observed for condensates moving towards left, now L_1 & ℓ_1, and right, now R_2 & r_2.

To clearly illustrate the polariton propagation explained in Fig. 3.2, a schema of the four polariton WPs propagating along the planar waveguide is shown in Fig. 3.3 for three time delays after their creation. Fig. 3.3(a) shows the initial conditions of the experiment ($t = 5$ ps) in which the same situation is found at the position of each laser beam, $B_{1,2}$; two WPs are created and accelerated in opposite directions along the x-axis, i. e., left (L_i) and right (R_i). As the WPs evolve with the same acceleration, interference fringes are expected to be found in the k-space emission between R_1 & R_2 and L_1 & L_2. At $t = 35$ ps [see Fig. 3.3(b)], the crossing between R_1 and L_2 occurs in the region $[-d/2, d/2]$. The overlap of their emissions produces interferences in real-space. Moreover, since the velocities of the four WPs remain constant, the interferences in k-space are still present. Finally, at $t = 55$ ps, R_1 and L_2 encounter the excitonic reservoirs at B_2 and B_1, respectively. The WPs momentarily halt in the presence of the reservoirs, which act as potential barriers, and reverse their direction of propagation. Since these WPs do not coincide in real-space, no fringes in the real-space emission are expected, by contrast, in k-space, R_1 and L_2 exhibit velocities close to zero, thus, fringes are expected to appear at $k \sim 0$ but with a sightly larger period, as mentioned before, because the distance in real-space between the condensates decreases. This process of bouncing back and forth in the range $[-d/2, d/2]$ is repeated until polaritons reach the end of their lifetime. L_1 and R_2 have exited from our detection area due to the long traveled distance, therefore, their emission can no longer be followed.

Stability of the fringes

The symmetry of the excitation conditions between condensates generated at both excitation spots are a key ingredient to observe the interference fringes. To reach the necessary conditions for interference, the power density of B_1 and B_2 must be adjusted so that the blue-shift of the emission (in our case, 0.6 meV) is the same in both polariton populations created from each excitation spot. As a result, the condensates move with equal momentum (k) in the same direction, i.e., equal kinetics. Since the period of the fringes in k-space ($\kappa_0 \equiv \Delta k$) is directly related to the separation between the condensates (d) by $\kappa_0 = 2\pi/d$ (section 1.6), special care must be taken with the spatial stability of B_1 and B_2. A fluctuation in the position of one of the laser beams will generate an interference pattern with a changing value of κ_0, blurring the fringes during the measurements. An example of the dependence between d and κ_0 is shown in Fig. 3.4(a). We have measured the emission profile in k-space at $t \sim 5$ ps for three selected distances between the laser beams, $d = 60, 80$ and 100 µm. The interference fringes are observed during the full range of the wave vector since the WPs move from the rest ($k = 0$) to $|k| \sim 1.2$ µm^{-1} with the same acceleration. As one should expect from the inversely proportional relation of κ_0 with d, the periodicity of the fringes decreases

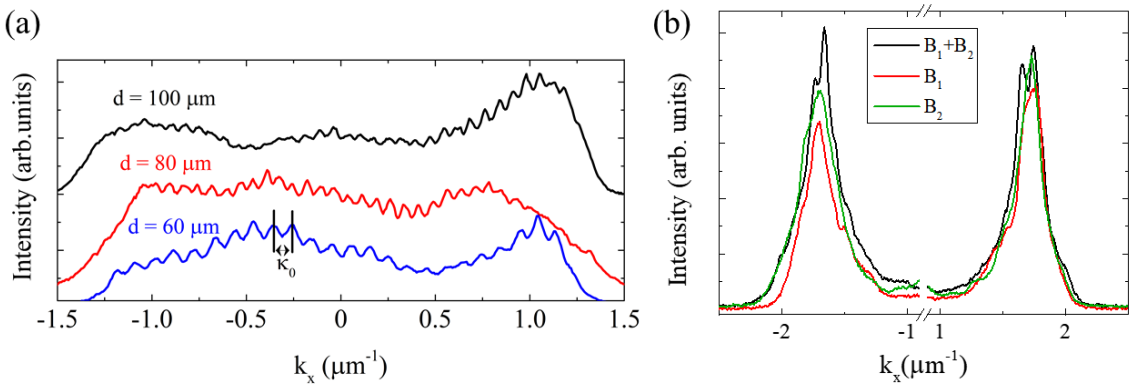

Figure 3.4. (a) PL intensity along k for a time delay of $t \sim 5$ ps. The PL is depicted for a three different distances between B_1 and B_2, $d = 60, 80$ and 100 μm. κ_0 denotes the periodicity of the interference pattern. (b) PL intensity along k for a time delay of $t \sim 35$ ps. The PL is measured when the structure is pumped at B_1, at B_2 or at both locations, $B_1 + B_2$.

as the distance is increased. The analysis of the data yields a value of $\kappa_0 \approx 0.105$ μm^{-1} for the shortest distance, corresponding to $d \approx 59$ μm, which agrees with the experimental observation of $d = 60$ μm. Similarly, for the case of $d = 80$ μm we obtain $\kappa_0 \approx 0.080$ μm^{-1} (that would give a distance in real-space of ≈ 79 μm) and finally for the larger distance $d = 100$ μm, the smallest value of $\kappa_0 \approx 0.065$ μm^{-1} is found (distance in real-space ≈ 97 μm).

We now turn our attention to the cases when we block one of the lasers. Since the interference in k-space occurs between two spatially separated WPs, created with different excitation beams, by eliminating one of the WPs the fringes should disappear. This is the case depicted in Fig. 3.4(b), in which the emission profile has been measured at $t \sim 35$ ps when exciting the structure with a) both laser beams ($B_1 + B_2$), b) just with B_1, blocking B_2, and c) vice versa. When only one laser beam pumps the structure, one WP travels to the left ($k < 0$) and the other one to the right ($k > 0$). Note that regardless of the laser beam used, B_1 or B_2, the value of the maximum momentum of the WPs results the same, ensuring the conditions for the interference. Only when both beams pump the sample, the fringes appear on the emission.

3.3 Analysis of the interference patterns

In this section we will concentrate on the analysis of the interference patterns at three different time intervals of interest: t_1, t_2 and t_3. The intervals t_1 and t_3 are selected from the analysis of the interference in momentum-space while t_2 is selected from the real-space analysis of

the fringes. The size of the time window is adjusted to guarantee that the amplitude of the fringes is constant. In momentun-space, we define t_1 from 13 ps to 39 ps, when $L_{1,2}$ ($R_{1,2}$) move with a negative (positive) constant maximum momentum, and t_3 from 42 ps to 57 ps, when L_1 and R_2 reach the vicinity of the excitonic reservoir, so they decelerate, coinciding at $k \sim 0$.

In real-space, we analyze the fringes appearing from 22 ps to 37 ps that correspond to the interval t_2; in this case, the fringes originate from the coexistence of R_1 and L_2 at the center of the ridge ($x \sim 0$). The WPs not only exhibit temporal and spatial coherence since their creation, as shown in the next section, but they evolve with the same kinetics, therefore, the required conditions to interfere and observe a pattern are met during all their lifetime.

We perform a detailed Fourier analysis of the interference patterns obtained from the emissions at the three time intervals. As an example, Fig. 3.5(a) depicts the PL emission profile integrated in the time range t_1 at the lowest temperature we have measured, 10 K. The emission we collect originates from two different contributions in the WPs: the condensed and the thermal, non-condensed polaritons. The former one shows a series of fringes due to the coherence between different WPs. The non-condensed contribution is apparent in the data as a background on top of which the fringes are observed, i.e., at the same k range. The baseline encompassing this contribution is shown by a red dashed line in Fig. 3.5(a). Since the non-condensed contribution cannot be approximated to a typical Gaussian or Lorentzian peak, due to the asymmetry of the emission, the baseline has been adjusted by hand. To obtain a clearer pattern, we remove the non-condensed part of the emission by subtracting this baseline from the data. The resulting profile is shown in Fig. 3.5(b), where two sets of fringes around $k = \pm\ 1.6\ \mu m^{-1}$ are noticeable. Although in Fig. 3.5(a) only 2 fringes are visible to the naked eye in the region $1.2 < |k| < 2.1\ \mu m^{-1}$, the simple process of subtracting the baseline reveals the presence of additional fringes in the same range of k. The Fourier analysis of the oscillations enclosed in this region is depicted in Fig. 3.5(c), which obtains the amplitudes of the different periods present in the interference pattern, $\kappa \equiv \Delta k$. The predominant peak reveals the period of the pattern in momentum-space, $\kappa_0 = 0.089$ μm^{-1}, which is related to the separation (d) between both excitation beams, B_1 and B_2, by $\kappa_0 = 2\pi/d$. Additionally, the Fourier analysis provides the average amplitude of the oscillations in the interferograms for each period. This amplitude can be directly related to the visibility of the fringes, which defines the degree of coherence, in this case, between two polariton condensates. To relate both the visibility and the amplitude, first the visibility of the oscillations shown in Fig. 3.5(b) is determined for a given temperature. We compute it,

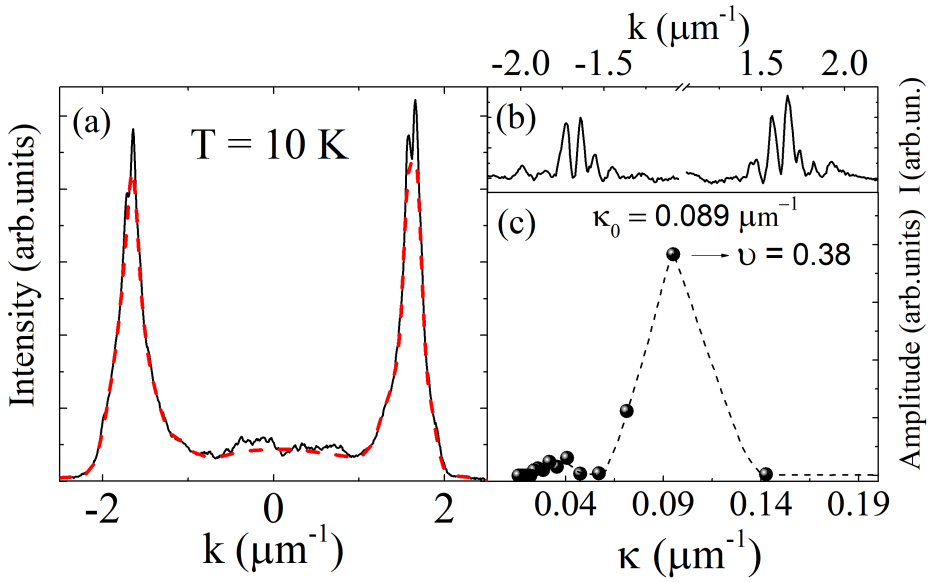

Figure 3.5. (a) Time-integrated PL emission in momentum-space for interval $t_1 \in [13,39]$ ps at 10 K. The baseline of the emission is indicated by a red dashed line. (b) PL profile showing a clean interference pattern after a baseline subtraction of the trace shown in (a). (c) Fourier analysis of the oscillations depicted in (b). The amplitude of the different contributions to the interferogram as a function of their period gives the main period of the fringes (κ_0) and the corresponding visibility (υ), as explained in the text. The dashed line shows a Bézier interpolation of the points. A 10 kW/cm^2 excitation laser was used for the measurements.

either in real- or momentum-space, as

$$\upsilon = \frac{1}{n}\sum_{i=1}^{n}\frac{I_{max}-I_{min}}{I_{max}-I_{min}} \tag{3.1}$$

where $I_{max}(I_{min})$ is the maximum (minimum) intensity of the interference oscillation i of the n oscillations observed in the full range of momenta. This value is used to scale the amplitude given by the Fourier analysis as depicted in Fig 3.5(c). We perform a similar Fourier analysis of the interferograms obtained for different temperatures and for different time intervals; note that since the shape of the emission depends on both, a slightly different baseline will be defined for each emission.

3.4 Determination of condensates' critical temperature

Polariton condensates are out of equilibrium systems. Furthermore, the population distribution consists, at very low temperatures, of a condensed, and therefore coherent population, and a non-condensed part. Comparing these systems with an ideal Bose-Einstein distribution

is not appropriate since it is not possible to define certain parameters such as the number of polaritons in the condensate or its temperature. Therefore, it is not evident how to determine a critical temperature for the phase transition of a polariton population to form a condensate, precisely because a temperature cannot be defined. Nonetheless, we can have some insight on the thermal robustness of the polariton condensate coherence, and therefore of a temperature at which the condensates emerge or dissapear, by studying the evolution of the interference fringes' visibility with the **lattice** temperature. In this section we study the temperature dependence of the mutual coherence between traveling polariton condensates through the visibility of interference fringes at different lattice temperatures.

We obtain the interference patterns in real- and k-space at temperatures ranging from 10 K up to 35 K, in steps of 2.5 K. As an example, Fig. 3.6 compiles the interferograms, after the baseline subtraction, for the interval t_1 for a power density of 10 kW/cm^2. At very low temperature, the fringes are clearly distinguished for positive and negative values of the wave vector. As the temperature is increased, the amplitude of the fringes shows a strong decay, resulting in a progressive worsening of the signal-to-noise ratio. The polaritons' life span drastically reduces with increasing temperature, hindering the polariton propagation as demonstrated by the strong drop in the PL intensity at large $|k|$ values. Consequently, the interference fringes vanish for temperatures above ~ 32.5 K. The condensates acquire a maximum momentum of $k = 1.70(2)$ µm^{-1}, which is slightly higher than that observed in Fig. 3.2. The excitation power is directly related to the blueshift of the emission and therefore, to the polariton's momentum. Thus, an increase of the power density will result in a populated state with higher energy in the LPB, resulting in this increase of k.

The analysis of the interferences in Fig. 3.6 yields to a temperature-independent period of the fringes $\kappa_0 = 0.089(6)$ µm^{-1}, which gives a distance in real-space of $71(5)$ µm. This behavior is expected since, for all temperatures, the separation between the two excitation laser beams is kept constant at $d = 70(1)$ µm.

The temperature dependence of the visibility of the fringes for the three time intervals is displayed in Fig. 3.7. An overview of the experimental data shows a clear decay of the visibility with increasing temperature, i.e., a progressive loss of coherence with increasing temperature. We identify this process as a signature of the BEC-like transition, thus, the critical temperature for BEC can be determined when the visibility drops to zero. In the case of t_1, Fig. 3.7(a), a critical temperature of $32(2)$ K is obtained.

The visibility in the interval t_3, defined when R_1 and L_2 meet at $k \sim 0$, shows a similar tendency with temperature to that obtained in the interval t_1. However, as seen in Fig. 3.7(c),

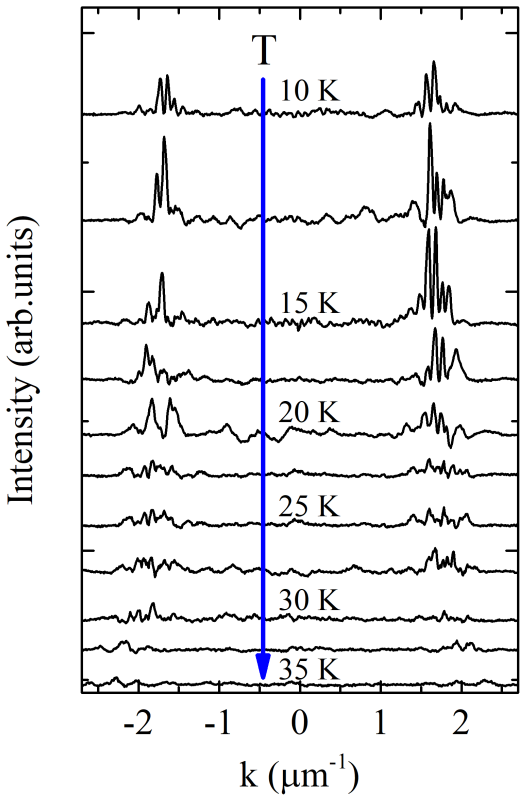

Figure 3.6. PL profiles at the interval t_1 in momentum-space. The temperature is varied from 10 K (top) up to 35 K (bottom) in steps of 2.5 K. The blue arrow indicates the direction of increasing temperature.

a shorter range of temperature has to be considered in this case. The visibility decays considerably faster than at the other time intervals, providing a critical temperature of 21(4) K for this set of fringes. Furthermore, for a given temperature, the value of the visibility at t_3 is significantly smaller than that obtained at t_1, revealing that the coherence gradually decreases with time as the polaritons travel along the sample. For instance, at 15 K, the value of the visibility corresponds to 0.39 at t_1, whereas at t_3 is 0.06. The origin of this effect relies in the proximity of the WPs to the excitonic reservoirs; the enhancement of the exciton-polariton scattering accelerates the decoherence process [33, 93, 94].

The Fourier analysis obtains a slightly larger period for these interference fringes, $\kappa_0 = 0.106(2)$ μm^{-1}, corresponding in real-space to 59(1) μm, a shorter distance than the experimental separation between B_1 and B_2. When the WPs R_1 and L_2 are not able to overcome the potential barriers created by the reservoirs, they halt before reaching the positions ±35 μm. In Fig. 3.2(a) this distance can be directly measured at $t \sim 50$ ps, giving a result of 60(1) μm between the WPs, in good agreement with the distance obtained from the Fourier analysis.

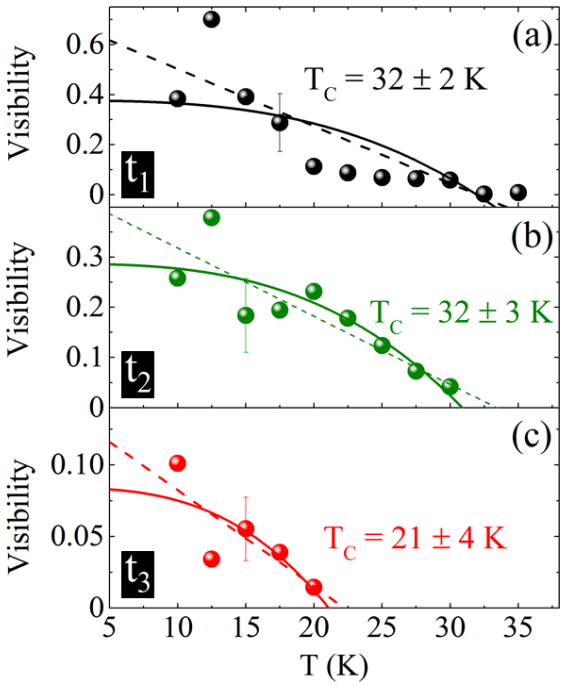

Figure 3.7. Visibility of the interference fringes as a function of temperature for time intervals (a) t_1 and (c) t_3 in k-space. The interval t_2 for real-space is plotted in (b). Two fits of the experimental data are made using Eq. 3.3: the dashed line corresponds to $\beta = 1$ and the solid line to $\beta = 3$.

When analyzing the interference fringes in real-space, we observe a decay of the visibility, shown in Fig. 3.7(b), comparable to those of the k-space. In this case only temperatures below 30 K are shown since the lifetime of the condensates limits the temperature range that can be considered in this sample. Since the time interval t_1 encompasses t_2, the general behavior of the coherence with increasing temperature is similar to that observed in momentum-space, as expected from the connection between real- and k-space. The visibility of the interference fringes, resulting from the crossing of R_1 and L_2 at $x \sim 0$, yields $T_C = 32(3)K$ for the BEC-like phase transition.

To fully analyze the real-space case, we finally consider the period of the interferences, as already shown in section 1.6. The real-space periodicity (ξ) is directly related to the separation of the momentum between the WPs R_1 and L_2 by,

$$\xi = \frac{2\pi}{\left|\vec{k}_{R_1} - \vec{k}_{L_2}\right|} \tag{3.2}$$

From the Fourier analysis, we obtain for these fringes $\xi = 1.8(1)$ µm, that provides a separation between the wave vectors of $\left|\vec{k}_{R_1} - \vec{k}_{L_2}\right| = 3.4(2)$ µm^{-1}. As observed in the

experiment, WPs moving in opposite directions have the same speed during t_2, $\left|\vec{k}_{R_1}\right| = \left|\vec{k}_{L_2}\right|$. Thus, we obtain a maximum momentum of $1.7(1)$ µm^{-1}, which agrees with the experimentally measured $1.70(2)$ µm^{-1}.

The Bose-Einstein transition can be characterized by a critical temperature that determines the condensate's formation, as observed by our results when the visibility decays to zero. Apart from the ideal Bose gas, the critical temperature for the BEC transition has been theoretically calculated in the literature for an homogeneous dilute gas using the renormalization-group theory, in which Bijlsma *et al.* obtained a critical temperature higher than that of the ideal Bose gas [95]. Furthermore, similar results have been also obtained using Monte Carlo simulations [96]. However, these theoretical models do not consider the out-of-equilibrium nature of polariton condensates, nor the existence of a non-condensed fraction. For this reason, we consider two situations that have been proposed in the literature for atomic systems composed of condensed and uncondensed fractions. The first model describes a mean field approach to a purely 2D weakly interacting atom Bose gas [97] while the second one considers a 3D gas of interacting cold atoms confined in a cigar-like trap [98]. Both models describe the temperature dependence of the fraction of condensed atoms (n_C) as,

$$n_C(T) = n_0 \left[1 - \left(\frac{T}{T_C}\right)^{\beta}\right] \tag{3.3}$$

where n_0 is the number of particles at $T = 0$. The index β acquires a value of 1 in the former model and 3 in the latter one. We consider both models and compare our results for the visibility of the patterns at the three time delays with their models.

In the experiment performed in this chapter, the appearance of the fringes is the result of the interference between two coherent, condensed, polariton populations. In the ideal case of purely condensed populations, the visibility of these fringes would result 1, however, the obtained values are lower and decrease with the temperature due to the presence of non-condensed polaritons. Therefore, the visibility provides a direct estimation of the evolution of the condensed population in a WP, allowing the comparison between our data and both theoretical models. The fits using Eq. 3.3 are represented in Fig. 3.7 for $\beta = 1$ and 3 with a dashed line and a solid line, respectively. At zero T, the models predict a condensed fraction of 1 while, as expected, our results for the visibility are far from this value due to the non-equilibrium nature of our condensates and the high contribution of non-condensed polaritons even at extremely low T [30].

We obtain from the fits critical temperatures comparable with those observed experimentally when the visibility decays to zero in every time interval. It should be noted that there is not a noticeable difference when determining T_C with $\beta = 1$ or $\beta = 3$. Moreover, the models provide an accurate value of T_C with a maximum deviation from the experiments of a 7 %. As seen in Fig. 3.7, both theories fit properly the results, implying that we cannot give a definite conclusion about which model is more adequate to describe the temperature dependence of the visibility, bringing forward the need for the development of a new theoretical model for an out of equilibrium condensate.

For the sake of completeness, we have obtained the fraction of condensed to uncondensed polariton population f_C. As explained above, the non-equilibrium nature of our polariton condensates hinders the determination of the number of particles. Although we are far from the BEC ideal case, we can address this problem by estimating the fraction of the condensed and the uncondensed population of the condensates. As already explained in section 3.3, we can distinguish the contribution of both populations to the PL: the background intensity arising below the fringes has its origin in the thermal, non-condensed population, whereas the fringes emerging on top of this background have their origin in the condensed population. Therefore, we can compute the area enclosed beneath the fringes and the baseline as the condensed population fraction and the area beneath the baseline as the uncondensed population fraction. The ratio between both contributions, f_C, is shown in Fig. 3.8.

The fraction f_C shows a similar decay to that observed in the visibility, revealing an increase of the non-condensed contribution with increasing T. Due to the signal-to-noise limitation at high temperatures, the maximum T considered is 30 K. At interval t_1 [Fig. 3.8(a)], only a 10 % of the WP is formed by condensed polaritons at very low temperatures (10 K). The coherent population vanishes when this fraction drops to zero at $34(3)$ K. Since t_1 and t_2 are comparable intervals, the data reveal a similar fraction of condensed polaritons in Fig. 3.8(b) at low T. A critical temperature of $33(2)$ K for condensation is obtained in this case, which is in good agreement with that of interval t_1. The interval t_3, is compiled in Fig. 3.8(c). In this case, the WPs show a reduction of the condensed fraction, now $f_C \sim 8\%$ at 10 K. This reduction is consistent with the nearness of the excitonic reservoirs, yielding $T_C = 25(4)$ K. The temperature that defines the phase transition for condensation obtained either through the visibility of the fringes or the fraction of condensed polaritons are compatible, demonstrating that both methods are equally valid.

Both theoretical models we have considered describe appropriately the decay of the experimental data with T. These fits, are represented in Fig. 3.8 as the dashed line for the

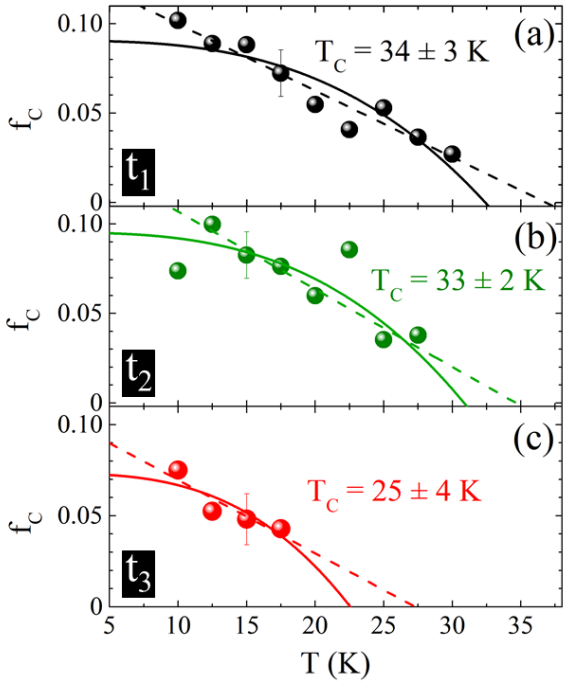

Figure 3.8. Fraction of the condensed to uncondensed polariton population as a function of the temperature. The fraction is calculated at three different times: (a) t_1 in k-space, (b) t_2 in real-space and (c) t_3 in k-space. The dashed and solid lines are fits with the form of Eq.3.3 for the cases $\beta = 1$ and $\beta = 3$ respectively.

linear tendency ($\beta = 1$) and the solid line for the cubic one ($\beta = 3$). A similar discussion to that made previously for the visibility can be made in this case. While the theoretical models assume a fraction of 1 at $T = 0$ for full condensate populations, a maximum fraction of ~ 0.15 is obtained at the lowest temperatures in our experiments. The origin of this discrepancy lies in the omnipresence of thermal, non-condensed polaritons. Furthermore, this fact implies that, even at extremely low temperature, there are significant effects arising from the out-of-equilibrium noise.

When the visibility is analyzed using both theoretical models [see Fig. 3.7], a similar T_C is obtained independently of the value of β. The same conclusion is obtained when the condensed to uncondesed fraction is analyzed [see Fig. 3.8]. Therefore, our experimental data do not allow to determine which model is more appropriate to describe the temperature dependence of the degree of coherence in non-equilibrium condensates, which demands a more adequate model that takes into account this non-equilibrium nature.

3.5 Conclusions

In this chapter, we have investigated the thermal robustness of the mutual coherence of polariton condensates in real- and momentum- space. The presence of interference fringes along the full polariton propagation reveals a time- and space-preserved phase correlation. Its temperature dependence has been evaluated at three time delays through two different methods: analyzing the interference pattern to obtain their visibility (υ) and calculating the fraction of condensed to uncondensed polariton population (f_C). A similar decrease of the coherence with increasing temperature has been found, both in real- and momentum-space that is correlated with the BEC-like transition. Moreover, a similar critical temperature for this transition has been obtained in both cases, when υ or f_C decay to zero. Our findings demonstrate the direct connection between real- and momentum-space although in the first case, the analyzed fringes arise from condensates overlapping in space and in the second case, from condensates spatially separated.

In addition, a faster decrease of the coherence is found when the emission is analyzed at longer times after the condensate's formation. At such times, the lifetime constraints of polaritons and the exciton-polariton scattering produce a decoherent effect, resulting in a weaker thermal robustness of the condensates. The results have been compared with two theoretical models available in the literature and developed for equilibrium atomic condensates. Since our condensates are out of the equilibrium systems and therefore, the temperature cannot be well-defined, these models do not provide a real temperature dependence of the condensed fraction. However, both theoretical models allow us to determine a critical temperature for the BEC transition.

Chapter 4

Polariton propagation in 1D - directional couplers

4.1 Introduction

In the last decades, the interest in increasing the speed and performance of conventional processors has led to the creation of photon-based devices [99–101]. The reason is the increase in processors' operation speed and the benefits of transferring and processing fully optical information [99, 102]. The development of these devices relies on the efficiency in confining and manipulating the light within a selected spatial region. In an attempt to address this need, several all-optical architectures based on microcavity polaritons have been realized [76, 77, 89, 103–108]. The design and construction of the fundamental parts of every integrated optical architecture to guide polaritons to different spatial regions of the sample involves the creation of a 1D planar straight waveguide. These systems have been frequently discussed in the literature and considered in polaritonic devices [58, 109–111]. Under high excitation power densities, polaritons in waveguides acquire a large wavevector value predominantly in one component, consequently, they are able to propagate large distances during their lifetime. However, real devices require more elaborated structures than straight waveguides. A precisely introduced defect or a modification in the shape of a straight waveguide enables the guiding of the polaritons through new curved trajectories. The overall losses in a bent waveguide determine the optical efficiency and therefore, the viability of large-scale optical devices. An important difference between conventional waveguides, used for light propagation, and polariton waveguides, is the possibility of switching from

single-mode to multi-mode operation, in which different propagating modes can be found. The inter-modal mixing does not usually happen for multi-mode propagation in a perfectly straight waveguide, nonetheless, when a perturbation such as a bend is introduced, it is possible to find mixing between the modes [112, 113]. Therefore, in the case of propagation of polariton condensates in waveguides, it is also expected that the deviation from a straight into a curved trajectory will result in the appearance of inter-modal mixing. Although many complex optical devices based on polaritons contain bent waveguides, the effects related to the presence of a curvature have not been practically studied [114, 115]. Here we shall address these effects and we investigate planar waveguides where a deviation of 45º at both ends of the structure has been introduced. Two of these waveguides, symmetrically placed at a short distance, compose the device dubbed as coupler that is investigated in this chapter.

Another attractive feature of polaritons is the feasibility to control their spin through the polarization state of the excitation light. This property opens the possibility of developing a new class of integrated spin-based devices, useful for applications such as polariton switches, logic gates and quantum computing, with efficient ultrafast operation [116–118]. Experimental works have shown that a spin-dependent polariton-polariton interaction allows the creation of these devices with an output spin state controlled by the polarization of the excitation light [29, 119–121]. As a starting point to study the possibility of exploiting the spin degree of freedom in a coupler device, in this chapter, we explore its response to a linear polarization.

This chapter is distributed as follows. In section 4.2, we characterize the coupler device considering the feasibility of its design for polaritonic-based circuits. We report a detailed study of the effect of introducing a 45º deviation in the polariton propagation. In section 4.3, we study the coupling of polaritons between two parallel waveguides that constitute the arm of the couplers. The selection of different size parameters in the couplers grants access to a wide variety of responses of the device under the same excitation conditions. For the sake of completeness, in section 4.4, the coupler's reaction to a linear polarization is analyzed. Finally, the conclusions of this chapter are summarized in section 4.5.

4.2 Characterization of the arms of the couplers

The coupler devices used in this chapter are described in detail in section 2.2.2. As shown in Fig. 4.1, they are composed by two double bent waveguides, referred as arms from now on. The size parameters that describe the dimensions of this device are indicated by L_c, d_c and w, which label the coupling length in the central region, the separation between the arms

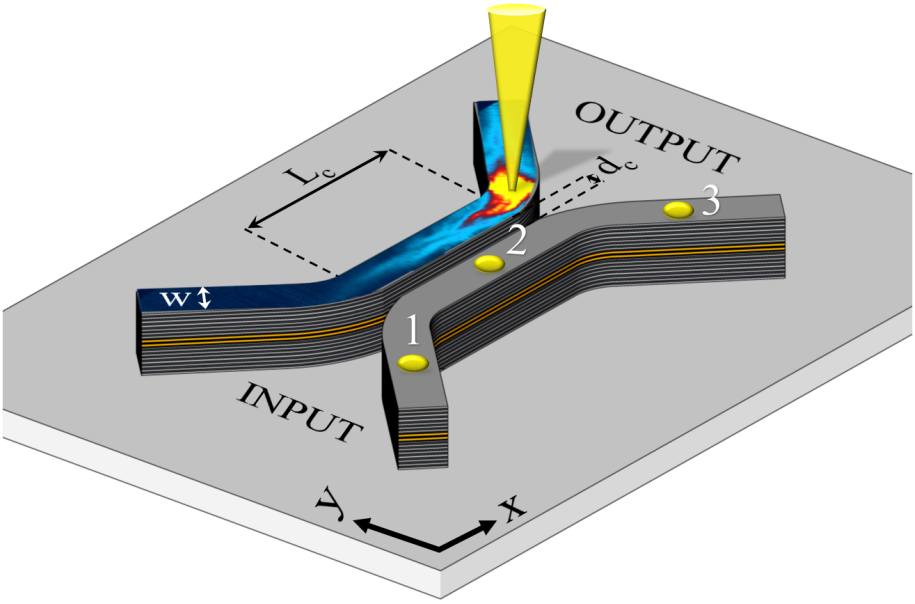

Figure 4.1. Sketch of a coupler device composed by two double bent waveguides. The dimensions of the device are defined through the coupling length L_c, the separation between the arms d_c and their width w. The positions 1, 2 and 3 mark the excitation points at which the emission has been measured. Input and output denote the terminals. As an illustration, the emission of polariton condensates propagating along the waveguide is depicted when the laser excites the structure in one arm.

and their width, respectively. The x and y axis are defined always in the same manner: x is parallel to the coupling region of the coupler and y is perpendicular to it. Three different positions labeled as 1, 2 and 3 are considered when exciting the device. Position 2 is located in the coupling region while 1 and 3 are placed in the input and output terminals, respectively.

The characterization of the couplers is performed under non-resonant excitation at 1.664 eV with a pulsed laser source. The excitation beam is focused onto the sample surface through a microscope objective with NA= 0.40 and $f = 10$ mm. The size of the spot is adjusted to fit, as accurately as possible, inside the waveguides that form the couplers. To modify the spot diameter, a combination of beam expanders with different magnifications are placed before the objective. Thus, for $w = 6$ µm, the diameter of the laser beam is set to ∼3.0 µm, measured at FWHM. During the experiments of this chapter, the temperature has been adjusted between 5 and 15 K. A spatial care has been taken when decreasing the temperature below 10 K, since the high flow of He introduces vibrations that may affect the resolution of the measurements.

4.2.1 Asymmetric band dispersion along the coupler

A characterization of the photonic landscape experienced by polariton condensates in their movement is necessary to fully understand their propagation and to improve the design of polaritonic circuits. For this purpose, the structure has been pumped at several locations in both arms, collecting the PL along the x- and y-directions from a total area of 60 μm^2 around the excitation spot. The PL emerging from the rest of the device has been removed from the emission by means of a spatial filter. Since the results obtained for both arms are completely equivalent, we will concentrate on the results acquired in just one of them and on the selected positions 1, 2 and 3 that summarize the results obtained along the whole structure. The dispersion relations at these positions are depicted in Fig. 4.2. Panels (a)-(c) show the momentum distribution for k_x at a low excitation power density, 0.6 kW/cm^2, for positions 1-3. These measurements are made for $k_y = 0$. Note that for position 2, the k_x and k_y directions are oriented along the longitudinal and transversal directions of the waveguide, respectively, while the terminals are rotated $\pm 45^{\circ}$ with respect to these axes. Let us start by analyzing the emission at position 2. In the case shown in panel (b), the dispersion is produced entirely by the contribution of polaritons distributed along the longitudinal direction of the waveguide, which coincides with the direction of detection. Polaritons can freely expand along the longitudinal direction of the guide so that no restriction is observed in the angular detection. When polaritons annihilate, photons are emitted at all possible angles along the x axis. Thus, the entire lower polariton branch (LPB) and the rest of the sub-bands are observed, displaying continuous energy bands in the full range of k_x. By contrast, the discontinuity in the refractive index in the transverse direction, created by the difference between the cavity and air, yields to a complete lateral confinement and hence to a full quantization of the transverse momentum. The allowed values of this wavevector are given by $k = (j+1)/w$, where w is the waveguide's width and j is the quantization number, integer and positive, that identifies each sub-band in the dispersion. Panel (e) demonstrates a completely discretized dispersion along k_y, due to the high confinement produced by the narrowness of the waveguide. The emission is split into several sub-bands whose antinodes are clearly visible. The superposition of the dispersions in panels (b) and (e) is responsible for the dispersion measured in the terminals of the waveguides, as it will be shown below.

Now, we analyze the dispersions along k_x at the terminals. Conversely to the symmetry discussed for the dispersions at the coupling region, the multiband structure between 1.584 and 1.598 eV, observed in the emission at the input terminal, position 1 [panel (a)], exhibits a peculiar asymmetry between negative and positive values of k_x, with a larger population observed in the former one. This dispersion relation, since the waveguide is rotated 45º with

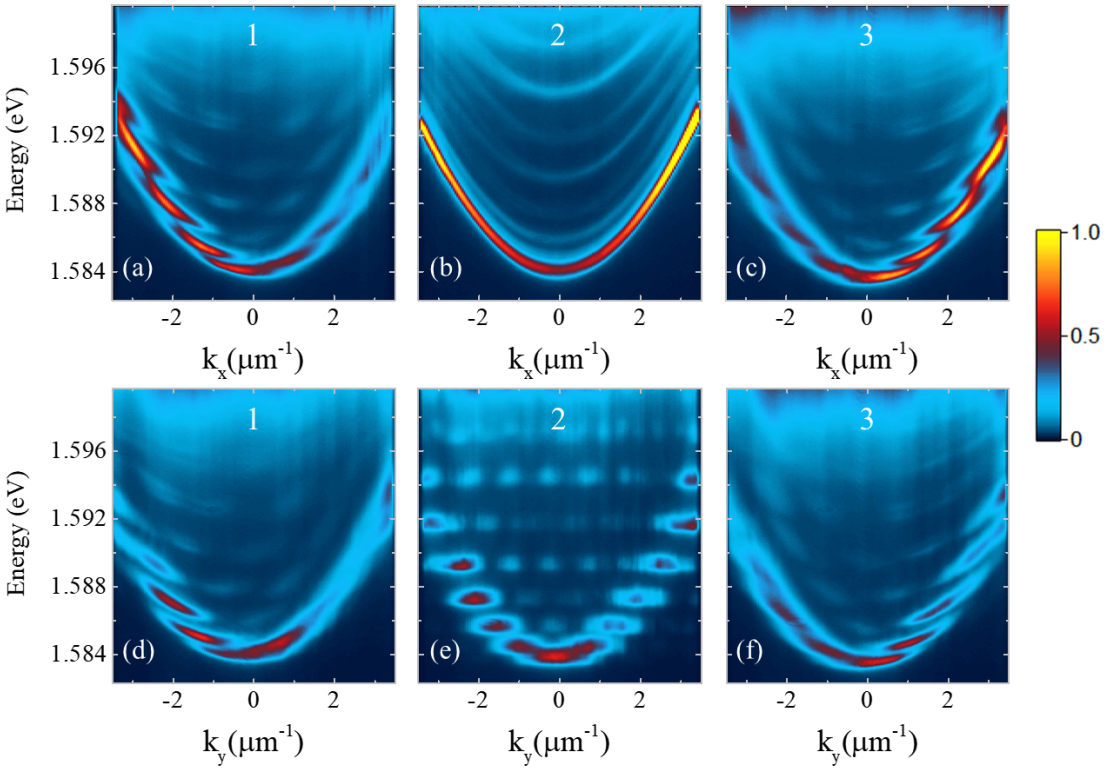

Figure 4.2. Polariton dispersion curves obtained along k_x ($k_y = 0$) at locations 1 (a), 2 (b) and 3 (c). The corresponding emissions along k_y ($k_x = 0$) are depicted in (d), (e) and (f), respectively. The emissions have been measured at a power density of 0.6 kW/cm^2.

respect to the detection axes, can be understood as a linear combination of those associated to the longitudinal and transversal wave vectors of the waveguide [122]. Furthermore, the position of the laser beam near the waveguide edge plays an important role as it introduces a strong asymmetry in the dispersion. An additional wave vector discretization along the longitudinal direction emerges due to the finite distance to the edge of the waveguide, resulting in an accentuated energy discontinuity at negative values of the momentum, $k_x < 0$. The quasi-confinement of polaritons between the edge of the waveguide and the exciton reservoir potential barrier at the excitation spot is responsible for the larger intensity obtained at negative values of k_x in the dispersion. For positive values there is no obstacle to the polariton expansion since they can travel at ease along the waveguide, so a more continuous band for $k_x > 0$ is found. Additional experimental evidences (not shown) reveal that the closer to the waveguide's edge the excitation, the more pronounced the asymmetry of the emission. This is due to the fact that the allowed values of the discretized longitudinal

wavevector are further separated because of the increasing proximity of the edge and also to the polariton population getting trapped in a smaller area of the waveguide (smaller the closer to the edge of the structure). The excitation at position 3 [panel (c)] obtains a similar dispersion relation to that shown in panel (a). However, in this case, the waveguide is rotated - 45º, and therefore, the emission shows quasi-discrete energy states at positive values of k_x.

The corresponding dispersions relations along k_y ($k_x = 0$) for positions 1 and 3 are shown in panels (d) and (f), respectively. Panel (d) exhibits a similar distribution to that of panel (a) due to the additional confinement created by the edge of the structure, which in this case also results on discretization at negative values of k_y. Due to the opposite angle of rotation, with respect to x, of the output terminal to that of the input one, panel (f) shows the reverse behavior to that of panel (d) with discrete values predominantly for $k_y > 0$. The superposition of both longitudinal and transverse wave vectors on k_x and k_y, together with the additional confinement at the end of the input and output terminals, provides a full understanding of the polariton dispersion relations, explaining also the smoother discretization of the energies at the terminals as compared to that observed in panel (e).

Increasing the excitation power density up to 24 kW/cm^2, well above the condensation threshold (12 kW/cm^2), the polariton condensates injected in the waveguide propagate all along the device. Fig. 4.3 presents the corresponding dispersion relations obtained for the same three excitation positions discussed earlier. The dashed lines mark the bottom of the LPB band when a low pump power is employed. The emission energy is blueshifted ~ 5 meV due to polariton-polariton interactions. Above threshold, two drops of condensates are created, propagating away from the excitation spot towards opposite longitudinal directions. We discuss again, for the sake of clarity, the case of excitation at the center of the coupling region, position 2. In this case, along the longitudinal direction of the waveguide, apart from some polaritons that stay at rest ($k_x \approx 0$), condensates propagate with $|k_x| \approx 2$ µm^{-1} at $\sim$1.588 eV [Fig. 4.3(b)]. In the transverse direction, condensates propagate mainly at an excited state with slightly higher energy, 1.589 eV, and lower momentum, $|k_y| \approx 1.5$ µm^{-1}, [Fig. 4.3(e)].

A more complicated situation arises at the input and output terminals. Additional to the frequent presence of polaritons halted at the excitation area by the potential created by the excitation beam, massive populations at positive and negative values of the momentum are observed in the interval $2.0 < |k_x| < 3.5$ µm^{-1} between the energies 1.589 eV and 1.596 eV. At the input terminal, some condensates travel from position 1 towards the center of the structure (position 2) exhibiting positive momenta while most of the condensed population

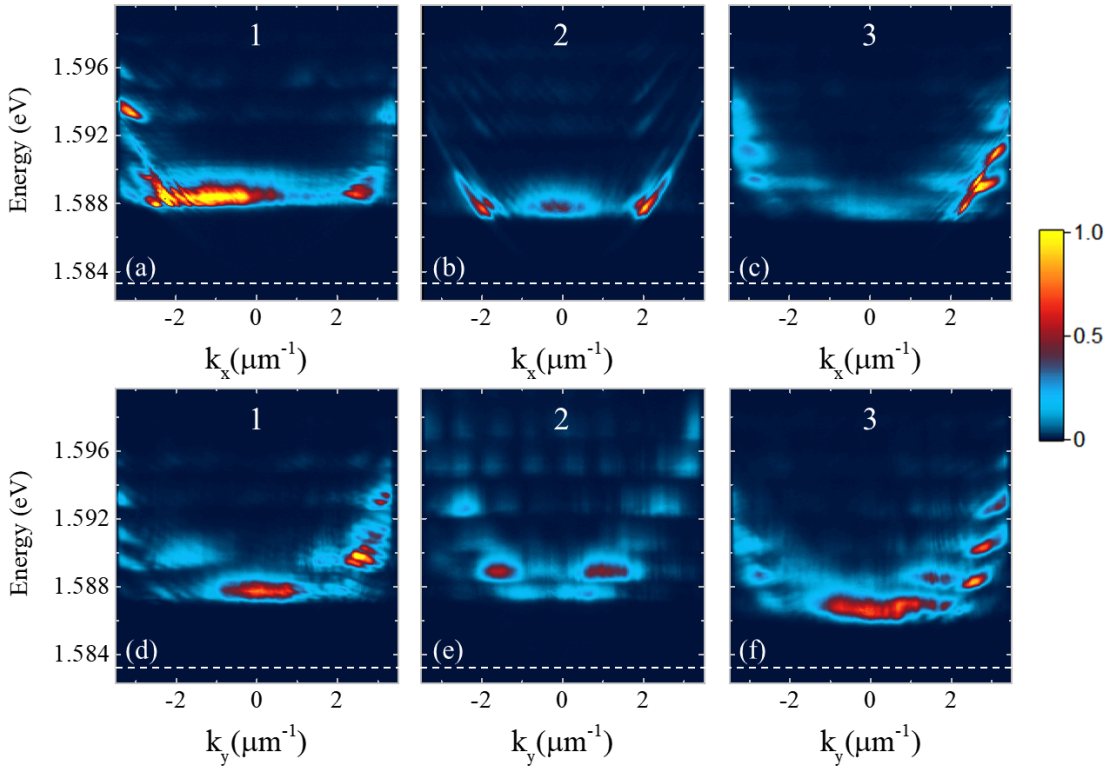

Figure 4.3. Polariton dispersion curves obtained for a high power density of 24 kW/cm^2, along k_x ($k_y = 0$) at locations 1 (a), 2 (b) and 3 (c). The corresponding emissions along k_y ($k_x = 0$) are depicted in (d), (e) and (f), respectively. The white dashed lines mark the bottom of the LPB.

travels towards the edge of the structure, and it is trapped, with negative values of the momenta, as demonstrated by the emission depicted in Fig. 4.3(a). The situation is inverted at the output terminal [panel (c)] due to the presence of the edge of the structure affecting now those polaritons travelling with $k_x > 0$. In contrast to the findings at the center of the coupler [panel (b)], where condensates travel mostly with a well-defined single mode, peculiar multi-mode dispersions characterize the polariton propagation at the terminals. A similar comment pertains when analyzing the behavior along k_y: panels (d) and (f), corresponding to the input and output terminals, respectively, exhibit the presence of up to 4 modes similarly populated at different energies, while panel (e) shows that at the coupling region polaritons propagate mostly at a single mode. Therefore, the 45º rotation of the waveguide not only reveals the appearance of new modes, but the transition from a single-mode to a multi-mode propagation.

4.2.2 Influence of the bend on polariton propagation

Polariton condensation in 1D-waveguides has been frequently reported under non-resonant excitation showing the formation of condensates propagating out of the excitation spot [91, 118, 123]. However, a locally induced variation in the trajectory of these condensates has important effects for their implementation in polariton circuits, as we will show here. An essential element example for integrated optics is a bent waveguide, as it is one of the key components of many potential devices. To our knowledge, the condensate's response under these conditions has been scarcely studied in the literature, with none of the works paying attention to the momenta distribution of propagating condensates [103, 107, 114, 115]. Here we address this issue by investigating the condensates' trajectory after excitation of the device in position 1 and analyzing the effect of the bend between the terminal and the coupling region on the condensate's wavevector.

Fig. 4.4(a) shows the time-integrated real-space map of two condensates propagating along the device in opposite directions. One of the drops, ejected to the left ($x < 0$), gets trapped between the edge of the waveguide and the excitation spot, bouncing repeatedly between these positions. The condensate ejected towards the right ($x > 0$) shows a remarkable decay of the emission intensity when reaching the bend of the structure. A similar decay has been observed by Liran *et al.*, who reported a more pronounced drop in the intensity when the condensates travel through a bent waveguide instead of a straight one [114]. However, as shown in the figure, beyond $x > 15$ µm the propagation is visible up to 80 µm (note that the intensity has been multiplied by a factor 3). The emission evidences a peculiar propagation along the device: condensates travel along two meandering parallel paths in the input terminal, mostly at the edges of the waveguide, while in the coupling region they merge and exhibit a zig-zag path. The fact that both, the intensity and the trajectory of the condensates, exhibit such a change in their behavior clearly evidences the impact of a bend on the polariton propagation.

To quantify the impact of bending the polariton trajectory by 45º, we measure the modulus of the polaritons' momentum at different propagation distances from the excitation spot. To do this, we spatially filter the condensates' PL at different locations along the device and collect the angle-resolved PL of the selected region. The evolution of the momentum for the condensate propagating along $x > 0$ is depicted in Fig. 4.4(b). The condensates traveling to the coupling region of the waveguide are initially injected with a momentum of 2.9 μm^{-1}. This value can be tuned through the power density of the excitation beam. Once they propagate a short distance from the excitation area, the momentum, and therefore the

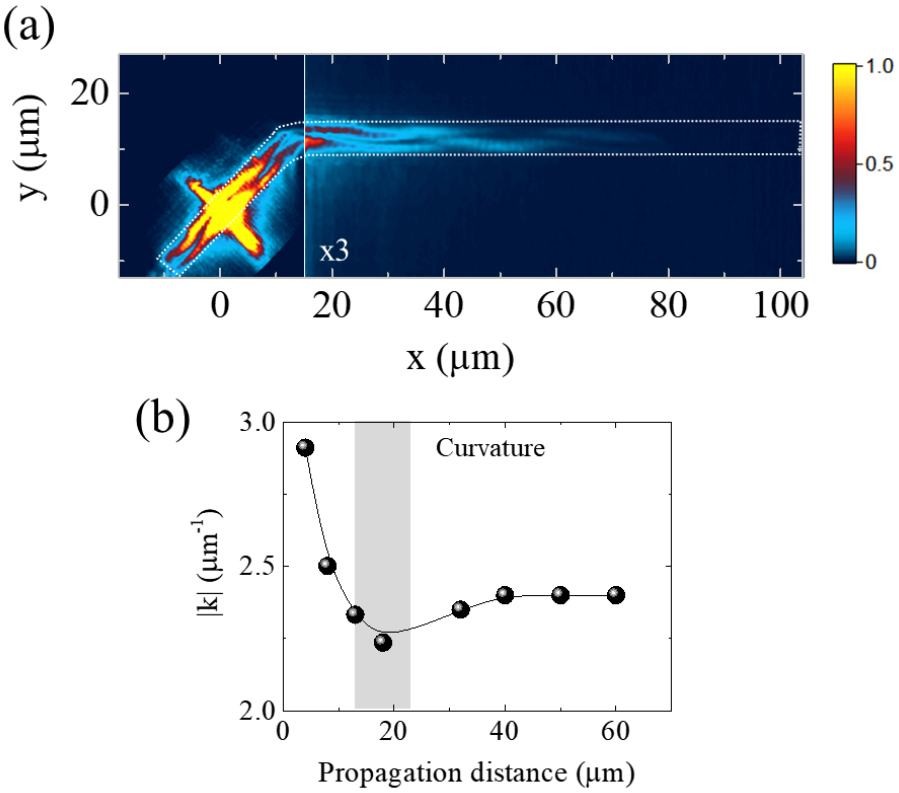

Figure 4.4. (a) Time-integrated real-space map of polariton condensates traveling along the waveguide while pumping on position 1. After passing the bend, polaritons follow a zig-zag trajectory. The intensity is scaled by a factor of 3 for $x > 15$ μm. (b) Decay of the condensate's momentum while propagating from the excitation spot at $x = 0$ μm. A maximum decay is observed at the bend of the waveguide, marked with the gray rectangle at ~ 20 μm.

velocity, suffers a significant decay ($\sim 25\%$). A minimum value of 2.2 μm^{-1} is obtained at the bend of the waveguide, marked with a gray rectangle in the figure. Nonetheless, as the condensate crosses this region, the momentum levels up and remains constant while propagating along the center of the device. The sharpness of the bend acts as an obstacle in the propagation of condensates, slowing down their movement. As mentioned above, the initial conditions are easily established, however, the control over the propagation is lost once the bend has been crossed. These results evidence the need for further investigation to improve propagation along more complex polariton circuits.

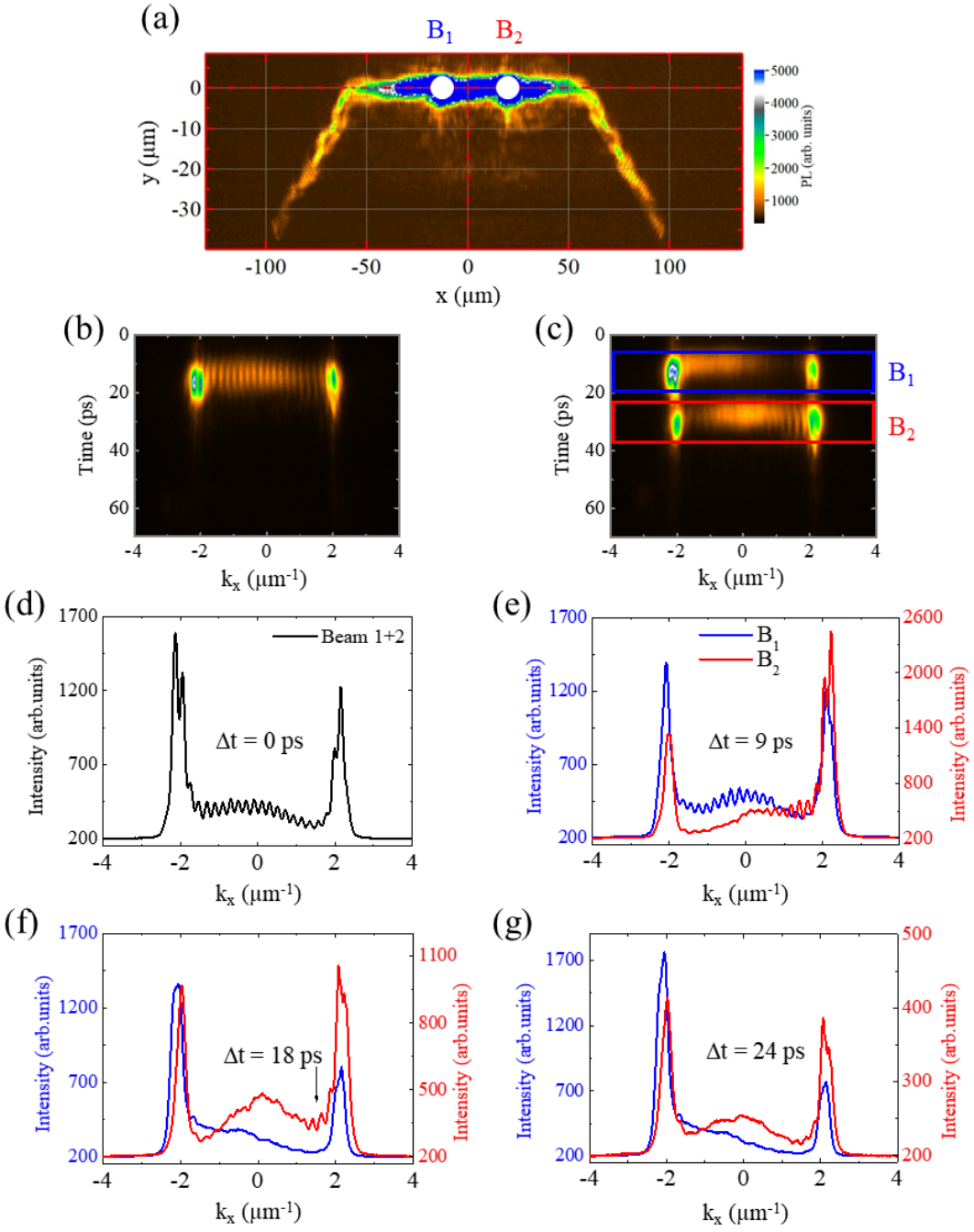

Figure 4.5. (a) Real-space map of polariton condensates propagating in one arm of the coupler device. The coupling region is pumped with two laser beams, B_1 and B_2, indicated by white circles. (b) Temporal evolution of the condensates momentum along k_x ($k_y = 0$) when the laser beams B_1 and B_2 are synchronized to arrive simultaneously to the arm of the coupler ($\Delta t = 0$). (c) Same as (b) for $\Delta t = 18$ ps. The upper (lower) emission arises from B_1 (B_2). (d) Time-integrated emission in momentum-space in an interval of 14 ps for $\Delta t = 0$ ps. (e), (f) and (g) depict the same emissions as in (d) for $\Delta t = 9, 18$, and 24 ps, respectively. The blue (red) profile corresponds to the blue (red) rectangle in (c), arising from B_1 (B_2). The arrow at (f) indicates the fringes appearing first at the emission from B_2. All the emissions are filtered at an energy of 1.5881 eV.

4.2.3 Demonstration of the condensed character of the polariton wave packets: coherence build-up

For the sake of completeness, we briefly discuss the coherence build-up of condensed polaritons. The coherence exhibited by these systems has been investigated by the observation of the interference between traveling condensates [48, 56, 58, 59]. As demonstrated in chapter 3, it is expected that with increasing temperature both the spatial and temporal coherence do vanish at a critical temperature. However, other factors also need to be precisely controlled: an important parameter to consider is the time delay between the emissions arising from different condensates. To study this effect, we excite the coupling region of one arm of the device with two pulsed laser beams (B_1 and B_2) separated by $d = 33 \pm 1$ µm. Fig. 4.5(a) shows the real-space map of the condensates propagating along the structure (at 1.5881 eV) while pumping in the coupling region. Two condensates are created from each laser source, traveling towards negatives and positives values of x. Condensates propagate in the coupling region following an approximately straight trajectory, however, after passing through the bend the path varies dramatically. A more complex trajectory is observed in the terminals, where condensates follow a zig zag path that can be distinguished by the presence of maxima and minima in the emission. The temporal coherence of these condensates is analyzed in the coupling region along the x-direction, where they travel with a similar momentum. The emission intensity along k_x is depicted in Fig. 4.5(b), which shows interference fringes in the full range of the emission, revealing that condensates move with a similar acceleration. An exponential decay fit of the intensity as a function of time yields an average polariton lifetime of just 5 ps in the couplers (not shown), establishing the synchronization between the beams as an essential parameter to control the communication between the condensates. When a time delay (Δt) of 18 ps is introduced between B_1 and B_2, the emission drastically changes [see Fig. 4.5(c)]. While the conditions for B_1 remain the same, B_2 is temporarily shifted by increasing the laser path in the experiment before the corresponding beam impinges on the sample. Consequently, the polariton emission arising as a result of each excitation beam suffers the same delay. In this case, the time delay is longer than the lifetime of particles, therefore, no interference fringes are observed in the condensates created by B_1 (upper emission). In contrast, small fringes are present at $k_x > 0$ for those created by B_2 (lower emission); despite being created at later times, they still can interfere with the residual polariton population from the earlier emission. To investigate this phenomena, the emissions are time-integrated in an interval of 14 ps, indicated by the colored rectangles in Fig. 4.5(c). The resulting profiles are compared in Fig. 4.5(d)-(g) for different time delays. Panel (d) shows the case when the time delay is negligible [same case as in panel (b)]. In this case, condensates are created at the same time from each laser source, allowing to observe fringes at the maximum momentum

value that condensates acquire, i.e., $\sim \pm 2$ μm^{-1}. A Fourier analysis of these fringes, as already described in Chapter 3, provides a period of 0.196 ± 0.003 μm^{-1}, which corresponds to a separation between the condensates in real-space of 32.0 ± 0.5 μm (see Eq. 1.34). This result agrees with the separation between the laser beams d set in the experiment. When the delay between the laser beams is increased to $\Delta t = 9$ ps, see panel (e), both emissions still overlap in time. As a result of the coherence between the condensates created in the structure, a clear set of fringes emerges in the emission originated from B_1. In the emission arising in B_2, fringes are only observed in the range $k_x > 0$. Note that in both emissions, the fringes are only visible in the interval $0 < |k_x| = 1.7$ μm^{-1}, which corresponds to the acceleration process of condensates before acquiring a maximum constant momentum. As already seen for $\Delta t = 18$, [panel (f)], small fringes emerge only in the emission corresponding to B_2 (marked with an arrow), since polaritons of B_1 have nearly reach the end of their life span before interacting with those at B_2. Panel (g) shows the case for $\Delta t = 24$ ps: under these conditions, neither the emission arising from B_1 (blue) nor that from B_2 (red) show any sign of interference effects. The different condensate populations are not able to interact due to the large time delay between them: polaritons initially created by B_1 have vanished before the second pulse excites the coupler.

4.3 Control of the output signal by engineering the size parameters of the couplers

Following the successful demonstration of polariton condensation in the coupler devices and the implication of a 45º bend in a waveguide, we focus now on the phenomena that can be accessed when the size of the couplers is reduced. In this section, we study couplers with narrower waveguides, $w = 2$ μm, in which, the separation between the guides has been varied from $d_c = 0.2$ up to 0.5 μm. These new conditions open the possibility of transferring condensates between the arms of the coupler, allowing the observation of Josephson oscillations.

4.3.1 Requirements for polariton coupling

To study these narrower structures, the diameter of the laser beam has been reduced to $\sim$1.5 μm. From now on, the couplers are pumped in position 1 in the experiments, at the input terminal. An important new aspect of the narrow couplers is that while one of the arms is excited by a laser beam generating condensates that travel along the device, the other arm becomes populated by the evanescent wave associated to these condensates. To ensure the

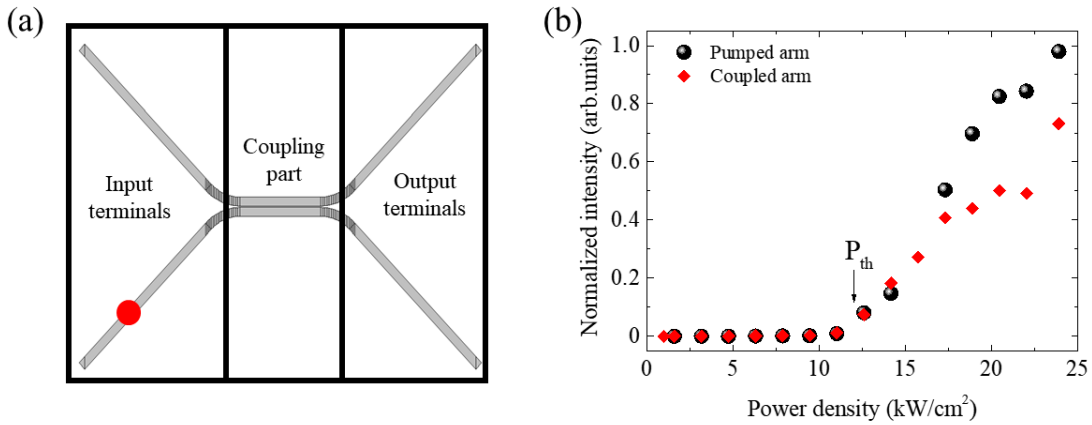

Figure 4.6. (a) Scheme of the filtered parts of a coupler in real-space. The red spot indicates the location of the laser beam. (b) Power-dependence of the normalized PL intensity in the pumped (black) and the coupled (red) arm.

coupling of polaritons, the energy states in each arm must be resonant and present a similar condensation threshold.

To study the fulfillment of these conditions in the couplers, we use a spatial filter in real-space to obtain a clean emission from the different parts of the coupler. A scheme of the filtering technique is shown in Fig. 4.6(a), where three different regions are selected: the input terminals, the coupling region and the output terminals. The laser beam (red spot) impinges on the lower input terminal generating a signal that propagates along the coupling region of the coupler. Finally, the signal arrives to the output terminals, in which the emission is observed either in one of the terminals or in both of them. This filtering technique allows the blocking of one or two of these regions. The signal intensity considerably decreases as polaritons propagate along the structure, therefore, emissions with different intensities are found at each part of the coupler. Blocking the region with the most intense emission allows the detection of weaker signals in other regions such as the output terminals, where signals 95% less intense than the signal initially injected have been found.

Using the spatial filter explained in Fig. 4.6(a) we study the response of a directional coupler device when condensates are coupled from the lower to the upper arm. For this experiment a coupler with $L_c = 100$ µm has been selected. The coupler is excited at position 1 at different power densities. Since the purpose of this experiment is to study the response of the device when polaritons couple, we measure the emission intensity in the coupling region while the emission from the input and output terminals is blocked using the spatial filter. We integrate the emission along the coupling region, distinguishing between the signal arising in the

pumped arm and the signal coupled to the other arm. Fig. 4.6(b) depicts the normalized intensity emission in the pumped lower arm (black) and the corresponding coupled emission in the upper arm (red). Up to ~ 11 kW/cm^2, the emission is negligible in both arms since a power density threshold needs to be exceeded to form polariton condensates that propagate along the structure. This threshold (P_{th}) is obtained for both emissions at a similar value, $P_{th} \approx 12$ kW/cm^2. The fact that the same threshold is found on both arms gives the idea that as soon as the condensates enter in the coupling region, they couple to the upper arm. Additionally, the signal at the coupled arm shows lower intensity emission than that at the pumped one. Note that condensates are coupled by evanescence, therefore, a lower intensity of the emission should be expected in the coupled signal. However, other factors can strongly influence this behavior, such as the presence of oscillations in the polariton emission, as will be shown below.

Using the same setup, we block the emission from the input terminal of different couplers with the same size parameters but different d_c. The real-space maps of these couplers are depicted in Fig. 4.7(a), from left to right: $d_c = 0.2, 0.3, 0.4$ and 0.5 µm. They are pumped on the filtered-out region of the top-left terminal of the structure, so that $x = 0$ marks the beginning of the coupling region. One clearly sees an exchange of particles between the two arms. This transfer is characterized by a strong oscillating signal between the two arms when they are sufficiently close to each other, with the contrast of the oscillations vanishing progressively as the separation d_c increases. The oscillating signal vanishes completely when d_c reaches 0.5 µm. We identify the oscillations in the microcavity emission as Josephson oscillations. The transfer of particles from one waveguide to the other one gives rise to a dynamical renormalization of the energy in each of them, resulting in harmonic oscillations. Therefore, the application of a laser beam gives rise to an oscillating flow of particles [44, 71]. When the periodicity of the Josephson oscillations appearing in one arm is analyzed for the cases shown in Fig. 4.7(a), a dependence with d_c is found: Fig. 4.7(b) shows the evolution of this period as a function of the separation between the waveguides; a linear dependence is observed. As stated in section 1.7, the Josephson current exhibits a harmonic dependence with an oscillation period proportional to $e^{\sqrt{d_c}}$. Therefore, one should expect an increasing period with larger distances between the waveguides following an exponential law. However, an exponential function in a reduced range may become indistinguishable from a linear function if the number of points is limited. Thus, the experimental data in Fig. 4.7(b) can be directly related to the interaction and coupling of polaritons giving rise to the Josephson effect.

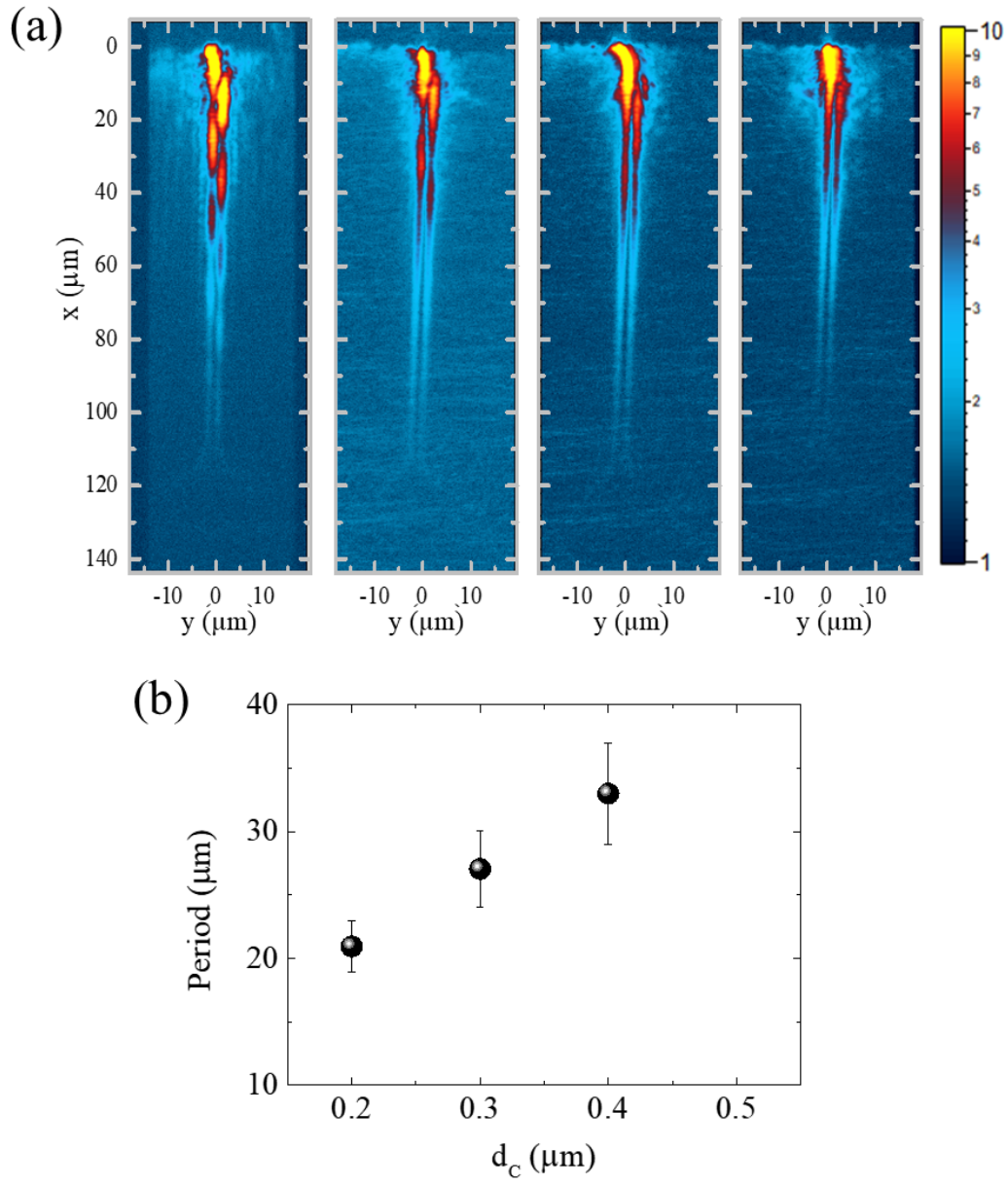

Figure 4.7. (a) Real-space maps of the coupling section of directional couplers with different separation between the arms; from left to right: $0.2, 0.3, 0.4$ and 0.5 µm. The pumped terminal is filtered out from the emission using a spatial filter. The intensity is in logarithmic false color scale. (b) Periodicity of the oscillations observed in the coupling region as a function of the separation between the arms.

4.3.2 Polariton propagation in directional couplers

As exposed along this chapter, the directional couplers exhibit interesting effects such as the appearance of Josephson oscillations when polaritons travel along these devices. Moreover, the high photonic character of the sample ejects polaritons from the excitation spot with a remarkable high velocity, and therefore, a large k value. In this section, we focus on the time-resolved PL of polariton condensates traveling in a coupler device.

We select a device with $L_c = 100$ µm, $w = 2$ µm, and the smallest separation between the two arms to ensure coupling during a long distance, $d_c = 0.2$ µm. We use the excitation scheme depicted in Fig. 4.6(a). In this case, we analyze the PL at three different parts of the coupler: input terminal, coupling region and output terminals. Each part has been measured using the temporal tomography technique, described in 2.1.2.3, either for real- and momentum-space while filtering out the remaining two other parts. Time-resolved PL snapshots of the condensates traveling in the input terminal are shown in Fig. 4.8(a.1). The laser impinges on the center of the input terminal at $x = y = 0$ creating two condensates that travel in diagonal direction, one propagates downwards, towards the edge on the waveguide, and the other upwards, to the coupling region. At 28 ps after the pulsed laser beam impinges on the sample, the condensates have propagated through the terminal, exhibiting a larger population traveling upwards. This behavior is inverted at 43 ps, in which the predominant population appears traveling downhill. At such long times, the polariton population traveling upwards has passed the bent part of the device and continues propagating through the device. However, those traveling downwards are trapped between the edge of the waveguide and the excitation spot. Thus, a persistent emission is observed at the bottom of the terminal. This behavior is confirmed by the corresponding measurements in momentum-space in Fig. 4.8(a.2). Since condensates travel in diagonal directions with respect to the definition of the x, y axes, one expects positive values of the momentum, $k_x > 0$ and $k_y > 0$, if the condensate propagates in the positive direction of x and y, i.e., upwards. On the contrary, one expects $k_x < 0$ and $k_y < 0$ for a condensate traveling downwards. This is what is observed both at 28 ps when the condensate travels with a positive value of the momentum and at 43 ps, when the predominant population acquires a negative momentum, respectively. In the latter case, an important contribution to the emission is also observed for positive values of the momentum. As already mentioned, part of the polariton population is trapped between the edge of the waveguide and the excitation beam, bouncing repeatedly between these two positions. Therefore, one should expect the simultaneous observation of positive and negative k values. It is worth emphasizing that the measurement of the emission in momentum-space gives access to important information not accessible by real-space measurements. As explained in

section 4.2.2, when polaritons propagate in the couplers, the movement is not only allowed in the longitudinal direction of the guides, but there is also a transversal movement from side to side following a meandering trajectory [see Fig. 4.4(a)]. As a consequence of this motion, the momentum is not restricted to a certain value, but it acquires values in a wide range, both for k_x and k_y.

Condensates pass through the bend and enter in the coupling region at 28 ps, as shown in Fig. 4.8(b.1). As a guide for the eye, the shape of the coupler in the coupling region and in the output terminals is drawn with white lines superimposed on the emission maps. The lines differentiate the lower arm of the coupler, which is pumped with the laser beam, and the upper arm, where part of the signal is coupled. At 43 ps, condensates are propagating along the coupling region now both in the lower and the upper arm. The path in this part is characterized by an alternating propagation in which local maxima and minima in both arms are visible. These oscillations are the Josephson oscillations, which have already been described in section 4.3.1. Additional information is found when the momentum-space is analyzed, as shown in Fig. 4.8(b.2). A spot with coordinates $(k_x, k_y) = (2, 1.6)$ µm^{-1} at 28 ps reflects the condensate located at the bend of the waveguide while entering in the coupling region. Since the terminal is oriented at 45º, one should expect $k_x = k_y$, nonetheless, a larger component is found along x due to the change from a diagonal path to a horizontal one. Interestingly, when at 43 ps condensates propagate throughout the coupling region there is not only propagation along the coupler, our results show three movements. A priori, one would think that the motion in this region would be completely horizontal along x. This horizontal motion is actually corroborated by a spot with $k_y = 0$ arising in the emission with a pure horizontal component in $k_x = 2.4$ µm^{-1}. However, the additional two spots with components $(2, \pm 1)$ reveal a simultaneous transfer from the lower to the upper arm and vice versa. This transfer is produced continuously along the device each time an oscillation appears.

Finally, we focus our attention on the output terminals. Depending on the details of the structure, this peculiar propagation yields a predominant population at one of the output terminals, either the lower or the upper one. In this specific case explained here, the population is guided to the upper arm, as shown at 57 ps in Fig. 4.8(c.1). Note that only $\sim 4\%$ of the injected polariton population [see panel (a.1)] is found on the output terminal [see panel (c.1)], revealing the large decay of the polariton population when they propagate along the device. At 78 ps the signal has vanished almost completely. Since the trajectory of the condensate is going upwards in the output terminal, only positive values of the momentum

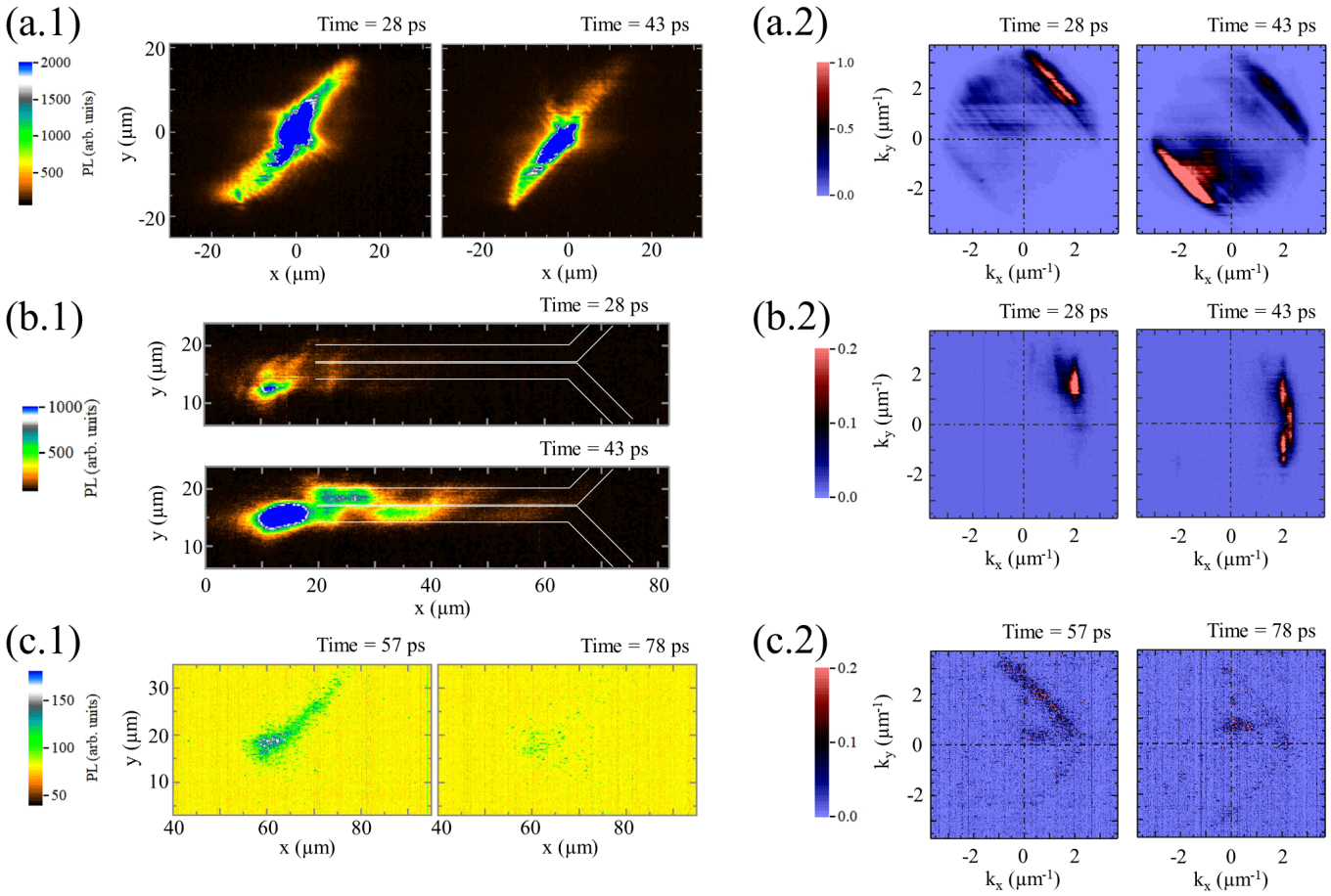

Figure 4.8. Time-resolved PL of polariton condensates traveling along the (a) input terminal (b) coupling region and (c) output terminals. The index 1 and 2 indicate the real-space and the corresponding momentum-space, respectively. The emissions are shown at 28 and 43 ps in the first two cases and 57 and 78 ps in the latter one. As a guide to the eye, the shape of the coupler is drawn in (b) with white lines. The emission intensities are comparable in all three regions, however, the color-scales are modified to visualize the decreasing polariton population along the device.

are observed in Fig. 4.8(c.2) at 57 ps. As expected, no emission is observed at 78 ps in k-space.

4.3.3 Splitted signal at the output terminals

The possibility of controlling the directionality of the signal towards the output terminals in a coupler opens a new way to design more complex polaritonic circuits. Following this idea, we investigate how the signal can be led to a certain terminal through the selection of specific size parameters of the coupler. We consider four devices with $w = 2$ µm and $d_c = 0.2$ µm, in which the coupling length L_c varies from < 2 to 50 µm. Real-space maps of the emission of different devices with varying coupling lengths are shown in Fig. 4.9(a), in which the results obtained in the shorter/longer device are displayed from left to right. All are pumped on the top-left terminal, creating condensates that travel throughout the coupler until they reach the left (L) or right (R) output terminals. In the case of $L_c < 2$ µm, the condensates are not able to couple to the other arm due to its short length, thus, the signal is mainly guided towards the L output terminal. When L_c is increased up to 10 µm, part of the signal is coupled to the neighboring arm, which results in the appearance of one Josephson oscillation on each arm. Since the coupling length is shorter than the period of the oscillations, the system is not able to transfer again polaritons to the pumped arm, thus, the signal is driven towards the R terminal. In the case of $L_c = 20$ µm, the signal is driven mostly towards the L terminal: due to the rise of a second oscillation in the pumped arm, the coupled polaritons are guided back to the pumped waveguide. Finally, in the case of 50 µm a new ratio in the distribution of the signal is found: the emission is comparable in both terminals, obtaining a population splitting of $\sim 50\%$.

For a further analysis, we calculate the ratio of the signal that is guided into the L terminal to the total intensity at the output terminals. To do this, the PL intensity is integrated in the output terminals, allowing to calculate the fraction $I_L/(I_L + I_R)$, where I_L (I_R) is the intensity of the signal in the left (right) output terminal. This quotient is plotted as a function of the coupling length in Fig. 4.9(b): the experimental points are obtained from the analysis of the emissions shown in Fig. 4.9(a). A dramatic change in the direction of the output signal can be clearly observed in the first three cases in which the signal on the L terminal varies from 85% to 15% with a change of the coupling length of just 10 µm. In the largest coupler, a more balanced distribution is obtained between both terminals, 55%. The directionality of the signal depends essentially on the Josephson oscillations, therefore, knowing their periodicity we can estimate the ratio of the splitted signal for any coupling length by predicting a simple oscillatory function. This harmonic function is represented as the blue line in Fig. 4.9(b).

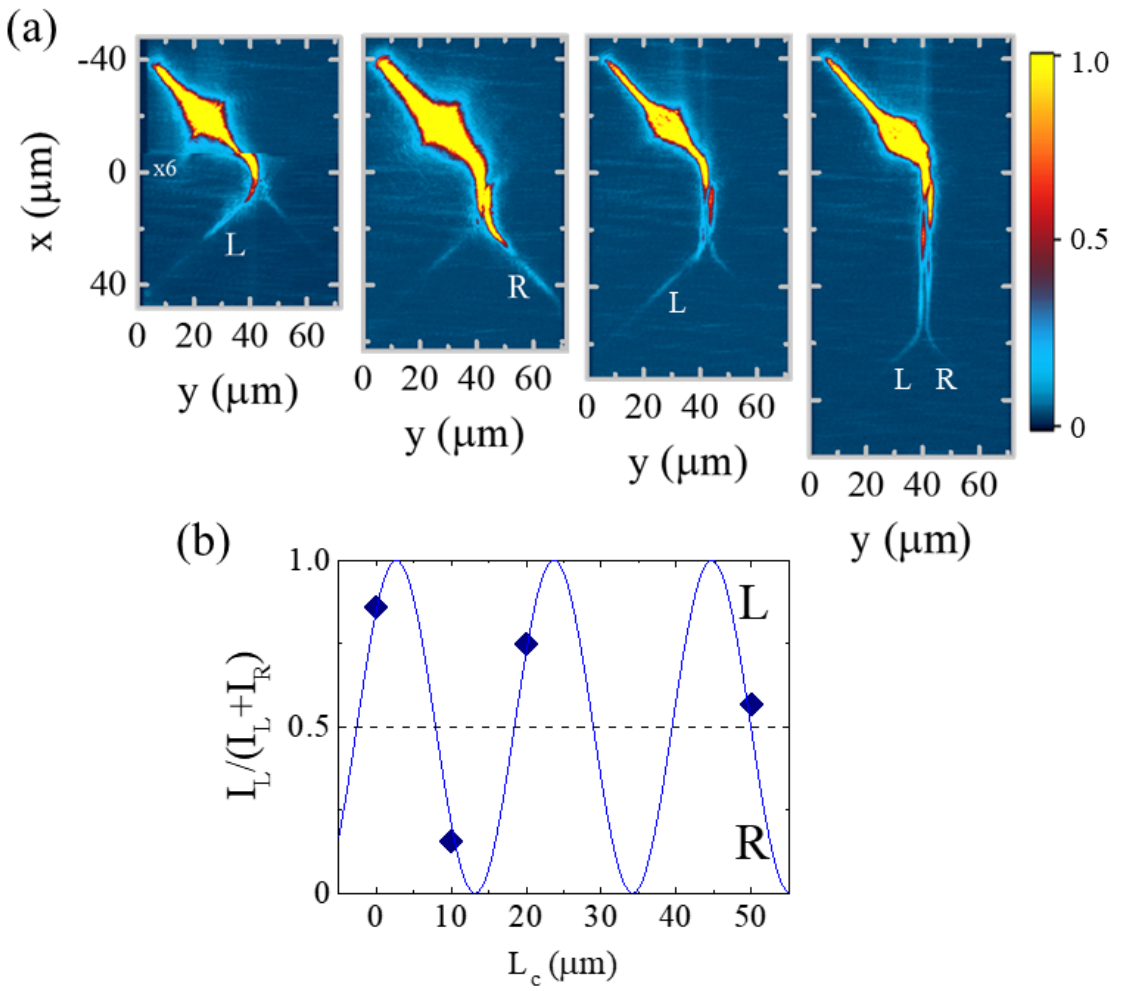

Figure 4.9. (a) Real-space maps of directional couplers with different coupling lengths; from left to right: $< 2, 10, 20$ and 50 μm. L and R label the left and right output terminals, respectively. (b) PL intensity integrated in the output left terminal (I_L) divided by the total intensity in both terminals ($I_L + I_R$) as a function of the coupling length. The horizontal dashed line marks the ratio 0.5 in which the same signal is found in both terminals. As a guide to the eye, the blue line depicts a simple oscillatory function.

Furthermore, these results demonstrate the functionality of the couplers as light-matter splitters, enabling a wide range of signal ratios just by changing one parameter.

4.4 Analysis of the linear polarization of the emission

The massive occupation of a single state and the exhibition of coherence, among others, are well-known properties of BEC systems. As stated in the last sections, these properties can be experimentally demonstrated by analyzing the PL from the microcavity since the emitted photons are actually part of the polariton wave function. This wave function can be described as a matter wave, so one should expect a well-defined polarization and phase across the condensate. Since the polarization of the emitted light is directly related to the spin of polaritons, the study and control of the polarization opens new possibilities of designing spin-based devices. Whatever the polarization of the excitation, several works confirmed, theoretically and experimentally, the buildup of a linear polarization in the PL spectra of microcavities due to the formation of polariton BECs [119–121]. In this chapter, we have already presented the formation, propagation and coherence of BECs, however, the analysis of the polarization of the emission has not yet been considered. In this section we analyze the linear polarization of the PL of a condensate propagating along a coupler device.

The experiment has been carried out in a coupler device located in a region of the sample with $\delta \approx -17$ meV. It is formed by waveguides of $w = 2$ µm width and separated by the minimum gap available, $d_c = 0.2$ µm. In addition, the coupling length has been selected to be $L_c = 10$ µm. To perform this investigation we pump non-resonantly only one terminal of the coupler with a power density of 26 kW/cm^2, well above the threshold for condensation. The selection of these conditions allows a large part of the polaritons generated in the pumped arm to couple to the neighboring arm, as shown in section 4.3. A single Josephson oscillation appears in the coupling region of each arm so that a transfer of polaritons is created from the pumped arm to the other one [as seen in Fig. 4.9(a)].

To study the linear polarization properties of the PL, the excitation beam is horizontally polarized along y ($\theta_i = 90º$), i.e., perpendicularly to the coupling region of the device. The linear polarization of the PL of the coupler is analyzed with a linear polarizer whose axis is varied from $\theta_d = 0º$ to 180º in steps of 10º. The PLs for several of these polarizations are depicted in Fig. 4.10. In this case, the coupler is pumped on the top-left terminal and its emission has been removed using a spatial filter to measure in detail the less intense emission from the rest of the structure. The emission from the polariton condensates arriving to the coupling part, after being generated in the terminal, is visible in the $50 < x < 60$ µm range.

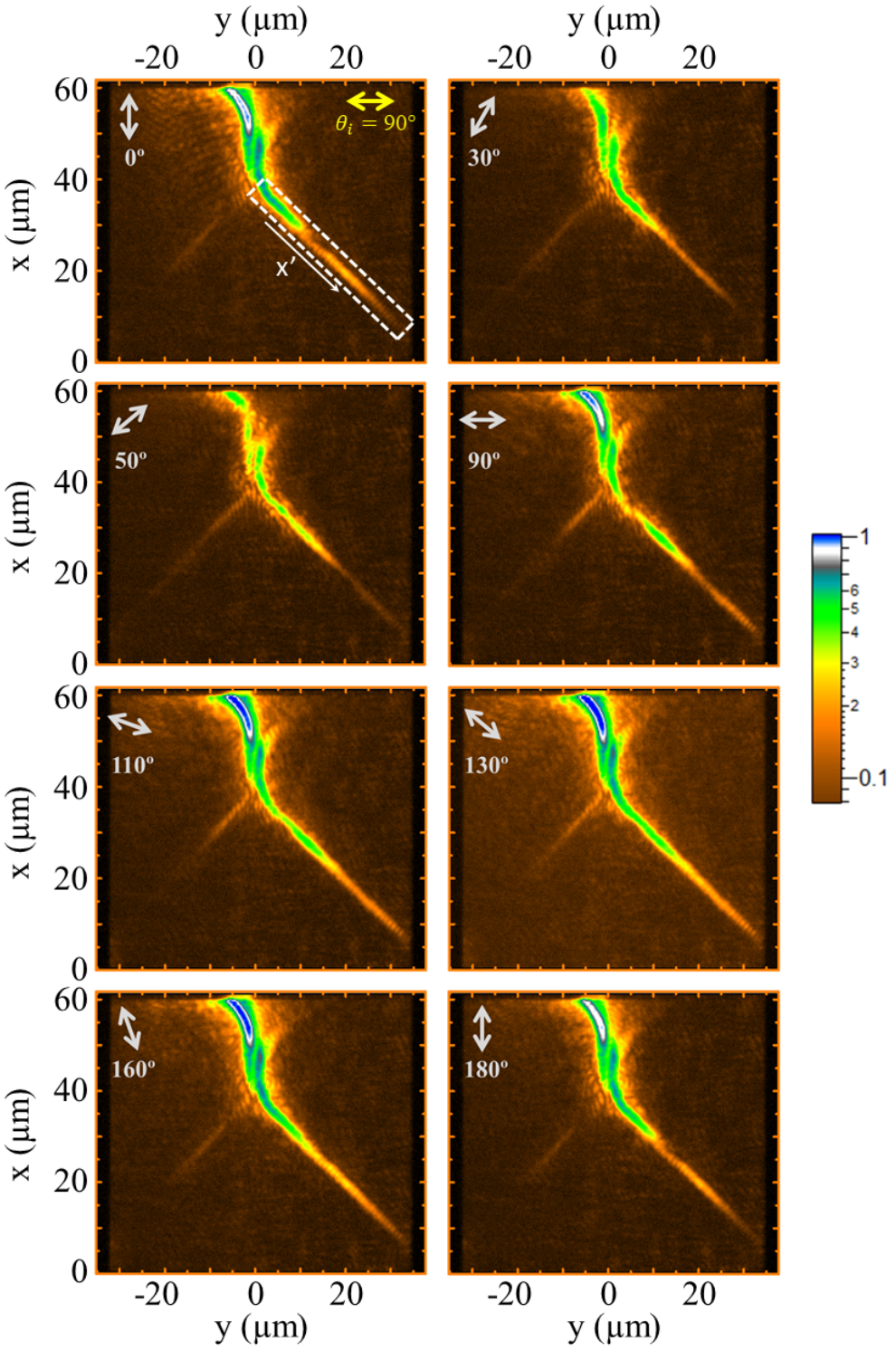

Figure 4.10. PL spectra of a coupler analyzed at different linear polarizations: θ_d =0º, 30º, 50º, 90º, 110º, 130º, 160º and 180º. The emission from the top terminals (at $x > 60$ μm) has been removed using a spatial filter. The horizontal polarization, θ_i =90º, of the excitation beam, is indicated in the first image with a yellow arrow. The white rectangle indicates the bottom-right terminal in which polarization-dependent oscillations are visible. The axis along this terminal is defined as x'. The PL is coded in a logarithmic false-color scale.

Its intensity decays considerably when analyzing the linear polarizations between 30º an 50º, however, as the angle of the polarization of the detection is further rotated, the intensity of the emission increases, reaching a maximum at ∼130º. When the polariton condensate is created in the input terminal, it propagates ballistically along the structure. Despite the fact that terminal is excited with $\theta_i = 90º$, the condensates' polarization is determined by the longitudinal direction of the input terminal, i.e., the propagation along x' [see Fig. 4.10]. Therefore, when the polarization is analyzed at an angle different to that corresponding to the x' one should expect a low intensity emission, as borne out by our experiments for the cases $\theta_d = 30º$ and 50º. By contrast, a maximum in the intensity of the emission appears when the angle for the analysis of the polarization is aligned with this direction, as in ∼130º.

After the condensate enters the coupling region, in which a polarization-dependent intensity is also observed, part of the condensate is coupled to the right arm and continues propagating through the structure. Interestingly, a new effect appears in the bottom-right terminal, in which not only intensity changes are present, but also a set of oscillations arise along the terminal. At 0º, two local maxima are clearly distinguished at $(x,y) = (30,5)$ and $(20,20)$ µm. This is in stark contrast with the emission observed at 90º, in which local minima appear at the same positions. In the intermediate polarizations, see for example 30º and 160º in Fig. 4.10, the oscillations vanish and only a progressive decay of the emission is visible. The same experiment has been performed for the incident polarizations $\theta_i = 0º$ and 135º. However, no correlation has been found between the linear polarization orientation of the excitation beam and the PL polarizations beyond the observation of a small optimization in the injection of polaritons for $\theta_i = 135º$. Therefore, it is clear that the geometry of the device plays an important role in the polarization of the PL and other factors such as a polarization inherited from the excitation, can be clearly discarded.

To fully understand the polarization effects, we focus on two main features: the dependence of the coupling of polaritons from the left to the right arm of the device and the evolution of the oscillations at the output terminal with the orientation of the detected polarization. To perform this analysis, the PL has been integrated along the coupling region, $40 < x < 50$ µm, in order to obtain the intensity distribution in both arms, which is depicted in Fig. 4.11 for four selected polarizations: θ_d =0º, 50º, 90º and 130º. Note that the y-direction is defined identically as in Fig. 4.10, and $y = 0$ marks the gap between both arms of the device. Thus, $y < 0$ coincides with the pumped terminal and $y > 0$ with the coupled one. The same dependence with θ_d is observed in both arms. A maximum intensity is obtained when the polarization is aligned with the longitudinal directions of either the coupling region or the pumped terminal, i.e. 0º or 130º, respectively. As explained for the results compiled in Fig.

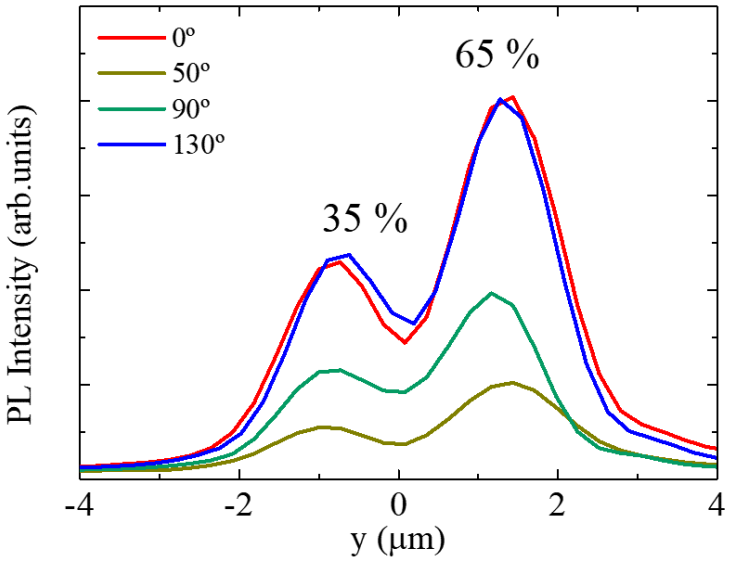

Figure 4.11. Emission spectra in the coupling region of a coupler device analyzed at four linear polarizations: θ_d =0º, 50º, 90º and 130º. The position $y = 0$ marks the center of the gap between the two arms of the device. Independently of the analyzed polarization the 65% of the emission is coupled to the right arm ($y > 0$).

4.10, the condensates' polarization is determined by the longitudinal direction of the input terminal (x'-direction). However, as polaritons continue their path and enter in the coupling region, their direction of propagation is rotated to the vertical axis. We find a maximum in the emission when the analyzed polarization corresponds to the vertical axis, i.e., θ_d =0º. The case of θ_d =130º shows a similar intensity emission than that observed for 0º, since polaritons enter in the coupling region with a polarization oriented in the x'-direction. By contrast, a minimum intensity is observed for 50º and 90º, which correspond to polarizations oriented in a different direction to that of the propagation of the condensates. The state of the polarization does not affect the proportion of the signal that couples to the right arm ($y > 0$): independently of the analyzed polarization, 35% of the population remains in the pumped terminal whereas the 65% of the population is coupled. These results reveal a preserved polarization of polaritons when they couple to the right waveguide.

We focus now on the analysis of the output terminals. We extract the profiles of the PL along the x' direction in the region marked with a white rectangle in Fig. 4.10. The resulting profiles for each analyzed polarization between 0º and 180º are compiled in Fig. 4.12(a). The zero position marks the beginning of the output terminal whereas the end of the structure is located at $x' \sim 45$ µm, as clearly evidenced by the decrease in the PL intensity signal. Two

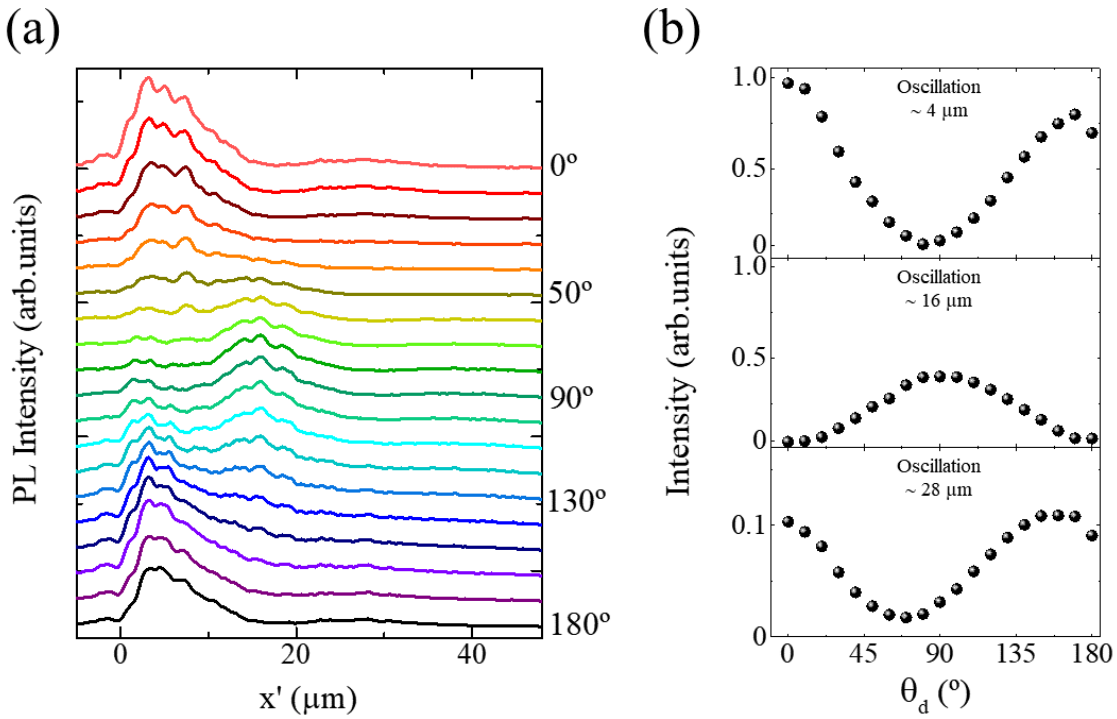

Figure 4.12. (a) Emission spectra integrated along the output terminal of a coupler device for a incident horizontal polarization. The analyzed polarization has been varied from $\theta_d = 0º$ (top) to 180º (bottom) in steps of 10º. As a guide to the eye, five of these values are indicated: 0º, 50º, 90º, 130º and 180º. (b) Normalized intensity (to the emission at $\theta_d = 0º$) of the oscillations observed in (a) centered at three positions: 4, 16 and 28 μm. The intensity has been averaged in a range of 5 μm around these values.

opposite oscillating behaviors are visible at different polarizations. For angles close to 0º (and equivalently 180º), the most intense signals are seen at the beginning of the terminal ($x' \sim 4$ μm). However, a remarkable decay of the intensity at this location is observed at angles close to 90º while, at once, a new maximum arises at $x' \sim 16$ μm.

A full characterization of the oscillating behavior observed in the emission spectra of Fig. 4.12(a) is shown in Fig. 4.12(b), where the emission intensities at three different x' are depicted for each θ_d. The intensity has been averaged in an interval of 5 μm in width around the center of three oscillations located at $x' \sim 4, 16$ and 28 μm. A similar evolution is observed for the first and third case, $x' \sim 4$ and 28 μm, revealing the same origin for both maxima of the oscillation. In the latter case, the intensity is reduced by a factor of 10, thus, it is not easily discernible in Fig. 4.12(a). In contrast to these cases, the intensity of the maximum oscillation observed at $x' \sim 16$ is clearly out of phase by 90º. In all three cases, the emission

intensity shows a progressive evolution with θ_d, in which minima and maxima are found for the different analyzed polarizations.

This pattern in the output terminal can be explained by the presence of coherent counter-propagating condensates and the interference between their corresponding WPs: one of the condensates propagates towards the end of the terminal while the counter-propagating one arises from the reflection at the edge of the waveguide. Since the coherence is maintained during the propagation and at the reflection, it is possible to observe interferences between both condensates [77]. Since BECs can be described as matter waves, we consider two waves with opposite propagation directions along the terminal ($\pm x'$).

$$\begin{aligned} \psi_1(x') &= \psi_1^0 e^{-\frac{x'}{\alpha}} e^{-i(kx'+\omega t)} \\ \psi_2(x') &= \psi_2^0 e^{-\frac{x'}{\alpha}} e^{-i(-kx'+\omega t)} e^{-i\phi} \end{aligned} \tag{4.1}$$

where ψ_1 describes the condensate propagating along $+x'$ and ψ_2 the one propagating backwards $-x'$. The initial amplitude at $x' = 0$ is indicated by $\psi_{1,2}^0$. The exponential decay of the polariton population with the traveled distance is considered in the term $e^{-\frac{x'}{\alpha}}$ where α is an attenuation constant. The wavevector and the angular frequency are introduced as k and ω, respectively. Additionally, a phase difference term ϕ is considered when the condensate is reflected at the edge of the structure. The total intensity is obtained by the superposition of both waves, which exhibits oscillations due to their interference and can be expressed as

$$|\psi_T(x')|^2 = |\psi_1(x') + \psi_2(x')|^2 = 2\psi_1^0\psi_2^0 e^{-\frac{2x'}{\alpha}} \left[1 + cos(2kx' + \phi)\right] \tag{4.2}$$

This model is quantitatively evaluated in Fig. 4.13(a), where it is compared with the profiles of the emissions analyzed at $\theta_d = 0^\circ$ and 90°. The fits of both sets of data using Eq. 4.2 are depicted by the gray and light blue lines, respectively. A similar attenuation constant is obtained in the fits, α= 10.6 μm^{-1}. Furthermore, the wavevector of the condensates given by $k = 2\pi/\lambda$, provides the same oscillating period for both interference patterns, $\lambda = 24$ µm. The variation of a single parameter is responsible for the difference between both patterns: the phase shift between the condensates. As indicated in Fig. 4.13(a), a value of $\phi = 0$ is obtained for $\theta_d = 0^\circ$ while for $\theta_d = 90^\circ$ the fit yields to $\phi = \pi$. This result implies that the analysis of the linear polarization selects a specific phase in the back-propagating condensate. Moreover, the profiles of the emission obtained for angles between $\theta_d = 0^\circ$ and $\theta_d = 90^\circ$ can be described as linear combination of these two states.

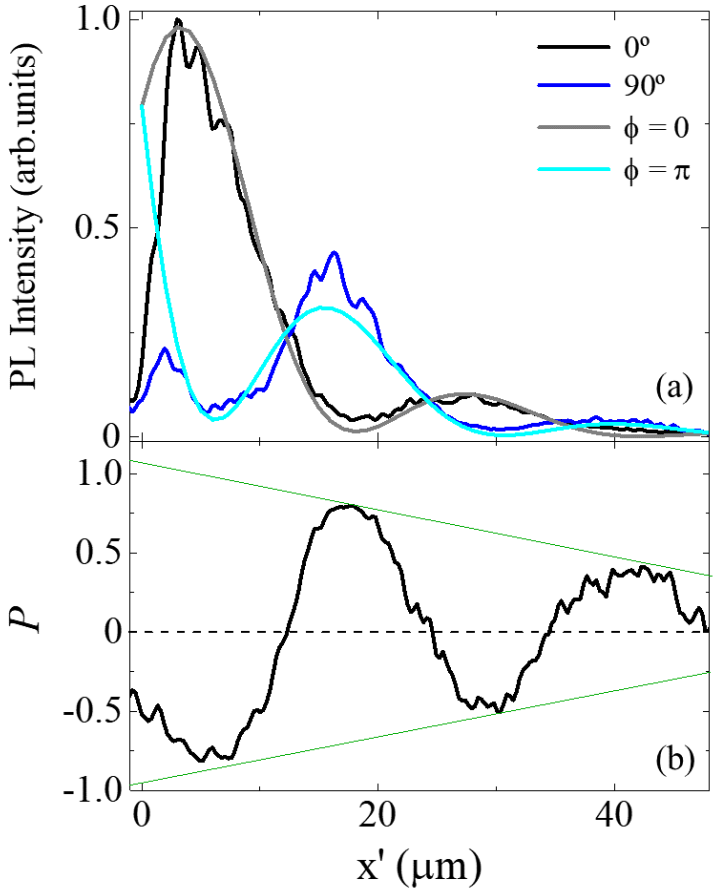

Figure 4.13. (a) Comparison of the normalized emission spectra at the orthogonal polarizations 0º and 90º. The data are fitted using the interference model described in Eq. 4.2. A phase difference ϕ of 0 and π are obtained for 0º and 90º, respectively. The parameters $\alpha = 10.6\ \mu m^{-1}$ and $k = 0.262\ \mu m^{-1}$ are common to both fits. (b) Spatial evolution of the polarization degree (P). This parameter has been calculated using Eq. 4.3 and the traces shown in (a). The green lines are a guide to the eye showing the gradual decay of the oscillating amplitude.

For the sake of completeness, the difference in the intensity of the oscillations in the emission is also investigated. To quantitatively describe the striking change observed in the polarized PL, we calculate the degree of polarization (P), which is given by,

$$P = \frac{I_{\parallel} - I_{\perp}}{I_{\parallel} + I_{\perp}} \tag{4.3}$$

where $I_{\parallel}$ / $I_{\perp}$ is the intensity of the emission when the polarization of excitation and detection are parallel ($\theta_d = 90º$) / perpendicular ($\theta_d = 0º$). Using the emissions of Fig. 4.12(a) as

input data in Eq. 4.3, the polarization degree as a function of the position x' is depicted in Fig. 4.13(b). Clear oscillations in the degree of polarization of the emission are observed along the terminal. In the first 10 µm, the emission is dominated by the 0º PL, resulting in a polarized state of -80%. As the second oscillation appears at $x' \sim 16$ µm, P rapidly increases obtaining a degree of polarization of $+75\%$. The sign inversion arises from the presence of the polarization-dependent oscillations. Furthermore, the oscillating amplitude of the degree of polarization gradually decays along the output terminal. Note that many factors influence the behavior of P, such as the presence of a counter-propagating condensate along the terminal. Determining the cause of this behavior requires a deeper analysis where all the parameters that characterize the state of polarization are considered, i.e, a complete analysis of the Stokes parameters.

4.5 Conclusions

We have evidenced the functionalities of the optical couplers under non-resonant excitation. The condensation in macroscopic states capable of traveling large distances, the coherence, the appearance of Josephson oscillations in polaritonic devices and of a defined polarization state have been successfully demonstrated in this chapter. We have investigated in detail the implications of using bent waveguides for the development of optical circuits based on polaritons. Our findings show the coexistence of multi- and single-mode propagation in these devices. In addition, we have revealed a significant decay of the polaritons' momentum as a consequence of the abrupt variation in the condensates trajectory. Furthermore, our results open the way to routing and splitting of the condensates towards different output terminals by the proper choice of the parameters defining the routers. We also reveal that counter-propagating condensates give rise to polarization-dependent interference patterns observed in the PL at the output terminals.

Chapter 5

Counter-directional polariton router

5.1 Introduction

In recent years, the interest in replacing conventional transistors with photon-based ones has increased considerably [99–101, 108, 124]. The operation frequency and power consumption of classical on-chip circuits is limited by the response of charged carriers to externally applied electric fields. By contrast, optical transistors exhibit significant benefits such as higher density of information in long connections and an important reduction of the energy required in communication networks [125]. Thus, photonic on-chip technologies for information processing, promise ultrafast operation speed and low power consumption thanks to a low loss rate.

Using nonlinear effects to design these devices is critical for a wide variety of optoelectronic applications such as signal processing for optical computing. In the literature, different approaches to optical-based transistors have been proposed. Some of these systems use laser gain [126], atoms [127] or quantum dots [128] to optically control light switching. These proposals require photons to interact and modify each others behavior, however, when two photons collide in vacuum, they do not interact, they simply pass through each other, highlighting the need of an operating medium to mediate interactions. Despite being excellent carriers of quantum information, when photons are created in a material medium, they interact weakly with themselves or their environment, thus, hindering the possibility of creating efficient photon-based logic devices [99].

Counter-directional polariton router

Strong interactions among photons can be induced using exciton-polaritons in semiconductor microcavities [12], offering a versatile platform to realize nonlinear optical technologies. Strong nonlinear properties are observed when polaritons condense, revealing their potential application in integrated optical elements [102, 129]. This fact can be used to implement high-speed photonic building blocks for information processing. Furthermore, the continuous development of high quality microcavities has enabled polaritons to travel macroscopic distances (> 100 μm) due to their effective ultralight mass, which is 4 orders of magnitude smaller than that of excitons [12, 130].

Several works have proposed the use of polariton condensates systems to realize spin-switches [116], transistors [76, 77, 106, 108], amplifiers [90, 131] and logic gates [110]. More advanced on-chip logic architectures based on the ultra-fast switching dynamics have been proposed for polaritonic circuits [103, 117]. Basic routing effects have been predicted and achieved for polaritons, which show some functionalities, but are mainly based on an active optical control via a tunable auxiliary exciton reservoir [75, 105, 132].

In this chapter, we report on an on-chip device for counter-directional propagation of polariton condensates that operates as a polaritonic resonant tunnel diode. We investigate the ultrafast dynamics of this device, consisting of two lithographically defined waveguides coupled to a microdisk, to implement polariton signal control by a photonic potential. Since it can be easily scaled to larger logic architectures without the requirement for external control parameters, we study the response when the size parameters are modified [107].

The chapter is organized as follows. In section 5.2, we present the operation of the polariton counter-directional router device with a detailed explanation of the condensates' propagation. In the following section, 5.3, we provide a theoretical model based on the stochastic Gross–Pitaevskii partial differential equation. We consider gain and loss coefficients to simulate a real Bose-Einstein condensate propagating though the device. Additionally, the effect of the size parameters in the polariton propagation is analyzed in section 5.4. We study in detail the emission of the device's exit waveguide, which exhibits a peculiar propagation when the size parameters are reduced. The conclusions of the experiment are outlined in section 5.5.

5.2 Polariton propagation in a counter-directional router

To date, we have witnessed a variety of demonstrator experiments for on-chip steering and manipulation of the movement of coherent polariton condensates, including condensates propagating along waveguides [54, 77, 89]. In our case, to implement a routing functionality, a symmetric design of the device is proposed: two planar waveguides are attached to opposite sides of a microdisk. By determining the photonic potential of these elements, the propagation direction of a polariton flow can be reversed. In this section, we describe the propagation along this device, acting as a counter-directional optical router: condensates are confined in 1D in the waveguides, while in the microdisk they are allowed to move in 2D.

The device has been sculpted in a GaAs-based microcavity. The investigation in this section focuses on the functionalities of a router with size parameters corresponding to 4.5 μm for the waveguide width and 40 μm for the disk diameter. Further details about the sample can be found in section 2.2.3. We focus the excitation laser beam on the sample using a microscope objective with NA= 0.42 and $f = 10$ mm. As a result, a diameter of 3 μm (FWHM) is obtained. We pump non-resonantly the input waveguide at an energy tuned to the first reflectivity minimum of the microcavity, 1.543 eV, and at a distance of 30 μm from the microdisk center, so that condensates are accelerated in the waveguide before they enter the central disk. In order to study the dynamics in the router, the excitation has been performed using a laser beam with a pulse duration of 2 ps and a power density above threshold for condensation, 18.4 kW/cm^2. To reduce the sample heating produced by such high excitation power, the laser beam is mechanically chopped with a ratio of 1:12 (bright:dark) and a frequency of rotation of 8000 rpm. The experimental measurements have been carried out at a fixed temperature of 12 K.

A real-space map of the polariton flow along the device is shown in Fig. 5.1(a). To improve the visibility of the propagating mode, the image is resolved at the energy of the traveling condensates, E = 1.5316 eV. The intensity of the top part of the image ($y > 45$ μm) is reduced by a factor of 10 by means of a neutral density filter. The white circle indicates the position of the excitation spot at $x \sim 45$ μm in the input waveguide. A similar process to that described in chapter 3 is observed when polariton condensates are created: due to the confinement along the y-direction in the waveguide, as soon as the condensates are formed, they are driven simultaneously towards the positive (right) and negative (left) x-direction. Two horizontal trails can be observed along the input waveguide. They originate from the coexistence of two propagating modes, with parallel paths, allowed by the width of the guide. When the flow generated by the excitation beam reaches the junction with the microdisk, it experiences a

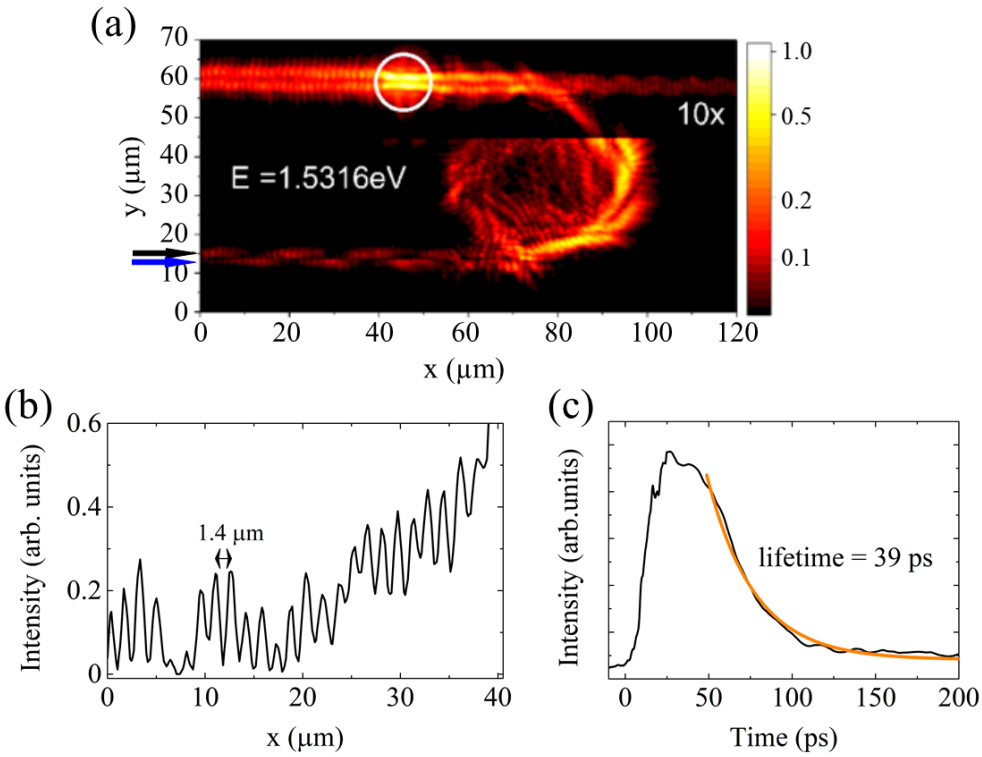

Figure 5.1. (a) Real-space image of the condensate propagating through the microdisk device. A neutral density filter (factor of 10) was present for the region $y > 45$ μm. The white circle indicates the position of the excitation spot. The emission is filtered at an energy of 1.5316 eV. (b) PL profile at the input waveguide integrated in the range $58 < y < 62$ μm. The oscillations observed in the profile show a period of 1.4 μm. (c) Decay curve of the emission measured at the excitation point of the input waveguide. The orange line shows an exponential decay fit to the data from which a lifetime of 39 ± 5 ps has been obtained.

deviation of its trajectory. The ingoing flow is transmitted to the microdisk since its energy is resonant with an allowed energy state in the 2D structure. As a result, close to 70% of the flow is guided by the photonic potential created by the disk structure. Polaritons rotate inside the disk due to internal reflections and reach the junction with the output waveguide at $y \approx 20$ μm. At this point, the flow is divided between those that continue the circular path within the disk and those that are redirected to the output waveguide. In the latter, the condensates propagate along the opposite direction to those injected at the input port, evidencing the routing capability of the structure. Note that due to the symmetry of the device, no matter which is the chosen injection port, polaritons will be guided to the output waveguide with reversed propagation momentum. We obtain a coupling efficiency of the device of $\sim 11.5\%$, defining it as the ratio between the emission just before the polaritons entrance into the microdisk and that just after their exit from the disk.

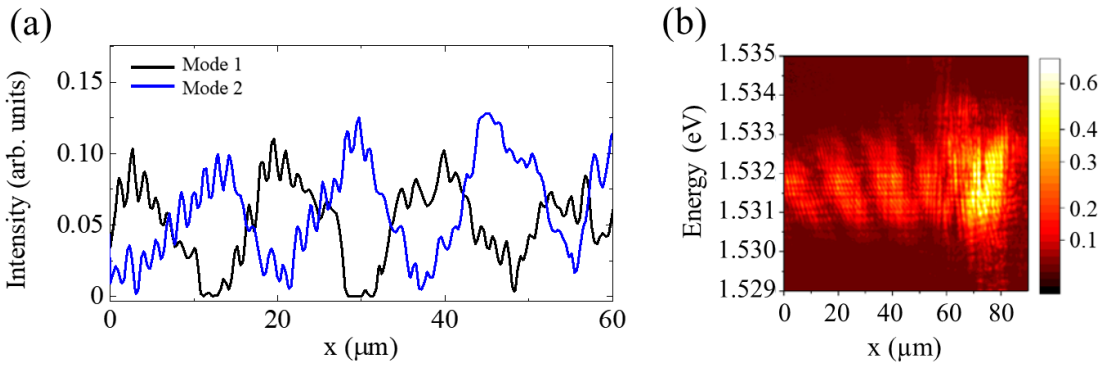

Figure 5.2. (a) PL profile of the modes 1 and 2 extracted at the position of the black and blue arrows, respectively, in Fig. 5.1(a). (b) Energy vs. real space-resolved signal extracted at the position of the mode 1. A clear tilt of the fringes is observed.

A clear interference pattern can be observed throughout the two waveguides. The profile of the emission taken along the input guide is shown in Fig. 5.1(b), which has been integrated in the interval [58, 62] μm along the y-direction. This pattern is caused by the interference between the forward propagating polaritons and those propagating backwards [91, 133, 134], after being reflected at the end of the guide at $x \approx 0$. To study these fringes, a Fourier analysis of the pattern has been performed, revealing a periodicity of 1.4 ± 0.1 μm and a constant amplitude of the stationary pattern along x. The high contrast of the interferences compared to the gradually attenuating background emission as one approaches to the end of the guide suggests a large reflection coefficient. On the right side of the structure similar fringes with lower amplitude are also observed. To produce the interference shown in Fig. 5.1(b), polaritons need to traverse the length of the guide from the excitation spot where they are generated (~ 50 μm), and return to observe interference in the full range of the structure.Time-resolved measurements reveal a condensate velocity of 6 μm/ps in the structure. As a consequence, polaritons need to survive a minimum time of the order of 17 ps. We can estimate the polariton lifetime from the temporal decay of the emission integrated in the excitation area. Fig. 5.1(c) depicts the PL at the input waveguide as a function of time. At ~ 30 ps after the laser pulse excites the device, a maximum in the emission is observed. The signal rapidly decays, vanishing at ~ 125 ps. Beyond this time, the intensity of the signal is comparable to the background noise, evidencing the finite life of the condensates. An exponential decay fit to the data, indicated by the orange line, provides a polariton lifetime of 39 ± 5 ps. This value is comparable to those reported in the literature for etched waveguide structures, where lifetimes of 17 ± 1 ps have been found [75–77], with propagation lengths of the order of 100 μm.

Interestingly, at the output waveguide, a clear mode beating pattern is observed. This effect is created by the disk resonantly feeding a superposition of two different modes in the outcoupling region. In order to investigate these states in more detail, we select a cut through mode 1, at $y = 15$ µm, and mode 2, at $y = 13$ µm, indicated by the black and blue arrows in Fig. 5.1(a), respectively. Both profiles are plotted in Fig. 5.2(a). The analysis of the intensity distribution reveals a similar long oscillation period for both modes, $T_m = 18 \pm 1$ µm, with a π phase shift between them. Furthermore, a similar interference pattern, with a much shorter period, as the one shown in Fig. 5.1(b) is superimposed to the emission of the modes. The interference pattern is distorted in both modes above 30 µm. After crossing the entire device, the condensate is close to the end of its life span and experiences a significant loss of the coherent condensed population, which is responsible for the disappearance of the fringes. This has been already seen in chapter 3 where a maximum of 10% of condensed population has been observed. In the output guide, the condensate travels from $x = 60$ µm, where it couples in the disk, to $x \sim 0$ µm, where the edge is located, and bounces back, making a total path of ~ 120 µm in the output waveguide. Note that the total distance traveled by the condensate is much larger, since it has traversed the entire device. The coherent population is not able to survive the large distance traveled in the output waveguide, so the fringes begin to fade when they exceed 90 µm of the path, that is, $x > 30$ µm.

The energy-resolved emission as a function of x in the outcoupling region is shown in Fig. 5.2(b) for mode 1. The emission displays a tilted pattern evidencing a change of the oscillation period with the propagation energy. For an energy of 1.5316 eV, a period $T_m = 17 \pm 1$ µm is obtained, which is in agreement to that obtained from Fig. 5.2(a). However, larger (smaller) periods are observed at higher (lower) energies, obtaining for example $T_m = 15 \pm 1$ µm at 1.5305 eV. A total variation of 25% is measured in the full range of the propagation energies. This behavior is a direct consequence of the change in the wavevectors of the competing modes along their dispersion. A similar effect was reported in 1D waveguides by Antón *et al.*, where a series of oscillations in the Stokes parameters S_y and S_z were observed across the PL energy revealing that polaritons with higher energies traveled at higher speeds [118].

We focus now on the propagation dynamics along the device. As we have mentioned, exciton-polaritons exhibit interesting characteristics due to their light-matter nature; a core property is their ultrafast dynamics while still possessing matter characteristics. To analyze the polariton dynamics, we obtain the real-space maps at given time delays. Fig. 5.3 summarizes a series of such measurements for a time window of 140 ps. Initially, polaritons are selectively injected in the waveguide and approximately 20 ps after the arrival of the excitation pulse, see Fig. 5.3(a), the condensates propagate along the waveguide. At $t = 30$ ps [panel (b)], the

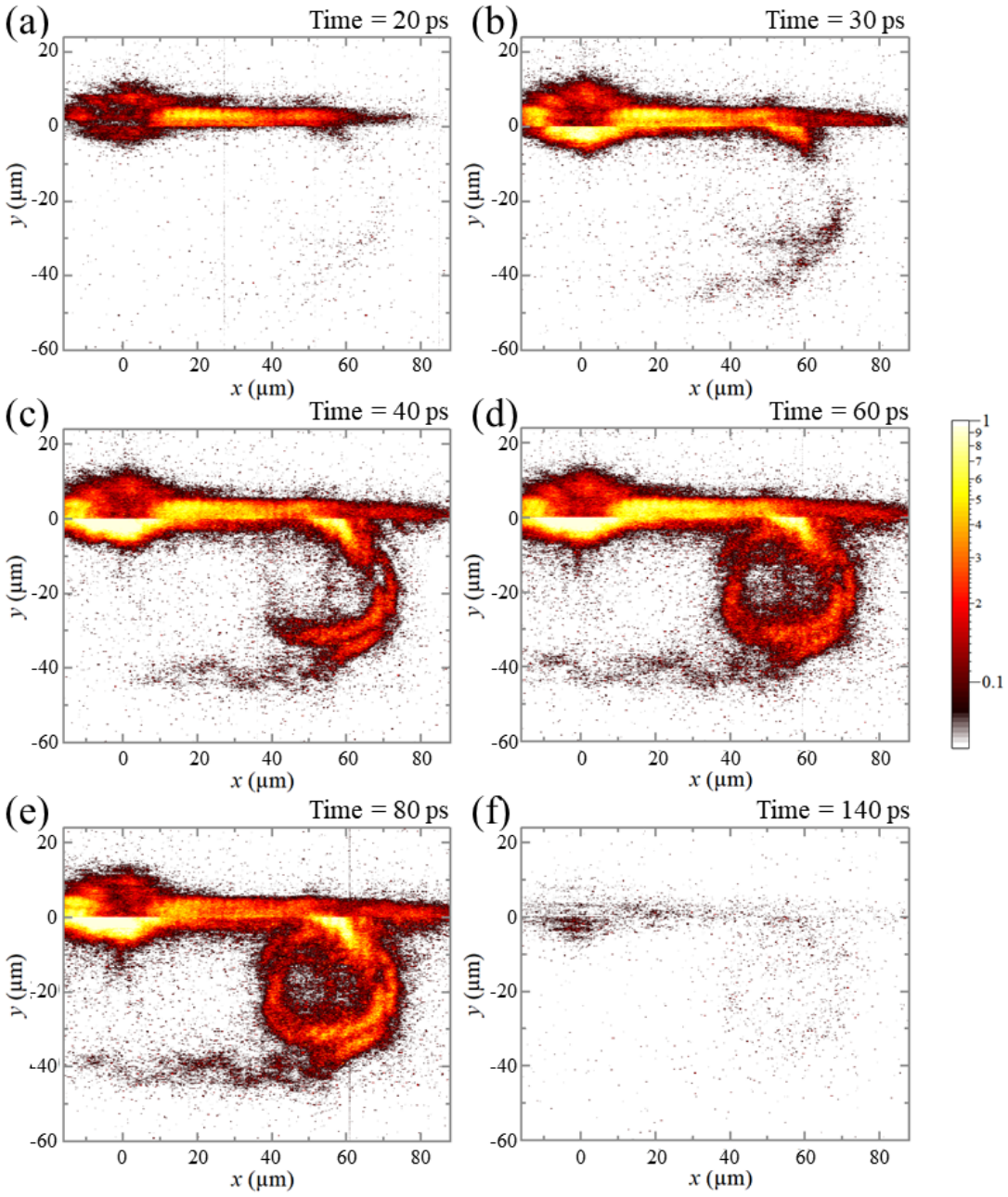

Figure 5.3. Time-resolved series of the polariton propagation along a microdisk device for an energy of 1.5314 eV. $y = 0$ indicates a change in gain of the streak camera, for negative values of y the emission is multiplied by a factor of 3. The spatial emission distribution at t$= 20 - 30$ ps shows polaritons starting to propagate along the input waveguide. At 40 ps, the emission reveals that polaritons have arrived at and crossed through the microdisk to the other adjacent waveguide. At 60 ps, the disk shows a circulating mode pattern and oscillations become visible at the exit waveguide. At 80 ps, the oscillations are apparent at the exit port. At 140 ps, most of the polaritons have decayed and the dynamics has ended.

polariton flow reaches the junction with the disk; while 30% of the flow continues traveling along the guide, 70% of the signal couples to the microdisk. The splitting of the population is in accordance to that observed in Fig. 5.1(a). A remarkable difference is observed in the distance traveled by both populations: the coupled signal shows a shorter trail due to a possible reduction of the condensates' momentum during this process. After the flow completes half a turn on the disk structure, it couples into the exit waveguide at $t = 40$ ps [panel (c)]. As shown in panel (d), most part of the flow remains in the central structure, completing an entire lap, while a small fraction of the population ($< 10\%$) travels throughout the exit guide. The direction of propagation of polariton condensates has been reversed by the action of the microdisk, confirming the router functionality of the device. The modes 1 and 2 are apparent between 60 and 80 ps [see panel (e)]. The visibility of this oscillation is lower than in Fig. 5.1(a) due to the time-resolved character of the image. Finally, at 140 ps, panel (d), the polariton dynamics inside the device has ceased due to polariton's finite lifetime of the order of 39 ps outside of the reservoir.

Note that up to 60 ps, a set of small fringes with a periodicity of 1.3 ± 0.4 µm is clearly visible in the input waveguide. These fringes arise even when polaritons have not reach the end of the waveguide, as evidenced at 20 ps. Thus, at short times, the interference originates from the backscattering produced by polaritons colliding near the coupling junction, at $x \sim 55$ µm in Fig. 5.3.

5.3 2D Ginzburg-Landau model

When a laser beam impinges on a semiconductor microcavity with a very low power density, the polariton relaxation from the excitonic reservoir to the fundamental state in the LPB is inefficient due to low cross-section of polariton-phonon scattering. Thus, polaritons are not thermalized. By contrast, when the power is considerably increased, a massive occupation of the fundamental state to which polaritons have relaxed takes place, creating a Bose-Einstein condensate. Ideally, under these circumstances, polaritons should exhibit a well-defined temperature and phase transition obeying a Bose-Einstein distribution [17]. However, in a real system, the exciton-polariton scattering becomes dominant in the relaxation process from the reservoir to the LPB [31]. A direct consequence of this scattering is the simultaneous occupation of several states with different k-vectors. Therefore, polariton condensates are defined as non-equilibrium systems. If the excitation power is increased well above the condensation threshold, a balance is created between the losses in the condensates and the

gain caused by the continuous feeding from the reservoir, establishing a direct analogy between a BEC system and laser emission.

The k vectors at which polariton condensation occurs are determined by the photonic potential of the microcavity. The design of this potential allows the formation of several discrete polariton levels, in which condensation can be produced simultaneously at different levels. This results in a multimode polariton emission. The theoretical model described in this section ignores the different polariton levels and focuses on single mode propagation. Driven-dissipative Bose-Einstein condensation in exciton-polariton systems can be modeled at a mean-field level by introducing the effect of pumping and losses in the Gross-Pitaevskii model. This results in the time-dependent complex Ginzburg-Landau (GL) equation, which is one of the most-studied nonlinear equations in the field of physics. It typically describes phenomena from nonlinear waves to second-order phase transitions, superconductivity, superfluidity and BEC [135]. Indeed, it has been specifically employed to describe the momentum distribution and propagation of non-equilibrium systems such as the one considered in this chapter. Thus, the theoretical approach to this equation considering the gain and losses in the macroscopic polariton field ψ is given by,

$$(i-\eta)\,\hbar\partial_t\psi = -\frac{\hbar^2}{2m}\Delta\psi + U(x)\,\psi + i\chi\psi + \left(\alpha_s - \frac{i\hbar}{2}\Gamma\right)|\psi|^2\psi \tag{5.1}$$

The equation shows different linear and nonlinear ($|\psi|^2$) terms contributing to the polariton condensate's propagation. On the left-hand side of the equation, a phenomenological energy relaxation rate that models the inelastic phonon scattering characteristic of nonresonant excitation is defined as $\eta = 10^{-2}\gamma$. The first term on the right-hand side of the equation determines the kinetic energy of the condensate. $U(x)$ defines the potential landscape originating in the photonic confinement of the etched structures. Note that due to the peculiar shape of the device, this confinement is different in the waveguides (1D) and in the microdisk (2D). α_s is the polariton scattering strength. The complex coefficients in the equation have important physical meanings in the dynamics of BEC systems; $\chi = \hbar(P-\gamma)/2$ is the net gain and is represented by the balance between the nonresonant optical excitation (P) and the polariton loss rate of a single condensate (γ). The modes with $\gamma > P$ experience loss, while the ones with $P > \gamma$ are amplified. Another important nonlinear contribution is the gain saturation magnitude, defined by the Γ parameter. If a system with physical stability is considered, the parameters m, η, α, Γ should be positive. The effect of the critical temperature is also present in Eq. 5.1. Near T_C the formation of the condensate becomes unstable and vanishes, thus, the pump rate equals the losses of the system and the net gain results zero.

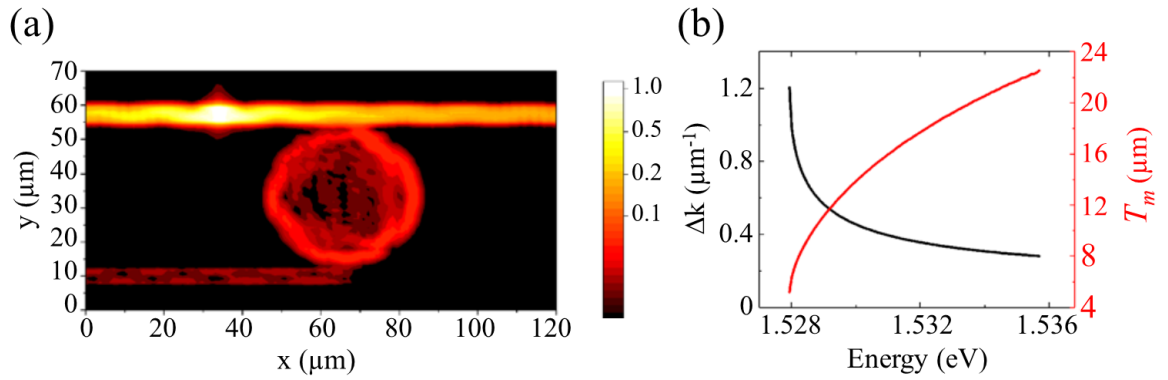

Figure 5.4. (a) Simulated plot of the intensity distribution and pattern mode. The excitation point is located at a similar position than in the experiment: 30 μm of distance from the center of the microdisk. (b) Theoretical oscillation frequency (black) and period T_m (red) dependent on propagation energy.

Consequently, the interaction strength drops to zero, resulting in the disappearance of the complex terms in the equation.

We, in collaboration with Dr. H. Flayac, from the École Polytechnique Fédérale de Lausanne (EPFL), who made the actual calculations [107], use this model to simulate the propagation of the polariton condensates along the device. The same conditions as in the experiment are emulated: the upper waveguide is initially excited at a distance of ~ 30 μm from the microdisk above threshold for propagation. The result of this model is depicted in Fig. 5.4(a) for a simulation of the whole device. The realistic values for the parameters used in the simulations are: $\alpha_s = 10^{-3}$ meV μm and loss rate $\gamma = 5 \times 10^{-2}$ ps^{-1}. We define the energy relaxation rate and the gain saturation magnitude proportional to γ, $\eta = 10^{-2}\gamma$ and $\Gamma = 0.1\gamma$. In this case, the potential $U(x)$ has been taken as the nominal layout of the etched structure where the waveguide width is 4 μm and the disk width is 40 μm. The laser source used in the experiment exhibits a gaussian intensity distribution, which we introduce in the simulation as an excitation profile of

$$P(x) = 50\gamma e^{\frac{-(x-x_0)^2}{dx^2}} e^{\frac{-(y-y_0)^2}{dy^2}} \tag{5.2}$$

with $dx = dy = 2.5$ μm. The confinement in the waveguides is higher in the y-direction than along the x-direction, where the condensates move without restriction. Therefore, when polaritons are selectively injected at the top guide, two flows can be distinguished from the excitation spot, one moving towards the left and one towards the right. The latter one is guided into the microdisk and rotates inside due to internal reflections. When polaritons reach the bottom part of the microdisk, the population is divided between those who are redirected

to the bottom guide and those who continue the circular path within the structure. Note that the presence of the microdisk reverses the propagation of the condensates, therefore, the flow at the bottom waveguide is directed to the left.

The slight discrepancies between the simulation [Fig. 5.4(a)] and the experimental results [Fig. 5.1(a)], stem from the dominance of the first excited state in the experiment and its faster decay rate. However, we note that the simulated intensity distribution at the microdisk and the bottom waveguide, which is the focus of this study, match well with the experimental one.

The oscillations observed at the output guide are also studied in detailed. The theoretical oscillation frequency (Δk) and its period as a function of the propagation energy are shown Fig. 5.4(b). They have been extracted from a fit of the two polariton branches of modes 1 and 2. The plot evidences the tilt of the oscillation period at different energies, as expected from the oscillations observed in Fig. 5.2(b). A period of $T_m = 16.2$ µm is theoretically predicted at 1.5316 eV, which is in good qualitative agreement with the measurements of modes 1 and 2 ($T_m = 17 \pm 1$ µm). We must emphasize that the observed effect is only visible for a waveguide wide enough such that the energy of a second transverse mode inside the waveguide overlaps with the energy resonant in the microdisk.

5.4 Engineering size parameters

The engineering of the structural size allows to additionally evidence the use of the counter-directional router as a polaritonic resonant diode. To demonstrate this application, in this section, we investigate the effect of higher confinement on the device through the variation of certain parameters such as the microdisk diameter and the waveguide width. By decreasing these parameters and using specific propagating modes, the router can be used as an energy filter obtaining a monochromatic signal at the output guide. Polaritons are only guided through the device if the energy levels at the waveguide are resonant with an allowed band of the microdisk, therefore, this layout allows tunneling or blocking the signal at the junction between both structures. For that reason, the disk diameter is chosen such that a high degree of discretization is observed in the mode structure to achieve a fine selection of the propagation energy.

As seen in this chapter, the analysis of the polariton dynamics in real-space provides an insight of the propagation and the origin of the interference fringes along the device. However, an analysis of the momentum-space obtains detailed information about the device operation.

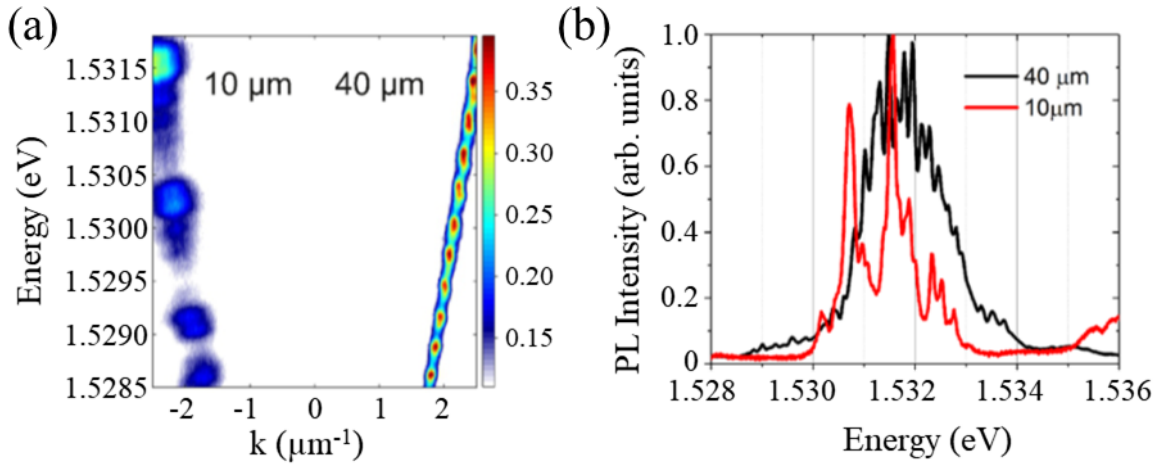

Figure 5.5. (a) Angle-resolved emission under low power excitation of microdisks with a diameter of 10 µm and 40 µm. To summarize and compare the results, only negative (positive) k values are shown for the 10 µm (40 µm) microdisk. (b) Energy-resolved emission in real-space of the condensate exiting at the junction of the microdisk and the exit waveguide. Both spectra are normalized.

A typical comparison of the dispersion bands displaying the polariton modes for two different microdisk structures is depicted in Fig. 5.5(a). The emission is obtained at very low power density, below the threshold for condensation. Since it is well-known that the dispersion band is symmetric in k, for a diameter of 10 µm (40 µm) only negative (positive) k values are shown. In etched cavities, photons are confined vertically by the DBRs and laterally by the index of refraction contrast between the air and the semiconductor. In the case of the waveguides, the lateral confinement is performed only along one direction (y) while keeping one degree of freedom along which polariton can move (x). In microdisks, the lateral confinement occurs in both dimensions, acting as a 2D trap. Therefore, the number of modes is restricted by the confinement in the microdisk. As expected, a stronger discretization of the photonic modes is clearly visible for the smaller diameter case (10 µm) in Fig. 5.5(a). For larger diameters, i.e. lower confinement, the frontier between isolated states and a continuum in the dispersion is not evident.

For the sake of comparison, we study the real-space emission when the power density is increased moderately above the threshold, so polariton condensates propagate along the device. We measure the energy-resolved PL, analyzed at the exit port inside the microdisk. The normalized PL intensity as a function of the energy is depicted in Fig. 5.5(b) for both diameters (10 and 40 µm). An evident change in the shape of the PL is observed for the two diameters: while for 40 µm the spectrum displays a nearly continuous band, a discretized emission is apparent for the smaller disk. Thus, significant differences in the polariton

propagation can be found when the microdisk diameter is reduced. The 40 μm disk does not exhibit a predominant energy, it reveals a broad energy spectrum. This spectrum is generated by several modes close in energy, eventually overlapping, coalescing into a broad energy mode. By contrast, in the 10 μm spectrum, two prominent peaks can be distinguished at 1.5307 eV and 1.5315 eV with intensities of 0.8 and 1, respectively. Between these maxima, the transmission rapidly decays by $\sim 75\%$, evidencing the presence of isolated energy levels as a result of the high confinement in the microdisk. An overall energy shift between both emissions is observed due to a slightly different detuning between the devices.

Now, we analyze in detail the discretized emission observed in the smallest microdisk. In this case, a counter-directional router with 10 μm diameter is coupled to 2 μm wide waveguides. In order to compare the isolated modes observed in the emission, we filter two different energies with high and low transmissions, from the disk to the exit waveguide, at 1.5307 eV and 1.5310 eV, respectively. The real-space maps under these conditions are summarized in Fig. 5.6(a), in which the top and bottom panels correspond to each energy, respectively. In both cases, interference fringes similar to those observed in Fig. 5.1(a), appear along the input waveguide. In the first case, when 1.5307 eV is selected (top panel), a propagating mode is observed through the microdisk, which couples to the exit waveguide. However, when 1.5310 eV is selected (bottom panel), no propagating modes are found, resulting in a lack of signal at the exit waveguide. Note that, even though in the two cases polaritons condense and propagate when a high excitation power is applied, the device does not exhibit the same behavior: when the condensate reaches the junction with the disk ($x \approx 43$ μm), no splitting of the population is observed between the input guide and the disk for 1.5310 eV. As a consequence, the entire generated population travels to the end of the input guide, showing higher intensity in the emission at this point: a remarkable difference in the emission intensity of this guide is observed between both energies at $x \sim 50$ μm. Hence, this device demonstrates the possibility to control the polariton propagation by selecting the appropriate energy, so there can be either propagation (top) or blockade (bottom).

We have proved that the propagation can only be observed in specific modes, while others are blocked due to the mode structure imposed by the photonic potential of the microdisk. To further illustrate this point, we collect the real-space PL at the exit guide in Fig. 5.6(b). The dashed black arrows indicate the energies shown in Fig. 5.6(a). A maximum in the emission is observed at the position of the disk junction. Propagation appears at two particular energies corresponding to maximum transmission peaks. For 1.5307 eV emission arising from polaritons coupled to the exit waveguide is observed. Moreover, another mode can be identified at 1.5316 eV, which corresponds to the case shown in Fig. 5.1(a). However, in the

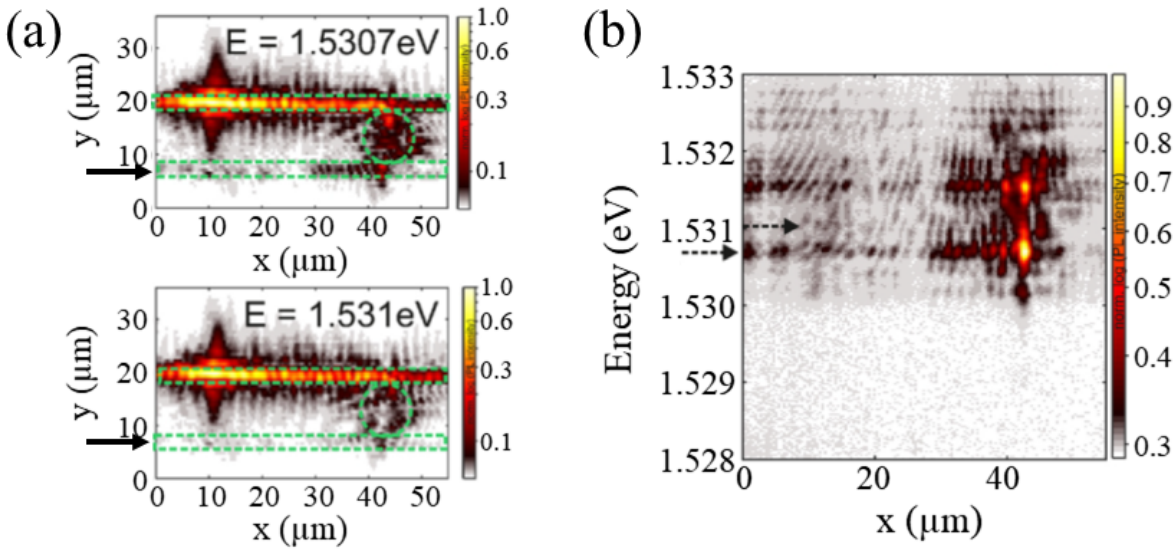

Figure 5.6. Real-space emission of the device with a 10 μm microdisk. (a) *Top:* Real-space map filtered at 1.5307 eV depicting the propagation of one mode through the disk into the bottom waveguide. The device layout is indicated by the green dashed lines. *Bottom:* Condensate propagation out of resonance with the microdisk mode, 1.5310 eV. In this case, no counter-directional coupling is observed. (b) Energy-resolved emission along the exit waveguide. The dashed black arrows mark the energies shown in (a).

case of 1.5310 eV, no signal is present along the exit guide, which evidences the potential of the device as an energy filter. This structure therefore enables mode selection in combination with flow direction manipulation for a polariton condensate, all without any external control parameter.

5.5 Conclusions

In this chapter we have demonstrated the possibility of creating an ultra-fast polariton counter-directional router. The device, based on an arrangement of 1D and 2D photonic confinements, allows polariton condensates to be coupled and guided through the circuit, reversing the propagation direction. This has been evidenced by a series of PL measurements involving energy- and time-resolved techniques, laying out the device capabilities. Additionally, a theoretical model that considers a driven-dissipative BEC system has been proposed to support our findings. It emulates successfully the propagation along the device and the presence of the oscillations arising at the exit waveguide. Furthermore, the design of the waveguide width and the microdisk diameter along with specific propagation modes allows the selection of discrete energies. As a result, for small size parameters, the router device operates as a polaritonic resonant tunnel diode, obtaining a monochromatic output signal.

As we have seen in this chapter, the configuration of these type of devices is easily scalable and integrable into polariton based logic networks. The study of these quantum fluids of light paves the way for harnessing their non-linearity in next generation photonics, for example, in the implementation of topologically non-trivial polariton networks based on coupled disks and waveguides [136].

Chapter 6

Landau levels in strained honeycomb lattices of photonic resonators

6.1 Introduction

In 2004, A. Geim and K. Novoselov reported for the first time the isolation of a single layer of graphene consisting of carbon atoms arranged in a 2D hexagonal lattice [137]. This exceptional feat along with their groundbreaking experiments led them to win the Nobel prize in physics in 2010. A great interest in this material rapidly arose and the observation of exceptional properties such as a high electron mobility, zero gap energy or a width thinner than a traditional 2D electron gas made graphene a rising star in material science. Consequently, a plethora of studies focused on the electronic and transport properties can be found in the literature (here some reviews are mentioned [79, 138–140]). While the electronic bands in semiconductors tend to show a quadratic dispersion, graphene exhibits a linear dispersion in the conduction and valence bands touching at the so-called Dirac points. This remarkable feature implies that electrons behave as relativistic particles with zero rest mass in the vicinity of the Dirac points. A similar singularity can arise in many other 2D materials, however, they are typically anisotropic and require a careful tuning of the lattice parameters to obtain symmetric and defect-free conditions. These conditions are easier to find in materials with triangular symmetry like honeycomb lattices. Hence, the search for graphene emulators in systems with a larger degree of control of the lattice geometry has attracted a lot of attention.

Landau levels in strained honeycomb lattices of photonic resonators

Polariton honeycomb lattices formed by semiconductor micropillars offer an interesting platform to emulate the transport and topological properties of graphene. They allow to control of the onsite energies, the nearest-neighbours coupling and grant direct access to the dispersion and wave functions by simple PL experiments due to the photonic nature of polaritons [141, 142]. Moreover, these systems offer the possibility of designing the lattice parameters and studying the Dirac physics in momentum-space in regimes that can not be easily reached in natural graphene. For instance, an aspect of particular interest in graphene consists of an observable integer quantum Hall effect (QHE) even at room temperature [79, 138, 143]. A proposal by Guinea *et al.* suggests that a specific distribution of strain results in a strong artificial magnetic field ($\vec{\mathfrak{B}}$) leading to the QHE [144, 145]. Different studies have attempted to reproduce this effect, however, the inability to achieve the highly anisotropic $\vec{\mathfrak{B}}$ distribution required to do so has hindered the observation of significant changes in graphene's bands [146, 147].

In an individual micropillar, polaritons are confined in the three directions in space, resulting in a discrete spectrum. However, when extending the micropillars to periodic structures, polaritons are able to tunnel from one micropillar to the other, which allows to engineer the polariton energy bands. The first two-dimensional polariton structure fabricated in fully etched microcavities was the honeycomb lattice [148], which shares the same geometry as graphene and therefore, the same dispersion. Thus, these quantum emulators of graphene brings the Dirac physics to photonic systems. Even though photons are barely sensitive to a real $\vec{B}$, it has been shown that the strain engineering creates an artificial valley dependent field [149]. We explore the implementation of a gauge field in polariton honeycomb lattices since the modulation of the hopping amplitude between two sites of the lattice permits the creation of uni-directional strain.

In this chapter, we investigate the emergence of discrete Landau levels in the band structure of a honeycomb lattice under the effect of a gauge field. We first comment the basis of the quantum Hall effect in section 6.2. Following the proposal of Guinea *et al.* on how to implement a gauge field engineering the lattice parameters [144], we describe a theoretical prediction of the experiments in section 6.3. The experimental observation of Landau levels in a polariton honeycomb lattice by modulating the hopping amplitude, together with a comparison between different strains, constitutes the main topic of the chapter and is adressed in section 6.4. Finally, in section 6.5, we summarize the main conclusions of the experiment.

6.2 Quantum Hall effect in a 2D gas

The quantum Hall effect is one of the most outstanding condensed-matter effects discovered in the 20th century. When 2D systems are subjected to strong magnetic fields and low temperatures, the Hall conductivity (σ_H) ceases to depend linearly on the magnetic field. At high magnetic fields, a quantization of the Hall conductivity emerges which is given only by fundamental physical constants,

$$\sigma_H = n\frac{e^2}{h} \tag{6.1}$$

The filling factor n takes an integer (1,2,3...) or a fractional ($\frac{1}{2}, \frac{1}{3}, \frac{2}{3}$...) value corresponding to the integer and fractional quantum Hall effect, respectively. In 1980, Klitzing *et al.* reported the first experimental demonstration of the QHE in an electron gas at the interfaces of a silicon-based MOSFET (metal-oxide-semiconductor field-effect transistor). They proved that the Hall conductivity was indeed exactly quantized, evidencing the integer QHE [150]. The recording of the measurements in the MOSFET device at a fixed magnetic field of 18 T and a temperature of 1.5 K is shown in Fig. 6.1 as a function of the gate voltage V_g. Note that the electron density is proportional to V_g. The inset illustrates a scheme of the device with several contacts, however, the sake of simplicity, we focus only on the Hall and potential probes. The voltage U_{PP}, measured between the potential probes, is directly proportional to the longitudinal resistivity of the device and shows an oscillating tendency with its amplitude gradually decaying with increasing V_g. At different electron densities, a counter-intuitive vanishing of the resistivity is observed. This decay isolates different working regions of the MOSFET device, defined by n in Fig. 6.1. Additional local minima due to the spin and valley degeneracy are clearly seen. At the same points where the resistivity drops to zero, the Hall voltage U_H, proportional to the Hall resistance $R_H = 1/\sigma_H$, exhibits different plateau regions, where it remains constant with V_g. The value of R_H in the plateaus is given by h/e^2 divided by an integer n. Another peculiarity of this effect is that the height of the plateaus depend on the quanta of conductance e^2/h. The QHE represents a highly accurate method for determining this constant of vital importance in quantum electrodynamics. Therefore, Klitzing *et al.* observed a quantized Hall conductivity, corresponding to Eq. 6.1. Furthermore, the magnetic field produces quantized energy levels known as Landau levels. The number of states, N_L, within each Landau level is given by $N_L = eB/h$. In the case of a 3D gas, the electron energy form k-dependent bands. However, in a 2D gas, the allowed energy states become discrete flat bands with equal energy gap between the different Landau levels. This particular case is shown in detail below.

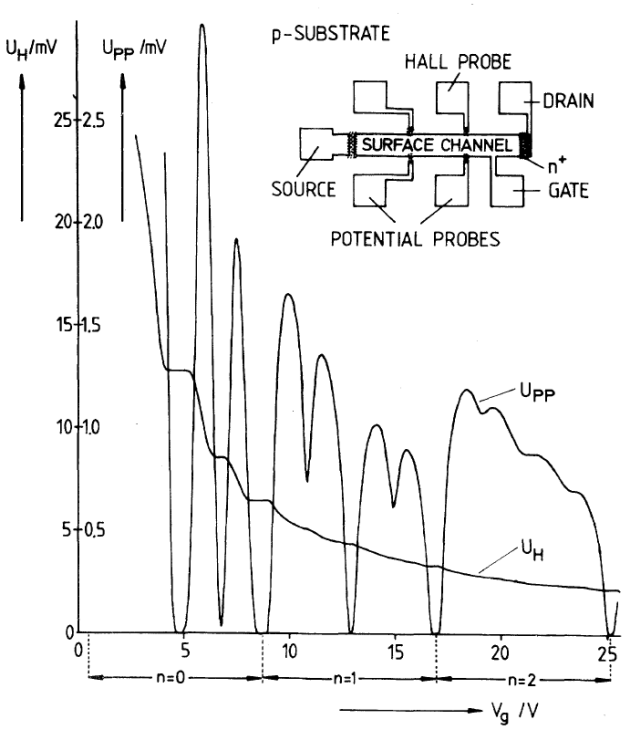

Figure 6.1. Hall voltage (U_H) and the voltage drop between the potential probes (U_{PP}) as a function of the gate voltage (V_g) in a MOSFET device (shown in the inset). The device is under a constant magnetic field of 18 T at $T = 1.5\,K$. Taken from [150].

In order to understand the properties of this quantized levels we describe how free electrons move under the influence of $\vec{B}$. We assume, as a first approximation, a 2D particle gas confined in the x-y plane, where the electronic movement is restricted. We consider a constant magnetic field applied in the z-direction. The vector potential arising as a consequence of $\vec{B}_z$ has, therefore, only components in the x-y plane, i.e., $\vec{A} = \nabla \times \vec{B}_z$. The Hamiltonian that describes this system is simply given by the momentum of the particle (p) and the vector potential $(\vec{A})$.

$$\widehat{H} = \frac{1}{2m}(\widehat{p} + e\widehat{A})^2 \tag{6.2}$$

where m is the free electron mass and, $\widehat{p}$ and $\widehat{A}$, are quantum operators corresponding to the momentum and vector potential, respectively. To solve this Hamiltonian and obtain the eigenvalues of the system we rewrite Eq. 6.2. We redefine first the quantum operators as $\pi = \widehat{p} + e\widehat{A}$. Since particles move freely along x and y direction, we can distinguish between π_x and π_y. These new variables follow the commutation relation $[\pi_x, \pi_y] = -i\hbar e B_z$. We introduce now the ladder operators as a function of π. These operators are analogous to the

ones corresponding to the quantum harmonic oscillator.

$$a^\dagger = \frac{1}{\sqrt{2\hbar e B_z}}(\pi_x - i\pi_y) \qquad a = \frac{1}{\sqrt{2\hbar e B_z}}(\pi_x + i\pi_y) \tag{6.3}$$

Recalculating the commutation relation for these operators yields to $\left[a, a^\dagger\right] = 1$. This result is precisely the same as the one obtained for the 1D harmonic oscillator, therefore, it is expected to obtain a Hamiltonian with the same form.

$$\widehat{H} = \frac{1}{2m}\pi\pi^\dagger = \hbar\omega\left(aa^\dagger + \frac{1}{2}\right) \tag{6.4}$$

where $\omega = eB_z/m$ is the cyclotron frequency. We introduce now the ground state $|0\rangle$ which obeys the rule $a|0\rangle = 0$. The rest of the levels are calculated following the ladder operators of the quantum harmonic oscillator: the creation operator $a^\dagger$ increases a quantum state by one and the annihilation operator a lowers it by one. They are defined as follows,

$$a^\dagger|n\rangle = \sqrt{n+1}\,|n+1\rangle \qquad a|n\rangle = \sqrt{n}\,|n-1\rangle \tag{6.5}$$

As a result, the eigenvalues of this system can be easily determined by $H|n\rangle = E_n|n\rangle$. Thus, an arbitrary state n has an energy equal to

$$E_n = \hbar\omega\left(n + \frac{1}{2}\right) \tag{6.6}$$

In the presence of B_z, the particles show only discrete energy values proportional to n. These quantized levels are the so-called Landau levels. The energy difference between two arbitrary levels is linearly dependent on the intensity of B_z due to the dependence on the cyclotron frequency. Note that all levels, even if we consider an infinite number of them, are always equally spaced. Moreover, the ground state of this system, $n = 0$, obtains an energy corresponding to $\hbar\omega/2$ and not zero, as a consequence of quantum mechanics. Even at absolute zero temperature, the particle is not completely at rest. This effect is responsible for preventing liquid helium (^{4}He) from freezing at atmospheric pressure. In Fig. 6.1, several Landau levels are clearly identified.

After the first successful discovery of the integer QHE in Si, a great interest aroused in other low-dimensional materials such as a 2D semiconductor heterostructure like the GaAs-AlGaAs heterojunction [151]. Hence, it is not surprising that when a single lattice of graphene was isolated, its transport and magneto properties were quickly measured [140]. The unusual nature of the charge carriers behaving like massless particles make graphene a

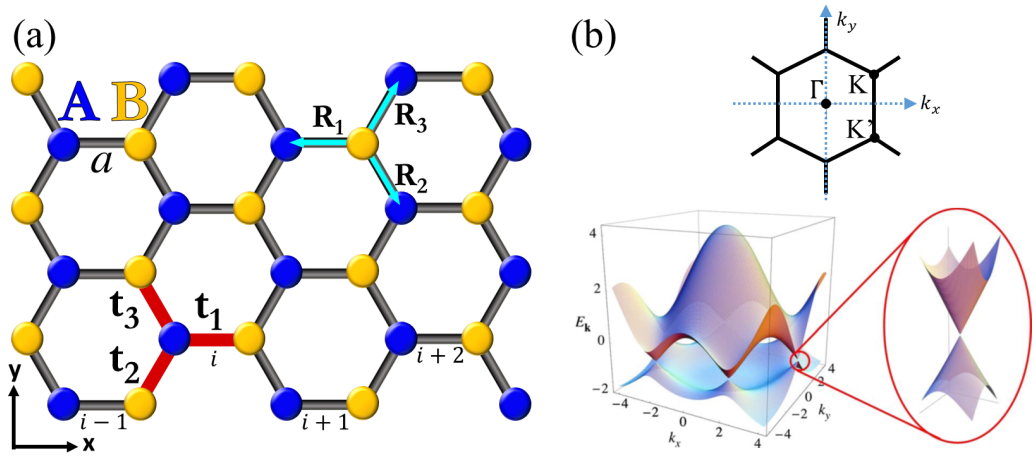

Figure 6.2. (a) Regular honeycomb lattice composed by two triangular sublattices: A (blue points) and B (yellow points). $t_{1,2,3}$ define the nearest neighbor hoppings and $R_{1,2,3}$ their corresponding positions. The position of the unit cells formed by the two lattice points (A and B) is labeled with an index i that varies its value by 1 from cell to cell. (b) Reciprocal-space lattice of the Bravais lattice shown in (a). The upper panel shows a sketch of the Brillouin zone. The vertices, marked by K and K', are known as Dirac points. The lower panel illustrates the electronic dispersion in the honeycomb lattice. A zoom of the energy bands around one of the Dirac points is displayed in which a linear dispersion is observed (Taken from [79]).

perfect candidate to observe the QHE even at room temperature [143]. The consequences of this linearity in the dispersion relation are numerous, however, we will concentrate in the particular behavior of electrons in the presence of a magnetic field. While in a 2D gas subjected to a magnetic field the same spectrum is observed as the one of the harmonic oscillator (linear dependence on n), in the case of zero mass particles, Landau levels depend on $|n|^{1/2}$, as we will discuss below.

Graphene is a single 2D layer of carbon atoms arranged in a hexagonal or honeycomb lattice. The hybridization between the orbitals S and P (sp2), leads to the formation of strong chemical bonds and defines the 120º angle between the atoms. Fig. 6.2(a) illustrates the hexagonal lattice composed by two interpenetrating triangular sublattices, A and B, displayed in blue and yellow, respectively. The lattice shows two of the most common terminations in graphene, the so-called zig-zag (left and right edges) and armchair (top and bottom). Only the former one exhibits localized states characterized by a flat dispersion linking the Dirac points (K and K') [152–154]. Taking into account that two adjacent points of each sublattice have a separation of $a = 1.42$ Å[79], we can define the position vectors of the nearest neighbors as $\vec{R}_1 = (-a, 0)$, $\vec{R}_2 = \left(a/2, -\sqrt{3}a/2\right)$ and $\vec{R}_3 = \left(a/2, \sqrt{3}a/2\right)$. The strength of the coupling between two atoms is given by the hopping coefficient t_i. In the case of a regular lattice of graphene the condition $t_1 = t_2 = t_3$ is fulfilled.

A sketch of the reciprocal-space lattice of graphene is shown in Fig. 6.2(b). The lower panel shows its band structure composed by the top and bottom parts of the S-band. The points where both parts touch are the so-called Dirac points (K and K'). At the energy of the Dirac points ($E = 0$), the momentum-space map exhibits a hexagonal Brillouin zone (see upper panel) that limits with these Dirac points, K and K'. They are located at $K = \left(\pm 2\pi/3a, 2\pi/3\sqrt{3}a\right), \left(0, -4\pi/3\sqrt{3}a\right)$ and $K' = \left(\pm 2\pi/3a, -2\pi/3\sqrt{3}a\right), \left(0, 4\pi/3\sqrt{3}a\right)$. Around these points special properties, such as a linear dispersion, are observed.

When a magnetic field is applied perpendicularly to the graphene lattice, electrons move in cyclotron trajectories and Landau levels are filled. The presence of $\vec{B}$ changes the mirror symmetry so that K and K' points become distinguishable [155]. Therefore, two kinds of electrons with opposite charge sign are observed: the sign is introduced in the equations by the valley index $\varepsilon = \pm 1$. Since graphene is composed by two sublattices, we write the 2D Hamiltonian in the A and B basis in momentum-space at each Dirac valley, taking the simple form of an anti-diagonal matrix [79].

$$\hat{H} = \begin{pmatrix} 0 & U'_\varepsilon \\ U'_\varepsilon & 0 \end{pmatrix} = U_\varepsilon \tag{6.7}$$

where U_ε is an operator defined as

$$U_\varepsilon = v_F \begin{pmatrix} 0 & \varepsilon\pi_x - i\pi_y \\ \varepsilon\pi_x + i\pi_y & 0 \end{pmatrix} \tag{6.8}$$

Since charge carriers in graphene behave like relativistic particles, they travel with an effective speed of light given by the Fermi velocity (v_F). Following a similar procedure as in the classical QHE, U_ε can be redefined considering the ladder operators described in Eq. 6.3. Different operators are obtained for each Dirac valley.

$$U_+ = \hbar\omega \begin{pmatrix} 0 & a^\dagger \\ a & 0 \end{pmatrix} \qquad U_- = \hbar\omega \begin{pmatrix} 0 & a \\ a^\dagger & 0 \end{pmatrix} \tag{6.9}$$

where $\omega = v_F\sqrt{2eB_z/\hbar}$. To find the eigenvalues of this system and the corresponding wave functions $\psi_{A,B}$ of the different Landau states in the A and B basis, we solve the Hamiltonian around one Dirac valley.

$$\hat{H}\begin{pmatrix} \psi_A \\ \psi_B \end{pmatrix} = \hbar\omega \begin{pmatrix} 0 & a \\ a^\dagger & 0 \end{pmatrix} \begin{pmatrix} \psi_A \\ \psi_B \end{pmatrix} = E_n \begin{pmatrix} \psi_A \\ \psi_B \end{pmatrix} \tag{6.10}$$

Redefining the equations, we can obtain the wave functions separately for each sublattice as

$$\begin{aligned}(\hbar\omega)^2 aa^\dagger \psi_A &= {E_n}^2 \psi_A \\ (\hbar\omega)^2 a^\dagger a \psi_B &= {E_n}^2 \psi_B\end{aligned} \tag{6.11}$$

The solution obtained for graphene is similar to that of a conventional 2D gas; both depend directly on the ladder operators, however, in this case the dependency is not linear. This significant change yields to a description of Landau levels around Dirac points given by [156],

$$E_n = \pm\hbar\omega\sqrt{n} = \pm v_F\sqrt{2e\hbar B_z|n|} \tag{6.12}$$

where the integer obeys $n \geq 0$. The energy of the dispersion bands reveals an important difference with the conventional case, the ground Landau level ($n = 0$) possesses zero-energy. Moreover, the distribution of the Landau levels changes drastically with a square-root dependence: while in a 2D gas they are equally separated, in graphene, the distance between two consecutive levels decreases with n. This is a direct consequence of the existence of Dirac cones and has been experimentally observed by different measurements with magnetic fields [157–159].

On the other hand, knowing that $a^\dagger a|n\rangle = n|n\rangle$, it is immediate to find that the wave function ψ_B is defined as the 1D harmonic oscillator function with frequency ω and is directly related to $|n\rangle$. Thus, there is a contribution of the sublattice B to the ground Landau state $|0\rangle$. The equation for the eigenstate ψ_A can be resolved using the solution for ψ_B and the ladder operators in Eq. 6.10.

$$\psi_A = \frac{\hbar\omega}{E_n} a|n\rangle = \frac{\hbar\omega}{\pm\hbar\omega\sqrt{n}}\sqrt{n}|n-1\rangle = \pm|n-1\rangle \tag{6.13}$$

For the ground state, a single state equal to $|-1\rangle = 0$ is found, thus, the sublattice A does not contribute to the emission, therefore, the fundamental Landau level is localized only in sublattice B. This fact is a key ingredient to experimentally identify this level.

6.3 Synthetic gauge field in a photonic honeycomb lattice

The optical properties of a single layer of graphene are limited primarily due to its negligible bandgap, which results in an absence of PL. However, its electronic properties can be controlled by applying a gate voltage. It has been shown that these properties can be modified

by elastic deformations as they can induce a gauge field [160]. Recent studies suggest that the engineering of strain, for instance, by applying a mechanical force, would result in the Landau quantization opening a bandgap between the levels [79]. Guinea *et al.* analyze explicitly this possibility, in which a particular uniaxial strain geometry could lead to a uniform pseudo-magnetic field [144].

Real graphene presents a particular high flexibility that allows the direct manipulation of the lattice; thus typical geometries such as nanotubes, nanoribbons or other deformations in 2D can be obtained. A general deformation can be induced, for example, by mechanically applying an external force so the atoms of the lattice are moved closer or farther away to each other. Nevertheless, graphene is not immune to disorder; defects are commonly found in different forms such as vacancies, cracks that act like localized edge states, or charges on top of the layer or the substrate where the graphene has been grown. The effect of the disorder can modify the graphene's band structure since it can locally change the on-site energy and the distance and the angle between the orbitals. As a consequence of the deformation introduced in the lattice, an artificial magnetic field ($\vec{\mathfrak{B}}$) is induced, which shows a highly anisotropic distribution that hinders the observation of Landau levels in the dispersion relation [146, 147, 161]. Therefore, to avoid the anisotropy of $\vec{\mathfrak{B}}$ and a significant back scattering due to the presence of defects, a system with a substantial degree of control in the lattice geometry needs to be considered.

Taking advantage of the light-matter nature of polaritons, honeycomb lattices made of coupled micropillars provide a new platform to explore the localization of photons with engineered dispersions [141]. Their topological properties make them particularly robust to deformations of the lattice[162, 163]. They exhibit Dirac cones that appear in pairs, as in real graphene. In the presence of time-reversal and inversion symmetries, they can only be annihilated by merging with Dirac cones of opposite charge. Furthermore, different designs of honeycomb terminations can be accurately obtained, e.g., the zig-zag, the armchair or even the bearded edge, which is not stable in real graphene. Thanks to the photonic content of polaritons, it is possible to induce a pseudo-magnetic field at optical frequencies, observing the characteristic Dirac dispersion through its PL. In order to understand how this magnetic field arises, first we take a theoretical overview.

We consider an arbitrary strained honeycomb lattice in which different hoppings, t_i, are considered in the direction of each nearest neighbor, $i = 1,2,3$. We start describing the

Hamiltonian in momentum-space, which takes the form of an anti-diagonal matrix [149]:

$$\hat{H} = \begin{pmatrix} 0 & U^*\left(\vec{k}\right) \\ U\left(\vec{k}\right) & 0 \end{pmatrix} \tag{6.14}$$

where the anti-diagonal components are defined by

$$U(\vec{k}) = \sum_{1}^{3} t_i e^{i\vec{k}\vec{R}_i} \tag{6.15}$$

We continue expanding the potential around the nonequivalent Dirac points. Further details about the mathematical procedure can be found in ref. [149].

$$U(\vec{k}) \approx -i\,\mathrm{v}_D^x\left(\hbar k_x + eA_x\right) + \mathrm{v}_D^y\left(\hbar k_y + eA_y\right) \tag{6.16}$$

As a consequence, the Hamiltonian now depends on both, the Dirac velocity $\left(\mathrm{v}_D^{x,y}\right)$ and the magnetic vector potential $(A_{x,y})$. These terms are strongly dependent to the hopping strength, so that the former ones are written as:

$$\begin{aligned} \mathrm{v}_D^x &= \frac{a}{4\hbar}\left[(4t_1 + t_2 + t_3) + i\varepsilon\sqrt{3}\,(t_2 - t_3)\right] \\ \mathrm{v}_D^y &= \frac{a}{4\hbar}\left[3\,(t_2 + t_3) - i\varepsilon\sqrt{3}\,(t_2 - t_3)\right] \end{aligned} \tag{6.17}$$

The parameter $\varepsilon = \pm 1$ indicates the valley index for the two Dirac points. Note that when a strain is applied to the lattice, the velocities show an anisotropic distribution. The existence of the vector potential $(\vec{A})$ is also linked to the presence of strain and it is written as follows:

$$\begin{aligned} eA_x &= \frac{\sqrt{3}}{2}\frac{\varepsilon}{\mathrm{v}_D^x}\,(t_2 - t_3) \\ eA_y &= \frac{1}{2}\frac{\varepsilon}{\mathrm{v}_D^y}\,(2t_1 - t_2 - t_3) \end{aligned} \tag{6.18}$$

Regardless of the value of $\mathrm{v}_D^{x,y}$, a lattice with equal hoppings yields a zero magnetic vector potential. Therefore, no $\vec{\mathfrak{B}}$ is observed in perfect honeycomb lattices. When the condition $t_1 = t_2 = t_3$ is broken, $\vec{A}$ arises, and as a result, the band dispersions are modified. The energy of the Dirac cones can be shifted allowing to merge or to separate the different bands of the dispersion by changing the lattice anisotropy [164].

The spatial distribution of the strain is a key ingredient to determine the direction and amplitude of the artificial magnetic field $(\vec{\mathfrak{B}})$. As the vector potential emerges in the in-plane

lattice, the resulting magnetic field, given by the curl of $\vec{A}$, will appear in the z-direction.

$$\mathfrak{B}_z = \partial_x A_y - \partial_y A_x \tag{6.19}$$

This strain-induced artificial field does not break time reversal symmetry, therefore, both fields, $\vec{A}$ and $\vec{\mathfrak{B}}$, exhibit opposite signs in the two Dirac valleys K and K'. This variation constitutes the main difference with a real magnetic field, which always points in the same direction along the lattice.

In the experiment described in section 6.4 (below), we consider a finite size lattice along the x axis and an infinite y dimension. We focus on the case of a honeycomb lattice with uniaxial strain along the x-direction: we assume equal hopping coefficients along $i = 2$ and $i = 3$, so that $t = t_2 = t_3$, and a non-uniform deformation t_1. The hopping that describes the form of the strain along x is defined as

$$t_1(x_i) = t\left(1 + \frac{x_i}{3a}\tau\right) \tag{6.20}$$

where the minimum (maximum) value of the hopping is located at the left (right) side of the sample. The index i denotes the position of the unit cells formed by the two lattice points (A and B). As shown in Fig. 6.2(a), the left column of hexagons in the lattice is assigned the index $i-1$, which is translated into a position $x_{i-1} = -1$. The adjacent column of hexagons on the right correspond to a position of $x_i = 0$, etc. At $x_i = 0$, the condition $t_1(0) = t$ is fulfilled.

As explained above, this particular uniaxial strain yields different values of the Dirac velocity in x and y directions. Introducing Eq. 6.20 in Eq. 6.17, two velocities are obtained

$$\begin{aligned} \mathrm{v}_D^x &= \frac{a}{2\hbar}\left(3t + 2\frac{x_i t}{3a}\tau\right) \\ \mathrm{v}_D^y &= \frac{a}{2\hbar}(3t) \end{aligned} \tag{6.21}$$

At the position $x_i = 0$ the anisotropy disappears. However, the further from the center, the greater the difference between both components of the velocity. Inserting the hopping amplitude along x in Eq. 6.18 one gets

$$\begin{aligned} eA_x &= 0 \\ eA_y &= \frac{\varepsilon}{\mathrm{v}_D^y}\left(\frac{xt}{3a}\tau\right) \end{aligned} \tag{6.22}$$

Under this spatial distribution of the strain $A_x = 0$, therefore $\vec{\mathfrak{B}}$ depends only on the A_y component. The presence of the parameter ε in Eq. 6.22 indicates the coexistence of fields of opposite sign in the same lattice. The artificial field $\vec{\mathfrak{B}}$ is then defined inserting Eq. 6.21 and 6.22 into Eq. 6.19.

$$B'_z = \frac{2\hbar}{9ea^2}\varepsilon\tau \tag{6.23}$$

The intensity of the field is linked to the hopping gradient (τ) and to the lattice spacing (a). Considering the separation between two carbon atoms in graphene, a, and the rest of physical constants in Eq. 6.23, an equivalent $\mathfrak{B}_z \sim 2 \times 10^3 \tau$ T is obtained.

To obtain analytically the Landau levels, Eqs. 6.21 and 6.22 are introduced in the potential defined in Eq. 6.16. The exact diagonalization of the Hamiltonian detailed in Eq. 6.14 under uniaxial strain provides the value of the energy as a function of n.

$$E_n = \pm t\sqrt{\tau\,|n|} \tag{6.24}$$

An infinite number of Landau levels $-\infty < n < +\infty$ with energies following a square-root law of n are found. Note that the same dependence with n is found either by applying a real B to graphene (Eq. 6.12) or by modulating the hopping amplitude along a single direction of the honeycomb lattice.

To better understand the implications of Eq. 6.24, the dispersion of a honeycomb lattice with 601 unit cells and a small strain ($\tau = 0.005$) is numerically obtained in Fig. 6.3. The energy is represented in units of the bare hopping t and, as the system is periodic along the y direction, the dispersion relation is displayed as a function of $k_y a$. A sketch of the lattice is shown in Fig. 6.3 in which sublattices A (blue) and B (yellow) are indicated. The appearance of discrete bands around K and K' as a consequence of the strain is clearly observed. Above these bands, several red lines are depicted using the analytical prediction for the Landau levels given by [149],

$$E_n = \pm t\sqrt{\tau\,|n|\,(1 - \varepsilon k_y a)} \tag{6.25}$$

where a small correction considering the spatial dependence of v_D^x has been taken into account. The fact that the expression of the energy includes the correction term, yields to a small energy-shift of each level around the Dirac points. It is important to notice that these levels are no longer flat bands, contrary to what happens when a real magnetic field is

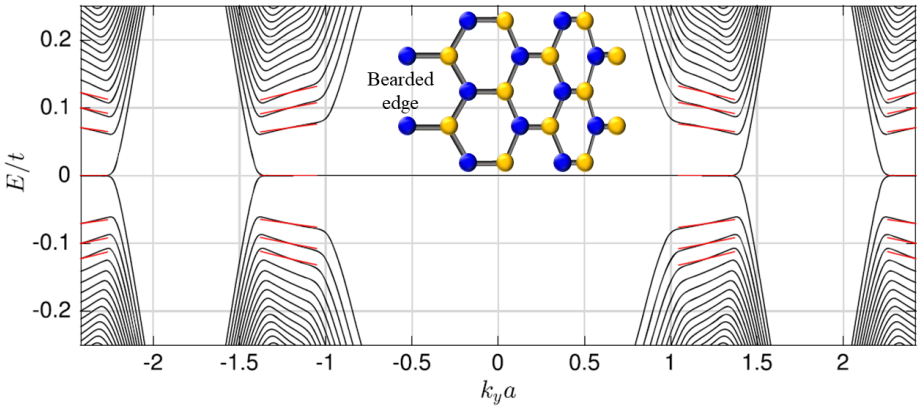

Figure 6.3. Numerically calculated band structure of a honeycomb lattice with 601 unit cells and a small strain, $\tau = 0.005$. The inset shows the lattice with bearded edges considered in the calculations. Landau levels are marked with red lines around Dirac points K and K' for $k_y a \simeq \pm 1.21, \pm 2.42$. Taken from [149].

applied, in which v_D is independent of the position and thus, the energy of the Landau levels is independent of k.

The flat bands appearing at zero energy in Fig. 6.3 are doubly degenerated: they correspond to the $n = 0$ Landau level and to a localized edge state arising from the bearded edge [149]. The type of edges that limit the lattice, in this case bearded (left and right) and armchair (top and bottom), give rise to these states with zero energy when nearest-neighbor hoppings are considered. If an armchair edge is present in an isotropic lattice, the localization length diverges, therefore, no edge state is observed. However, when strain is applied to the lattice and the hopping t_i is modified at least in one direction, an armchair edge state is found [152, 154, 165].

6.4 Observation of photonic Landau levels

To the best of our knowledge, the first and only realization so far of a strain induced pseudomagnetic field at optical frequencies in a photonic lattice has been performed by Rechtsman *et al.* [166]. They emulate the graphene lattice through a series of elliptical waveguides arranged in a honeycomb distribution. They apply different strains to the system that would yield to an equivalent $\vec{\mathfrak{B}}$ of the order of 5.500 T. They report the existence of Landau levels based on a strong emission related to an edge state, however, no emission from the rest of the lattice (bulk) is observed at high strain. In this chapter, we propose an alternative photonic platform to investigate the emergence of Landau levels in the presence

of uniaxial strain gradients in a honeycomb lattice studying the observation of isolated bands in the dispersion relation and their corresponding PL maps in real-space.

The polariton honeycomb lattices used in this experiment consist of coupled GaAs micropillars organized in a hexagonal lattice. We study the response of four lattices with different strain gradient along x-direction $\tau = 0, 0.42, 0.56$ and 1.27. Since the gradient has a positive value, the highest strain will be located at the right edge. We pump the sample non-resonantly with a cw laser. A very low excitation density is chosen in order to be in the linear regime and to observe the polariton relaxation in the full band structure. The excitation beam is carefully centered in the lattice, with approximately equal distance to both, left and right, edges. We set the energy of the Dirac points, $E_0 = 1569$ meV, as the zero energy. The details of the samples used in this experiment and the excitation conditions are described in section 2.2.4. We measure the real-space and the momentum distribution PL of the lattices and we compare the results with the theoretical predictions presented in section 6.3.

We first compare the momentum-space maps for two cases, $\tau = 0$ and 1.27, in Fig. 6.4(a,b). Both PL maps are filtered at zero energy, where Dirac points are located. The momentum distribution at zero energy for the unstrained case is depicted in Fig. 6.4(a), which reveals a hexagonal structure similar to that of conventional graphene [Fig. 6.2(b)]. The six Dirac points corresponding to the vertices of the hexagon are clearly observed as local intensity maxima. When τ is increased up to 1.27, Fig. 6.4(b), the characteristic hexagonal shape is deformed: the Dirac points at $k_x \sim 0$ seem to extend, creating a continuous band between $2 < |k_y| < 4$. The rest of the Dirac points are no longer easily discernible. As we will show later, this deformation is related to the presence of a Landau level at zero energy.

For a greater understanding of the effect of the strain and therefore, the appearance of $\vec{\mathfrak{B}}$, we show in Fig. 6.4(c) the dispersion relation for $\tau = 0$ at the positions marked at $k_x(2\pi/3a) = -1.1$ (position 1) and 0 (position 2) with a white dashed line in panel (a). The dispersion obtained at position 1 shows a profile of the bottom S-band located at one edge of the hexagon in which the highest intensity is observed at the center of the band. The dispersion measured at position 2 shows the bottom of the S-band. Due to destructive interference along the highly symmetric crystallographic directions, characteristic of these bipartite lattices, it is not possible to visualize the upper part of the S-band [167]. Therefore, determining the exact positions of Dirac points through the dispersion, where both parts touch, requires a more rigorous study than the one made here, based only on the PL maps where all bands can be clearly observed.

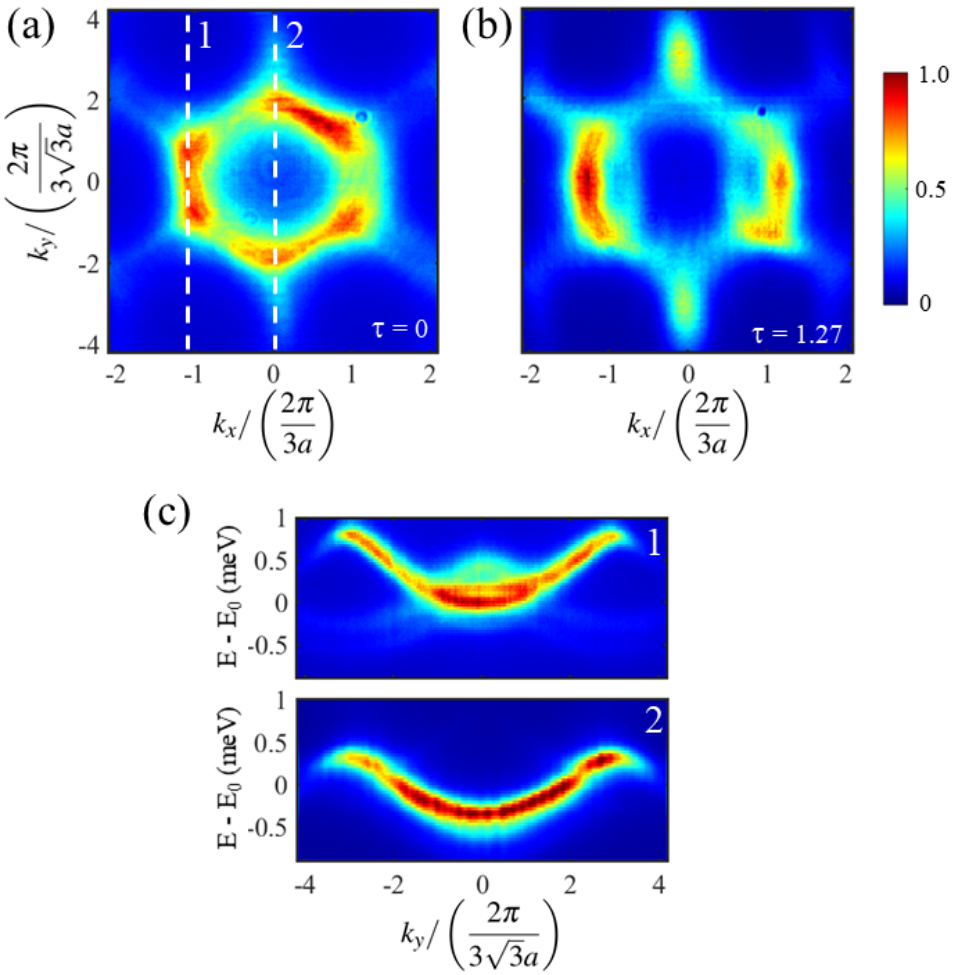

Figure 6.4. Momentum-space PL of two honeycomb lattices with strain gradients 0 (a) and 1.27 (b) filtered at zero energy. Two white dashed lines in (a) mark the values of k_x at which the profiles shown in (c) have been obtained. The position 1 and 2 in (c) show the dispersion relation as a function of k_y at $k_x = -1.1$ and 0, respectively. The emission intensity is in a false-color scale.

The dispersions along k_y for several strained lattices, selected at $k_x = 0$, are collected in Fig. 6.5. For the unstrained lattice, Fig. 6.5(a), the dispersion shows a continuous S-band consistent with the characteristic dispersion of graphene. For comparison, the dispersion is theoretically calculated and depicted as a solid line. The theoretical and experimental dispersions are clearly in accordance, yet, the top band cannot be observed due to the aforementioned interference [167]. The intersection between the top and bottom bands reveals the position of the Dirac points for which the dispersion is linear in their vicinity. As a guide to the eye, a dashed line shows this crossing point at zero energy where no evidences of gap or localized states are found. The fact that the experimental dispersion resembles

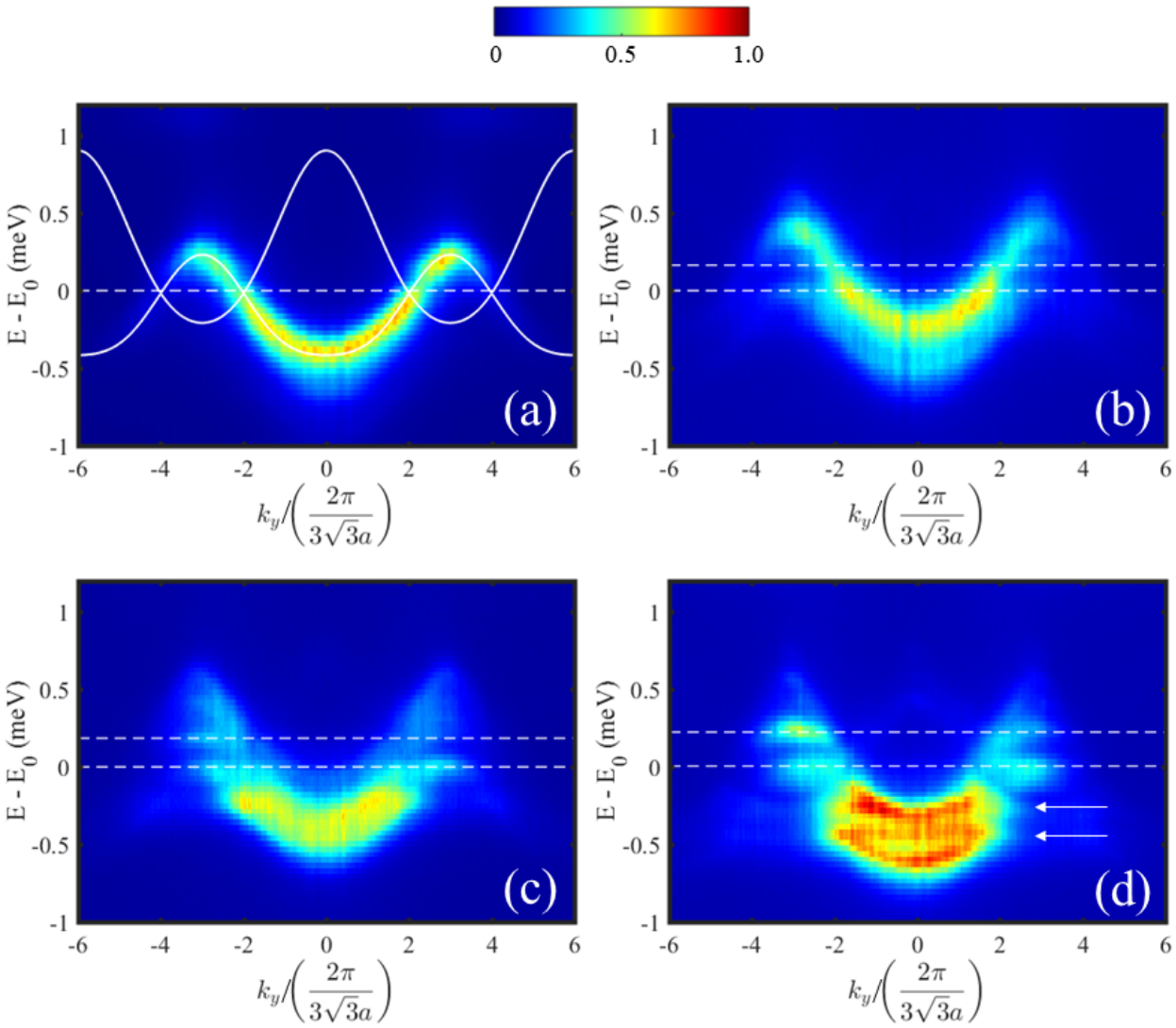

Figure 6.5. Dispersion relation of a polariton honeycomb lattice at $k_x = 0$ for different strain gradients: 0 (a), 0.42 (b), 0.56 (c) and 1.27 (d). In case (a), the solid lines show the calculated dispersion for graphene.The dashed line is depicted at zero energy as a guide to the eye. In cases (b)-(d), the dashed lines indicate the energy of the identified Landau levels $n = 0, 1$. The white arrows in (d) indicate the possible emergence of Landau levels at negative energies. The emission intensities are in a false-color scale.

that of graphene confirms the appropriateness of polariton honeycomb lattices as graphene emulators.

As the strain increases, an energy gap emerges at the Dirac points giving rise to several flat bands identified as Landau levels. These bands become visible for the cases (b) and (c), in which a separation between the flat bands is observed. In both cases, the gap is evident as a drop in the intensity between the bands. Following the expected energy for each Landau level given by Eq. 6.24, we identify the first band appearing at zero energy as the Landau level $n = 0$ and the second band at ~ 0.2 meV as $n = 1$. Furthermore, we observe a linewidth broadening of the bottom of the S-band with increasing τ at negative energies; although its origin is still unclear, the superposition of the bottom of the S-band and the possible $n < 0$ Landau states could blur the emission at negative energies. In the case of the highest τ, Fig. 6.5(d), the dispersion is significantly deformed and only a vague resemblance to the graphene's dispersion remains. At zero and positive energies, an increase of the polariton population with respect to the previous cases is observed. Moreover, the gap between both levels is considerably larger than in panels (b) and (c), as expected from the action of the pseudo-magnetic field [see Eq. 6.24]. In cases (c) and (d), the emergence of flat bands at negative energies (~ -0.2 and ~ -0.5 meV) is hinted [see white arrows in Fig. 6.5(d)], however, the occupation in these levels is similar to that of the S-band, which hinders their clear identification. Thus, we are not able to identify unambiguously the $n < 0$ levels.

As we have seen, Landau states appear at discrete values of the energy with a separation between them related to the hopping gradient. To further support our results we focus now on the the wave function of the ground Landau level. The corresponding real-space emission maps for the same strain gradients shown in Fig. 6.5 are depicted in Fig. 6.6, filtered at zero energy. In the unstrained case, Fig. 6.6(a), the hexagonal structure of the lattice is easily recognizable. As expected, no localization is observed in this case. The distribution of the emission corresponds to the Gaussian shape of the laser beam over the lattice. When the strain is increased up to $\tau = 1.27$, cases (b), (c) and (d), an asymmetry in the PL is observed: the predominant emission is located in sublattice B. This asymmetry has been theoretically predicted when a strain-induced gauge field is applied to selected geometries [149]. As explained in section 6.3, the wave function of a strained honeycomb lattice describes a fundamental Landau state restricted to only one sublattice (B) for a positive τ. The emission from sublattice A has almost vanished for the case of $\tau = 1.27$. It is unquestionable to conclude that the effect of the deformation significantly modifies the PL, demonstrating that the engineering of the hopping parameters gives rise to discrete Landau states.

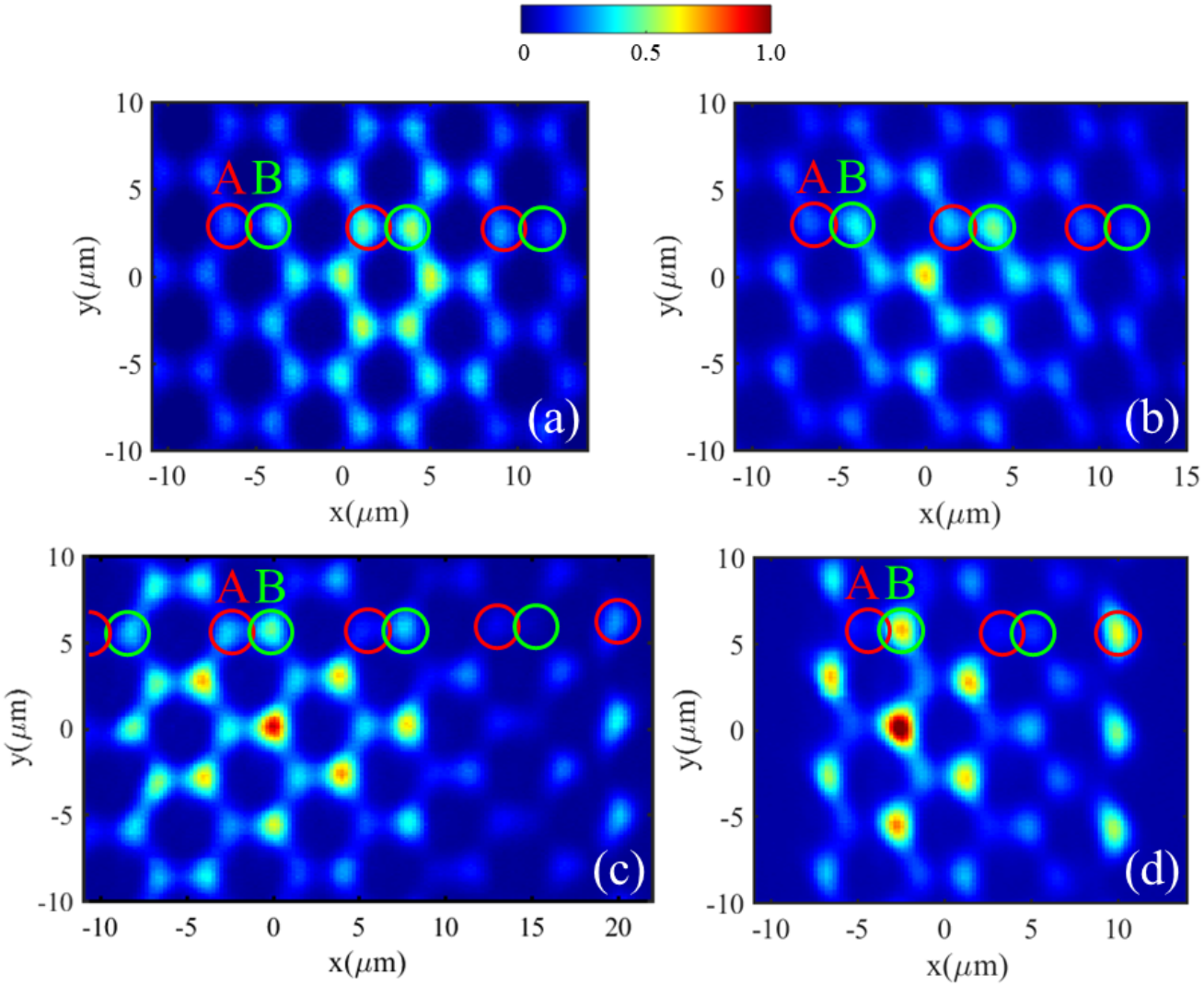

Figure 6.6. Real-space maps of polariton honeycomb lattice filtered at zero energy for different strain gradients: τ =0 (a), 0.42 (b), 0.56 (c) and 1.27 (d). The circles depicted in (a)-(d) illustrate the micropillars that compose the lattice. The sublattice A (B) is marked in red (green). The emission intensities are in a false-color scale.

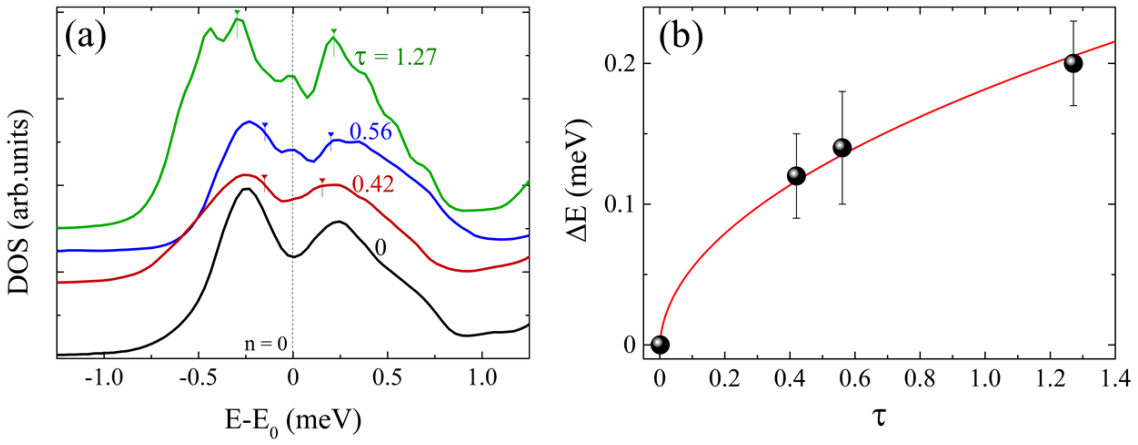

Figure 6.7. (a) Normalized DOS of the S-band at different hopping gradients (τ). The energy of the fundamental Landau level is set at zero (marked with a vertical dashed line). Other peaks suggesting the presence of Landau levels are indicated by a short vertical mark. (b) Energy gap between $n = 0$ and the first Landau level (± 1). The red line fits the experimental data following the square root law $\Delta E = \pm t\sqrt{\tau}$ where $t = 0.14 \pm 0.03$ meV.

Apart from the value of τ, the size of the sample is also an important factor when studying the real-space emission. By increasing the hopping (t_1) along the x-direction the width of the lattice is drastically reduced. Since the lattice is considerably large and the excitation conditions are well-below the propagation threshold, the probability of polaritons reaching the edge is limited. As we have already mentioned, the edge states are also localized at zero energy for a specific shape termination of the honeycomb lattice: the zig-zag edge. In this experiment, the optimal conditions to observe an edge state appear at Fig. 6.6(c) and (d) in which a slight emission can be distinguished on the right side, where the deformation is higher. Note that the edge state is located in A sublattice (red circles).

For the sake of completeness, the density of states (DOS) for the S-band has been calculated. The normalized DOS are depicted in Fig. 6.7(a) for different values of the strain parameter τ. The vertical dashed line marks the zero energy point, where the level $n = 0$ is located. As expected, no remarkable occupation is observed in this level for $\tau = 0$, where a drop of the polariton population can be clearly appreciated. This confirms the similarity of our polariton honeycomb lattice with that of real graphene. However, when τ is increased, a local maximum arises at zero energy. The lattices with $\tau \neq 0$ not only show a well-defined $n = 0$ level, but other nearby local maxima appearing at both positive and negative energies, which are indicated by a short vertical mark in the figure. The appearance of these maxima could be related to the presence of the first Landau levels $n = \pm 1$. Since the identification of these levels in the dispersion is not trivial [as seen in Fig. 6.5], we calculate the energy gap

($\Delta E = E_{n=\pm1} - E_{n=0}$) between the ground state and the first Landau level. The energy gap as a function of the strain gradient is shown in Fig. 6.7(b). The experimental data are fitted following the evolution of the energy in a strained lattice given by Eq. 6.24. The energy gap between this two consecutive Landau levels is consistent with the theoretical proposal, within the experimental accuracy, confirming the identification of the $n = \pm1$ Landau levels as the local maxima arising in the vicinity of $n = 0$ [short vertical mark in Fig. 6.7(a)]. In addition, a precise value of the hopping amplitude at $x = 0$ is obtained, $t = 0.14 \pm 0.03$ meV.

6.5 Conclusions

We have experimentally demonstrated the existence of Landau levels in honeycomb lattices of photonic resonators subject to an artificial gauge field. Coupled micropillars provide an excellent platform to emulate the topological properties of 2D materials since they display a band dispersion similar to that of graphene in which Dirac cones are visible. This has been evidenced in the dispersion measured for the unstrained honeycomb lattice ($\tau = 0$). The engineering of the gradient of the hopping amplitude between sites of the honey-comb lattice creates an artificial valley dependent magnetic field capable of emulating values of the order of 10^3 T. Due to the appearance of the artificial magnetic field, a gap opens in the Dirac cones at zero energy and several quantized Landau levels arise in their proximity. Additionally, we have been able to measure the wave function of the fundamental Landau level, which is localized on one sublattice at zero energy. Finally, we have compared the size of the energy gap between two consecutive Landau levels with a square-root law, theoretically predicted, which confirms the expected evolution of the energy of these states with the gradient of the hopping amplitude.

The semiconductor micropillars employed in this work open exciting possibilities to study phenomena at the crossroad of solid-state physics and photonics. Taking advantage of the strong coupling between quantum well excitons embedded in the micropillars and the confined photons our platform opens the way to study Landau levels subject to polariton-polariton interactions and lasing in flat bands [168].

Chapter 7

General conclusions and future perspectives of the thesis

In this thesis we have investigated the properties of polariton condensates in patterned microcavities either in real- or momentum-space. Following the ordering of the chapters, we summarize the main achievements of this thesis:

The thermal robustness of the coherence of non-equilibrium polariton condensates is addressed in chapter 3. This coherence, evidenced by the presence of interference fringes along the full polariton propagation, reveals a time- and space-preserved phase correlation. The fringes are observed in momentum-space when condensates, which are spatially separated, travel with the same velocity. Additional fringes are observed at the crossing of condensates in real-space. The analysis of both, the visibility of the fringes (υ) and the fraction of condensed to uncondensed polariton populations (f_C) leads to the same result: both magnitudes allows us to infer a critical temperature for the BEC-like transition when they decay to zero, despite the non-equilibrium nature of polariton condensates. A comparison of the results with two theoretical models developed for equilibrium atomic condensates yields a critical temperature which is very similar in both models. This is the reason why we have been unable to identify which model fits more accurately our non-equilibrium condensates' results. Therefore, a more adequate theoretical proposal that takes into account the characteristics of polariton condensates is required.

The experiments performed on the devices dubbed as couplers, summarized in chapter 4, demonstrate their functionality as full optical devices, opening the way to routing and

splitting the condensates towards different output terminals by properly selecting the size parameters. First, we have investigated the implications of the use of bent waveguides in the propagation of polariton condensates: due to the abrupt variation of 45º in the condensates' trajectory, a significant decay of the polaritons' momentum is observed. We are able to select a specific value of the polaritons' momentum during their creation, but after reaching the bend, the control over the momentum is lost. Therefore, it would be convenient to investigate whether a reduction of the bend's angle could help to control the polaritons momentum over the entire device. Furthermore, our measurements show that, depending on the size parameters, polaritons are able to couple between the two arms that compose the couplers. As a consequence of the interaction between both populations, Josephson oscillations are observed. These oscillations together with the selection of the length of the coupling region allows guiding the polariton population at will to just one or to the two output terminals. Additionally, our study on the polarization-resolved PL has revealed a conspicuous interference in the output terminals. It results from the interference of forward and backward's moving polaritons. Up to now, we have only addressed the linear polarization dependence of this interference but a careful analysis of the degree of circular polarization of the coupler emission could set the basis for the development of spin-based logic devices employing these couplers, which would be capable of monitoring and controlling the spin of polaritons in the output terminals.

The device proposed in chapter 5 has demonstrated its functionality as an ultrafast counter-directional polariton router. The astute combination of 1D and 2D confinement on the different parts of the device allows the direct manipulation of the condensates' trajectory without any external control parameter, laying out the device capabilities to reverse the propagation direction. Furthermore, our experimental measurements demonstrate that by engineering the size parameters of the polariton router, a filtering of modes with discrete energies at the output port is achieved. This functionality would allow in future experiments the use of the device as a transistor switch, capable of controlling the emergence of a monochromatic signal at the output port. In this way, more complex architectures could be designed by connecting several of these routers or combining them with additional devices. We have obtained a coupling efficiency between the different parts of the router of $\sim$11.5 %, which considerably limits the propagation of the signal. Therefore, further investigations are needed to enhance the counter-directional device efficiency.

In Chapter 6 we have reported a direct measurement of the $n = 0$ Landau level wavefunctions in a photonic honeycomb lattice of polaritons under the effect of a synthetic magnetic field. The use of these structures allows to emulate the transport and topological properties of

graphene, as it has been proven by the dispersion relation of the honeycomb lattices, where Dirac cones are visible. Due to the appearance of a synthetic magnetic field of the order of 10^3 T, created by modulating the inter-pillar distance of the micropillars that compose the lattice, several quantized Landau levels arise in the proximity of the Dirac cones. The Landau levels here reported are promising for the study of strongly correlated photonic phases: taking advantage of the strong coupling between excitons and photons, polariton honeycomb lattices open the way to study the lasing in Landau levels.

All the devices used in this thesis are easily scalable and integrable into networks based on polaritons. Our methods allow the optical generation and manipulation of 1D and 2D condensates in arbitrary locations inside semiconductor structures in the micrometer scale. We have demonstrated how to control the trajectory, flow speed and interaction between polaritons in these microstructures. The study of these light-matter states paves the way to take advantage of their nonlinearity in the next generation of photonics.

Conclusiones generales y perspectivas futuras de esta tesis

En esta tesis hemos investigado, tanto en espacio real como en el de momentos, las propiedades de los condensados de polaritones en microcavidades esculpidas. Siguiendo el orden de los capítulos, resumimos a continuación los principales logros de esta tesis:

La robustez térmica de la coherencia de los condensados de polaritones se aborda en el capítulo 3. Esta coherencia, evidenciada por la presencia de franjas de interferencia a lo largo de la propagación de los polaritones, revela una correlación de las fases de los condensados, conservada en el tiempo y el espacio. Las franjas se observan en el espacio de momentos cuando los condensados, que están separados espacialmente, viajan con la misma velocidad. De forma adicional, se observan franjas durante el cruce de los condensados en el espacio real. El análisis de la visibilidad de las franjas (υ) y la fracción de polaritones condensados (f_C) conduce al mismo resultado: ambas magnitudes nos permiten determinar una temperatura crítica para la condensación tipo Bose-Einstein cuando decaen a cero, a pesar de que los condensados de polaritones son sistemas fuera de equilibrio. La comparación de los resultados con dos modelos teóricos desarrollados para condensados atómicos en equilibrio conduce a un valor de la temperatura crítica que es muy similar para ambos modelos. Esta es la razón por la cual no hemos podido identificar qué modelo ajusta con mayor precisión los resultados. Por lo tanto, sería necesario el desarrollo de una teoría más adecuada, que tenga en cuenta las características de condensados polaritónicos.

En el capítulo 4 se resumen los experimentos realizados con los dispositivos denominados *acopladores*. Los resultados demuestran la funcionalidad de estos acopladores como dispositivos totalmente ópticos, estableciendo el camino hacia el enrutamiento y guiado de los condensados hacia diferentes terminales de salida seleccionando adecuadamente las dimensiones de los dispositivos. En primer lugar hemos investigado las implicaciones del uso de

guías de ondas dobladas en la propagación de los condensados de polaritones: una variación abrupta de 45º en su trayectoria produce una disminución significativa del momento de los polaritones. Es posible seleccionar un valor específico del momento durante la creación de estas partículas, sin embargo, después de sobrepasar la curva, se pierde el control sobre su velocidad. Por lo tanto, sería deseable investigar si los efectos de una disminución del ángulo de la curva podría ayudar a controlar el momento de los polaritones en todo el dispositivo. En segundo lugar, nuestras medidas muestran que, dependiendo de las dimensiones de los dispositivos, los polaritones pueden transferirse entre las dos guías de ondas que componen los acopladores. Como resultado de la interacción entre ambas poblaciones, se observan oscilaciones de Josephson. Estas oscilaciones, junto con la selección del tamaño de la región de acoplamiento, permiten guiar la población de polaritones a voluntad hacia solo uno de los terminales o repartirla entre ambos. Adicionalmente, nuestro estudio sobre la polarización de la fotoluminiscencia ha revelado pronunciadas oscilaciones de la intensidad de la emisión para determinadas orientaciones de la polarización. Este resultado se produce por la interferencia entre polaritones moviéndose hacia adelante y hacia atrás en el terminal de salida. Hasta ahora, solo hemos abordado el análisis de la polarización lineal de esta interferencia pero un estudio cuidadoso del grado de polarización circular de la emisión del acoplador podría sentar las bases para el uso de estos acopladores como dispositivos lógicos basados en el espín, empleando estos acopladores, con los que sería posible monitorizar y controlar el espín de los polaritones en los terminales de salida.

El dispositivo propuesto en el capítulo 5 ha demostrado su funcionalidad como enrutador contradireccional ultrarrápido. La astuta combinación de confinamiento en 1D y en 2D a lo largo de las diferentes partes del dispositivo permite la manipulación directa de la trayectoria de los condensados sin ningún parámetro de control externo, estableciendo así la capacidad del dispositivo para invertir la dirección de propagación. Además, nuestras medidas experimentales demuestran que al diseñar las dimensiones del enrutador, se logra un filtrado de modos con energías discretas en el puerto de salida. Este funcionamiento permitiría en futuros experimentos usar el dispositivo como un interruptor, capaz de controlar la aparición de una señal monocromática en el puerto de salida. De esta forma, se podrían diseñar construcciones más complejas, conectando varios de estos enrutadores o combinándolos con otros dispositivos. En los experimentos, hemos obtenido una eficiencia de acoplamiento entre las diferentes partes del enrutador del $\sim$11.5 %, lo que limita considerablemente la propagación de los polaritones. Por lo tanto, es necesario continuar investigando alternativas que permitan mejorar la eficiencia del dispositivo.

En el capítulo 6 hemos realizado una medida directa de la función de ondas del nivel $n = 0$ de Landau en una red fotónica de panal de abeja bajo el efecto de un campo magnético artificial. El uso de estas estructuras permite simular las propiedades topológicas y de transporte del grafeno, tal como se ha demostrado por la presencia de conos de Dirac en la relación de dispersión de redes de panal de abeja. La modulación de la distancia entre los micropilares que componen la red puede inducir la aparición de un campo magnético artificial del orden de 10^3 T, lo que produce la aparición de varios niveles de Landau cuantizados en la proximidad de los conos de Dirac. Los niveles de Landau aquí investigados son prometedores para el estudio de fases fotónicas fuertemente correlacionadas: aprovechando el acoplamiento fuerte entre los excitones y los fotones, las redes de panal de abeja abren el camino para estudiar la emisión láser en estos niveles de Landau.

Todos los dispositivos utilizados en esta tesis son fácilmente reescalables e integrables en redes basadas en polaritones. Nuestros métodos experimentales permiten no solo la generación óptica sino también la manipulación de condensados en 1D y 2D en regiones espaciales arbitrarias dentro de microestructuras semiconductoras. A lo largo de esta tesis, hemos demostrado cómo controlar la trayectoria, la velocidad del flujo y la interacción entre polaritones en dichas microestructuras. Por tanto, el estudio de los estados mixtos de luz y materia, como lo son los polaritones, allana el camino para utilizar sus nolinealidades en la próxima generación de dispositivos fotónicos.

Appendix A

Polariton energy relaxation in a 1D waveguide

When a semiconductor microcavity is optically excited with an excess of energy, polaritons suffer an energy relaxation process until they reach the fundamental state. Here, we address this relaxation dynamics in a planar waveguide after two pulsed laser beams excite the structure under quasi-resonant conditions (at 1.5459 eV) and with a power above the threshold for condensation. The excitation scheme is the same as that used in Chapter 3. Fig. A.1 depicts the time-resolved PL at different time delays after the laser beams impinge on the sample at $t = 0$. The real- and k-space are indicated by the indexes 1 and 2, respectively. To avoid saturation in the streak camera due to the emission of the laser, only energies up to 1.5445 eV are shown. Panel (a) shows the emission at 15 ps. The excitons created by the two laser beams start to decrease their energy towards the polariton states in the LPB (extended from 1.5398 to 1.5420 eV). The emission in real-space reveals that at this time delay polaritons do not extend beyond the excitation area while decreasing their energy. Furthermore, the corresponding k-space shows that this small population of polaritons is initially created with $k_x = 0$. The intensity has been intentionally saturated in panel (a.2) in order to observe the contribution from the lower energies. When the time is further increased just by 10 ps, panel (b), the polariton population considerably increases around ~ 1.541 eV. Their momentum now shows a wide distribution in the range $0 < |k_x| < 1.5$ μm^{-1}, since polaritons start to move in the positive and negative x-direction. In panel (c), the emission in real-space shows the formation of two polariton condensates from each laser source, propagating towards the left/right hand side of the excitation spot. As a result, these condensates show discrete values of the wave vector, ± 1.6 μm^{-1}, negative

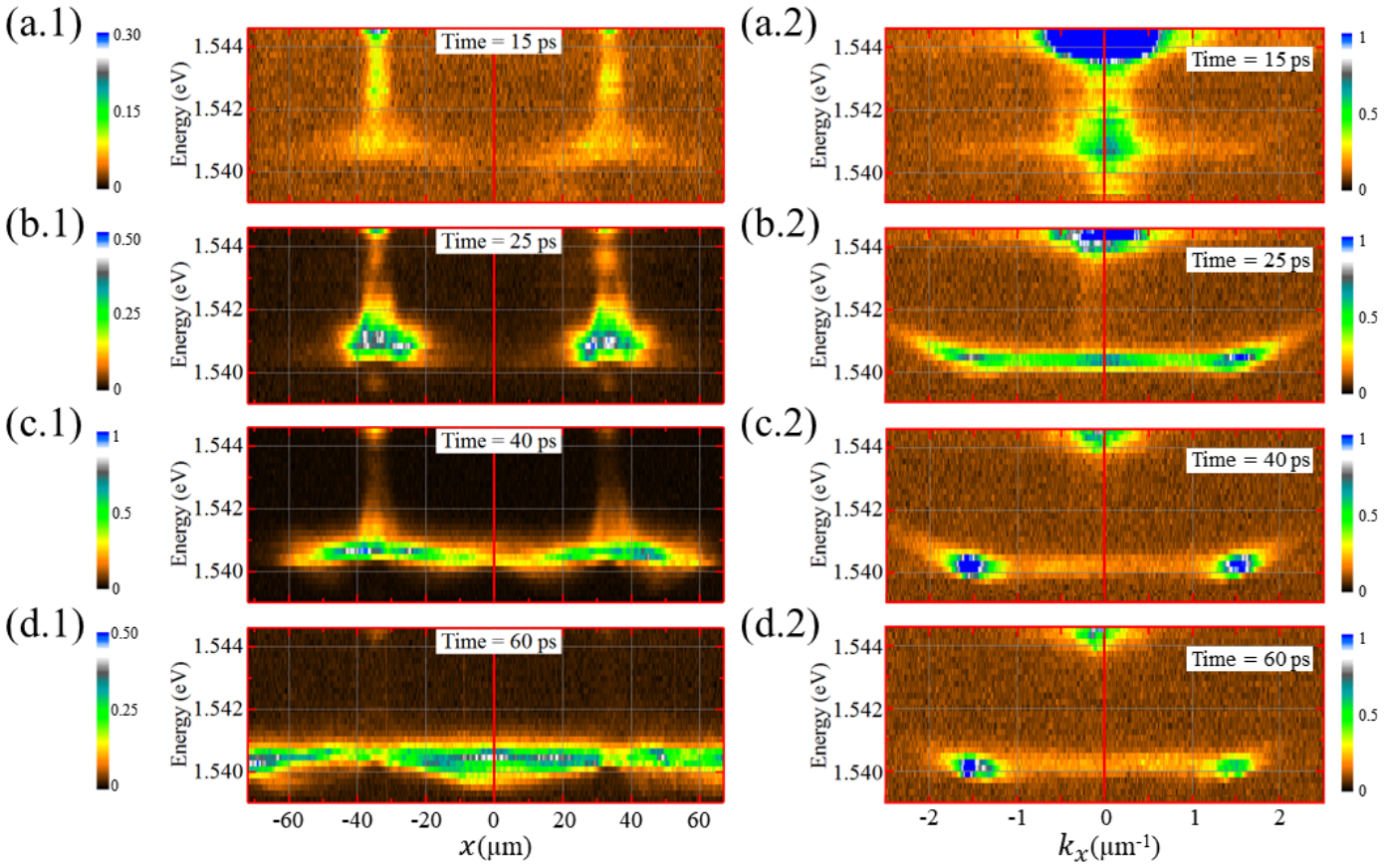

Figure A.1. Energy relaxation process in a 1D waveguide under quasi-resonant excitation with two laser beams. The time-resolved PL is shown at four different time delays: (a) 15, (b) 25, (c) 40 and (d) 60 ps after the laser excites the sample ($t = 0$). The indexes 1 and 2 refer to real- and k-space, respectively. The red solid line in real- /momentum-space marks the position $x = 0/k_x = 0$. The intensity is coded in linear false-color scale. The emissions have been measured with a power density of 9 kW/cm^2.

(positive) for those traveling towards left (right). Note that at this time, 40 ps, the PL is practically concentrated at a discrete energy level at 1.5404 eV. Finally, at 60 ps [panel (d)], the condensates propagate along the structure and only emission arising from the fundamental state is observed. Therefore, the energy relaxation dynamics clearly demonstrate the macroscopic occupation of the fundamental level when a polariton condensate is created.

References

[1] P. Saurel, "On the classification of crystals," Bulletin of the American Mathematical Society **17**, 398 (1911).

[2] M. P. Marder, *Condensed Matter Physics* (John Wiley & Sons, Hoboken, New Jersey, 2010).

[3] M. Cardona and P. Yu, *Fundamentals of Semiconductors* (Springer, Berlin, 2005).

[4] E. Hanamura and H. Haug, "Condensation effects of excitons," Physics Reports **33**, 209 (1977).

[5] A. Kavokin, J. Baumberg, G. Malpuech, and F. Laussy, *Microcavities*, Oxford science publications (OUP Oxford, 2011).

[6] I. Hernández-Romano, M. A. Cruz-Garcia, C. Moreno-Hernández, D. Monzón-Hernández, E. O. López-Figueroa, O. E. Paredes-Gallardo, M. Torres-Cisneros, and J. Villatoro, "Optical fiber temperature sensor based on a microcavity with polymer overlay," Optics Express **24**, 5654 (2016).

[7] F. Favero, L. Araujo, G. Bouwmans, V. Finazzi, J. Villatoro, and V. Pruneri, "Spheroidal Fabry-Perot microcavities in optical fibers for high-sensitivity sensing," Optics Express **20**, 7112 (2012).

[8] K. J. Vahala, "Optical microcavities," Nature **424**, 839 (2003).

[9] V. Savona, "Strong coupling of exciton-polaritons in semiconductor microcavities," Journal of Crystal Growth **184**, 737 (1998).

[10] H. Deng, H. Haug, and Y. Yamamoto, "Exciton-polariton Bose-Einstein condensation," Reviews of Modern Physics **82**, 1489 (2010).

[11] J. Gerard and B. Gayral, "InAs quantum dots: artificial atoms for solid-state cavity-quantum electrodynamics," Physica E: Low-dimensional Systems and Nanostructures **9**, 131 (2001).

[12] D. Sanvitto and V. Timofeev, *Exciton polaritons in microcavities: new frontiers*, Vol. **172** (Springer Science & Business Media, Berlin, 2012).

[13] J. Hopfield, "Theory of the contribution of excitons to the complex dielectric constant of crystals," Physical Review **112**, 1555 (1958).

[14] E. T. Jaynes and F. W. Cummings, "Comparison of quantum and semiclassical radiation theories with application to the beam maser," Proceedings of the IEEE **51**, 89 (1963).

[15] R. G. Ulbrich and C. Weisbuch, "Resonant Brillouin Scattering of Excitonic Polaritons in Gallium Arsenide," Physical Review Letters **38**, 865 (1977).

[16] C. Weisbuch, M. Nishioka, A. Ishikawa, and Y. Arakawa, "Observation of the coupled exciton-photon mode splitting in a semiconductor quantum microcavity," Physical Review Letters **69**, 3314 (1992).

[17] T. Byrnes, N. Y. Kim, and Y. Yamamoto, "Exciton-polariton condensates," Nature Physics **10**, 803 (2014).

[18] C. Ciuti, V. Savona, C. Piermarocchi, A. Quattropani, and P. Schwendimann, "Role of the exchange of carriers in elastic exciton-exciton scattering in quantum wells," Physical Review B **58**, 7926 (1998).

[19] S. N. Bose, "Plancks Gesetz und Lichtquantenhypothese," Zeitschrift für Physik **26**, 178 (1924).

[20] A. Einstein, "Quantentheorie des einatomigen idealen Gases," Akademie der Wissenschaften **1**, 3 (1924).

[21] M. H. Anderson, J. R. Ensher, M. R. Matthews, C. E. Wieman, and E. A. Cornell, "Observation of Bose-Einstein Condensation in a Dilute Atomic Vapor," Science **269**, 198 (1995).

[22] K. B. Davis, M. O. Mewes, M. R. Andrews, N. J. van Druten, D. S. Durfee, D. Kurn, and W. Ketterle, "Bose-Einstein condensation in a gas of sodium atoms," Physical Review Letters **75**, 3969 (1995).

[23] "The Nobel Prize in Physics 2001," Nobel Media (2020). https://www.nobelprize.org/prizes/physics/2001/summary/

[24] T. Greicius, "Space Station Experiment Reaches Ultracold Milestone," NASA Media (2018). https://www.nasa.gov/feature/jpl/space-station-experiment-reaches-ultracold-milestone

[25] K. Lagoudakis, *The Physics of Exciton-Polariton Condensates*, Physics (EPFL Press, Lausanne, Switzerland, 2013).

[26] A. Imamoglu, R. J. Ram, S. Pau, and Y. Yamamoto, "Non-equilibrium condensates and lasers without inversion: Exciton-polariton lasers," Physical Review A **53**, 4250 (1996).

[27] P. Savvidis, J. Baumberg, R. Stevenson, M. Skolnick, D. Whittaker, and J. Roberts, "Angle-resonant stimulated polariton amplifier," Physical Review Letters **84**, 1547 (2000).

[28] R. Stevenson, V. Astratov, M. Skolnick, D. Whittaker, M. Emam-Ismail, A. Tartakovskii, P. Savvidis, J. Baumberg, and J. Roberts, "Continuous wave observation of massive polariton redistribution by stimulated scattering in semiconductor microcavities," Physical Review Letters **85**, 3680 (2000).

[29] J. Kasprzak, M. Richard, S. Kundermann, A. Baas, P. Jeambrun, J. M. J. Keeling, F. M. Marchetti, M. H. Szymańska, R. André, J. L. Staehli, V. Savona, P. B. Littlewood, B. Deveaud, and L. S. Dang, "Bose-Einstein condensation of exciton polaritons," Nature **443**, 409 (2006).

[30] E. Del Valle, D. Sanvitto, A. Amo, F. Laussy, R. André, C. Tejedor, and L. Viña, "Dynamics of the formation and decay of coherence in a polariton condensate," Physical Review Letters **103**, 096 404 (2009).

[31] A. I. Tartakovskii, M. Emam-Ismail, R. M. Stevenson, M. S. Skolnick, V. N. Astratov, D. M. Whittaker, J. J. Baumberg, and J. S. Roberts, "Relaxation bottleneck and its suppression in semiconductor microcavities," Physical Review B **62**, R2283 (2000).

[32] F. Tassone, C. Piermarocchi, V. Savona, A. Quattropani, and P. Schwendimann, "Bottleneck effects in the relaxation and photoluminescence of microcavity polaritons," Physical Review B **56**, 7554 (1997).

[33] D. Porras, C. Ciuti, J. Baumberg, and C. Tejedor, "Polariton dynamics and Bose-Einstein condensation in semiconductor microcavities," Physical Review B **66**, 085 304 (2002).

[34] D. M. Coles, P. Michetti, C. Clark, W. C. Tsoi, A. M. Adawi, J.-S. Kim, and D. G. Lidzey, "Vibrationally Assisted Polariton-Relaxation Processes in Strongly Coupled Organic-Semiconductor Microcavities," Advanced Functional Materials **21**, 3691 (2011).

[35] E. Burstein and C. Weisbuch, *Confined electrons and photons: New physics and applications*, Vol. 340 (Springer Science & Business Media, Boston, Massachusetts, 2012).

[36] J. R. Anglin and W. Ketterle, "Bose–Einstein condensation of atomic gases," Nature **416**, 211 (2002).

[37] R. Houdré, C. Weisbuch, R. Stanley, U. Oesterle, and M. Ilegems, "Coherence effects in light scattering of two-dimensional photonic disordered systems: Elastic scattering of cavity polaritons," Physical Review B **61**, R13 333 (2000).

[38] D. Snoke, "Spontaneous Bose coherence of excitons and polaritons," Science **298**, 1368 (2002).

[39] F. Laussy, G. Malpuech, A. Kavokin, and P. Bigenwald, "Coherence dynamics in microcavities and polariton lasers," Journal of Physics: Condensed Matter **16**, S3665 (2004).

[40] M. Richard, J. Kasprzak, R. Romestain, R. André, and L. S. Dang, "Spontaneous coherent phase transition of polaritons in CdTe microcavities," Physical Review Letters **94**, 187 401 (2005).

[41] I. Carusotto and C. Ciuti, "Spontaneous microcavity-polariton coherence across the parametric threshold: Quantum Monte Carlo studies," Physical Review B **72**, 125 335 (2005).

[42] H. Deng, G. S. Solomon, R. Hey, K. H. Ploog, and Y. Yamamoto, "Spatial coherence of a polariton condensate," Physical Review Letters **99**, 126 403 (2007).

[43] D. Whittaker and P. Eastham, "Coherence properties of the microcavity polariton condensate," EPL (Europhysics Letters) **87**, 27 002 (2009).

[44] K. Lagoudakis, B. Pietka, M. Wouters, R. André, and B. Deveaud-Plédran, "Coherent oscillations in an exciton-polariton Josephson junction," Physical Review Letters **105**, 120 403 (2010).

[45] I. Aleiner, B. Altshuler, and Y. Rubo, "Radiative coupling and weak lasing of exciton-polariton condensates," Physical Review B **85**, 121 301 (2012).

[46] R. Spano, J. Cuadra, G. Tosi, C. Antón, C. A. Lingg, D. Sanvitto, M. D. Martín, L. Viña, P. R. Eastham, M. van der Poel, and J. M. Hvam, "Coherence properties of exciton polariton OPO condensates in one and two dimensions," New Journal of Physics **14**, 075 018 (2012).

[47] A. Hayat, C. Lange, L. A. Rozema, R. Chang, S. Potnis, H. M. van Driel, A. M. Steinberg, M. Steger, D. W. Snoke, L. N. Pfeiffer, et al., "Enhanced coherence between condensates formed resonantly at different times." Optics Express **22**, 30 559 (2014).

[48] G. Christmann, G. Tosi, N. G. Berloff, P. Tsotsis, P. S. Eldridge, Z. Hatzopoulos, P. G. Savvidis, and J. J. Baumberg, "Oscillatory solitons and time-resolved phase locking of two polariton condensates," New Journal of Physics **16**, 103 039 (2014).

[49] K. Ji, V. N. Gladilin, and M. Wouters, "Temporal coherence of one-dimensional nonequilibrium quantum fluids," Physical Review B **91**, 045 301 (2015).

[50] K. S. Daskalakis, S. A. Maier, and S. Kéna-Cohen, "Spatial coherence and stability in a disordered organic polariton condensate," Physical Review Letters **115**, 035 301 (2015).

[51] S. Kim, B. Zhang, Z. Wang, J. Fischer, S. Brodbeck, M. Kamp, C. Schneider, S. Höfling, and H. Deng, "Coherent Polariton Laser," Physical Review X **6**, 011 026 (2016).

[52] A. Demenev, Y. V. Grishina, S. Novikov, V. Kulakovskii, C. Schneider, and S. Höfling, "Loss of coherence in cavity-polariton condensates: Effect of disorder versus exciton reservoir," Physical Review B **94**, 195 302 (2016).

[53] D. Caputo, D. Ballarini, G. Dagvadorj, C. S. Muñoz, M. D. Giorgi, L. Dominici, K. West, L. N. Pfeiffer, G. Gigli, F. P. Laussy, M. H. Szymańska, and D. Sanvitto, "Topological order and thermal equilibrium in polariton condensates," Nature Materials **17**, 145 (2018).

[54] J. Fischer, I. Savenko, M. Fraser, S. Holzinger, S. Brodbeck, M. Kamp, I. Shelykh, C. Schneider, and S. Höfling, "Spatial coherence properties of one dimensional exciton-polariton condensates," Physical Review Letters **113**, 203 902 (2014).

[55] A. A. High, J. R. Leonard, A. T. Hammack, M. M. Fogler, L. V. Butov, A. V. Kavokin, K. L. Campman, and A. C. Gossard, "Spontaneous coherence in a cold exciton gas," Nature **483**, 584 (2012).

[56] M. R. Andrews, "Observation of Interference Between Two Bose Condensates," Science **275**, 637 (1997).

[57] C. Antón, G. Tosi, M. D. Martín, Z. Hatzopoulos, G. Konstantinidis, P. S. Eldridge, P. G. Savvidis, C. Tejedor, and L. Viña, "Quantum coherence in momentum space of light-matter condensates," Physical Review B **90**, 081 407(R) (2014).

[58] E. Rozas, M. D. Martín, C. Tejedor, L. Viña, G. Deligeorgis, Z. Hatzopoulos, and P. G. Savvidis, "Temperature dependence of the coherence in polariton condensates," Physical Review B **97**, 075 442 (2018).

[59] E. Rozas, M. D. Martín, C. Tejedor, L. Viña, G. Deligeorgis, Z. Hatzopoulos, and P. G. Savvidis, "Determination of polariton condensates' critical temperature," Physica Status Solidi (b) p. 1800519 (2019).

[60] L. Pitaevskii and S. Stringari, "Interference of Bose-Einstein condensates in momentum space," Physical Review Letters **83**, 4237 (1999).

[61] B. D. Josephson, "Possible new effects in superconductive tunnelling," Physics Letters **1**, 251 (1962).

[62] P. W. Anderson and J. M. Rowell, "Probable Observation of the Josephson Superconducting Tunneling Effect," Physical Review Letters **10**, 230 (1963).

[63] A. Barone and G. Paterno, *Physics and applications of the Josephson effect* (Wiley, Hoboken, New Jersey, 1982).

[64] F. Sols, "Josephson effect between Bose condensates," Proceedings of the International School of Physics Enrico Fermi **140**, 453 (1999).

[65] S. Raghavan, A. Smerzi, S. Fantoni, and S. Shenoy, "Coherent oscillations between two weakly coupled Bose-Einstein condensates: Josephson effects, π oscillations, and macroscopic quantum self-trapping," Physical Review A **59**, 620 (1999).

[66] R. Gati and M. K. Oberthaler, "A bosonic Josephson junction," Journal of Physics B: Atomic, Molecular and Optical Physics **40**, R61 (2007).

[67] M. Chuchem, K. Smith-Mannschott, M. Hiller, T. Kottos, A. Vardi, and D. Cohen, "Quantum dynamics in the bosonic Josephson junction," Physical Review A **82**, 053 617 (2010).

[68] O. Morsch and M. Oberthaler, "Dynamics of Bose-Einstein condensates in optical lattices," Reviews of Modern Physics **78**, 179 (2006).

[69] Y. Shin, G.-B. Jo, M. Saba, T. A. Pasquini, W. Ketterle, and D. E. Pritchard, "Optical Weak Link between Two Spatially Separated Bose-Einstein Condensates," Physical Review Letters **95**, 170 402 (2005).

[70] I. A. Shelykh, D. D. Solnyshkov, G. Pavlovic, and G. Malpuech, "Josephson effects in condensates of excitons and exciton polaritons," Physical Review B **78**, 041 302 (2008).

[71] M. Abbarchi, A. Amo, V. Sala, D. Solnyshkov, H. Flayac, L. Ferrier, I. Sagnes, E. Galopin, A. Lemaître, G. Malpuech, et al., "Macroscopic quantum self-trapping and Josephson oscillations of exciton polaritons," Nature Physics **9**, 275 (2013).

[72] F. Meier and W. Zwerger, "Josephson tunneling between weakly interacting Bose-Einstein condensates," Physical Review A **64**, 033 610 (2001).

[73] J. Klaers, F. Vewinger, and M. Weitz, "Thermalization of a two-dimensional photonic gas in a 'white wall'photon box," Nature Physics **6**, 512 (2010).

[74] A. Amo, J. Lefrère, S. Pigeon, C. Adrados, C. Ciuti, I. Carusotto, R. Houdré, E. Giacobino, and A. Bramati, "Superfluidity of polaritons in semiconductor microcavities," Nature Physics **5**, 805 (2009).

[75] F. Marsault, H. S. Nguyen, D. Tanese, A. Lemaître, E. Galopin, I. Sagnes, A. Amo, and J. Bloch, "Realization of an all optical exciton-polariton router," Applied Physics Letters **107**, 201 115 (2015).

[76] T. Gao, P. S. Eldridge, T. C. H. Liew, S. Tsintzos, G. Stavrinidis, G. Deligeorgis, Z. Hatzopoulos, and P. G. Savvidis, "Polariton condensate transistor switch," Physical Review B **85**, 235 102 (2012).

[77] C. Anton, T. C. H. Liew, G. Tosi, M. D. Martin, T. Gao, Z. Hatzopoulos, P. S. Eldridge, P. G. Savvidis, and L. Viña, "Dynamics of a polariton condensate transistor switch," Applied Physics Letters **101**, 261 116 (2012).

[78] C. Antón, *On the physics of exciton-polariton condensates: from fundamental phenomena to emergent applications*, Ph.D. thesis, Universidad de Madrid (2015). https://repositorio.uam.es/handle/10486/666358

[79] A. H. Castro Neto, F. Guinea, N. M. R. Peres, K. S. Novoselov, and A. K. Geim, "The electronic properties of graphene," Reviews of Modern Physics **81**, 110 (2009).

[80] W. Li, A. K. Tuchman, H.-C. Chien, and M. A. Kasevich, "Extended coherence time with atom-number squeezed states," Physical Review Letters **98**, 040 402 (2007).

[81] T. Billam and S. Gardiner, "Coherence and instability in a driven Bose–Einstein condensate: a fully dynamical number-conserving approach," New Journal of Physics **14**, 013 038 (2012).

[82] S. Bernon, H. Hattermann, D. Bothner, M. Knufinke, P. Weiss, F. Jessen, D. Cano, M. Kemmler, R. Kleiner, D. Koelle, et al., "Manipulation and coherence of ultra-cold atoms on a superconducting atom chip," Nature Communications **4**, 2380 (2013).

[83] R. Balili, V. Hartwell, D. Snoke, L. Pfeiffer, and K. West, "Bose-Einstein Condensation of Microcavity Polaritons in a Trap," Science **316**, 1007 (2007).

[84] I. Bloch, T. W. Hänsch, and T. Esslinger, "Measurement of the spatial coherence of a trapped Bose gas at the phase transition," Nature **403**, 166 (2000).

[85] R. Gati, B. Hemmerling, J. Fölling, M. Albiez, and M. K. Oberthaler, "Noise thermometry with two weakly coupled Bose-Einstein condensates," Physical Review Letters **96**, 130 404 (2006).

[86] R. Gati, J. Esteve, B. Hemmerling, T. Ottenstein, J. Appmeier, A. Weller, and M. Oberthaler, "A primary noise thermometer for ultracold Bose gases," New Journal of Physics **8**, 189 (2006).

[87] C. Ouellet-Plamondon, G. Sallen, F. Morier-Genoud, D. Oberli, M. Portella-Oberli, and B. Deveaud, "Reservoir-induced decoherence of resonantly excited confined polaritons," Physical Review B **95**, 085 302 (2017).

[88] C. Anton, T. C. H. Liew, G. Tosi, M. D. Martin, T. Gao, Z. Hatzopoulos, P. S. Eldridge, P. G. Savvidis, and L. Viña, "Energy relaxation of exciton-polariton condensates in quasi-one-dimensional microcavities," Physical Review B **88**, 035 313 (2013).

[89] C. Antón, T. C. H. Liew, D. Sarkar, M. D. Martín, Z. Hatzopoulos, P. S. Eldridge, P. G. Savvidis, and L. Viña, "Operation speed of polariton condensate switches gated by excitons," Physical Review B **89**, 235 312 (2014).

[90] E. Wertz, A. Amo, D. Solnyshkov, L. Ferrier, T. Liew, D. Sanvitto, P. Senellart, I. Sagnes, A. Lemaître, A. Kavokin, et al., "Propagation and amplification dynamics of 1D polariton condensates," Physical Review Letters **109**, 216 404 (2012).

[91] E. Wertz, L. Ferrier, D. D. Solnyshkov, R. Johne, D. Sanvitto, A. Lemaître, I. Sagnes, R. Grousson, A. V. Kavokin, P. Senellart, G. Malpuech, and J. Bloch, "Spontaneous formation and optical manipulation of extended polariton condensates," Nature Physics **6**, 860 (2010).

[92] D. Tanese, D. D. Solnyshkov, A. Amo, L. Ferrier, E. Bernet-Rollande, E. Wertz, I. Sagnes, A. Lemaître, P. Senellart, G. Malpuech, and J. Bloch, "Backscattering Suppression in Supersonic 1D Polariton Condensates," Physical Review Letters **108**, 036 405 (2012).

[93] G. Dasbach, T. Baars, M. Bayer, A. Larionov, and A. Forchel, "Coherent and incoherent polaritonic gain in a planar semiconductor microcavity," Physical Review B **62**, 13 076 (2000).

[94] P. Savvidis, C. Ciuti, J. Baumberg, D. Whittaker, M. Skolnick, and J. Roberts, "Off-branch polaritons and multiple scattering in semiconductor microcavities," Physical Review B **64**, 075 311 (2001).

[95] M. Bijlsma and H. Stoof, "Renormalization group theory of the three-dimensional dilute Bose gas," Physical Review A **54**, 5085 (1996).

[96] P. Grüter, D. Ceperley, and F. Laloë, "Critical temperature of Bose-Einstein condensation of hard-sphere gases," Physical Review Letters **79**, 3549 (1997).

[97] N. Prokof'ev and B. Svistunov, "Two-dimensional weakly interacting Bose gas in the fluctuation region," Physical Review A **66**, 043 608 (2002).

[98] S. Giorgini, L. Pitaevskii, and S. Stringari, "Condensate fraction and critical temperature of a trapped interacting Bose gas," Physical Review A **54**, R4633 (1996).

[99] D. A. B. Miller, "Are optical transistors the logical next step?" Nature Photonics **4**, 3 (2010).

[100] W. Chen, K. M. Beck, R. Bücker, M. Gullans, M. D. Lukin, H. Tanji-Suzuki, and V. Vuletic, "All-optical switch and transistor gated by one stored photon," Science **341**, 768 (2013).

[101] A. Goodarzi and M. Ghanaatshoar, "Coherent all-optical transistor based on frustrated total internal reflection," Scientific Reports **8**, 5069 (2018).

[102] D. Sanvitto and S. Kéna-Cohen, "The road towards polaritonic devices," Nature Materials **15**, 1061 (2016).

[103] T. Liew, A. Kavokin, and I. Shelykh, "Optical circuits based on polariton neurons in semiconductor microcavities," Physical Review Letters **101**, 016 402 (2008).

[104] V. M. Menon, L. I. Deych, and A. A. Lisyansky, "Towards polaritonic logic circuits," Nature Photonics **4**, 345 (2010).

[105] H. S. Nguyen, D. Vishnevsky, C. Sturm, D. Tanese, D. Solnyshkov, E. Galopin, A. Lemaître, I. Sagnes, A. Amo, G. Malpuech, et al., "Realization of a double-barrier resonant tunneling diode for cavity polaritons," Physical Review Letters **110**, 236 601 (2013).

[106] D. Ballarini, M. De Giorgi, E. Cancellieri, R. Houdré, E. Giacobino, R. Cingolani, A. Bramati, G. Gigli, and D. Sanvitto, "All-optical polariton transistor," Nature Communications **4**, 1 (2013).

[107] M. Klaas, J. Beierlein, E. Rozas, S. Klembt, H. Suchomel, T. H. Harder, K. Winkler, M. Emmerling, H. Flayac, M. D. Martín, L. Viña, S. Höfling, and C. Schneider, "Counter-directional polariton coupler," Applied Physics Letters **114**, 061 102 (2019).

[108] A. V. Zasedatelev, A. V. Baranikov, D. Urbonas, F. Scafirimuto, U. Scherf, T. Stöferle, R. F. Mahrt, and P. G. Lagoudakis, "A room-temperature organic polariton transistor," Nature Photonics **13**, 378 (2019).

[109] L. Ferrier, E. Wertz, R. Johne, D. D. Solnyshkov, P. Senellart, I. Sagnes, A. Lemaître, G. Malpuech, and J. Bloch, "Interactions in Confined Polariton Condensates," Physical Review Letters **106**, 126 401 (2011).

[110] C. Antón, T. C. H. Liew, J. Cuadra, M. D. Martín, P. S. Eldridge, Z. Hatzopoulos, G. Stavrinidis, P. G. Savvidis, and L. Viña, "Quantum reflections and shunting of polariton condensate wave trains: Implementation of a logic AND gate," Physical Review B **88**, 245 307 (2013).

[111] J. Ciers, J. G. Roch, J.-F. Carlin, G. Jacopin, R. Butté, and N. Grandjean, "Propagating polaritons in III-nitride slab waveguides," Physical Review Applied **7**, 034 019 (2017).

[112] Z. Han, P. Zhang, and S. I. Bozhevolnyi, "Calculation of bending losses for highly confined modes of optical waveguides with transformation optics," Optics Letters **38**, 1778 (2013).

[113] L. H. Gabrielli, D. Liu, S. G. Johnson, and M. Lipson, "On-chip transformation optics for multimode waveguide bends," Nature Communications **3**, 1 (2012).

[114] D. Liran, I. Rosenberg, K. West, L. Pfeiffer, and R. Rapaport, "Fully Guided Electrically Controlled Exciton Polaritons," ACS Photonics **5**, 4249 (2018).

[115] C. Sturm, D. Tanese, H. Nguyen, H. Flayac, E. Galopin, A. Lemaître, I. Sagnes, D. Solnyshkov, A. Amo, G. Malpuech, et al., "All-optical phase modulation in a cavity-polariton Mach–Zehnder interferometer," Nature Communications **5**, 3278 (2014).

[116] A. Amo, T. Liew, C. Adrados, R. Houdré, E. Giacobino, A. Kavokin, and A. Bramati, "Exciton–polariton spin switches," Nature Photonics **4**, 361 (2010).

[117] T. Espinosa-Ortega and T. C. H. Liew, "Complete architecture of integrated photonic circuits based on AND and NOT logic gates of exciton polaritons in semiconductor microcavities," Physical Review B **87**, 195 305 (2013).

[118] C. Antón, S. Morina, T. Gao, P. S. Eldridge, T. C. H. Liew, M. D. Martín, Z. Hatzopoulos, P. G. Savvidis, I. A. Shelykh, and L. Viña, "Optical control of spin textures in quasi-one-dimensional polariton condensates," Physical Review B **91**, 075 305 (2015).

[119] M. D. Martin, D. Ballarini, A. Amo, Ł. Kłopotowsi, L. Viña, A. Kavokin, and R. André, "Striking dynamics of II–VI microcavity polaritons after linearly polarized excitation," Physica Status Solidi (c) **2**, 3880 (2005).

[120] J. Kasprzak, R. André, L. S. Dang, I. A. Shelykh, A. V. Kavokin, Y. G. Rubo, K. V. Kavokin, and G. Malpuech, "Build up and pinning of linear polarization in the Bose condensates of exciton polaritons," Physical Review B **75**, 045 326 (2007).

[121] J. J. Baumberg, A. V. Kavokin, S. Christopoulos, A. J. D. Grundy, R. Butté, G. Christmann, D. D. Solnyshkov, G. Malpuech, G. Baldassarri Höger von Högersthal, E. Feltin, J.-F. Carlin, and N. Grandjean, "Spontaneous polarization buildup in a room-temperature polariton laser," Physical Review Letters **101**, 136 409 (2008).

[122] T. Lecomte, V. Ardizzone, M. Abbarchi, C. Diederichs, A. Miard, A. Lemaître, I. Sagnes, P. Senellart, J. Bloch, C. Delalande, J. Tignon, and P. Roussignol, "Optical parametric oscillation in one-dimensional microcavities," Physical Review B **87**, 155 302 (2013).

[123] L. Liao, Y. Ling, S. Luo, Z. Zhang, J. Wang, and Z. Chen, "Propagation of a polariton condensate in a one-dimensional microwire at room temperature," Applied Physics Express **12**, 052 009 (2019).

[124] M. Pärs, C. C. Hofmann, K. Willinger, P. Bauer, M. Thelakkat, and J. Köhler, "An organic optical transistor operated under ambient conditions," Angewandte Chemie International Edition **50**, 11 405 (2011).

[125] K. Jain and G. W. Pratt, "Optical transistor," Applied Physics Letters **28**, 719 (1976).

[126] J. Oksanen and J. Tulkki, "Coherent optical logic by laser amplifiers with feedback," Journal of Lightwave Technology **24**, 4918 (2006).

[127] H. Mabuchi, "Cavity-QED models of switches for attojoule-scale nanophotonic logic," Physical Review A **80**, 045 802 (2009).

[128] I. Fushman, D. Englund, A. Faraon, N. Stoltz, P. Petroff, and J. Vučković, "Controlled phase shifts with a single quantum dot," Science **320**, 769 (2008).

[129] M. Vladimirova, S. Cronenberger, D. Scalbert, K. V. Kavokin, A. Miard, A. Lemaître, J. Bloch, D. Solnyshkov, G. Malpuech, and A. V. Kavokin, "Polariton-polariton interaction constants in microcavities," Physical Review B **82**, 075 301 (2010).

[130] B. Nelsen, G. Liu, M. Steger, D. W. Snoke, R. Balili, K. West, and L. Pfeiffer, "Dissipationless flow and sharp threshold of a polariton condensate with long lifetime," Physical Review X **3**, 041 015 (2013).

[131] D. Niemietz, J. Schmutzler, P. Lewandowski, K. Winkler, M. Aßmann, S. Schumacher, S. Brodbeck, M. Kamp, C. Schneider, S. Höfling, and M. Bayer, "Experimental realization of a polariton beam amplifier," Physical Review B **93**, 235 301 (2016).

[132] H. Flayac and I. G. Savenko, "An exciton-polariton mediated all-optical router," Applied Physics Letters **103**, 201 105 (2013).

[133] J. C. Weeber, J. R. Krenn, A. Dereux, B. Lamprecht, Y. Lacroute, and J. P. Goudonnet, "Near-field observation of surface plasmon polariton propagation on thin metal stripes," Physical Review B **64**, 045 411 (2001).

[134] R. Su, J. Wang, J. Zhao, J. Xing, W. Zhao, C. Diederichs, T. C. Liew, and Q. Xiong, "Room temperature long-range coherent exciton polariton condensate flow in lead halide perovskites," Science Advances **4**, eaau0244 (2018).

[135] U. C. Täuber and S. Diehl, "Perturbative field-theoretical renormalization group approach to driven-dissipative Bose-Einstein criticality," Physical Review X **4**, 021 010 (2014).

[136] V. K. Kozin, I. A. Shelykh, A. V. Nalitov, and I. V. Iorsh, "Topological metamaterials based on polariton rings," Physical Review B **98**, 125 115 (2018).

[137] K. S. Novoselov, A. K. Geim, S. V. Morozov, D. Jiang, Y. Zhang, S. V. Dubonos, I. V. Grigorieva, and A. A. Firsov, "Electric field effect in atomically thin carbon films," Science **306**, 666 (2004).

[138] A. K. Geim and K. Novoselov, "The rise of graphene," Nature Materials **6**, 183 (2007).

[139] S. D. Sarma, S. Adam, E. H. Hwang, and E. Rossi, "Electronic transport in two-dimensional graphene," Reviews of Modern Physics **83**, 407 (2011).

[140] D. R. Cooper, B. D'Anjou, N. Ghattamaneni, B. Harack, M. Hilke, A. Horth, N. Majlis, M. Massicotte, L. Vandsburger, E. Whiteway, and V. Yu, "Experimental review of graphene," ISRN Condensed Matter Physics **2012** (2012).

[141] M. Polini, F. Guinea, M. Lewenstein, H. C. Manoharan, and V. Pellegrini, "Artificial honeycomb lattices for electrons, atoms and photons," Nature Nanotechnology **8**, 625 (2013).

[142] A. Amo and J. Bloch, "Exciton-polaritons in lattices: A non-linear photonic simulator," Comptes Rendus Physique **17**, 934 (2016).

[143] K. S. Novoselov, Z. Jiang, Y. Zhang, S. V. Morozov, H. L. Stormer, U. Zeitler, J. C. Maan, G. S. Boebinger, P. Kim, and A. K. Geim, "Room-temperature quantum Hall effect in graphene," Science **315**, 1379 (2007).

[144] F. Guinea, M. I. Katsnelson, and A. K. Geim, "Energy gaps and a zero-field quantum Hall effect in graphene by strain engineering," Nature Physics **6**, 30 (2010).

[145] N. Levy, S. A. Burke, K. L. Meaker, M. Panlasigui, A. Zettl, F. Guinea, A. H. C. Neto, and M. F. Crommie, "Strain-Induced Pseudo–Magnetic Fields Greater Than 300 Tesla in Graphene Nanobubbles," Science **329**, 544 (2010).

[146] F. Guinea, B. Horovitz, and P. Le Doussal, "Gauge field induced by ripples in graphene," Physical Review B **77**, 205 421 (2008).

[147] T. O. Wehling, A. V. Balatsky, A. M. Tsvelik, M. I. Katsnelson, and A. I. Lichtenstein, "Midgap states in corrugated graphene: Ab initio calculations and effective field theory," Europhysics Letters **84**, 17 003 (2008).

[148] T. Jacqmin, I. Carusotto, I. Sagnes, M. Abbarchi, D. Solnyshkov, G. Malpuech, E. Galopin, A. Lemaître, J. Bloch, and A. Amo, "Direct observation of Dirac cones and a flatband in a honeycomb lattice for polaritons," Physical Review Letters **112**, 116 402 (2014).

[149] G. Salerno, T. Ozawa, H. M. Price, and I. Carusotto, "How to directly observe Landau levels in driven-dissipative strained honeycomb lattices," 2D Materials **2**, 034 015 (2015).

[150] K. v. Klitzing, G. Dorda, and M. Pepper, "New method for high-accuracy determination of the fine-structure constant based on quantized Hall resistance," Physical Review Letters **45**, 494 (1980).

[151] M. A. Paalanen, D. C. Tsui, and A. C. Gossard, "Quantized Hall effect at low temperatures," Physical Review B **25**, 5566 (1982).

[152] M. Milićević, T. Ozawa, P. Andreakou, I. Carusotto, T. Jacqmin, E. Galopin, A. Lemaître, L. Le Gratiet, I. Sagnes, J. Bloch, and A. Amo, "Edge states in polariton honeycomb lattices," 2D Materials **2**, 034 012 (2015).

[153] K. Nakada, M. Fujita, G. Dresselhaus, and M. S. Dresselhaus, "Edge state in graphene ribbons: Nanometer size effect and edge shape dependence," Physical Review B **54**, 17 954 (1996).

[154] M. Kohmoto and Y. Hasegawa, "Zero modes and edge states of the honeycomb lattice," Physical Review B **76**, 205 402 (2007).

[155] Z. Jiang, Y. Zhang, Y. W. Tan, H. L. Stormer, and P. Kim, "Quantum Hall effect in graphene," Solid State Communications **143**, 14 (2007).

[156] Z. F. Ezawa, *Quantum Hall effects: field theoretical approach and related topics Second Edition* (World Scientific Publishing Company, Singapore, 2008).

[157] Z. Jiang, E. A. Henriksen, L. Tung, Y.-J. Wang, M. Schwartz, M. Y. Han, P. Kim, and H. L. Stormer, "Infrared spectroscopy of Landau levels of graphene," Physical Review Letters **98**, 197 403 (2007).

[158] M. L. Sadowski, G. Martinez, M. Potemski, C. Berger, and W. A. de Heer, "Landau level spectroscopy of ultrathin graphite layers," Physical Review Letters **97**, 266 405 (2006).

[159] G. Li, A. Luican, and E. Y. Andrei, "Scanning tunneling spectroscopy of graphene on graphite," Physical Review Letters **102**, 176 804 (2009).

[160] C. Lee, X. Wei, J. W. Kysar, and J. Hone, "Measurement of the elastic properties and intrinsic strength of monolayer graphene," Science **321**, 385 (2008).

[161] T. Low and F. Guinea, "Strain-induced pseudomagnetic field for novel graphene electronics," Nano Letters **10**, 3551 (2010).

[162] S. Klembt, T. H. Harder, O. A. Egorov, K. Winkler, R. Ge, M. A. Bandres, M. Emmerling, L. Worschech, T. C. H. Liew, M. Segev, C. Schneider, and S. Höfling, "Exciton-polariton topological insulator," Nature **562**, 552 (2018).

[163] M. C. Rechtsman, J. M. Zeuner, Y. Plotnik, Y. Lumer, D. Podolsky, F. Dreisow, S. Nolte, M. Segev, and A. Szameit, "Photonic Floquet topological insulators," Nature **496**, 196 (2013).

[164] L. Tarruell, D. Greif, T. Uehlinger, G. Jotzu, and T. Esslinger, "Creating, moving and merging Dirac points with a Fermi gas in a tunable honeycomb lattice," Nature **483**, 302 (2012).

[165] Y. Hasegawa, R. Konno, H. Nakano, and M. Kohmoto, "Zero modes of tight-binding electrons on the honeycomb lattice," Physical Review B **74**, 033 413 (2006).

[166] M. C. Rechtsman, J. M. Zeuner, A. Tünnermann, S. Nolte, M. Segev, and A. Szameit, "Strain-induced pseudomagnetic field and photonic Landau levels in dielectric structures," Nature Photonics **7**, 153 (2013).

[167] E. L. Shirley, L. Terminello, A. Santoni, and F. Himpsel, "Brillouin-zone-selection effects in graphite photoelectron angular distributions," Physical Review B **51**, 13 614 (1995).

[168] Y. V. Kartashov and D. V. Skryabin, "Two-dimensional topological polariton laser," Physical Review Letters **122**, 083 902 (2019).